Dissertation zur Erlangung des Doktorgrades der Naturwissenschaften

vorgelegt beim Fachbereich 14 Biochemie, Chemie, Pharmazie

der Johann Wolfgang-Goethe-Universität

Frankfurt am Main

Biophysical investigations on the crosstalk and kinetics of the bacterial ABC-exporter MsbA by MAS-NMR

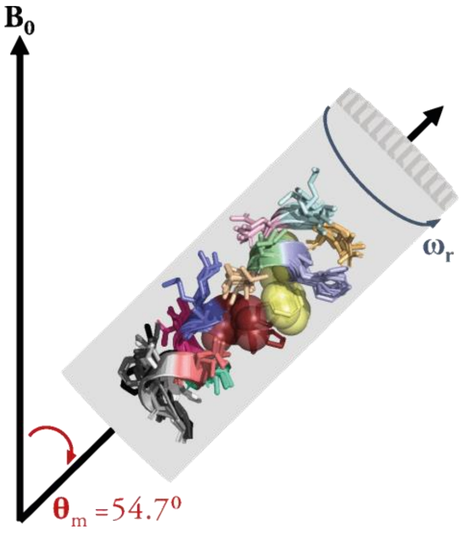

Von

S. Y. Phoebe Novischi

aus ’s-Gravenhage, Niederlande

Frankfurt am Main, 2023

Diese Arbeit wurde in der Arbeitsgruppe von Prof. Dr. Clemens Glaubitz im Institut für Biophysikalische Chemie an der Johann Wolfgang-Goethe-Universität in Frankfurt am Main durchgeführt und vom Fachbereich 14 (Biochemie, Chemie und Pharmazie) als Dissertation angenommen.

Dekan (Dean): Prof. Dr. Clemens Glaubitz

1. Gutachter (Primary advisor): Prof. Dr. Clemens Glaubitz

2. Gutachter (Secondary Advisor): Prof Dr. Martin Pos

Datum der Disputation:

“Rome ne fut pas faite toute en un jour.”

Li Proverbe au Vilain, c. 1190

Acknowledgement

First and foremost, I would like to express my gratitude to Prof. Dr Clemens Glaubitz for giving me the opportunity to do this PhD in his lab, for his patience and motivation, for being my support, guidance, and supervisor during my PhD, and for the freedom which allowed me to learn and work freely on and around my research projects. I would like to thank Dr Johanna Baldus-Becker for the support, guidance, and useful discussions around my research projects, but mostly for her incredible NMR brain that helped me set up the NMR experiments and through my puzzling NMR challenges, my NMR to-go-to person. I am very grateful for the laboratory and technical support from Ingrid Weber, the administrative support and the German pep talks from Simone Kobylka, and the help-XYZ-is-broken-in-our-lab technical support from Manfred Stumpf.

I would also like to express my gratitude to Prof. Dr Harald Schwalbe for allowing me to use the solution NMR facilities for my research project. I also wanted to thank Dr Christian Richter and Dr Elke Duchardt-Ferner for their support in the solution NMR facilities. And I would like to thank Heidi Zetsche, especially for helping me set up the solution NMR experiments. Furthermore, I would like to thank Dr Arne Moeller for his collaboration in the cryo-EM part. I would like to thank the TRAM SFB 807 members, Dr Rupert Abele and Dr Frank Bernhard as mentoring committee members for their insightful comments and discussions on my research projects, Prof. Dr Martin Pos, and Dr Eric Geertsma for sharing their great research knowledge and advice, and Katherina Welling and Jutta Uphoff for providing the funding throughout the project and the organization of talks, workshops, and retreats. I would like to thank Dr Reinke Müller for teaching me how to set up the screening conditions for the cellular assays. Many thanks to Dr Thomas Hackl from Hamburg University for his kind help with fitting the Lambert ω function and sending me the MATLAB script.

My special thanks go to the Glaubitz lab for the support, advice, counter advice, small talks, intermediate talks, big talks, boring talks, I-am-so-upset talks, pep talks, chitchats, all the cakes and cookies and alcohol, and for creating such a tremendous work atmosphere and for making our time fun and unforgettable, even during the everlasting two years COVID-19 pandemic! "So, I say thank you for the music, the songs I am singing, thanks for all the joy they are bringing. Who can live without it? I ask in all honesty. What would life be? Without a song or a dance, what are we?" [ABBA et al. 1977, The Album] So I say thank you for the music… Clara, Orawan (Dr. Jakdetchai), Kerby, Samuel, Marina, Aaron, Christian, Anne, Mahmoud (Dr. Doroudgar), Jagdeep (Dr. Kaur), Jiafei (Dr. Mao), Dr. Hundeep Kaur, Dr. Jakob Maciejko, Dr. Julian de Mos, and Dr. Kristin Möbius.

Last but not least, I would like to thank my family and friends, for bringing me so much joy and warmth, for being there and listening to their support and encouragement, but perhaps most importantly, for not giving up on me. I want to thank Nancy and Femke for coming to visit me. I would like to thank Ires for always being such a great listener and simply exceptionally good friend even if she is 1000 miles away. Finally, Iulian, my husband, my friend, my Clyde, my greatest fan. Thank you for believing in me!

Thank you all!

Summary

Chapter 1

The number of Gram-negative bacteria on the antibiotic resistance list of the WHO has grown significantly in the past several decades. It is estimated that by 2050 antibiotic resistance will be deadlier than cancer. The outer Gram-negative bacterial membrane is highly adaptive to environmental changes due to its major structural component, namely lipopolysaccharide (LPS). The LPS makes Gram-negative bacteria inherently resistant to many antibiotics, thus leading to antibiotic resistance. The bacterial ATP-binding cassette (ABC) transporter MsbA plays a critical role in the regulation of the bacterial outer membrane by flopping core LPS across the inner membrane of Gram-negative bacteria via ATP-hydrolysis. Blocking MsbA, thus prohibiting LPS transport, would make the pathogens more susceptible. Additionally, this floppase acts as an efflux pump by translocating drugs through the inner membrane, hence making it an interesting drug target. It is suggested that the coupling helices (CHs), located between the transmembrane region (TMD) and the nucleotide-binding domain (NBD) are involved in the cross-talk of MsbA lipid flopping. To this end, special attention is devoted to the interplay between the TMD and NBD via the CHs, with the aim to understand the substrate translocation process by using functional assays and solid-state NMR.

Chapter 2

Solid-state NMR allows a more native state of membrane proteins as the protein can be reconstituted into phospholipid bilayers that resemble the native phospholipid bilayer environment. Numerous membrane protein studies have been conducted using solid-state NMR which resulted in different scientifically relevant aspects. Furthermore, solid-state NMR could also be used to study protein dynamics of membrane proteins in the lipid bilayer through two-dimensional spectroscopy. Additionally, multidimensional as well as deuterium and phosphorus-31 NMR can be used to assign and highlight crucial residues in various states. This has been done for several ABC transporters, i.e., LmrA, BmrA, MsbA, and ArtMP. By using ^{31}P-NMR it was possible to 1) trap MsbA in various states (**Chapters 5-6**) and 2) study time-resolved ATP hydrolysis (**Chapter 4**). These states could then be used to determine important residues or parts of the protein within the different functions, e.g., nucleotide binding or substrate binding.

Chapter 3

MsbA was cloned with the pET19b expression vector and overexpressed in *E. coli* C43(DE3) cells. The membrane protein contains a 10x His-tag at the N-terminal which is connected by an 11 amino acid peptide linker. MsbA is initially cultured in Luria Broth and then transferred to the minimal microbial growth medium (M9 medium) or M9+ media with additional supplements. The minimal medium allows slow growth of the cells. Upon isopropyl β- d-1-thiogalactopyranoside (IPTG) induction the cells expressed significantly more MsbA. Membrane protein solubilisation is carried out by extracting the membrane of the cells. The cells are ruptured by running the suspension through a French press. Membranes are solubilised overnight. Upon 10x His-tag MsbA purification, the protein is reincorporated in a more native environment via a reconstitution process. For the reconstitution of MsbA, a mixture of 1,2-dimyristoyl-sn-glycero-3-phosphocholine (DMPC) and 1,2-dimyristoyl-sn-glycero-3-phosphate (DMPA) is used, with a 9 to 1 ratio, respectively. Reconstitution of MsbA in 1-palmitoyl-2-oleoyl-sn-glycero-3-phosphoethanolamine (POPE) and 1-Palmitoyl-2-Oleoyl-sn-Glycero-3-Phosphoglycerol (POPG) was done similarly as for MsbA in DMPC/DMPA. In this dissertation, the colourimetric assay is based on the molybdate assay to determine the catalytic activity of MsbA.

Chapter 4

The SDS-PAGE and western blot identified MsbA around 65 kDa. Similarly, for the blue native PAGE, the dimeric form of MsbA in DDM shows a maximum MsbA weight of 129 kDa with a 1.8x detergent factor, giving a total weight of approximately 232 kDa. MsbA was then further characterised with an ATPase assay. The sucrose gradient of reconstituted MsbA visualising no aggregations occurred during the reconstitution process. Additionally, the size exclusion chromatogram and cryo-EM showed no signs of aggregation. The resulting V_{MAX} values were 12.1, 8.5, and 13.9 µmol/min/mg, respectively for $_{WT}MsbA_{DDM}$, $_{WT}MsbA_{DMPC/DPMA}$, and $_{WT}MsbA_{POPE/POPG}$. The K_M values were 0.41, 0.35, and 0.44 µmol/min/mg, respectively. Across the various batches, both the V_{MAX} and K_M values were in the same order of magnitude. Stimulation of MsbA by Hoechst resulted in the highest stimulated activity at 100 µM Hoechst 33342.

Chapter 5

The allosteric interplay between substrate binding in the transmembrane domains and ATP binding and turnover in the nucleotide-binding domains must be mediated via the NBD/TMD interface. Biochemical data suggest the involvement of two intracellular loops called coupling helix 1 and 2 (CH1, CH2). This chapter demonstrates that substantial chemical shift changes within both CH1 and CH2 occur upon substrate binding, in the ATP hydrolysis transition state and upon inhibitor binding. CH2 is domain-swapped within the MsbA structure and it is noteworthy that especially substrate binding induces a much larger response in CH2 compared to CH1. This chapter shows the first direct evidence of structural changes within the coupling helices of type IV ABC transporters upon switching from the IF to the OF state and upon substrate and inhibitor binding. The data show that ADP.Vi binding and the IF→OF transition causes at the NBD-TMD interface a stronger response in CH1 while substrate binding has a stronger effect in CH2. It is noteworthy that the latter is based on a domain-swapped interaction with the NBD. Both cases are caused by stimuli with different vectoriality, namely nucleotide binding to the NBD and substrate binding to the TMD, which might then involve different pathways for NBD→TMD and TMD→NBD crosstalk. The data also demonstrate that CH-mediated crosstalk plays a role in the mechanism of an allosteric MsbA inhibitor, which binds in the TMD but prevents ATP hydrolysis in the NBD. The observed spectral signatures are different compared to the substrate-bound state, which indicates a different interaction pathway. This chapter provides selective data, which is highly complementary to the available 3D structures. Future solid-state NMR experiments will address the potential interaction between CH1 and CH2 and connect NMR data and 3D structures via computational approaches.

Chapter 6

MsbA is found in some of the ESKAPE pathogens strains (***E***. *faecium*, ***S***. *aureus*, ***K***. *pneumoniae*, ***A***. *baumannii*, ***P***. *aeruginosa, and* ***E***. *species*), that contribute to over 40% of the infections in the intensive care unit. Four out of six ESKAPE strains are Gram-negative bacteria. Recently, two distinct classes of MsbA inhibitors were discovered. Tetrahydrobenzothiophene (TBT)-based (1) which abolishes LPS transport, whilst allowing ATP-hydrolysis. On the other hand, the quinoline derivatives (2) block both ATP-hydrolysis and LPS translocation. In the latter, asymmetry was reported in the structure of MsbA. This chapter is focused on interactions of MsbA with G907, in particular, the role of the coupling helices to further understand the crosstalk of MsbA during ATP hydrolysis and substrate translocation. The binding of G907 resulted in substantial chemical shift changes for F115/F116 in CH1, while no change was detected for CH2. The proposed inhibition mechanism involves IF-state dependent binding of G907 which prevents transition to the OF state as well as asymmetric NBD-NBD uncoupling. Here, the NCA spectrum of [^{13}C, ^{15}N-K]-MsbA is similar to the IF- apo state spectrum but with some specific differences. For example, additional intensities occur around the K118/K465 cross peak and K328 appears shifted. Overall, a general structural asymmetry cannot be concluded from this spectrum, but the additional peak intensities could be an indication. In summary, the data show that G907 binding in the NBDs triggers signalling into the NBDs involving at least CH1 and stabilizing an IF state.

Chapter 7

Naturally, ABC transporters have their primary reaction where energy is obtained via ATP hydrolysis where ATP is converted into ADP and inorganic phosphate. However, recent NMR studies have shown that for MsbA under ATP depletion, a secondary reaction can take place. This secondary reaction is also known as the adenylate kinase reaction. Here ATP (+ AMP) is regenerated via two ADP molecules. This *de novo* adenine nucleotide synthesis was described previously as a function of a sufficient cellular energy regulation of nucleotide synthesis and nucleotide ratio in various cell compartments. It appears that in MsbA the second reaction is coupled with the primary ATP hydrolysis. This process could be important for the cell when ATP is exhausted. Therefore, the adenylate kinase reaction in MsbA was further explored using time-resolved ^{31}P NMR. MsbA appears to have undergone the adenylate kinase reaction, which resulted in a clear ATP build-up. The maximum ATP build-up in the MsbA apo state was approximately 10% based on the initially added ADP in the reaction. The build-up with substrates was particularly higher, approximately 4-6-fold (40-60%) when compared to the apo state. Possibly, in this way, MsbA can transport the substrates using the primary ATP hydrolysis. Based on the results of the ATP hydrolysis in ^{31}P lsNMR and ssNMR, MsbA primarily hydrolyses ATP. The k_{ATP} is generally higher than the k_{ADP}. Interestingly, the ADP consumption appears to be rather slow in the apo state when MsbA sits in membranes. Depending on the substrates or depletion conditions MsbA has the ability to (re)generate ATP via the adenylate kinase reaction, which has already been indicated by the ADP consumption using various substrates.

Outlook

This dissertation provides selective data, which are highly complementary to the available 3D structures. Future solid-state NMR experiments will address the potential interaction between CH1 and CH2 and connect NMR data and 3D structures via computational approaches. Furthermore, a more in-depth progress curve analysis could provide more information in addition to the rate analysis. Together, the observations here indicate that MsbA can (re)generate ATP via the adenylate kinase reaction under certain conditions (i.e., ATP depletion, substrates, and substrate physicochemical properties) and this appears to be coupled to the substrate transport. Hence, MsbA should be a good candidate to further explore novel antibiotics in ESKAPE pathogen strains.

Zusammenfassung

Kapitel 1

Die Zahl der gramnegativen Bakterien, die auf der Antibiotikaresistenzliste der WHO stehen, ist in den letzten Jahrzehnten erheblich gestiegen. Man schätzt, dass die Antibiotikaresistenz bis 2050 tödlicher sein wird als Krebs. Die äußere Membran gramnegativer Bakterien ist aufgrund ihrer wichtigsten Strukturkomponente, dem Lipopolysaccharid (LPS), sehr anpassungsfähig an Umweltveränderungen. Das LPS macht gramnegative Bakterien von Natur aus resistent gegen viele Antibiotika und führt so zur Antibiotikaresistenz. Der bakterielle ATP-bindende Kassetten-Transporter (ABC-Transporter) MsbA spielt eine entscheidende Rolle bei der Regulierung der bakteriellen Außenmembran, indem er in einigen schädlichen ESKAPE-Erregerstämmen Kern-LPS durch ATP-Hydrolyse über die Innenmembran von gramnegativen Bakterien schiebt. Es tut dies, indem es Kern-LPS über die innere Membran in gramnegativen Bakterien als Teil des LPS-Schutzweges zur äußeren gramnegativen bakteriellen Zellwand schiebt. Die Blockierung von MsbA und damit die Unterbindung des LPS-Transports würde die Krankheitserreger anfälliger machen. In den letzten zwei Jahrzehnten wurden viele Kristallstrukturen von MsbA gefunden, die verschiedene Konformationen zeigen. Es wurde eine breitere Apo- oder nach innen gerichtete Konformation diskutiert, die möglicherweise eher auf eine Detergenzmizellen-Umgebung des Membranproteins als auf eine nativere Lipiddoppelschicht-Umgebung zurückzuführen ist. Daher wurde MsbA zur Untersuchung menschlicher ABC-Transporter-Homologe wie P-Glykoprotein verwendet. Darüber hinaus fungiert diese Floppase als Efflux-Pumpe, die Medikamente durch die innere Membran transportiert, was sie zu einem interessanten Ziel für Medikamente macht. Es wird vermutet, dass die koppelnden Helices (CHs), die sich zwischen der Transmembranregion (TMD) und der Nukleotid-bindenden Domäne (NBD) befinden, am Cross-Talk des MsbA-Lipid-Floppings beteiligt sind. Zu diesem Zweck wird dem Zusammenspiel zwischen der TMD und der NBD über die CHs besondere Aufmerksamkeit gewidmet, mit dem Ziel, den Prozess der Substrattranslokation mit Hilfe von funktionellen Assays und Festkörper-NMR zu verstehen.

Kapitel 2

Die Festkörper-NMR ermöglicht einen nativeren Zustand von Membranproteinen, da das Protein in Phospholipiddoppelschichten rekonstituiert werden kann, die der nativen Umgebung der Phospholipiddoppelschicht ähneln. Zahlreiche Untersuchungen von Membranproteinen wurden mit Hilfe der Festkörper-NMR durchgeführt und ergaben verschiedene wissenschaftlich relevante Aspekte. Darüber hinaus könnte die Festkörper-NMR auch zur Untersuchung der Proteindynamik von Membranproteinen in der Lipiddoppelschicht durch zweidimensionale Spektroskopie eingesetzt werden. MsbA wurde durch Röntgen-, Kryo-EM- und NMR-Spektroskopie in vielen verschiedenen Zuständen erfasst. Letztere zeigte verschiedene Zustände, wie ADP.Vi+ADPβS und ADP.Vi+AMP, die zuvor nicht in Röntgen- oder Kryo-

EM-Strukturen von MsbA beobachtet wurden. Daher scheint MsbA einen de novo Adenin-Nukleotid-Synthesemechanismus zu haben, der als Adenylat-Kinase-Reaktion bezeichnet wird. Echtzeit-31P-Lösung und Festkörper-NMR sind gute Methoden, um diese Reaktionen genau zu untersuchen. Es wird angenommen, dass diese Hydrolysereaktionen mit dem MsbA-Transport von LPS und anderen Substraten über die Kopplungshelices gekoppelt sind. Einzigartige Paarmarkierungen in der ssNMR führten zu spezifischen Peaks mit guter Auflösung und ermöglichten einen detaillierteren Blick auf die Konformationsdynamik und das Übersprechen der Kopplungshelices von MsbA in DMPC/DPMA (9:1) und POPE/POPG (4:1) Membranen. Zusätzlich können multidimensionale sowie Deuterium- und Phosphor-31-NMR verwendet werden, umentscheidende Rückstände in verschiedenen Zuständen zuzuordnen und hervorzuheben. Dies wurde für mehrere ABC-Transporter, d. h. LmrA, BmrA, MsbA und ArtMP, durchgeführt. Durch den Einsatz von 31P-NMR war es möglich, 1) MsbA in verschiedenen Zuständen einzufangen (Kapitel 5-6) und 2) die zeitaufgelöste ATP-Hydrolyse zu untersuchen (Kapitel 4). Diese Zustände konnten dann verwendet werden, um wichtige Reste oder Teile des Proteins im Rahmen der verschiedenen Funktionen zu bestimmen, z. B. Nukleotidbindung oder Substratbindung.

Kapitel 3

MsbA wurde mit dem pET19b-Expressionsvektor kloniert und in *E. coli* C43(DE3) -Zellen überexprimiert. Das Membranprotein enthält am N-Terminus einen 10x His-Tag, der durch einen 11 Aminosäuren langen Peptidlinker verbunden ist. MsbA wird zunächst in Luria-Bouillon kultiviert und dann mit zusätzlichen Zusätzen auf das minimale mikrobielle Wachstumsmedium (M9-Medium) oder M9+-Medium übertragen. Das Minimalmedium ermöglicht ein langsames Wachstum der Zellen. Nach der Induktion von Isopropyl-β-d-1-thiogalactopyranosid (IPTG) exprimierten die Zellen deutlich mehr MsbA. Die Solubilisierung von Membranproteinen erfolgt durch Extraktion der Zellmembran. Die Zellen werden aufgebrochen, indem man die Suspension durch eine French Press laufen lässt. Membranen werden über Nacht solubilisiert. Nach der 10-fachen His-Tag-MsbA-Reinigung wird das Protein über einen Rekonstitutionsprozess in einer nativeren Umgebung wieder eingebaut. Zur Rekonstitution von MsbA wird eine Mischung aus 1,2-Dimyristoyl-sn-glycero-3-phosphocholin (DMPC) und 1,2-Dimyristoyl-sn-glycero-3-phosphat (DMPA) im Verhältnis 9 zu 1 verwendet Verhältnis bzw. Die Rekonstitution von MsbA in 1-Palmitoyl-2-oleoyl-sn-glycero-3-phosphoethanolamin (POPE) und 1-Palmitoyl-2-Oleoyl-sn-glycero-3-phosphoglycerol (POPG) erfolgte ähnlich wie für MsbA in DMPC/ DMPA. In dieser Dissertation basiert der kolorimetrische Assay auf dem Molybdat-Assay zur Bestimmung der katalytischen Aktivität von MsbA.

Kapitel 4

Die SDS-PAGE und der Western Blot identifizierten MsbA mit etwa 65 kDa. In ähnlicher Weise zeigt die dimere Form von MsbA in DDM für die blaue native PAGE ein maximales MsbA-Gewicht von 129 kDa mit einem 1,8-fachen Detergensfaktor, was ein Gesamtgewicht von etwa 232 kDa ergibt. MsbA wurde dann mit einem ATPase-Assay weiter charakterisiert. Der Saccharosegradient von rekonstituiertem MsbA zeigt, dass während des Rekonstitutionsprozesses keine Aggregationen auftraten. Darüber hinaus zeigten das Größenausschlusschromatogramm und die Kryo-EM keine Anzeichen einer Aggregation. Die resultierenden V_{MAX}-Werte betrugen 12,1, 8,5 bzw. 13,9 µmol/min/mg für $_{WT}\mathrm{MsbA}_{DDM}$, $_{WT}\mathrm{MsbA}_{DMPC/DPMA}$ und $_{WT}\mathrm{MsbA}_{POPE/POPG}$. Die K_M-Werte betrugen 0,41, 0,35 bzw. 0,44 µmol/min/mg. Über die verschiedenen Chargen hinweg lagen sowohl die V_{MAX}- als auch die K_M-Werte in der gleichen Größenordnung. Die Stimulation von MsbA durch Hoechst führte zur höchsten stimulierten Aktivität bei 100 µM Hoechst 33342.

Kapitel 5

Das allosterische Zusammenspiel zwischen der Substratbindung in den Transmembrandomänen und der ATP-Bindung und dem ATP-Umsatz in den Nukleotidbindungsdomänen muss über die NBD/TMD-Schnittstelle vermittelt werden. Biochemische Daten deuten auf die Beteiligung zweier intrazellulärer Schleifen hin, die als Kopplungshelix 1 und 2 (CH1, CH2) bezeichnet werden. Dieses Kapitel zeigt, dass bei der Substratbindung, im ATP-Hydrolyse-Übergangszustand und bei der Inhibitorbindung erhebliche chemische Verschiebungsänderungen sowohl in CH1 als auch in CH2 auftreten. CH2 ist innerhalb der MsbA-Struktur domänengetauscht und es ist bemerkenswert, dass insbesondere die Substratbindung in CH2 im Vergleich zu CH1 eine viel größere Reaktion hervorruft. Dieses Kapitel zeigt den ersten direkten Beweis für strukturelle Veränderungen innerhalb der Kopplungshelices von Typ-IV-ABC-Transportern beim Wechsel vom IF- in den OF-Zustand und bei der Substrat- und Inhibitorbindung. Die Daten zeigen, dass die ADP.Vi-Bindung und der IF→OF-Übergang an der NBD-TMD-Schnittstelle eine stärkere Reaktion in CH1 hervorrufen, während die Substratbindung eine stärkere Wirkung in CH2 hat. Bemerkenswert ist, dass Letzteres auf einer domänengetauschten Interaktion mit dem NBD basiert. Beide Fälle werden durch Reize mit unterschiedlicher Vektorialität verursacht, nämlich durch Nukleotidbindung an die NBD und Substratbindung an die TMD, die dann möglicherweise unterschiedliche Wege für NBD→TMD und TMD→NBD-Crosstalk beinhalten. Die Daten zeigen auch, dass CH-vermittelter Crosstalk eine Rolle im Mechanismus eines allosterischen MsbA-Inhibitors spielt, der im TMD bindet, aber die ATP-Hydrolyse im NBD verhindert. Die beobachteten spektralen Signaturen unterscheiden sich im Vergleich zum substratgebundenen Zustand, was auf einen anderen Wechselwirkungsweg hinweist. Dieses Kapitel stellt ausgewählte Daten bereit, die die verfügbaren 3D-Strukturen in hohem Maße ergänzen. Zukünftige Festkörper-NMR-Experimente werden sich mit der möglichen Wechselwirkung zwischen CH1 und CH2 befassen und NMR-Daten und 3D-Strukturen über rechnerische Ansätze verbinden.

Kapitel 6

MsbA findet sich in einigen der ESKAPE-Erregerstämme (E. faecium, S. aureus, K. pneumoniae, A. baumannii, P. aeruginosa und E. species), die zu über 40 % der Infektionen auf der Intensivstation beitragen. Vier von sechs ESKAPE-Stämmen sind gramnegative Bakterien. Vor kurzem wurden zwei verschiedene Klassen von MsbA-Inhibitoren entdeckt. Tetrahydrobenzothiophen (TBT) (1), das den LPS-Transport unterbindet, aber die ATP-Hydrolyse ermöglicht. Die Chinolinderivate (2) hingegen blockieren sowohl die ATP-Hydrolyse als auch die LPS-Translokation. Bei letzterem wurde eine Asymmetrie in der Struktur von MsbA festgestellt. Dieses Kapitel konzentriert sich auf die Wechselwirkungen von MsbA mit G907, insbesondere auf die Rolle der Kopplungshelices, um das Zusammenspiel von MsbA während der ATP-Hydrolyse und der Substrattranslokation besser zu verstehen. Die Bindung von G907 führte zu erheblichen Veränderungen der chemischen Verschiebung von F115/F116 in CH1, während für CH2 keine Veränderung festgestellt wurde. Der vorgeschlagene Hemmungsmechanismus beinhaltet eine vom IF-Zustand abhängige Bindung von G907, die den Übergang in den OF-Zustand verhindert, sowie eine asymmetrische NBD-NBD-Entkopplung. Das NCA-Spektrum von [13C, 15N-K]-MsbA ähnelt dem Spektrum des IF-Apo-Zustands, weist jedoch einige spezifische Unterschiede auf. So treten beispielsweise zusätzliche Intensitäten um den K118/K465-Kreuzungspeak auf, und K328 erscheint verschoben. Insgesamt kann aus diesem Spektrum nicht auf eine allgemeine strukturelle Asymmetrie geschlossen werden, aber die zusätzlichen Peakintensitäten könnten ein Hinweis darauf sein. Zusammenfassend zeigen die Daten, dass die Bindung von G907 in den NBDs eine Signalübertragung in die NBDs auslöst, an der mindestens CH1 beteiligt ist und die einen IF-Zustand stabilisiert.

Kapitel 7

Die Hauptreaktion der ABC-Transporter besteht natürlich in der Energiegewinnung durch ATP-Hydrolyse, bei der ATP in ADP und anorganisches Phosphat umgewandelt wird. Jüngste NMR-Studien haben jedoch gezeigt, dass bei MsbA unter ATP-Mangel eine Sekundärreaktion stattfinden kann. Diese Sekundärreaktion wird auch als Adenylatkinasereaktion bezeichnet. Dabei wird ATP (+ AMP) über zwei ADP-Moleküle regeneriert. Diese de novo Adenin-Nukleotid-Synthese wurde früher als Funktion einer ausreichenden zellulären Energieregulierung der Nukleotid-Synthese und des Nukleotid-Verhältnisses in verschiedenen Zellkompartimenten beschrieben. Es scheint, dass in MsbA die zweite Reaktion mit der primären ATP-Hydrolyse gekoppelt ist. Dieser Prozess könnte für die Zelle wichtig sein, wenn das ATP erschöpft ist. Daher wurde die Adenylatkinase-Reaktion in MsbA mit zeitaufgelöster 31P-NMR weiter untersucht. Die Untersuchung von MsbA mit 31P-lsNMR bestätigte, dass MsbA die Adenylatkinase-Reaktion durchläuft, wenn ATP verbraucht ist, wie frühere Studien gezeigt haben. Darüber hinaus scheint MsbA bei Zugabe von Substraten wie Vinblastin und H33342 die Adenylatkinase-Reaktion durchlaufen zu haben, was zu einem deutlichen ATP-Aufbau führte. Außerdem wird gezeigt, dass das Molekulargewicht, die Anzahl der Wasserstoffbrückenbindungsakzeptoren und -donatoren, die polare Oberfläche, log D und log P der Substrate mit dem AMP/Pi-Verhältnis korreliert sind. Im Allgemeinen ist die ATP-Hydrolyse unter den verschiedenen getesteten Bedingungen (DDM-Mizellen, DMPC/DMPA, POPE/POPG(/CL)) recht schnell. Andererseits scheint der ADP-Verbrauch eher von der Proteinumgebung abzuhängen. Befindet sich MsbA in einer nativeren Umgebung, z. B. in POPE/POPG- oder POPE/POPG/Kardiolipin-Membranen, scheint der ADP-Verbrauch im Vergleich zu MsbA in DDM-Micellen und in DMPC/DMPA-Membranen sehr langsam zu sein. MsbA scheint die Adenylatkinase-Reaktion durchlaufen zu haben, was zu einem deutlichen ATP-Aufbau führte. Der maximale ATP-Aufbau im MsbA-Apo-Zustand betrug ca. 10 %, bezogen auf das ursprünglich zugegebene

ADP in der Reaktion. Der Aufbau mit Substraten war besonders hoch, etwa 4-6-fach (40-60%) im Vergleich zum apo-Zustand. Möglicherweise kann MsbA auf diese Weise die Substrate über die primäre ATP-Hydrolyse transportieren. Basierend auf den Ergebnissen der ATP-Hydrolyse in 31P lsNMR und ssNMR, hydrolysiert MsbA primär ATP. Der k_{ATP}-Wert ist im Allgemeinen höher als der k_{ADP}-Wert. Interessanterweise scheint der ADP-Verbrauch im apo-Zustand eher langsam zu sein, wenn MsbA in Membranen sitzt. Abhängig von den Substraten oder den Verarmungsbedingungen hat MsbA die Fähigkeit, ATP über die Adenylatkinase-Reaktion (wieder) zu erzeugen, was bereits durch den ADP-Verbrauch unter Verwendung verschiedener Substrate angedeutet wurde. MsbA scheint seine primäre ATP-Hydrolysereaktion gegenüber dem ADP-Nukleotid zu bevorzugen, worauf auch der ADP-Verbrauch unter Verwendung verschiedener Substrate hinweist.

Ausblick

Diese Dissertation liefert selektive Daten, die die verfügbaren 3D-Strukturen in hohem Maße ergänzen. Zukünftige Festkörper-NMR-Experimente werden sich mit der potenziellen Wechselwirkung zwischen CH1 und CH2 befassen und NMR-Daten und 3D-Strukturen über rechnerische Ansätze miteinander verbinden. Darüber hinaus könnte eine eingehendere Analyse der Verlaufskurve zusätzlich zur Ratenanalyse weitere Informationen liefern. Insgesamt deuten die hier gemachten Beobachtungen darauf hin, dass MsbA unter bestimmten Bedingungen (d. h. ATP-Abnahme, Substrate und physikochemische Eigenschaften des Substrats) ATP über die Adenylatkinase-Reaktion (wieder) erzeugen kann, und dies scheint an den Substrattransport gekoppelt zu sein. Daher sollte MsbA ein guter Kandidat für die weitere Erforschung neuer Antibiotika in ESKAPE-Pathogenstämmen sein.

Table of Contents

PART I General Introduction

PART II The influence of nucleotides and substrates on MsbA

APPENDIX

A

PART I

General introduction

Chapter 1 The essence of membrane proteins

Chapter 2 Application of nuclear magnetic resonance spectroscopy

Chapter 3 The preparation of the bacterial membrane protein MsbA

Chapter 1

The essence of membrane proteins

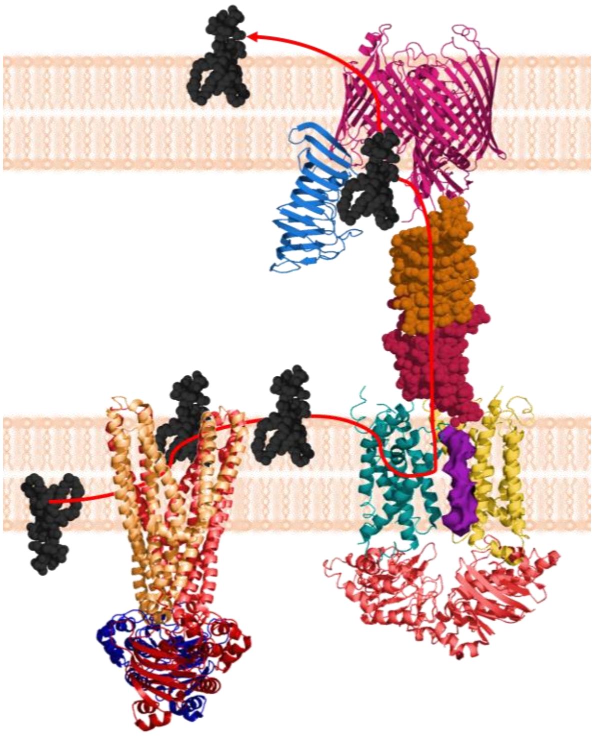

"Logic will get you from A to B. Imagination will take you everywhere."

– *Albert Einstein*

1.1 Membrane proteins: a pharmacological hotspot

The human genome consists of thirty to forty thousand protein-encoding genes[1]. Thirty per cent of these proteins represent membrane proteins[2-4]. Membrane proteins play an essential role in biological processes. They are involved in numerous processes such as maintaining homeostasis, determination of cell shape, redox reactions, signalling transduction, energy production, cell-cell interactions, protein-protein interactions, and transportation of nutrients and small molecules[5-7].

Due to their abundance, membrane proteins play an important role in various types of pathologies. G-coupled protein receptors (GPCRs), major facilitator superfamily – *including solute carrier proteins (SLCs)* – and ATP-binding cassette (ABC) transporters are amongst the largest membrane protein superfamilies.[2,8-10] These three groups alone already play a major role in diseases, such as cancer[11-13], diabetes mellitus[13,14], Alzheimer's disease[15-17], cardiovascular diseases[18-21], and tuberculosis[22], which are listed by the World Health Organization and the Centres for Disease Control and Prevention as the worlds' top ten deathliest diseases[23,24].

Based on their secondary structure in the transmembrane region, these proteins can be divided into two groups. The transmembrane regions with β-barrels (**figure 1.1G**) can be found in the outer membrane layer of mitochondria, chloroplasts, and Gram-negative bacteria. The α-helices provide functional diversity and are therefore more common and abundantly distributed[25].

There are seven types of membrane proteins, which can be divided into three main groups, namely integral, peripheral, and lipid-anchored proteins. Integral membrane proteins are transmembrane proteins due to their hydrophobic protrusion, hence making it difficult to remove them from their native environment (**figure 1.1A-D**). Peripheral membrane proteins form electrostatic interactions and hydrogen bonds with the bilayer (**figure 1.1E**). Lastly, the covalent bilayer anchored proteins contain a fatty acid linkage, usually an isoprenyl or a glycosylphosphatidylinositol (GPI) group (**figure 1F**)[26,27].

Drug and target discovery, hence modern medicines, would not be possible without structural protein knowledge. Currently, membrane proteins represent more than half of the druggable targets on the pharmaceutical market[25,28,29]. The Protein Data Bank holds over 155.000 structural data acquired by crystallography, NMR spectroscopy, and (cryo) electron microscopy[28]. Despite this, membrane proteins remain challenging to study[30,31]. It has been long known that membrane proteins need their biological environment (i.e. lipid bilayer) to support their structure and function, as for any other protein[32,33].

However, the conventional method to yield them from their natural environment is detergent solubilization. This bottleneck initially could lead to flexibility, instability, and unfolding[31,34,35]. Besides this, protein overexpression and purification share a challenging workflow[31,36]. An emerging method to overcome these complications is cell-free protein synthesis (CFPS). Here, the protein can be yielded immediately in lipid and nanodiscs and avoid detergent contact. Nevertheless, this is not so straightforward as cell-free expression encounters similar challenges as in detergent solubilization when it comes to providing a proper environment for protein folding[37-39]. Additionally, data collection of crystallized or reconstituted membrane proteins is not always effortless, due to e.g. unnatural micelle environments[40], lateral diffusion, and heterogeneities[41,42].

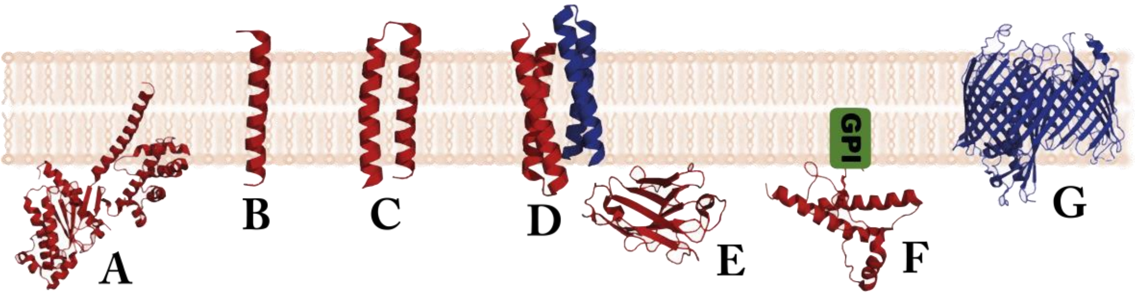

Figure 1.1 Schematic overview of main membrane protein classes. Integral membrane or transmembrane proteins (a) integral monotopic protein, b single-pass protein, c polytopic protein, and d multi-subunit complex) contain one or more hydrophobic regions that penetrate the lipid bilayer. Peripheral proteins (e) interact with the lipid bilayer through electrostatic interactions and hydrogen bonds. Lipid-anchored proteins (f) are covalently linked to the lipid bilayer through a fatty acid[26]. Finally, an example showed a bacterial β-barrel (g). *Protein structures from the protein data bank were used and adapted to visualize the explanation above.*

Some membrane proteins are involved in the transport of compounds such as nutrients and cellular waste. Membrane transporters not only play a vital role in the transportation of endogenous and exogenous compounds, but their mechanism has acquired an important place in contemporary medicines. Their role can be critical in pharmacology concerning absorption, distribution, metabolism, and excretion (ADME), which involves drug delivery, therapeutic efficacy, and adverse drug reactions[43]. They also contribute to multidrug resistance of antibiotics and therapeutic cancer treatments. Multidrug resistance regards drug disposition caused by multidrug-resistant protein (MRP) and multidrug and toxin extrusion transporter (MATE) families[43]. P-glycoprotein (also known as MDR1, ABCB1, and cluster of differentiation CD243) is a well-known and extensively studied example of an ABC transporter/efflux pump[43-46].

There are several membrane transport mechanisms in which cells can import and export compounds in and out of the cell (figure 1.2). This can be divided into four main pathways, namely simple diffusion, facilitated diffusion (also known as passive transport), active transport, and endo- and exocytosis. Simple diffusion and passive transport are spontaneous processes that are based on the movement towards the equilibrium, hence, the concentration gradient. Active transport is based on four types of ATPases (i.e. P-type, V-type, F-type, and ABC-type ATPases), thus requiring an exogenic reaction such as ATP hydrolysis to transport compounds across membranes[26,27]. In the context of general therapeutic interests described above, in this dissertation, the focus lies on the ACB-type ATPases, generally known as ABC transporters, emphasising ABC exporters.

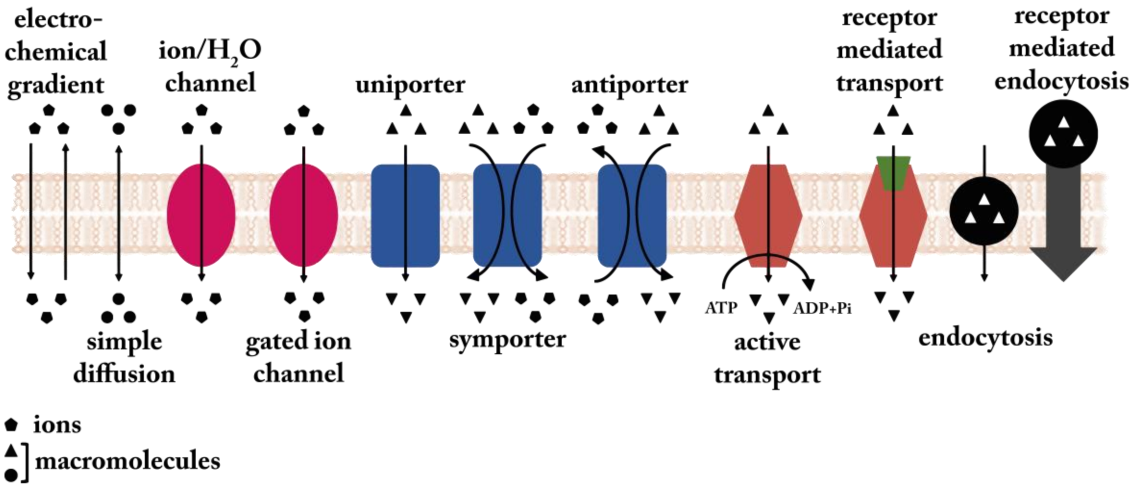

Figure 1.2. Schematic overview of main membrane transport mechanisms. Simple diffusion and passive transport (pink and blue) are spontaneous processes that are based on movement with the concentration gradient, including receptor-mediated transport (orange). Active transport (orange) requires ATP hydrolysis to execute transport across the membrane. Endocytosis (and exocytosis, black and grey) is a unique process that requires the cell wall to form a vesicle and ingest the compounds for transport[26,47].

1.2 The ATP-Binding Cassette Superfamily

ABC transporters are known to be involved in multiple cancerous diseases and antibiotic resistance in diseases such as tuberculosis, as described previously. In the case of protein dysfunction, it can lead to diseases such as cystic fibrosis caused by a mutation in the cystic fibrosis transmembrane conductance regulator (CFTR, also known as ABCC7). When this ABC transport protein is not functioning correctly, chloride can no longer be transported to the cell surface, and mucus will accumulate in various vital organs such as the lungs, pancreas, and intestines[48,49].

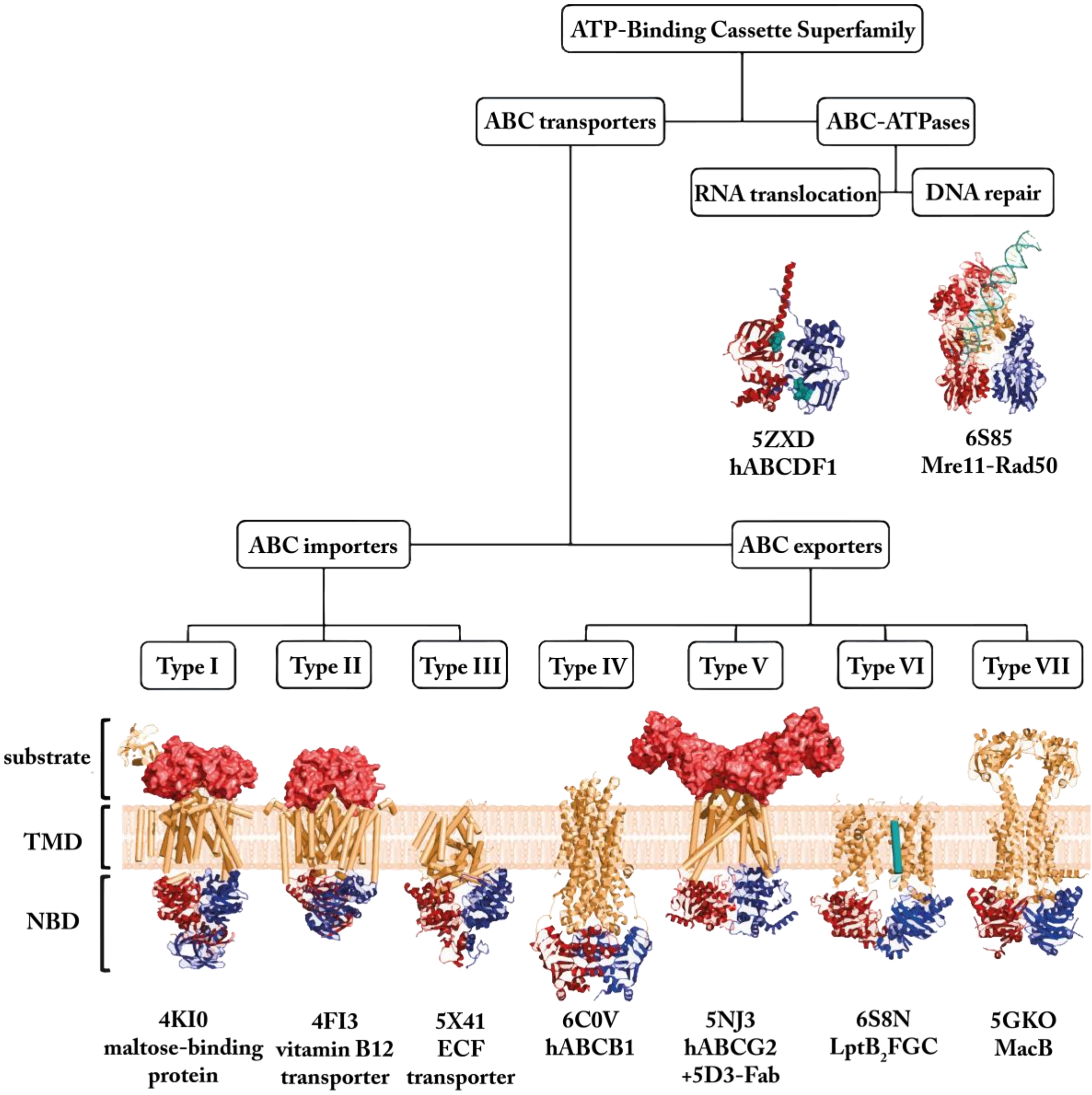

Figure 1.3. Overview of various example types of ABC transporters. 4KI0.pdb *E. coli* maltose transporter MalFGK. 4FI3.pdb *E. coli* vitamin B12 transporter BtuCDF. 5X41.pdb *R. capsulatus* cobalt energy-coupling factor transporter. 6C0V.pdb *H. sapiens* P-glycoprotein. 5NJ3.pdb *H. sapiens* multidrug transporter ABCG2. 6S8N.pdb *E. coli* LtpB$_2$FGC. 5GKO.pdb *A. baumannii* MacB. 5ZXD.pdb the *H. sapiens* ABCF1 (ABC50) involves RNA translation processes. 6S85.pdb *E. coli* DNA binding protein Mre11-Rad50.

The ABC superfamily has various subtypes (figure 1.3). Firstly, it can be divided into two main groups, the ABC transporters and the ABC-ATPases, respectively with and without transmembrane regions. The

ABC-ATPases have two subgroups that are involved in RNA translation and DNA repair. The membrane transporters can be further divided into various subtypes of ABC importers and exporters. Furthermore, the transporters can be homodimers (e.g., MsbA), heterodimers (e.g., TmrAB), or made up of dimeric sets of transmembrane (TMD) and nucleotide-binding domain (NBD) subunits (e.g., LtpB$_2$FG).

The three types of ABC importers regulate the uptake of bacterial nutrients. Type I and II have two NBDs and a TMD that penetrate the lipid bilayers and allow substrate binding through a substrate-binding protein (SBP). The uptake of small molecules such as sugars, metabolites, amino acids, peptides, and ions is facilitated by type I importers such as the bacterial maltose transporter (MalFGK). Larger and more hydrophobic substrates such as iron-containing complexes and vitamins are imported via type II transporters (e.g., vitamin B12 BtuCD-F). Additionally, type III importers (also known as energy-coupling factor (EFC) proteins) allow the uptake of cofactors, metal ions, and amino acids (e.g., thiamin, riboflavin, folate, and biotin). Type III ABC importers consist of a transmembrane coupling domain (EcfT) in addition to the two NBDs[50-55]. Furthermore, importers that have similar structural folds to exporters have also been reported (YbtPQ, figure 1.4)[56].

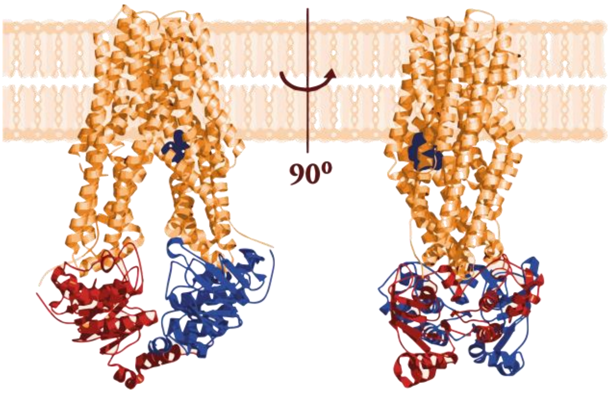

Figure 1.4. An example of an ABC importer folded as an ABC exporter. 6P6J.pdb Structure of *E. coli* YbtPQ importer with substrate Ybt-Fe bound (in deep teal) captured by cryo-electron microscopy in 2,2-didecylpropane-1,3-bis-β-D-maltopyranoside (LMNG) detergent.

Unlike prokaryotes which have both ABC importers and exporters to facilitate nutrients and toxins, humans only have exporters. ABC exporters are the main reason behind therapeutic failures due to its drug resistance efflux mechanism in humans whilst parasitic, fungal, and bacterial cells. Currently, forty-nine genes in this cluster are classified into seven subfamilies (A-G) serving as channels, receptors, or transporters: ABCA (13 members), ABCB (11 members), ABCC (11 members), ABCD (4 members), ABCE (1 member), ABCF (3 members), and ABCG (5 members). Consequently, protein misfolding and/or protein mutations lead to many lethal diseases[57-59].

The ABCA subclass consists of 13 members and is expressed abundantly in the human body across the brain, lung, skeletal muscle, kidney, liver, placenta, heart, stomach, trachea, testis, and bone marrow[60]. Furthermore, it plays a role in the shuttling of vitamin E, and this in turn can affect neurological diseases such as Alzheimer's and Parkinson's[61]. Additionally, high expression levels of various ABCA transporter genes are found to be associated with a poor outcome in epithelial ovarian cancer[62]. Functional deficiency of the ABCA subtypes 3 and 12 leads to Harlequin ichthyosis[63]. In the case of subtype 1, ABCA1 appears to have an important role in HDL cholesterol transport, and polymorphism has been associated with Tangier disease, atherosclerosis, coronary artery disease, and diabetes[64,65].

A familiar ABCB transporter protein is the P-glycoprotein, which resides in the brain and is responsible for multidrug resistance, particularly over the blood-brain barrier[66]. In addition, this protein is known to be highly expressed in cancer cells, thus resulting in an efflux of anticancer drugs[67,68]. Moreover, it is also a known efflux pump for β-adrenoceptor antagonists, Ca^{2+} channel blockers, HIV protease inhibitors, steroids, immunosuppressants, antiemetic drugs, antibiotics, antimicrobials, antiretrovirals, lipid-lowering agents, histamine H1-receptor antagonists, phenobarbital, phenytoin, and more[69]. The subtypes 4 and 11 have been related to progressive familial intrahepatic cholestasis (PFIC). This group of rare liver diseases is heterogeneous. It is an autosomal recessive inheritance and presents intrahepatic cholestasis in infancy or early childhood and results in end-stage liver disease (ESLD) and death without liver transplantation[70].

The multidrug resistance protein 1 (MPR1) is part of the ABCC subclass, alongside CFTR as described earlier[71]. High expression of MPR1 is known to be associated with a poor outcome of neuroblastomas and relapse in acute lymphoblastic leukaemia in paediatric patients[72,73]. Paclitaxel and doxorubicin are known substrates to this subtype[74]. ABCC plays an important role in human homeostasis through the transport of leukotriene, bilirubin glucuronides, prostaglandins E1 and E2, cGMP, and some glucuronosyl or sulfatide steroids[75,76]. Furthermore, ABCC is amply distributed in the human body. Subtype 1 is found in the lung, testis, kidney, skeletal, blood–tissue barriers, cardiac muscles, placenta, and macrophages. ABCC2, ABCC3, and ABCC6 are found in vital organs, such as the liver, kidney, small intestine, colon, gallbladder, placenta, lungs, adrenal gland, pancreas, and gut. Whereas type 5 is found in skeletal muscle and cardiac and cardiovascular myocytes. For ABCC10 high expressions are found in the colon, skin, and testes. Lastly, subtype 11 is found highest in the liver, brain, placenta, breasts, and testes[77].

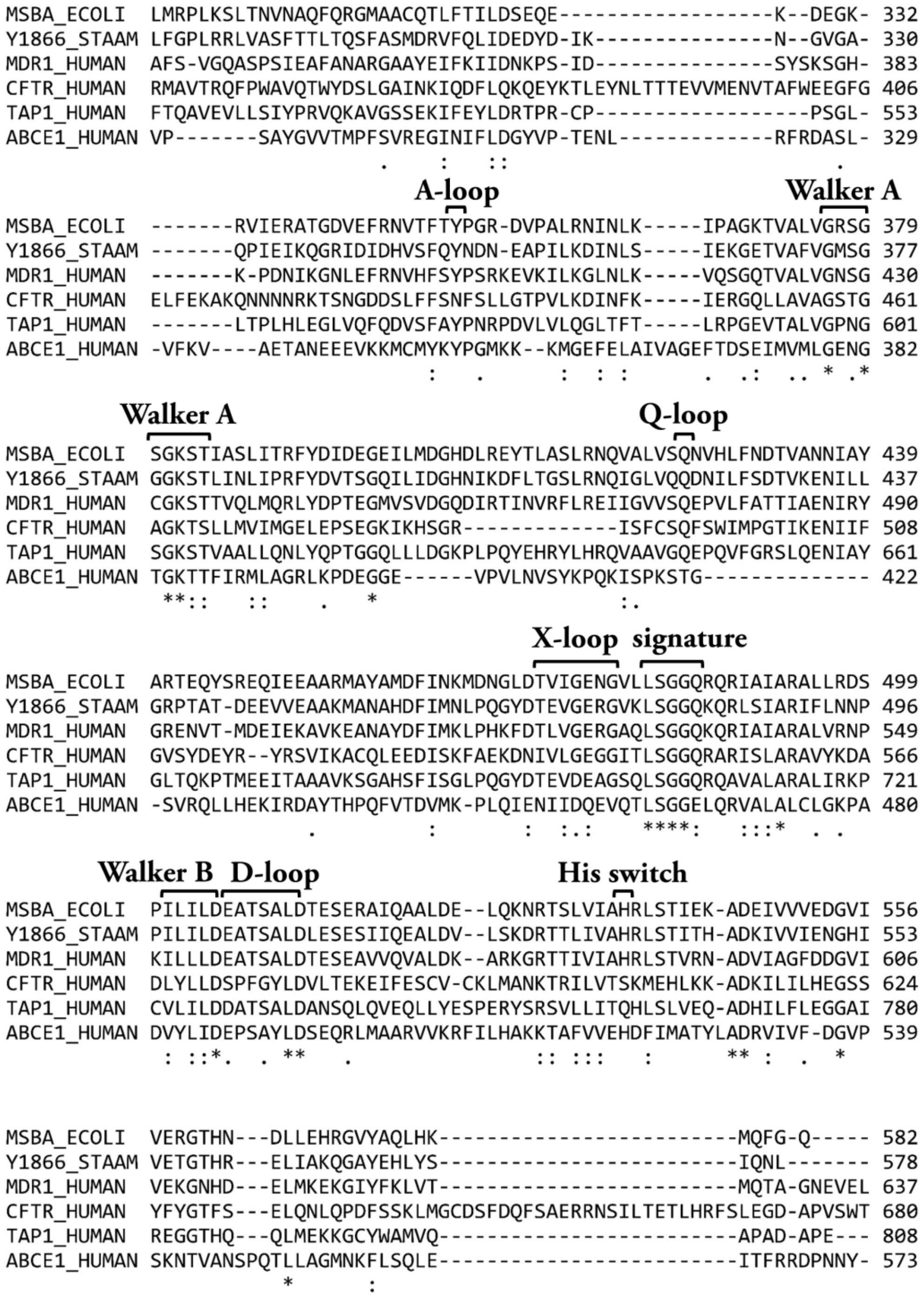

```
MSBA_ECOLI  LMRPLKSLTNVNAQFQRGMAACQTLFTILDSEQE-----------------K--DEGK- 332
Y1866_STAAM LFGPLRRLVASFTTLTQSFASMDRVFQLIDEDYD-IK---------------N--GVGA- 330
MDR1_HUMAN  AFS-VGQASPSIEAFANARGAAYEIFKIIDNKPS-ID---------------SYSKSGH- 383
CFTR_HUMAN  RMAVTRQFPWAVQTWYDSLGAINKIQDFLQKQEYKTLEYNLTTTEVVMENVTAFWEEGFG 406
TAP1_HUMAN  FTQAVEVLLSIYPRVQKAVGSSEKIFEYLDRTPR-CP------------------PSGL- 553
ABCE1_HUMAN VP-------SAYGVVTMPFSVREGINIFLDGYVP-TENL-------------RFRDASL- 329
                               .    :   ::                           .

MSBA_ECOLI  -------RVIERATGDVEFRNVTFTYPGR-DVPALRNINLK-----IPAGKTVALVGRSG 379
Y1866_STAAM -------QPIEIKQGRIDIDHVSFQYNDN-EAPILKDINLS-----IEKGETVAFVGMSG 377
MDR1_HUMAN  -------K-PDNIKGNLEFRNVHFSYPSRKEVKILKGLNLK-----VQSGQTVALVGNSG 430
CFTR_HUMAN  ELFEKAKQNNNNRKTSNGDDSLFFSNFSLLGTPVLKDINFK-----IERGQLLAVAGSTG 461
TAP1_HUMAN  -------LTPLHLEGLVQFQDVSFAYPNRPDVLVLQGLTFT-----LRPGEVTALVGPNG 601
ABCE1_HUMAN -VFKV----AETANEEEVKKMCMYKYPGMKK--KMGEFELAIVAGEFTDSEIMVMLGENG 382
                                   :   .      :  : :      .  .:  .. * .*

MSBA_ECOLI  SGKSTIASLITRFYDIDEGEILMDGHDLREYTLASLRNQVALVSQNVHLFNDTVANNIAY 439
Y1866_STAAM GGKSTLINLIPRFYDVTSGQILIDGHNIKDFLTGSLRNQIGLVQQDNILFSDTVKENILL 437
MDR1_HUMAN  CGKSTTVQLMQRLYDPTEGMVSVDGQDIRTINVRFLREIIGVVSQEPVLFATTIAENIRY 490
CFTR_HUMAN  AGKTSLLMVIMGELEPSEGKIKHSGR-------------ISFCSQFSWIMPGTIKENIIF 508
TAP1_HUMAN  SGKSTVAALLQNLYQPTGGQLLLDGKPLPQYEHRYLHRQVAAVGQEPQVFGRSLQENIAY 661
ABCE1_HUMAN TGKTTFIRMLAGRLKPDEGGE------VPVLNVSYKPQKISPKSTG-------------- 422
             **::   ::    .   *                    :.

MSBA_ECOLI  ARTEQYSREQIEEAARMAYAMDFINKMDNGLDTVIGENGVLLSGGQRQRIAIARALLRDS 499
Y1866_STAAM GRPTAT-DEEVVEAAKMANAHDFIMNLPQGYDTEVGERGVKLSGGQKQRLSIARIFLNNP 496
MDR1_HUMAN  GRENVT-MDEIEKAVKEANAYDFIMKLPHKFDTLVGERGAQLSGGQKQRIAIARALVRNP 549
CFTR_HUMAN  GVSYDEYR--YRSVIKACQLEEDISKFAEKDNIVLGEGGITLSGGQRARISLARAVYKDA 566
TAP1_HUMAN  GLTQKPTMEEITAAAVKSGAHSFISGLPQGYDTEVDEAGSQLSGGQRQAVALARALIRKP 721
ABCE1_HUMAN -SVRQLLHEKIRDAYTHPQFVTDVMK-PLQIENIIDQEVQTLSGGELQRVALALCLGKPA 480
                         .         :       :  :.:    ****:   :::*  . .

MSBA_ECOLI  PILILDEATSALDTESERAIQAALDE--LQKNRTSLVIAHRLSTIEK-ADEIVVVEDGVI 556
Y1866_STAAM PILILDEATSALDLESESIIQEALDV--LSKDRTTLIVAHRLSTITH-ADKIVVIENGHI 553
MDR1_HUMAN  KILLLDEATSALDTESEAVVQVALDK--ARKGRTTIVIAHRLSTVRN-ADVIAGFDDGVI 606
CFTR_HUMAN  DLYLLDSPFGYLDVLTEKEIFESCV-CKLMANKTRILVTSKMEHLKK-ADKILILHEGSS 624
TAP1_HUMAN  CVLILDDATSALDANSQLQVEQLLYESPERYSRSVLLITQHLSLVEQ-ADHILFLEGGAI 780
ABCE1_HUMAN DVYLIDEPSAYLDSEQRLMAARVVKRFILHAKKTAFVVEHDFIMATYLADRVIVF-DGVP 539
             : ::*.  . **   .               :: :::   :      ** :  .  *


MSBA_ECOLI  VERGTHN---DLLEHRGVYAQLHK------------------------MQFG-Q----- 582
Y1866_STAAM VETGTHR---ELIAKQGAYEHLYS------------------------IQNL------- 578
MDR1_HUMAN  VEKGNHD---ELMKEKGIYFKLVT------------------------MQTA-GNEVEL 637
CFTR_HUMAN  YFYGTFS---ELQNLQPDFSSKLMGCDSFDQFSAERRNSILTETLHRFSLEGD-APVSWT 680
TAP1_HUMAN  REGGTHQ---QLMEKKGCYWAMVQ------------------------APAD-APE--- 808
ABCE1_HUMAN SKNTVANSPQTLLAGMNKFLSQLE------------------------ITFRRDPNNY- 573
                       *      :
```

Figure 1.5. Sequence alignment of various ABC transporters. Here, the conserved regions in the nucleotide-binding domain are shown across different ABC transporters, i.e., bacterial MsbA and Sav1866, and human transporters P-glycoprotein, CFTR, TAP1, and ABCE1.

The class D transporters play a role in the transport of lipids, bile acids, and vitamin B12[78]. Underexpression of the subtype 1 leads to the accumulation of very long-chain fatty acids in the brain leading to demyelination of neuronal axons and eventually brain damage[79]. Additionally, mutations lead to adrenoleukodystrophy (ALD) and it is associated with peroxisomal disorders and diabetes[80-83]. Finally, in non-small cell lung cancer overexpressed ABCD4 appears to mediate the resistance to cisplatin[84].

The family classes E and F only consist of the nucleotide-binding domain[85]. ABCE1 (single member) is also known as RLI or HP68. It is considered to be a host factor of HIV-1 assembly[86]. For the class F member, there are 3 subtypes, with a total of 26 proteins due to alternative transcriptions[87]. ABCF1 plays a role in migration and epithelial-mesenchymal transition in cancer cells. Despite not being a transporter, ABCF1 is also associated with chemotherapy resistance in hepatocellular carcinoma cells[88].

Finally, the G class of the ABC transporter family is involved with lipid metabolism[89,90]. It is associated with a wide range of diseases, cellular toxicity, the pharmacokinetics of drugs, stress in pregnancy sitosterolaemia, breast cancer, hyperuricemia, gout, obesity, diabetes, atherosclerosis, and ischemic stroke[91-104].

There is a high similarity between different ABC exporters, specifically in the NBD region (**figure 1.5**). For instance, the human P-glycoprotein and the bacterial efflux pump MsbA share 30% identity and 46% similarity. Within the NBD region, they are 51% identical and share 66% similarity.[105] The NBDs of ABC transporters contain highly similar sequences that allow them to hydrolyse ATP (**figure 1.6A**). Within this catalytic domain, the Walker A (GXXGXGKS/T) and Walker B motifs (φφφφD where φ is a hydrophobic residue) can be found, originally discovered, and named after Sir John Ernest Walker. The Walker A motif is a glycine-rich motif known as the phosphate-binding loop (P-loop) and is extended by an α-helix. The Walker B motif forms electrostatic interactions with ATP and a hydrogen bond with the catalytic Mg^{2+} ion. Accordingly, both highly conserved motifs interact with ATP[106-110].

In addition, the NBD contains the LSGGQ signature sequence, which has a dipole moment of the ATP, whilst interacting with the nucleotide of the opposing monomer (**figure 1.6B**). Furthermore, the NBDs have an A-loop (tyrosine), D-loop (EATSALD), Q-loop (glutamine), and His-switch (histidine, also called H-loop or switch region). Mutational studies have shown that an aromatic residue (tyrosine, tryptophan, phenylalanine) is needed to form a π-π stacking with the aromatic ring of the adenosine ring of ATP. Hence, the Y-loop (tyrosine) was renamed to the A-loop (A for aromatic). The conserved glutamine of the Q-loop is part of the TMD interface. It coordinates the Mg^{2+}-ATP bound site and links the α-subdomains and the ATP core. The D-loop is proposed to mediate inter-monomer interactions and engages the opposing NBD through cooperative allostery. Furthermore, the H-loop interacts with the conserved glutamate of the D-loop and subsequently interacts with the γ-phosphate group of the ATP[110-119].

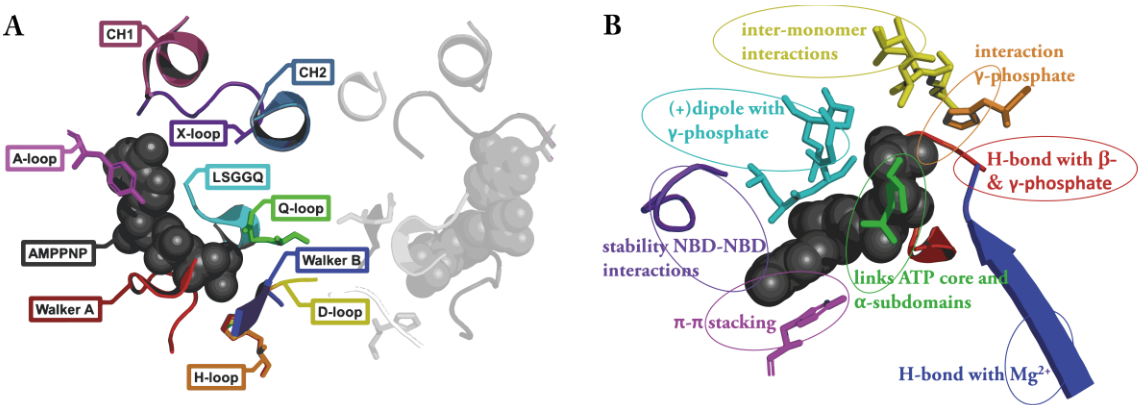

Figure 1.6. Highlights of the nucleotide-binding domain. A) The nucleotide-binding domain of bacterial MsbA (pdb 3B60) is shown with AMPPNP (grey spheres) bound. The highly conserved sequences are highlighted and labelled for this schematic overview. B) The role of the conserved sequences is summarized and given in the same colours.

1.3 The bacterial floppase: MsbA

In 1993, Karow and Georgopoulos first discovered the *msbA* gene as a multicopy suppressor of *htrB* mutations, while they were looking at the HtrB protein as part of the cell wall biosynthesis of Gram-negative bacteria. In the protein sequence analysis of MsbA, they discovered this 64.460 kDa membrane protein shares a high amino acid sequence identity and similarity with the ABC family[105]. Shortly after, MsbA was discovered as a part of the elucidating mechanism of the lipid A and/or lipopolysaccharide (LPS) from the inner leaflet to the outer membrane of Gram-negative bacteria[120-122]. Indeed, the bacterial ABC-exporter is a half-transporter that consists of 6 transmembrane helices (TM) and a nucleotide binding sites, taken together with a 12 TM homodimer containing one or multiple substrate binding site for core LPS (figure 1.7) and other amphiphilic drugs whilst using the two vital NDBs for hydrolysis ATP[123-129].

Over the past two decades, there have been many crystal structures of MsbA showing various conformations (figure 1.7). A wider apo or inward-facing conformation has been debated, possibly due to a detergent micelles environment of the membrane protein rather than a more native lipid bilayer environment. However, recently an EPR study has shown that MsbA natively adopts a wide inward-facing conformation[130]. Several cryo-EM structures have provided a less wide open inward-facing conformation to even a more occluded open state (figure 1.7), which could be the result of lateral pressure of the environment MsbA is surrounded by in nanodiscs. Some structures were captured with lipid A or LPS and others without substrates, once more leading to various widening of the inward-facing state. In addition, several MbsA structures with the G-compounds[131] and TBT1[132] have been reported. The G-compounds block MbsA ATP hydrolysis by separating the NBD domains and thereby preventing ATP hydrolysis and substrate translocation[131]. The TBT1 inhibitor decouples MsbA. By doing so, the transport mechanism is deactivation despite ATP hydrolysis taking place[132].

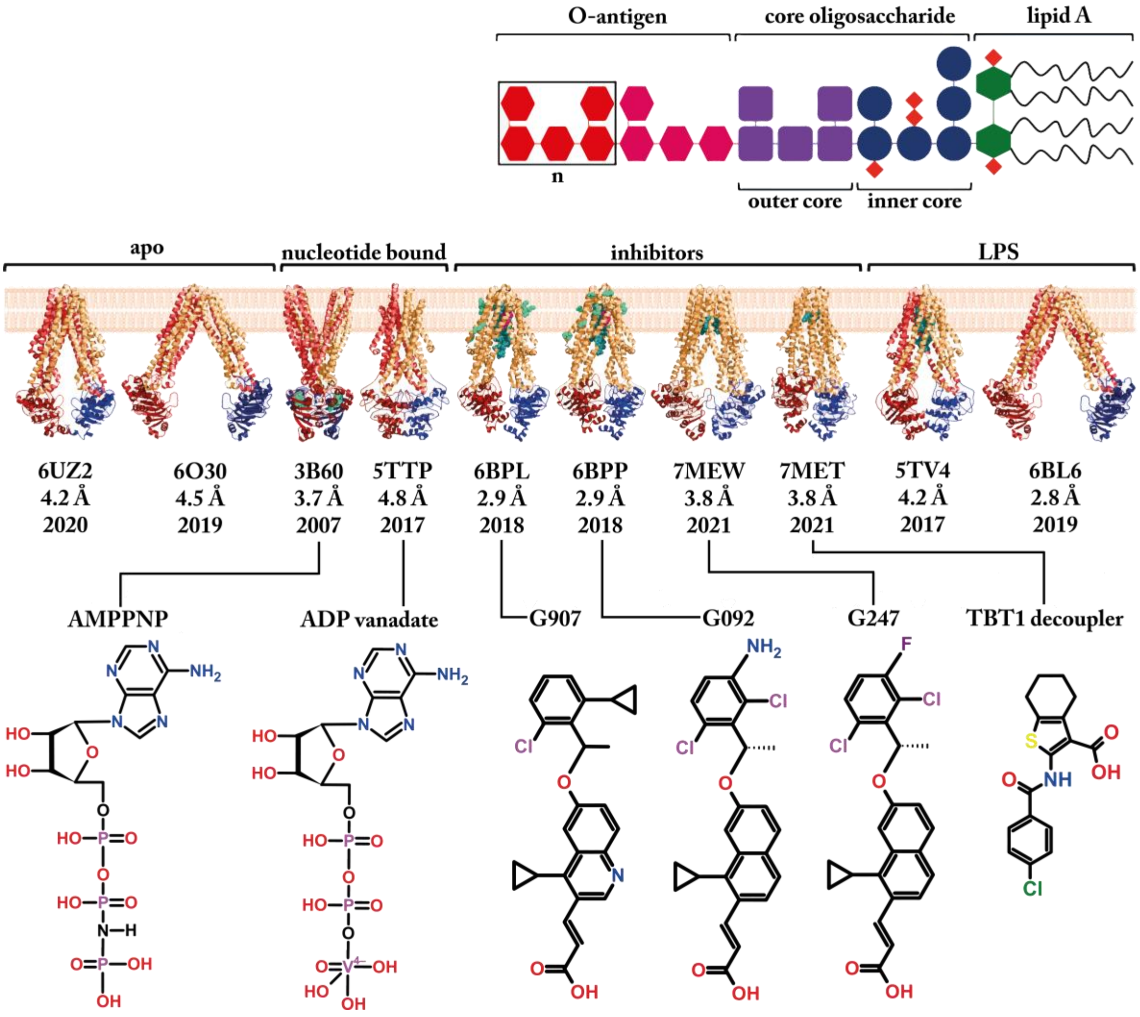

Figure 1.7. Overview of MsbA crystal structures. On the left apo MsbA (6UZ2 and 6O30) are shown here with two different widths of inward-facing state. On the far right, MsbA is shown with LPS bound in nanodiscs (5TV4) versus detergent micelles(6BL6). In between are various trapped states depicted. MsbA is trapped with AMPPNP in detergent micelles or with ADP vanadate in nanodiscs. Lastly, three G-compounds bound MsbA (6BPL, 6BPP, and 7MEW) and MsbA with the TBT1 decoupler (7MET) are depicted.

Lipid A forms an essential part of Gram-negative bacteria's protective outer membrane layer. In 1884, the Danish Hans Gram developed a staining protocol that allows the distinction of four bacterial groups based on the morphology and cell wall structure (i.e., Gram-positive cocci, Gram-negative cocci, Gram-positive rods, Gram-negative rods) using crystal violet-iodine complex to identify Gram-positive bacteria and pink safranin counter stain for the identification of Gram-positive bacteria. The cell walls of Gram-negative bacteria are composed of an outer membrane linked by lipoproteins, more specifically, from LPS to a thin monolayered peptidoglycan sheath located in the periplasmic space outside the cytoplasmic membrane[133,134].[133,134]

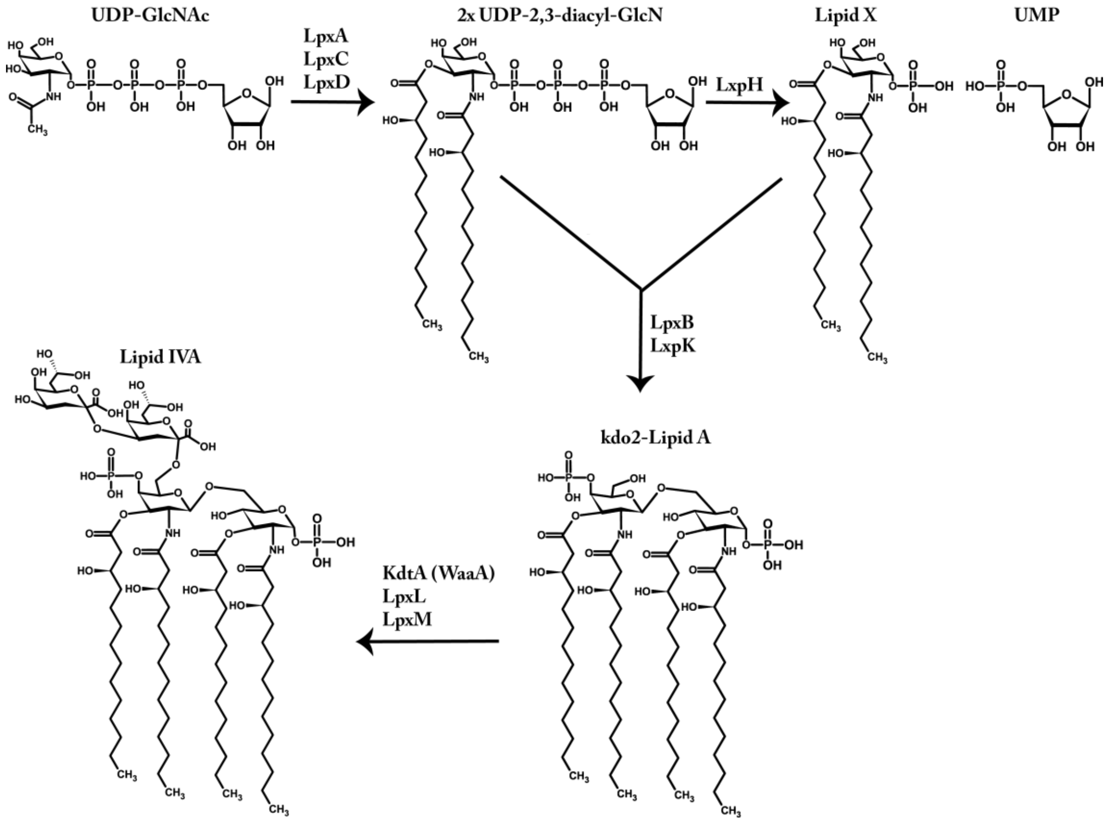

Figure 1.8. Schematic overview of the Raetz pathway of lipid A synthesis based on Raetz et al. 2009, J. Lipid Res. and Li et al. 2011.

It has been known for more than 60 years that lipid A is the hydrophobic moiety for LPS. As described above the latter forms the protection in Gram-negative bacteria against external agents. In the general synthesis of lipid A (figure 1.8), UDP-GlcNAc is catalysed via the acyltransferase LpxA. As LpxA catalyses a thermodynamically unfavourable reaction, the second step via UDP-GlcNAc deacetylase (LpxC) is devoted. The product is converted by LpxD into UDP-2,3-diacyl-GlcN and via LpxH converted into Lipid X. LpxB turns the latter products into disaccharide-1-P. With the addition of ATP, LpxK forms Lipid IV_A. Kdo_2 is added to the reaction with KdtA (WaaA) to form Kdo_2-Lipid IV_A. Finally, via LpxL and LpxM Kdo_2-Lipid A is synthesized[135-142].

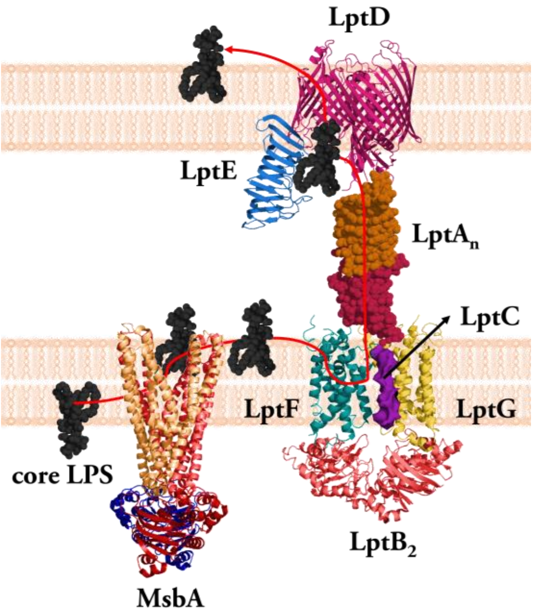

Figure 1.9. LPS transport pathway from MsbA to the Lpt system. Core LPS (ACD/ChemSketch 2018 academic license) is translocated by MsbA (3B60.pdb) into the periplasmic side where LPS is further assembled. In the periplasmic leaflet core, LPS is extracted by LptB2FGC (6S8N.pdb) and passed on to LptDE (5IV9.pdb). Finally, the lipid is transported once more into the outer membrane by LptA (2R1A.pdb) where it can be inserted into the outer membrane of Gram-negative bacteria.

Essentially, core LPS is translocated by MsbA into the periplasm where the O-antigen is ligated to the lipid A core. Matured LPS is then extracted from the periplasm by the Lpt system, initially via $LptB_2FGC$, followed by $LptA_n$, and finally LptDE to the outer membrane and inserted into the leaflet (figure 1.9)[120,141,143-151]. As LPS is the central component of the Gram-negative bacteria membrane, it plays a vital role in the pathogenesis, and as a result, LPS has an impact on antibiotic resistance[152,153].[152,153] Since Alexander Fleming's penicillin in 1929, the market grew full of antibiotics. By the 1950s penicillin antibiotic resistance had already led to, then, the novel β-lactam antibiotics. By the end of the 1960s, the first case of antibiotic resistance developed and was soon followed up by other resistant treatments (figure 1.10). The pharmaceutical industry has continuously developed new antibiotics[133,154-156133,154-157].

Consequently, physicians are daily challenged by current MDR bacteria. The emergence of antimicrobial resistance (AMR) demands research on targets such as MsbA.

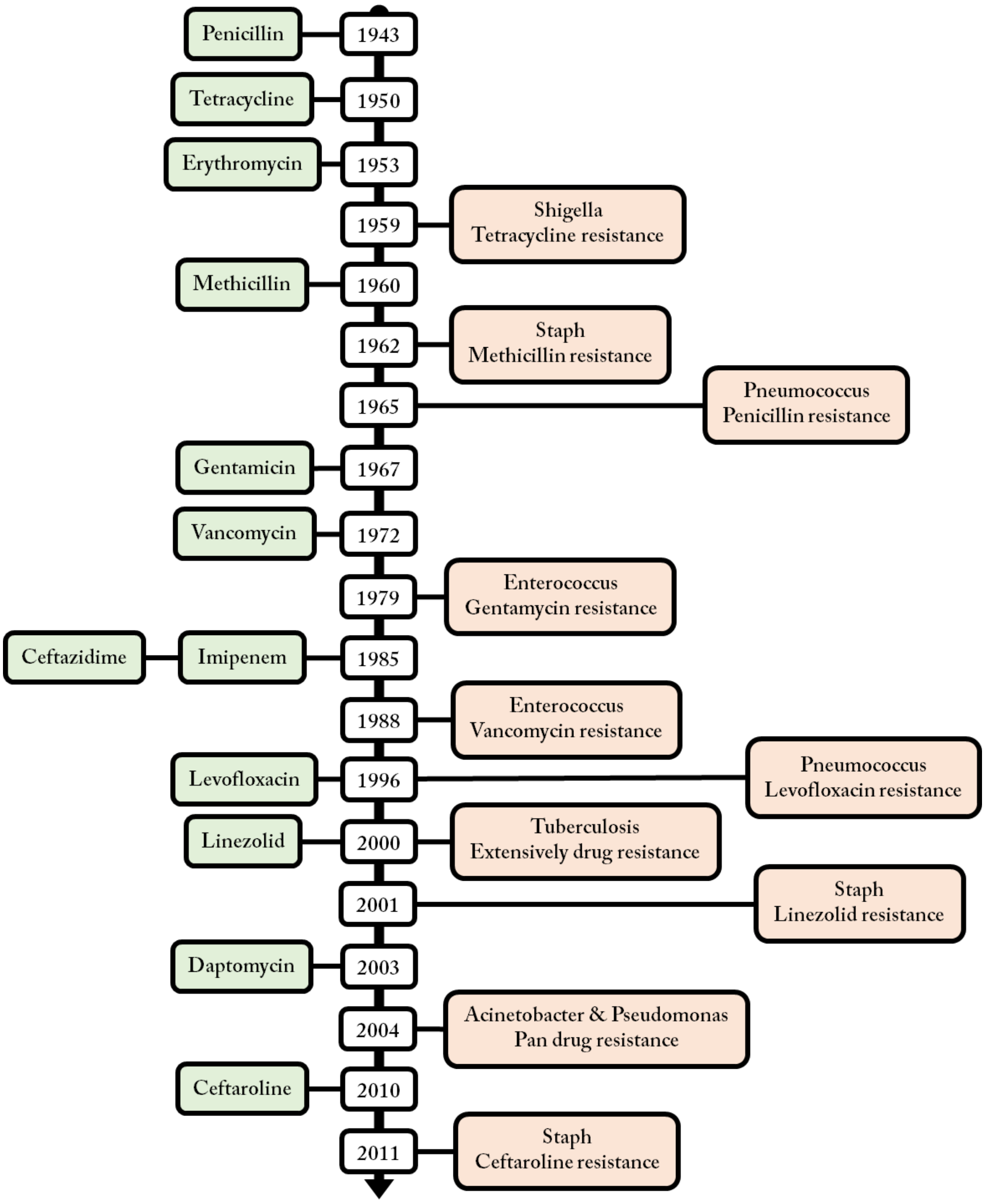

Figure 1.10. Schematic overview of the antibiotic resistance pipeline. The top shows the timeline of antibiotic introduction, and the bottom shows the timeline of antibiotic resistance identification. *Based on Annunziato G. Int J Mol Sci. 2019.*

References

1 Lander, E. S. *et al.* Initial sequencing and analysis of the human genome. *Nature* **409**, 860-921, doi:10.1038/35057062 (2001).

2 Hoglund, P. J., Nordstrom, K. J., Schioth, H. B. & Fredriksson, R. The solute carrier families have a remarkably long evolutionary history with the majority of the human families present before divergence of Bilaterian species. *Mol Biol Evol* **28**, 1531-1541, doi:10.1093/molbev/msq350 (2011).

3 Almen, M. S., Nordstrom, K. J., Fredriksson, R. & Schioth, H. B. Mapping the human membrane proteome: a majority of the human membrane proteins can be classified according to function and evolutionary origin. *BMC Biol* **7**, 50, doi:10.1186/1741-7007-7-50 (2009).

4 Liu, Y., Engelman, D. M. & Gerstein, M. Genomic analysis of membrane protein families: abundance and conserved motifs. *Genome Biology* **3**, research0054.0051–0054.0012 (2002).

5 Link, A. J. & Georgiou, G. Advances and challenges in membrane protein expression. *Aiche Journal* **53**, 752-756, doi:10.1002/aic.11107 (2007).

6 Trotschel, C. & Poetsch, A. Current approaches and challenges in targeted absolute quantification of membrane proteins. *Proteomics* **15**, 915-929, doi:10.1002/pmic.201400427 (2015).

7 Yin, H. & Flynn, A. D. Drugging Membrane Protein Interactions. *Annu Rev Biomed Eng* **18**, 51-76, doi:10.1146/annurev-bioeng-092115-025322 (2016).

8 Oberai, A., Ihm, Y., Kim, S. & Bowie, J. U. A limited universe of membrane protein families and folds. *Protein Sci* **15**, 1723-1734, doi:10.1110/ps.062109706 (2006).

9 Orelle, C., Mathieu, K. & Jault, J. M. Multidrug ABC transporters in bacteria. *Res Microbiol*, doi:10.1016/j.resmic.2019.06.001 (2019).

10 Diez-Alarcia, R. *et al.* Big Data Challenges Targeting Proteins in GPCR Signaling Pathways; Combining PTML-ChEMBL Models and [35S]GTPgammaS Binding Assays. *ACS Chem Neurosci*, doi:10.1021/acschemneuro.9b00302 (2019).

11 Begicevic, R. R., Arfuso, F. & Falasca, M. Bioactive lipids in cancer stem cells. *World J Stem Cells* **11**, 693-704, doi:10.4252/wjsc.v11.i9.693 (2019).

12 Kozielewicz, P., Turku, A. & Schulte, G. Molecular Pharmacology of Class F Receptor Activation. *Mol Pharmacol*, doi:10.1124/mol.119.117986 (2019).

13 Garibsingh, R. A. & Schlessinger, A. Advances and Challenges in Rational Drug Design for SLCs. *Trends Pharmacol Sci*, doi:10.1016/j.tips.2019.08.006 (2019).

14 Gendaszewska-Darmach, E., Drzazga, A. & Koziolkiewicz, M. Targeting GPCRs Activated by Fatty Acid-Derived Lipids in Type 2 Diabetes. *Trends Mol Med*, doi:10.1016/j.molmed.2019.07.003 (2019).

15 Haran, J. P. *et al.* Alzheimer's Disease Microbiome Is Associated with Dysregulation of the Anti-Inflammatory P-Glycoprotein Pathway. *MBio* **10**, doi:10.1128/mBio.00632-19 (2019).

16 Franco, R. *et al.* Potentiation of cannabinoid signaling in microglia by adenosine A2A receptor antagonists. *Glia* **67**, 2410-2423, doi:10.1002/glia.23694 (2019).

17 Pahnke, J., Langer, O. & Krohn, M. Alzheimer's and ABC transporters--new opportunities for diagnostics and treatment. *Neurobiol Dis* **72 Pt A**, 54-60, doi:10.1016/j.nbd.2014.04.001 (2014).

18 Zhou, Y., Little, P. J., Ta, H. T., Xu, S. & Kamato, D. Lysophosphatidic acid and its receptors: pharmacology and therapeutic potential in atherosclerosis and vascular disease. *Pharmacol Ther*, 107404, doi:10.1016/j.pharmthera.2019.107404 (2019).

19 Falk, S., Lund, C. & Clemmensen, C. Muscarinic receptors in energy homeostasis: Physiology and pharmacology. *Basic Clin Pharmacol Toxicol*, doi:10.1111/bcpt.13311 (2019).

20 Wang, D. *et al.* Bilirubin Decreases Macrophage Cholesterol Efflux and ATP-Binding Cassette Transporter A1 Protein Expression. *J Am Heart Assoc* **6**, doi:10.1161/JAHA.117.005520 (2017).

21 Mauerer, R., Ebert, S. & Langmann, T. High glucose, unsaturated and saturated fatty acids differentially regulate expression of ATP-binding cassette transporters ABCA1 and ABCG1 in human macrophages. *Exp Mol Med* **41**, 126-132, doi:10.3858/emm.2009.41.2.015 (2009).

22 Heinkel, F. *et al.* Phase separation and clustering of an ABC transporter in Mycobacterium tuberculosis. *Proc Natl Acad Sci U S A* **116**, 16326-16331, doi:10.1073/pnas.1820683116 (2019).

23 WHO. *The top 10 causes of death*, <https://www.who.int/news-room/fact-sheets/detail/the-top-10-causes-of-death> (2018).

24 CDC. *Leading Causes of Death*, <https://www.cdc.gov/nchs/fastats/leading-causes-of-death.htm> (2017).

25 Fagerberg, L., Jonasson, K., von Heijne, G., Uhlen, M. & Berglund, L. Prediction of the human membrane proteome. *Proteomics* **10**, 1141-1149, doi:10.1002/pmic.200900258 (2010).

26 Jeff Hardin, G. B., Lewis J. Kleinsmith *Becker's World of the Cell* 8th edn, (Pearson Benjamin Cummings 2012).

27 Bruce Alberts, A. J., Julian Lewis, Martin Raff, Keith Roberts, Peter Walter. *Molecular Biology of the Cell.* 5th edn, (Garland Science).

28 Goodsell, D. S. *et al.* RCSB Protein Data Bank: Enabling biomedical research and drug discovery. *Protein Sci*, doi:10.1002/pro.3730 (2019).

29 Leopoldo, M. *et al.* An updated patent review on P-glycoprotein inhibitors (2011-2018). *Expert Opin Ther Pat* **29**, 455-461, doi:10.1080/13543776.2019.1618273 (2019).

30 Babcock, J. J. & Li, M. Deorphanizing the human transmembrane genome: A landscape of uncharacterized membrane proteins. *Acta Pharmacol Sin* **35**, 11-23, doi:10.1038/aps.2013.142 (2014).

31 Carpenter, E. P., Beis, K., Cameron, A. D. & Iwata, S. Overcoming the challenges of membrane protein crystallography. *Curr Opin Struct Biol* **18**, 581-586, doi:10.1016/j.sbi.2008.07.001 (2008).

32 Anfinsen, C. B. Principles that govern the folding of protein chains. *Science* **181**, 223-230, doi:10.1126/science.181.4096.223 (1973).

33 Cross, T. A., Sharma, M., Yi, M. & Zhou, H. X. Influence of solubilizing environments on membrane protein structures. *Trends Biochem Sci* **36**, 117-125, doi:10.1016/j.tibs.2010.07.005 (2011).

34 Seddon, A. M., Curnow, P. & Booth, P. J. Membrane proteins, lipids and detergents: not just a soap opera. *Biochim Biophys Acta* **1666**, 105-117, doi:10.1016/j.bbamem.2004.04.011 (2004).

35 Kotov, V. *et al.* High-throughput stability screening for detergent-solubilized membrane proteins. *Sci Rep* **9**, 10379, doi:10.1038/s41598-019-46686-8 (2019).

36 Rawson, S., Davies, S., Lippiat, J. D. & Muench, S. P. The changing landscape of membrane protein structural biology through developments in electron microscopy. *Mol Membr Biol* **33**, 12-22, doi:10.1080/09687688.2016.1221533 (2016).

37 Zemella, A., Thoring, L., Hoffmeister, C. & Kubick, S. Cell-Free Protein Synthesis: Pros and Cons of Prokaryotic and Eukaryotic Systems. *Chembiochem* **16**, 2420-2431, doi:10.1002/cbic.201500340 (2015).

38 Jermutus, L., Ryabova, L. A. & Pluckthun, A. Recent advances in producing and selecting functional proteins by using cell-free translation. *Current Opinion in Biotechnology* **9**, 534-548, doi:Doi 10.1016/S0958-1669(98)80042-6 (1998).

39 Focke, P. J. *et al.* Combining in Vitro Folding with Cell Free Protein Synthesis for Membrane Protein Expression. *Biochemistry* **55**, 4212-4219, doi:10.1021/acs.biochem.6b00488 (2016).

40 Loll, P. J. Membrane proteins, detergents and crystals: what is the state of the art? *Acta Crystallogr F Struct Biol Commun* **70**, 1576-1583, doi:10.1107/S2053230X14025035 (2014).

41 Siontorou, C. G., Nikoleli, G. P., Nikolelis, D. P. & Karapetis, S. K. Artificial Lipid Membranes: Past, Present, and Future. *Membranes (Basel)* **7**, doi:10.3390/membranes7030038 (2017).

42 Lindblom, G. & Oradd, G. Lipid lateral diffusion and membrane heterogeneity. *Biochim Biophys Acta* **1788**, 234-244, doi:10.1016/j.bbamem.2008.08.016 (2009).

43 International Transporter, C. *et al.* Membrane transporters in drug development. *Nat Rev Drug Discov* **9**, 215-236, doi:10.1038/nrd3028 (2010).

44 Holland, I. B. Rise and rise of the ABC transporter families. *Res Microbiol*, doi:10.1016/j.resmic.2019.08.004 (2019).

45 Moravcikova, E., Meyer, E. M., Corselli, M., Donnenberg, V. S. & Donnenberg, A. D. Proteomic Profiling of Native Unpassaged and Culture-Expanded Mesenchymal Stromal Cells (MSC). *Cytometry A* **93**, 894-904, doi:10.1002/cyto.a.23574 (2018).

46 Chen, S. *et al.* Interaction of WBP2 with ERalpha increases doxorubicin resistance of breast cancer cells by modulating MDR1 transcription. *Br J Cancer* **119**, 182-192, doi:10.1038/s41416-018-0119-5 (2018).

47 Krämer, R. & Ziegler, C. *Membrane Transport Mechanism.* (Springer-Verlag Berlin Heidelberg, 2014).

48 Fay, J. F. *et al.* Cryo-EM Visualization of an Active High Open Probability CFTR Anion Channel. *Biochemistry* **57**, 6234-6246, doi:10.1021/acs.biochem.8b00763 (2018).

49 Sigoillot, M. *et al.* Domain-interface dynamics of CFTR revealed by stabilizing nanobodies. *Nat Commun* **10**, 2636, doi:10.1038/s41467-019-10714-y (2019).

50 Tanaka, K. J., Song, S., Mason, K. & Pinkett, H. W. Selective substrate uptake: The role of ATP-binding cassette (ABC) importers in pathogenesis. *Biochim Biophys Acta Biomembr* **1860**, 868-877, doi:10.1016/j.bbamem.2017.08.011 (2018).

51 ter Beek, J., Guskov, A. & Slotboom, D. J. Structural diversity of ABC transporters. *J Gen Physiol* **143**, 419-435, doi:10.1085/jgp.201411164 (2014).

52 Locher, K. P. Mechanistic diversity in ATP-binding cassette (ABC) transporters. *Nat Struct Mol Biol* **23**, 487-493, doi:10.1038/nsmb.3216 (2016).

53 Lewinson, O. & Livnat-Levanon, N. Mechanism of Action of ABC Importers: Conservation, Divergence, and Physiological Adaptations. *J Mol Biol* **429**, 606-619, doi:10.1016/j.jmb.2017.01.010 (2017).

54 Rice, A. J., Park, A. & Pinkett, H. W. Diversity in ABC transporters: type I, II and III importers. *Crit Rev Biochem Mol Biol* **49**, 426-437, doi:10.3109/10409238.2014.953626 (2014).

55 Rempel, S., Stanek, W. K. & Slotboom, D. J. ECF-Type ATP-Binding Cassette Transporters. *Annu Rev Biochem* **88**, 551-576, doi:10.1146/annurev-biochem-013118-111705 (2019).

56 Wang, Z., Hu, W. & Zheng, H. Pathogenic siderophore ABC importer YbtPQ adopts a surprising fold of exporter. *Sci Adv* **6**, eaay7997, doi:10.1126/sciadv.aay7997 (2020).

57 Dean, M., Rzhetsky, A. & Allikmets, R. The human ATP-binding cassette (ABC) transporter superfamily. *Genome Res* **11**, 1156-1166, doi:10.1101/gr.184901 (2001).

58 Vasiliou, V., Vasiliou, K. & Nebert, D. W. Human ATP-binding cassette (ABC) transporter family. *Human Genomics* **3**, 281, doi:10.1186/1479-7364-3-3-281 (2008).

59 El-Awady, R. *et al.* The Role of Eukaryotic and Prokaryotic ABC Transporter Family in Failure of Chemotherapy. *Front Pharmacol* **7**, 535, doi:10.3389/fphar.2016.00535 (2016).

60 Albrecht, C. & Viturro, E. The ABCA subfamily--gene and protein structures, functions and associated hereditary diseases. *Pflugers Arch* **453**, 581-589, doi:10.1007/s00424-006-0047-8 (2007).

61 Lee, P. & Ulatowski, L. M. Vitamin E: Mechanism of transport and regulation in the CNS. *IUBMB Life* **71**, 424-429, doi:10.1002/iub.1993 (2019).

62 Hedditch, E. L. *et al.* ABCA transporter gene expression and poor outcome in epithelial ovarian cancer. *J Natl Cancer Inst* **106**, doi:10.1093/jnci/dju149 (2014).

63 Akiyama, M. Pathomechanisms of harlequin ichthyosis and ABCA transporters in human diseases. *Arch Dermatol* **142**, 914-918, doi:10.1001/archderm.142.7.914 (2006).

64 Hasan, M. M., Hosen, M. B., Rahman, M. M., Howlader, M. Z. H. & Kabir, Y. Association of ATP binding cassette transporter 1 (ABCA 1) gene polymorphism with type 2 diabetes mellitus (T2DM) in Bangladeshi population. *Gene* **688**, 151-154, doi:10.1016/j.gene.2018.12.003 (2019).

65 Quazi, F. & Molday, R. S. Differential phospholipid substrates and directional transport by ATP-binding cassette proteins ABCA1, ABCA7, and ABCA4 and disease-causing mutants. *J Biol Chem* **288**, 34414-34426, doi:10.1074/jbc.M113.508812 (2013).

66 Stieger, B. & Gao, B. Drug transporters in the central nervous system. *Clin Pharmacokinet* **54**, 225-242, doi:10.1007/s40262-015-0241-y (2015).

67 Varma, A., Mathaiyan, J., Shewade, D., Dubashi, B. & Sunitha, K. Influence of ABCB-1, ERCC-1 and ERCC-2 gene polymorphisms on response to capecitabine and oxaliplatin (CAPOX) treatment

in colorectal cancer (CRC) patients of South India. *J Clin Pharm Ther* **45**, 617-627, doi:10.1111/jcpt.13166 (2020).

68 Sarkadi, B., Homolya, L., Szakacs, G. & Varadi, A. Human multidrug resistance ABCB and ABCG transporters: participation in a chemoimmunity defense system. *Physiol Rev* **86**, 1179-1236, doi:10.1152/physrev.00037.2005 (2006).

69 Veiga-Matos, J., Remiao, F. & Motales, A. Pharmacokinetics and Toxicokinetics Roles of Membrane Transporters at Kidney Level. *J Pharm Pharm Sci* **23**, 333-356, doi:10.18433/jpps30865 (2020).

70 Srivastava, A. Progressive familial intrahepatic cholestasis. *J Clin Exp Hepatol* **4**, 25-36, doi:10.1016/j.jceh.2013.10.005 (2014).

71 Lee, J. Y. & Rosenbaum, D. M. Transporters Revealed. *Cell* **168**, 951-953, doi:10.1016/j.cell.2017.02.033 (2017).

72 Brodeur, G. M. Knowing your ABCCs: novel functions of ABCC transporters. *J Natl Cancer Inst* **103**, 1207-1208, doi:10.1093/jnci/djr277 (2011).

73 Mehrvar, N. *et al.* Pattern of ABCC Transporter Gene Expression in Pediatric Patients with Relapsed Acute Lymphoblastic Leukemia. *Rep Biochem Mol Biol* **8**, 184-193 (2019).

74 Cui, H., Zhang, A. J., Chen, M. & Liu, J. J. ABC Transporter Inhibitors in Reversing Multidrug Resistance to Chemotherapy. *Curr Drug Targets* **16**, 1356-1371, doi:10.2174/1389450116666150330113506 (2015).

75 Gu, X. & Manautou, J. E. Regulation of hepatic ABCC transporters by xenobiotics and in disease states. *Drug Metab Rev* **42**, 482-538, doi:10.3109/03602531003654915 (2010).

76 Nies, A. T., Schwab, M. & Keppler, D. Interplay of conjugating enzymes with OATP uptake transporters and ABCC/MRP efflux pumps in the elimination of drugs. *Expert Opin Drug Metab Toxicol* **4**, 545-568, doi:10.1517/17425255.4.5.545 (2008).

77 Franco, R. & Zavala-Flores, L. ABCC Transporters. 1-5, doi:10.1007/978-3-642-27841-9_7076-2 (2012).

78 Hlavac, V. & Soucek, P. Role of family D ATP-binding cassette transporters (ABCD) in cancer. *Biochem Soc Trans* **43**, 937-942, doi:10.1042/BST20150114 (2015).

79 Hartz, A. M. & Bauer, B. ABC transporters in the CNS - an inventory. *Curr Pharm Biotechnol* **12**, 656-673, doi:10.2174/138920111795164020 (2011).

80 Baker, A. *et al.* Peroxisomal ABC transporters: functions and mechanism. *Biochem Soc Trans* **43**, 959-965, doi:10.1042/BST20150127 (2015).

81 Kawaguchi, K. & Morita, M. ABC Transporter Subfamily D: Distinct Differences in Behavior between ABCD1-3 and ABCD4 in Subcellular Localization, Function, and Human Disease. *Biomed Res Int* **2016**, 6786245, doi:10.1155/2016/6786245 (2016).

82 Dashora, U. *et al.* Association of British Clinical Diabetologists (ABCD) and Diabetes UK joint position statement and recommendations for non-diabetes specialists on the use of sodium glucose co-transporter 2 inhibitors in people with type 2 diabetes (January 2021). *Clin Med (Lond)* **21**, 204-210, doi:10.7861/clinmed.2021-0045 (2021).

83 Turk, B. R., Theda, C., Fatemi, A. & Moser, A. B. X-linked adrenoleukodystrophy: Pathology, pathophysiology, diagnostic testing, newborn screening and therapies. *Int J Dev Neurosci* **80**, 52-72, doi:10.1002/jdn.10003 (2020).

84 Panneerselvam, J. *et al.* DCLK1 Regulates Tumor Stemness and Cisplatin Resistance in Non-small Cell Lung Cancer via ABCD-Member-4. *Mol Ther Oncolytics* **18**, 24-36, doi:10.1016/j.omto.2020.05.012 (2020).

85 Takenaka, S., Itoh, T. & Fujiwara, R. Expression pattern of human ATP-binding cassette transporters in skin. *Pharmacol Res Perspect* **1**, e00005, doi:10.1002/prp2.5 (2013).

86 Smirnova, E. V. *et al.* TULA proteins bind to ABCE-1, a host factor of HIV-1 assembly, and inhibit HIV-1 biogenesis in a UBA-dependent fashion. *Virology* **372**, 10-23, doi:10.1016/j.virol.2007.10.012 (2008).

87 Juan-Carlos, P. M., Perla-Lidia, P. P., Stephanie-Talia, M. M., Monica-Griselda, A. M. & Luz-Maria, T. E. ABC transporter superfamily. An updated overview, relevance in cancer multidrug resistance and perspectives with personalized medicine. *Mol Biol Rep* **48**, 1883-1901, doi:10.1007/s11033-021-06155-w (2021).

88 Fung, S. W. *et al.* The ATP-binding cassette transporter ABCF1 is a hepatic oncofetal protein that promotes chemoresistance, EMT and cancer stemness in hepatocellular carcinoma. *Cancer Lett* **457**, 98-109, doi:10.1016/j.canlet.2019.05.010 (2019).

89 Kerr, I. D., Hutchison, E., Gerard, L., Aleidi, S. M. & Gelissen, I. C. Mammalian ABCG-transporters, sterols and lipids: To bind perchance to transport? *Biochim Biophys Acta Mol Cell Biol Lipids* **1866**, 158860, doi:10.1016/j.bbalip.2020.158860 (2021).

90 Schmitz, G., Langmann, T. & Heimerl, S. Role of ABCG1 and other ABCG family members in lipid metabolism. *Journal of Lipid Research* **42**, 1513-1520, doi:10.1016/s0022-2275(20)32205-7 (2001).

91 Safar, Z., Kis, E., Erdo, F., Zolnerciks, J. K. & Krajcsi, P. ABCG2/BCRP: variants, transporter interaction profile of substrates and inhibitors. *Expert Opin Drug Metab Toxicol* **15**, 313-328, doi:10.1080/17425255.2019.1591373 (2019).

92 Sun, Y. *et al.* Molecular basis of cholesterol efflux via ABCG subfamily transporters. *Proc Natl Acad Sci U S A* **118**, doi:10.1073/pnas.2110483118 (2021).

93 Woodward, O. M., Kottgen, A. & Kottgen, M. ABCG transporters and disease. *FEBS J* **278**, 3215-3225, doi:10.1111/j.1742-4658.2011.08171.x (2011).

94 Velamakanni, S., Wei, S. L., Janvilisri, T. & van Veen, H. W. ABCG transporters: structure, substrate specificities and physiological roles : a brief overview. *J Bioenerg Biomembr* **39**, 465-471, doi:10.1007/s10863-007-9122-x (2007).

95 Tarr, P. T., Tarling, E. J., Bojanic, D. D., Edwards, P. A. & Baldan, A. Emerging new paradigms for ABCG transporters. *Biochim Biophys Acta* **1791**, 584-593, doi:10.1016/j.bbalip.2009.01.007 (2009).

96 Horsey, A. J., Cox, M. H., Sarwat, S. & Kerr, I. D. The multidrug transporter ABCG2: still more questions than answers. *Biochem Soc Trans* **44**, 824-830, doi:10.1042/BST20160014 (2016).

97 Sarkadi, B., Homolya, L. & Hegedus, T. The ABCG2/BCRP transporter and its variants - from structure to pathology. *FEBS Lett* **594**, 4012-4034, doi:10.1002/1873-3468.13947 (2020).

98 Matsuo, H. *et al.* ABCG2 dysfunction increases the risk of renal overload hyperuricemia. *Nucleosides Nucleotides Nucleic Acids* **33**, 266-274, doi:10.1080/15257770.2013.866679 (2014).

99 Matsuo, M. ABCA1 and ABCG1 as potential therapeutic targets for the prevention of atherosclerosis. *J Pharmacol Sci* **148**, 197-203, doi:10.1016/j.jphs.2021.11.005 (2022).

100 Aye, I. L. & Keelan, J. A. Placental ABC transporters, cellular toxicity and stress in pregnancy. *Chem Biol Interact* **203**, 456-466, doi:10.1016/j.cbi.2013.03.007 (2013).

101 Kusuhara, H. & Sugiyama, Y. ATP-binding cassette, subfamily G (ABCG family). *Pflugers Arch* **453**, 735-744, doi:10.1007/s00424-006-0134-x (2007).

102 Liu, T. *et al.* Association of ABCG2 polymorphisms with ischemic stroke in a Chinese population. *Ann Hum Genet* **82**, 325-330, doi:10.1111/ahg.12258 (2018).

103 Yin, H., Liu, N. & Chen, J. The Role of the Intestine in the Development of Hyperuricemia. *Front Immunol* **13**, 845684, doi:10.3389/fimmu.2022.845684 (2022).

104 Eckenstaler, R. & Benndorf, R. A. The Role of ABCG2 in the Pathogenesis of Primary Hyperuricemia and Gout-An Update. *Int J Mol Sci* **22**, doi:10.3390/ijms22136678 (2021).

105 Karow, M. & Georgopoulos, C. The essential Escherichia coli msbA gene, a multicopy suppressor of null mutations in the htrB gene, is related to the universally conserved family of ATP-dependent translocators. *Molecular Microbiology* **7** 69-79 (1993).

106 Walker, J. E., Saraste, M., Runswick, M. J. & Gay, N. J. Distantly Related Sequences in the Alpha-Subunits and Beta-Subunits of Atp Synthase, Myosin, Kinases and Other Atp-Requiring Enzymes and a Common Nucleotide Binding Fold. *Embo Journal* **1**, 945-951, doi:DOI 10.1002/j.1460-2075.1982.tb01276.x (1982).

107 Jones, P. M. & George, A. M. Mechanism of ABC transporters: a molecular dynamics simulation of a well characterized nucleotide-binding subunit. *Proc Natl Acad Sci U S A* **99**, 12639-12644, doi:10.1073/pnas.152439599 (2002).

108 Jones, P. M. & George, A. M. The ABC transporter structure and mechanism: perspectives on recent research. *Cell Mol Life Sci* **61**, 682-699, doi:10.1007/s00018-003-3336-9 (2004).

109 Jones, P. M. & George, A. M. Nucleotide-dependent allostery within the ABC transporter ATP-binding cassette: a computational study of the MJ0796 dimer. *J Biol Chem* **282**, 22793-22803, doi:10.1074/jbc.M700809200 (2007).

110 George, A. M. *ABC Transporters—40 Years on.* (Springer International Publishing AG, 2016).

111 Smith, P. C. *et al.* ATP binding to the motor domain from an ABC transporter drives formation of a nucleotide sandwich dimer. *Mol Cell* **10**, 139-149, doi:10.1016/s1097-2765(02)00576-2 (2002).

112 Rees, D. C., Johnson, E. & Lewinson, O. ABC transporters: the power to change. *Nat Rev Mol Cell Biol* **10**, 218-227, doi:10.1038/nrm2646 (2009).

113 Kim, I. W. *et al.* The conserved tyrosine residues 401 and 1044 in ATP sites of human P-glycoprotein are critical for ATP binding and hydrolysis: evidence for a conserved subdomain, the A-loop in the ATP-binding cassette. *Biochemistry* **45**, 7605-7616, doi:10.1021/bi060308o (2006).

114 Masia, R. & Nichols, C. G. Functional clustering of mutations in the dimer interface of the nucleotide binding folds of the sulfonylurea receptor. *J Biol Chem* **283**, 30322-30329, doi:10.1074/jbc.M804318200 (2008).

115 Oloo, E. O., Fung, E. Y. & Tieleman, D. P. The dynamics of the MgATP-driven closure of MalK, the energy-transducing subunit of the maltose ABC transporter. *J Biol Chem* **281**, 28397-28407, doi:10.1074/jbc.M513614200 (2006).

116 Carrier, I., Urbatsch, I. L., Senior, A. E. & Gros, P. Mutational analysis of conserved aromatic residues in the A-loop of the ABC transporter ABCB1A (mouse Mdr3). *FEBS Lett* **581**, 301-308, doi:10.1016/j.febslet.2006.12.030 (2007).

117 Ambudkar, S. V., Kim, I. W., Xia, D. & Sauna, Z. E. The A-loop, a novel conserved aromatic acid subdomain upstream of the Walker A motif in ABC transporters, is critical for ATP binding. *FEBS Lett* **580**, 1049-1055, doi:10.1016/j.febslet.2005.12.051 (2006).

118 Jones, P. M. & George, A. M. Role of the D-loops in allosteric control of ATP hydrolysis in an ABC transporter. *J Phys Chem A* **116**, 3004-3013, doi:10.1021/jp211139s (2012).

119 Jones, P. M., O'Mara, M. L. & George, A. M. ABC transporters: a riddle wrapped in a mystery inside an enigma. *Trends Biochem Sci* **34**, 520-531, doi:10.1016/j.tibs.2009.06.004 (2009).

120 Doerrler, W. T. & Raetz, C. R. ATPase activity of the MsbA lipid flippase of Escherichia coli. *J Biol Chem* **277**, 36697-36705, doi:10.1074/jbc.M205857200 (2002).

121 Doerrler, W. T., Gibbons, H. S. & Raetz, C. R. MsbA-dependent translocation of lipids across the inner membrane of Escherichia coli. *J Biol Chem* **279**, 45102-45109, doi:10.1074/jbc.M408106200 (2004).

122 Doerrler, W. T. Lipid trafficking to the outer membrane of Gram-negative bacteria. *Mol Microbiol* **60**, 542-552, doi:10.1111/j.1365-2958.2006.05130.x (2006).

123 Reuter, G. *et al.* The ATP binding cassette multidrug transporter LmrA and lipid transporter MsbA have overlapping substrate specificities. *J Biol Chem* **278**, 35193-35198, doi:10.1074/jbc.M306226200 (2003).

124 Siarheyeva, A. & Sharom, F. J. The ABC transporter MsbA interacts with lipid A and amphipathic drugs at different sites. *Biochem J* **419**, 317-328, doi:10.1042/BJ20081364 (2009).

125 Smriti, Zou, P. & McHaourab, H. S. Mapping daunorubicin-binding Sites in the ATP-binding cassette transporter MsbA using site-specific quenching by spin labels. *J Biol Chem* **284**, 13904-13913, doi:10.1074/jbc.M900837200 (2009).

126 Woebking, B. *et al.* Drug-lipid A interactions on the Escherichia coli ABC transporter MsbA. *J Bacteriol* **187**, 6363-6369, doi:10.1128/JB.187.18.6363-6369.2005 (2005).

127 Woebking, B. *et al.* Functional role of transmembrane helix 6 in drug binding and transport by the ABC transporter MsbA. *Biochemistry* **47**, 10904-10914, doi:10.1021/bi800778d (2008).

128 Zou, P. & McHaourab, H. S. Alternating access of the putative substrate-binding chamber in the ABC transporter MsbA. *J Mol Biol* **393**, 574-585, doi:10.1016/j.jmb.2009.08.051 (2009).

129 Spadaccini, R., Kaur, H., Becker-Baldus, J. & Glaubitz, C. The effect of drug binding on specific sites in transmembrane helices 4 and 6 of the ABC exporter MsbA studied by DNP-enhanced solid-state NMR. *Biochim Biophys Acta Biomembr* **1860**, 833-840, doi:10.1016/j.bbamem.2017.10.017 (2018).

130 Galazzo, L. *et al.* The ABC transporter MsbA adopts the wide inward-open conformation in E. coli cells. *Sci Adv* **8**, eabn6845, doi:10.1126/sciadv.abn6845 (2022).

131 Ho, H. *et al.* Structural basis for dual-mode inhibition of the ABC transporter MsbA. *Nature* **557**, 196-201, doi:10.1038/s41586-018-0083-5 (2018).

132 Thelot, F. A. *et al.* Distinct allosteric mechanisms of first-generation MsbA inhibitors. *Science* **374**, 580-585, doi:10.1126/science.abi9009 (2021).

133 Breijyeh, Z., Jubeh, B. & Karaman, R. Resistance of Gram-Negative Bacteria to Current Antibacterial Agents and Approaches to Resolve It. *Molecules* **25**, doi:10.3390/molecules25061340 (2020).

134 Moyes, R. B., Reynolds, J. & Breakwell, D. P. Differential staining of bacteria: gram stain. *Curr Protoc Microbiol* **Appendix 3**, Appendix 3C, doi:10.1002/9780471729259.mca03cs15 (2009).

135 Li, C., Guan, Z., Liu, D. & Raetz, C. R. Pathway for lipid A biosynthesis in Arabidopsis thaliana resembling that of Escherichia coli. *Proc Natl Acad Sci U S A* **108**, 11387-11392, doi:10.1073/pnas.1108840108 (2011).

136 Emiola, A., George, J. & Andrews, S. S. A Complete Pathway Model for Lipid A Biosynthesis in Escherichia coli. *PLoS One* **10**, e0121216, doi:10.1371/journal.pone.0121216 (2014).

137 Fathy Mohamed, Y., Hamad, M., Ortega, X. P. & Valvano, M. A. The LpxL acyltransferase is required for normal growth and penta-acylation of lipid A in Burkholderia cenocepacia. *Mol Microbiol* **104**, 144-162, doi:10.1111/mmi.13618 (2017).

138 Raetz, C. R. *et al.* Discovery of new biosynthetic pathways: the lipid A story. *J Lipid Res* **50 Suppl**, S103-108, doi:10.1194/jlr.R800060-JLR200 (2009).

139 Raetz, C. R., Reynolds, C. M., Trent, M. S. & Bishop, R. E. Lipid A modification systems in gram-negative bacteria. *Annu Rev Biochem* **76**, 295-329, doi:10.1146/annurev.biochem.76.010307.145803 (2007).

140 Raetz, C. R. & Whitfield, C. Lipopolysaccharide endotoxins. *Annu Rev Biochem* **71**, 635-700, doi:10.1146/annurev.biochem.71.110601.135414 (2002).

141 Reynolds, C. M. & Raetz, C. R. Replacement of lipopolysaccharide with free lipid A molecules in Escherichia coli mutants lacking all core sugars. *Biochemistry* **48**, 9627-9640, doi:10.1021/bi901391g (2009).

142 Chung, H. S. & Raetz, C. R. Interchangeable domains in the Kdo transferases of Escherichia coli and Haemophilus influenzae. *Biochemistry* **49**, 4126-4137, doi:10.1021/bi100343e (2010).

143 Simpson, B. W. *et al.* Identification of Residues in the Lipopolysaccharide ABC Transporter That Coordinate ATPase Activity with Extractor Function. *MBio* **7**, doi:10.1128/mBio.01729-16 (2016).

144 Ma, B., Reynolds, C. M. & Raetz, C. R. Periplasmic orientation of nascent lipid A in the inner membrane of an Escherichia coli LptA mutant. *Proc Natl Acad Sci U S A* **105**, 13823-13828, doi:10.1073/pnas.0807028105 (2008).

145 Zhang, G. *et al.* Cell-based screen for discovering lipopolysaccharide biogenesis inhibitors. *Proc Natl Acad Sci U S A* **115**, 6834-6839, doi:10.1073/pnas.1804670115 (2018).

146 Zhou, Z., White, K. A., Polissi, A., Georgopoulos, C. & Raetz, C. R. Function of Escherichia coli MsbA, an essential ABC family transporter, in lipid A and phospholipid biosynthesis. *J Biol Chem* **273**, 12466-12475, doi:10.1074/jbc.273.20.12466 (1998).

147 Zhang, X. *et al.* Identification of an anti-Gram-negative bacteria agent disrupting the interaction between lipopolysaccharide transporters LptA and LptC. *Int J Antimicrob Agents* **53**, 442-448, doi:10.1016/j.ijantimicag.2018.11.016 (2019).

148 Sperandeo, P. *et al.* Characterization of lptA and lptB, two essential genes implicated in lipopolysaccharide transport to the outer membrane of Escherichia coli. *J Bacteriol* **189**, 244-253, doi:10.1128/JB.01126-06 (2007).

149 Sperandeo, P. *et al.* Functional analysis of the protein machinery required for transport of lipopolysaccharide to the outer membrane of Escherichia coli. *J Bacteriol* **190**, 4460-4469, doi:10.1128/JB.00270-08 (2008).

150 Okuda, S., Freinkman, E. & Kahne, D. Cytoplasmic ATP hydrolysis powers transport of lipopolysaccharide across the periplasm in E. coli. *Science* **338**, 1214-1217, doi:10.1126/science.1228984 (2012).

151 Suits, M. D., Sperandeo, P., Deho, G., Polissi, A. & Jia, Z. Novel structure of the conserved gram-negative lipopolysaccharide transport protein A and mutagenesis analysis. *J Mol Biol* **380**, 476-488, doi:10.1016/j.jmb.2008.04.045 (2008).

152 Maldonado, R. F., Sa-Correia, I. & Valvano, M. A. Lipopolysaccharide modification in Gram-negative bacteria during chronic infection. *FEMS Microbiol Rev* **40**, 480-493, doi:10.1093/femsre/fuw007 (2016).

153 Ebbensgaard, A., Mordhorst, H., Aarestrup, F. M. & Hansen, E. B. The Role of Outer Membrane Proteins and Lipopolysaccharides for the Sensitivity of Escherichia coli to Antimicrobial Peptides. *Front Microbiol* **9**, 2153, doi:10.3389/fmicb.2018.02153 (2018).

154 Ventola, C. L. The Antibiotic Resistance Crisis. *Pharmacy and Therapeutics* **40**, 277-283 (2015).

155 Simons, A., Alhanout, K. & Duval, R. E. Bacteriocins, Antimicrobial Peptides from Bacterial Origin: Overview of Their Biology and Their Impact against Multidrug-Resistant Bacteria. *Microorganisms* **8**, doi:10.3390/microorganisms8050639 (2020).

156 Hoffman, P. S. Antibacterial Discovery: 21st Century Challenges. *Antibiotics (Basel)* **9**, doi:10.3390/antibiotics9050213 (2020).

157 Annunziato, G. Strategies to Overcome Antimicrobial Resistance (AMR) Making Use of Non-Essential Target Inhibitors: A Review. *Int J Mol Sci* **20**, doi:10.3390/ijms20235844 (2019).

Chapter 2

Application of nuclear magnetic resonance spectroscopy

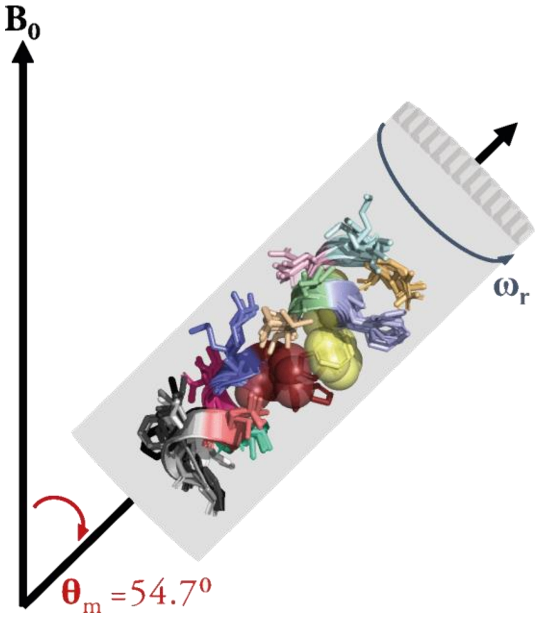

> "There never was a time when there was no motion."
>
> – *Aristoteles*

2.1 NMR studies on membrane proteins

In 1971, in Brookhaven, New York, the Protein Data Bank (PDB) was established to archive biological macromolecular structures[1]. By early 2016, about 120.000 protein structures were recorded in the PDB. At that time, less than 2% were membrane proteins with only very few solved by nuclear magnetic resonance spectroscopy (NMR)[2]. As of today (November 2022), the PDB counts for approximately 200.000 structures with nearly 7% of the structures determined by NMR and over one million computed models. Interestingly, the fraction of membrane proteins solved remained around 2.5% albeit membrane proteins account for 30% of all proteins[3-5]. Out of these 5000 membrane protein structures, less than 10% are solved by solution NMR, and even less than 1% are solved by solid-state NMR[1].

Despite the small fraction of membrane protein structures solved by NMR, this spectroscopic method has complemented the structural data of X-ray or electron microscopy (EM) structures.[6] NMR can give insight into structural and dynamic information at an atomic level without intrusive labelling while allowing flexible experimental conditions[7]. In addition, NMR allows titration experiments and other time-resolved experiments that can follow dynamic changes in the protein and multiple reaction components over time[8-10]. However, the application of NMR comes with limits and challenges, such as the structural integrity upon preparation with detergent micelles, which have long been known to be non-native.

The critical micelle concentration (CMC) and harsh detergents can deform the native membrane protein structures. Whereas the elucidation of protein with mild detergents can accommodate solution NMR[11]. Nevertheless, detergent micelles, bicelles, and amphipols are still considered to be non-native conditions (**figure 2.1**). Alternatively, a more native method to accommodate membrane protein in solution NMR is the use of nanodiscs, developed in the 1990s by Stephen G. Sligar and coworkers[12-17]. However, under these conditions, protein size is often restricted as the larger proteins tumble slower and have shorter relaxation times. This in turn leads to a lower sensitivity and a crowded spectrum due to the increased number of active nuclei[18]. The latter challenge can be overcome by selective labelling schemes (**paragraph 2.8**)[19,2019,20].

Solid-state NMR allows an even more native state of membrane proteins as the protein can be reconstituted into phospholipid bilayers that resemble the native phospholipid bilayer environment. In addition to membrane protein studies, solid-state NMR could also accommodate NMR in vitro studies such as whole cells, intact and partial human tissues of the brain, tumours, bones, and teeth[21-26]. Molecular size limit concerns mainly the sample packing into an NMR rotor for solid-state NMR rather than the solid-state NMR hardware, as the measurements can be recorded statically. Perhaps an even more important aspect of solid-state NMR is the fast sample rotation at the magic angle (MAS) of 54.7°, which averages out the anisotropic interactions as chemical shifts or dipolar couplings and leads to less line-broadening and a well-resolved spectrum[27].

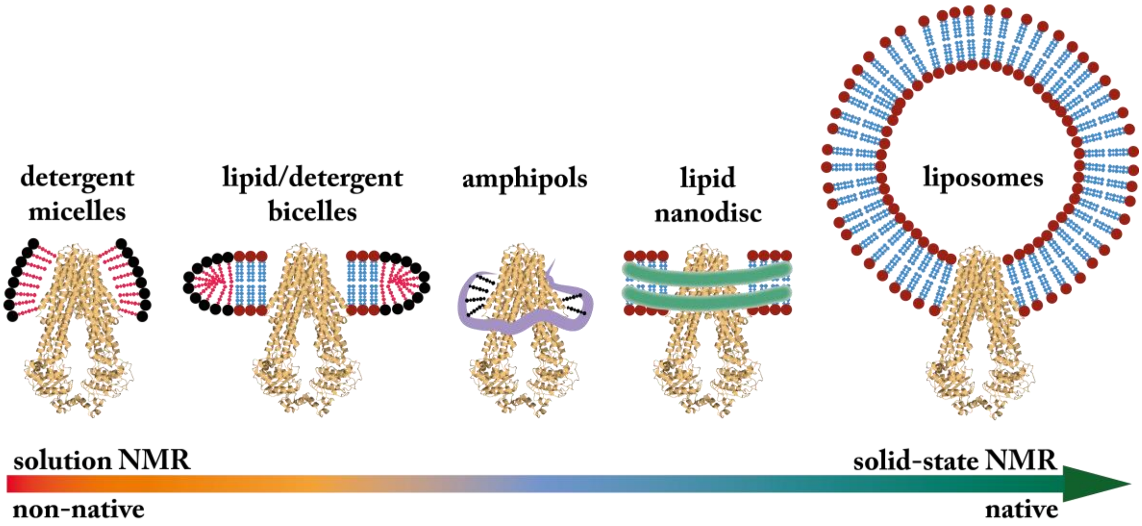

Figure 2.1. Overview of membrane protein conditions in NMR spectroscopy ranging from non-native to native environments.

Numerous membrane protein studies have been conducted using solid-state NMR which resulted in different scientifically relevant aspects. EmrE (Small Multidrug Resistance Transporter Family) solid-state NMR studies showed recognition of the SMR protein by ^{19}F-NMR[28-30]. Furthermore, solid-state NMR could also be used to study protein dynamics of membrane proteins in the lipid bilayer through two-dimensional spectroscopy, e.g., EGFR[31] (epidermal growth factor receptor) and KscA[32] (potassium channel). In addition, various states of KscA have been recorded by the titration of potassium in solid-state-NMR[33]. Similarly, for KR2 (microbial rhodopsin), various photo intermediate states have been recorded by solid-state NMR[34,35]. Moreover, solid-state NMR could be used to probe crosstalk in protomers such as green proteorhodopsin[36,37].[36,37]

Additionally, multidimensional as well as deuterium and phosphorus-31 NMR can be used to assign and highlight crucial residues in various states. This has been done for several ABC transporters, i.e., LmrA[38,39], BmrA[40-42], MsbA[43-45], and ArtMP[46]. By using ^{31}P-NMR it was possible to 1) trap MsbA in various states (Chapters 5-6) and 2) study time-resolved ATP hydrolysis (Chapter 4) [44]. These states could then be used to determine important residues or parts of the protein within the different functions, e.g., nucleotide binding or substrate binding[43,45]. For instance, transmembrane helix 6 appears to play a crucial role in homodimeric MsbA[45]. In the case of BmrA, ^{31}P-NMR revealed changes in protein symmetry and asymmetry in certain stages.

It is inherently challenging to study biological macromolecules due to their weight altogether with the low sensitivity of NMR. Since the 1990s, the introduction of the 600 MHz NMR spectrometer made the study of such large molecules feasible. More high-field NMR machines have been developed since then (e.g. 800 MHz, 950 MHz, 1.2 GHz)[47]. Various studies have compared the differences in magnetic fields ranging from 500 MHz to 1.2 GHz[48-51]. The outcome of these studies all showed that high-field NMR improved the resolution of macromolecules significantly. Additionally, ultra-high field NMR allows the studies of in-cell NMR[52]. Furthermore, these developments expanded the list of possible NMR experiments[53]. Further improvement in resolution, line width, and sensitivity is allowed by ultra-fast MAS (>100 kHz) in solid-state NMR in combination with high-field NMR[54-62].

2.2 NMR basic principles

Nuclear spins, angular momentum, and magnetic moments[63,64]

In NMR the active nuclei possess nuclear spins with quantum number spin $s \geq \frac{1}{2}$, which is an intrinsic angular momentum. In the absence of a magnetic field B_0 the spin energy levels are degenerate. In the presence of B_0 spins populate discrete energy levels. Nuclear spins undergo different energy states in the absence of a magnetic field. By applying the radiation necessary to produce NMR transitions or radio frequency field, the spins can transition between different states. The magnitude of a spin angular momentum S is described with:

$$|\vec{S}| = \sqrt{S(S+1)}\hbar$$

where the magnitude is in units of ħ(h/2π), and the spin quantum number l of a nucleus can be $\frac{1}{2}$ (1H, 13C) and 1(14N).

The z-component of the spin is described as:

$$S_z = m_s\hbar$$

where m_s is the magnetic quantum number with 2s+1 values between-s, s+1, and +s has magnetic moments of nuclei:

$$\vec{\mu} = \gamma\vec{S}$$

In the presence of a magnetic field the spins of the magnetic moments of the nuclei have an intersection energy:

$$E = -\vec{\mu}\vec{B}_0$$

where B_0 represents the magnetic field. In a strong magnetic field, the spin quantization axis (z) coincides with the field direction and:

$$E = -\vec{\mu}\vec{B}_0 = -\mu_z B_0 \qquad B_0 = \begin{pmatrix} 0 \\ 0 \\ B_0 \end{pmatrix}$$

where B_0 is the magnitude of the vector B_0 and μ_z is the z-component leading to:

$$\mu_z = \gamma s_z = \gamma m_s \hbar$$

$$E_{m_s} = -m_s \hbar \gamma B_0$$

with the resonance condition and resonance frequency (ΔE/h)

$$\Delta E = \hbar |\gamma| B_0$$

$$V_0 = \frac{|\gamma| B_0}{2\pi}$$

Spin relaxation

During an NMR experiment, the net magnetisation of the spins will return to its equilibrium. This process to recover equilibrium is called relaxation. The relaxation contributes to the NMR linewidths. Spin-lattice relaxation enables spins to move between their energy levels to establish the Boltzmann population difference Δn_{eq}. This is also known as longitudinal relaxation. By approaching the equilibrium energy is released to its surroundings or lattice. The changes are characterized by the T_1 time, a first-rate order constant for the relaxation.

$$\Delta n(t) = \Delta n_{eq}\left[1 - \exp\left(-\frac{t}{T_1}\right)\right]$$

and the general rate equation for non-equilibrium spin populations:

$$\frac{d\Delta n}{dt} = -\frac{1}{T_1}\left(\Delta n - \Delta n_{eq}\right)$$

Thus, spin-lattice relaxation time is the decay constant for the recovery of the z component of the spin magnetization. The inversion recovery method is a common method to measure the longitudinal relaxation by applying a 180° pulse to allow the magnetization to run form z to -z over time. The magnetization can be described by:

$$M_z(t) - M_0 = [M_z(0) - M_0]\exp\left(-\frac{t}{T_1}\right)$$

Upon a 90° pulse, the transverse magnetization to the xy plane takes place. The measurement is more precise with a longer recycle delay[64-67]. The NMR intensity can be determined with:

$$S(\tau) = \left[1 - 2\exp\left(-\frac{\tau}{T_1}\right)\right]S(\infty)$$

T1 is a time constant that describes the return of the spin system to equilibrium after a 90° pulse. Equilibrium here means that the net magnetization M_0 is aligned again along B_0 (z-axis). It determines the repetition delay time between consecutive spin system preparation steps and can be simplified as:

$$M_z(t) = M_0(1 - \exp\left(-\frac{t}{T_1}\right))$$

Transverse relaxation or spin-spin relaxation time T_2 is the decay constant for the xy component of the spin magnetization perpendicular to B_0.

$$\frac{1}{\pi T_2} = \Delta v$$

Here, Δv is the relaxation-induced linewidth. The T_2 time increases with faster molecular tumbling, resulting in narrower lines as the dipolar interaction is more efficiently averaged[63,68]. A method used to determine the T_2 time is the Hahn echo or spin echo experiment.

$$M_x(t) = M_0\sin(\omega_0 t)\exp\left(-\frac{t}{T_2}\right)$$

$$M_y(t) = -M_0\sin(\omega_0 t\exp\left(-\frac{t}{T_2}\right)$$

A 90° pulse is applied to make the total magnetization precess and the vectors move away from the xy plane. This process decreases transverse magnetization. Subsequently, a 180° pulse allows precession to continue for period τ by flipping the magnetization around the y-axis to s symmetrical position in the xy plane. This refocusing of the dephasing caused by field inhomogeneity using a 180° pulse is called a spin echo. The NMR intensity is independent of the field inhomogeneity and is given by

$$S(2\pi) = S(0)\exp\,(-\frac{2\tau}{T_2})$$

and T_2 is obtained by plotting τ against $\ln[S(2\pi)]$[63,69,70].

Free induction decay and Fourier transformation

The magnetization in the NMR coil is detected in the NMR probe and forms the free induction decay (FID) the FID is the sum of the oscillating waves of frequencies, amplitudes, and phases. The detected frequencies are in the form $\omega_{rf} + \Omega$ with the transmitter frequency $v_{rf} = \frac{\omega_{rf}}{2\pi}$ (MHz) and the resonance offsets $\frac{\Omega}{2\pi}$ in the order of the chemical shift range (kHz). Two signals are acquired for each resonance as cosine and sine functions of the offset frequency Ω with a decay rate of $\frac{1}{T_2}$:

$$S(t) = [\cos\Omega t + i\sin\Omega t]\exp\left(-\frac{t}{T_2}\right) = \exp(i\Omega t)\exp\left(-\frac{t}{T_2}\right) \quad t \geq 0$$

$$S(t) = 0 \quad t < 0$$

Using Fourier transformation this can be converted into a spectrum $S(\omega)$:

$$S(\omega) = \int_{-\infty}^{\infty} s(t)\exp(-i\omega t)\,dt$$

$$S(\omega) = A(\Delta\omega) - iD(\Delta\omega)$$

$$(\Delta\omega) = \frac{1/T_2}{(\frac{1}{T_2})^2 + (\Delta\omega)^2}$$

$$D(\Delta\omega) = \frac{\Delta\omega}{(\frac{1}{T_2})^2 + (\Delta\omega)^2}$$

$\Delta\omega = \omega - \Omega$ is the frequency parameter which is defined by the centre of the resonance at $\omega = \Omega$. The real and imaginary part $A(\Delta\omega)$ and $D(\Delta\omega)$ respectively, correspond to the absorptive and dispersive Lorentzian. The real absorptive part of the spectrum gives narrower lines and maximum amplitude at the frequency of interest.

Quantum mechanics

The Hamiltonian is one of the most important operators in the quantum mechanical description of any system. It determines the total energy of the system described by the Schrödinger equation with ψ as a wavefunction for the system, $\hat{H}$ is the Hamiltonian operator, and E is an allowed energy corresponding to the wavefunction

$$\hat{H}\psi = E\psi$$

$$E = \langle\hat{H}\rangle = \langle\psi|\hat{H}|\psi\rangle$$

For nuclear spins and its surrounding system this can be described as:

$$\hat{H} = \hat{H}_i + \hat{H}_{i,e} + \hat{H}_e$$

With $\hat{H}_i$ only depending internally on the nuclear spins, $\hat{H}_e$ externally independent of the nuclear spin, and $\hat{H}_{i,e}$ depending on both the nuclear spins and its surrounding[64,71,72]. Internal interactions are shielding (δ), dipolar coupling (D), indirect coupling (J, scalar coupling, or spin-spin coupling), and quadrupolar coupling (Q). External interactions are the Zeeman effect which is a result of a strong field. The external magnetic field results in the Zeeman splitting with the radio frequency (RF) pulses.

Among the internal interactions, all are anisotropic, with the exception of J-coupling. Scalar coupling is the magnetic interaction between nuclei. It is considered to be an isotropic interaction and this spin-spin coupling, or indirect dipole-dipole coupling, with J-coupling through bond, dipolar coupling through space, both for spins $s = \frac{1}{2}$ [63,64,73,74].[63,64,73,74]

Dipole-dipole (dipolar) coupling[73,75-77]

In solids, the dipolar coupling can be mathematically described by the dipolar interaction Hamiltonian. Dipolar coupling arises from the interaction between two nuclear spins through their electric dipole moments. The strength of the coupling depends on the distance between the nuclei, their relative orientations, and the gyromagnetic ratio of the nuclei. Dipolar coupling results in the splitting of NMR signals into multiple peaks (multiplets), providing information about the number and arrangement of neighbouring nuclei.

The main difference between heteronuclear and homonuclear dipolar couplings lies in the gyromagnetic ratios of the nuclei involved. The gyromagnetic ratio determines the strength of the dipolar coupling, and in heteronuclear coupling, the differing gyromagnetic ratios contribute to the complexity and diversity of the observed coupling patterns in solid-state NMR spectra.

Heteronuclear dipolar coupling refers to the dipolar interaction between nuclei of different elements or isotopes. This occurs when the interacting nuclei have different gyromagnetic ratios ($\gamma_1 \neq \gamma_2$). Heteronuclear dipolar coupling is often observed in solid-state NMR experiments involving multiple types of nuclei, such as ^{1}H-^{13}C or ^{1}H-^{15}N couplings. Heteronuclear dipolar coupling can be mathematically described by:

$$\hat{H}_{IS} = d_{IS} 2 I_Z S_Z$$

$$d_{IS} = b_{IS} \frac{1}{2} (3\cos^2\beta - 1)$$

$$b_{IS} = \left(\frac{\mu_0}{4\pi}\right) \frac{\hbar \gamma_I \gamma_S}{r_{IS}^3}$$

Homonuclear dipolar coupling, on the other hand, refers to the dipolar interaction between nuclei of the same element or isotope. In this case, the interacting nuclei have the same gyromagnetic ratio ($\gamma_1 = \gamma_2$). Homonuclear dipolar couplings are commonly observed in solid-state NMR experiments involving nuclei of the same type, such as ^{1}H-^{1}H couplings. Homonuclear dipolar coupling can be mathematically described by:

$$\hat{H}_{IS} = d_{IS}(3 I_Z S_Z - \vec{I}\,\vec{S})$$

Decoupling

Unwanted J-couplings or dipolar couplings are removed by a technique called decoupling. This is particularly important in multi-dimensional NMR experiments to simplify the information obtained from the cross peaks rather than the information collected from the coupling. This approach used a continuous strong radiofrequency field during a so-called decoupling period. Partial decoupling or offset decoupling is introduced by using a weaker radiofrequency field. Full decoupling can be homonuclear or heteronuclear, depending on the chosen decoupling, the same or the other observed nuclei can be decoupled. In specific or soft decoupling, the radiofrequency only covers the specific radiofrequency for the intended nuclei[64].

Cross-polarisation

Cross-polarisation (CP) or proton-enhanced nuclear induction spectroscopy is a specific technique used in solid-state NMR. During the CP magnetization is transferred from the nuclei of one nucleus to another. An example of a CP experiment used in this dissertation is given in figure 2.2. The introduction of the 90° pulse along the x-axis, rotates the magnetization onto the y-axis. This is followed by the CP contact time where the ^{1}H magnetization is transferred to other nuclei X, e.g., ^{13}C, ^{15}N, ^{31}P, and magnetization will build up during this contact time. Finally, in the acquisition time the NMR signal of X is detected under high-power decoupling. The polarization of the nuclei is induced with radiofrequency under matching Hartmann-Hahn conditions, meaning that cross polarisation occurs when the H and X nutation frequencies are equal:

$$\gamma^H {B_1}^H = \gamma^X {B_1}^X \pm \omega_R$$

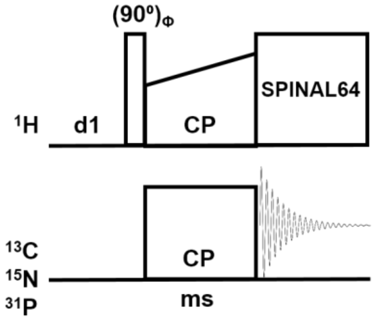

Figure 2.2. The cross-polarisation pulse sequence.

Chemical shift[63,64]

Not all nuclei have identical resonance frequencies. Therefore, ν_{CS} depends on the nucleus position in the molecule or the local electron distribution, also known as the chemical shift. This arises from B_{local} which is smaller than B_0. B_{local} can cause shielding or deshielding, depending on the electron environment. Shielding is described by a constant σ, which is the constant of the proportion between B_{local} and B_0. The nuclei frequency ten changes to:

$$\nu_{CS} = -\frac{\gamma B_0}{2\pi}(1-\sigma)$$

For chemical shift, the relation $\delta = -\sigma$ applies. The chemical shift is referenced by the difference between the Larmor frequency of the nuclei of interest and a reference nucleus ($\nu_{0,\mathrm{ref}}$) in parts per million (ppm):

$$\delta = 10^{6}\left(\frac{\nu_{0}-\nu_{0,\mathrm{ref}}}{\nu_{0,\mathrm{ref}}}\right)$$

The smaller the shielding, the larger the chemical shift, where δ is the chemical shift, σ_{ref} is the chemical shift of the reference compound, and the chemical shifts can be converted back to frequencies:

$$\delta = \frac{\nu_{\mathrm{ref}}\ (\mathrm{Hz})}{\nu_{\mathrm{spectrometer}}\ (\mathrm{MHz})}$$

2.3 Solid-state NMR

Solid-state NMR dates back to nearly a century of trial and error, when in 1936 C. J. Gorter et al. made de first attempts to measure condensed matter[78,79]. Nearly a decade later the first successful measurements were conducted by E. M. Purcell et al. and H. Bloch et al.[80,81]. By the end of the 1950s, MAS- NMR came to light where sample spinning at the magic angle θ_{m} of 54.74° removes anisotropic line-broadening by removing the $(3\cos^{2}\theta_{\mathrm{m}} - 1)$ term in the chemical shift and dipolar coupling Hamiltonian[82-86]:

$$\langle 3\cos^{2}\theta - 1\rangle = \frac{1}{2}(3\cos^{2}\theta_{\mathrm{m}} - 1)\ (3\cos^{2}\beta - 1)$$

where β is the angle between e.g. two different coupled nuclei and the axis of the of rotation, but θ_{m} is fixed by the experimenter (figure 2.3)[68,87]. By setting $\theta_{\mathrm{m}} is$ to 54.74°, then $(3\cos^{2}\theta_{\mathrm{m}} - 1) = 0$. Therefore, the average $\langle 3\cos^{2}\theta - 1\rangle$ is also zero. This leads to the averaging of anisotropy associated with any interaction that results in a shift in the Zeeman spin function energies[74]. Despite the early discovery of magic angle sample spinning, it took a long time before it became routine to use ssNMR as a biophysical method for studies.

Polycrystalline samples lead to powder patterns in a static measurement (figure 2.4). Different shielding anisotropy gives rise to various shielding powder patterns or chemical shift anisotropy (CSA). The presence of electrons results in the shielding of nuclei of molecules in a magnetic field, leading to a shielding field or the chemical shift described by:

$$\hat{\mathrm{H}}_{\mathrm{CS}} = -\gamma_{\mathrm{I}}\mathrm{I}\overleftrightarrow{\delta}^{\mathrm{LAB}}\overrightarrow{\mathrm{B}}_{0} = -\gamma\mathrm{I}_{\mathrm{Z}}\delta_{\mathrm{ZZ}}^{\mathrm{LAB}}\mathrm{B}_{0}$$

The δ represents the tensor which are property of internal orientation-dependent interactions involved in NMR where the general tensor is δ:

$$\overleftrightarrow{\delta}^{\mathrm{LAB}} = \begin{pmatrix} \delta_{\mathrm{XX}}^{\mathrm{LAB}} & \delta_{\mathrm{XY}}^{\mathrm{LAB}} & \delta_{\mathrm{XZ}}^{\mathrm{LAB}} \\ \delta_{\mathrm{XY}}^{\mathrm{LAB}} & \delta_{\mathrm{YY}}^{\mathrm{LAB}} & \delta_{\mathrm{YZ}}^{\mathrm{LAB}} \\ \delta_{\mathrm{ZX}}^{\mathrm{LAB}} & \delta_{\mathrm{ZY}}^{\mathrm{LAB}} & \delta_{\mathrm{ZZ}}^{\mathrm{LAB}} \end{pmatrix}$$

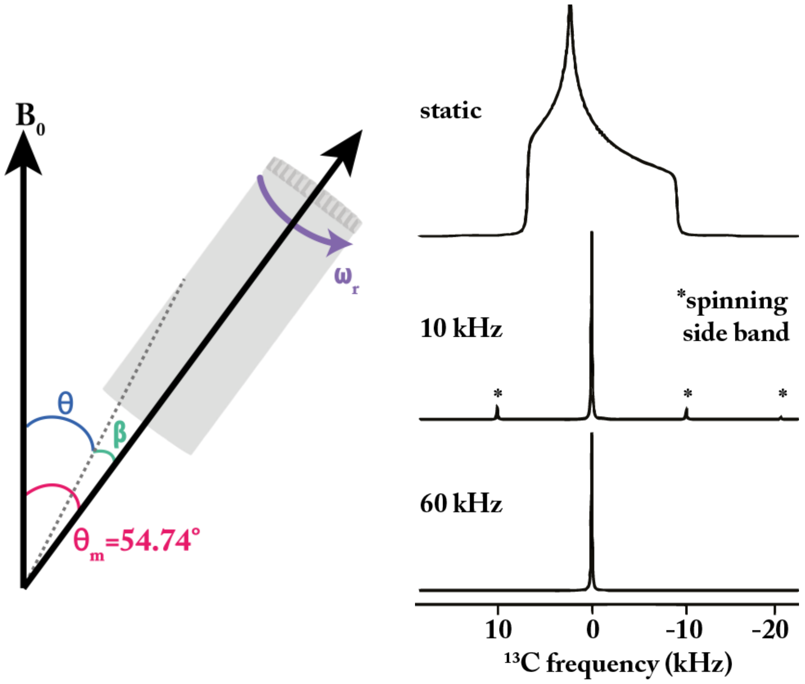

Figure 2.3. The angles θ, β, and θ_m are shown with respect to the equation above. The vector is represented by the grey dotted line. The axis of rotation is guided by ω_r. An example of the spectra with and without MAS is shown on the right. *This figure was adapted from Polenova et al. 2015 Anal. Chem*[88]*. with permission from American Chemical Society, Copyright © 2015.*

$\vec{B}_0$ is directed along z and leads to the following components:

$$\vec{B}_0 = \begin{pmatrix} 0 \\ 0 \\ B_0 \end{pmatrix}$$

with

$$\vec{B}_{\mathrm{local}} = \delta\vec{B}_0 \begin{pmatrix} B_X \\ B_Y \\ B_Z \end{pmatrix}_{\mathrm{local}} = \delta \begin{pmatrix} 0 \\ 0 \\ B_0 \end{pmatrix}$$

Therefore, the shielding is generally not parallel to the applied field. In its principal axis system (PAS), the tensors become diagonal δ:

$$\overleftrightarrow{\delta}^{\mathrm{PAS}} \rightarrow \begin{pmatrix} \delta_{\mathrm{XX}}^{\mathrm{PAS}} & 0 & 0 \\ 0 & \delta_{\mathrm{YY}}^{\mathrm{PAS}} & 0 \\ 0 & 0 & \delta_{\mathrm{ZZ}}^{\mathrm{PAS}} \end{pmatrix}$$

where $\delta_{\mathrm{XX}}^{\mathrm{PAS}}$, $\delta_{\mathrm{YY}}^{\mathrm{PAS}}$, and $\delta_{\mathrm{ZZ}}^{\mathrm{PAS}}$ are principal components of the tensor. The rotational tensor transformation from a general frame is with respect to the PAS reference. Eventually, leading to the isotropic average:

$$\delta_{iso} = \frac{1}{3}(\delta_{\mathrm{XX}} + \delta_{\mathrm{YY}} + \delta_{\mathrm{ZZ}})$$

$$|\delta_{\mathrm{ZZ}} - \delta_{\mathrm{iso}}| \geq |\delta_{\mathrm{XX}} - \delta_{\mathrm{iso}}| \geq |\delta_{\mathrm{YY}} - \delta_{\mathrm{iso}}|$$

as observed in liquid-state NMR due to its invariant to rotational transformation. In solids, this is one of the three measured parameters, where the second parameter is anisotropy δ_{aniso}:

$$\Delta\delta = \delta_{\mathrm{ZZ}} - \frac{1}{2}(\delta_{\mathrm{XX}} + \delta_{\mathrm{YY}})$$

$$\delta_{\mathrm{aniso}} = \delta_{\mathrm{ZZ}} - \delta_{\mathrm{iso}}$$

Lastly, the asymmetry η is defined by:

$$\eta = \frac{(\delta_{\mathrm{YY}} - \delta_{\mathrm{XX}})}{\delta_{\mathrm{aniso}}}$$

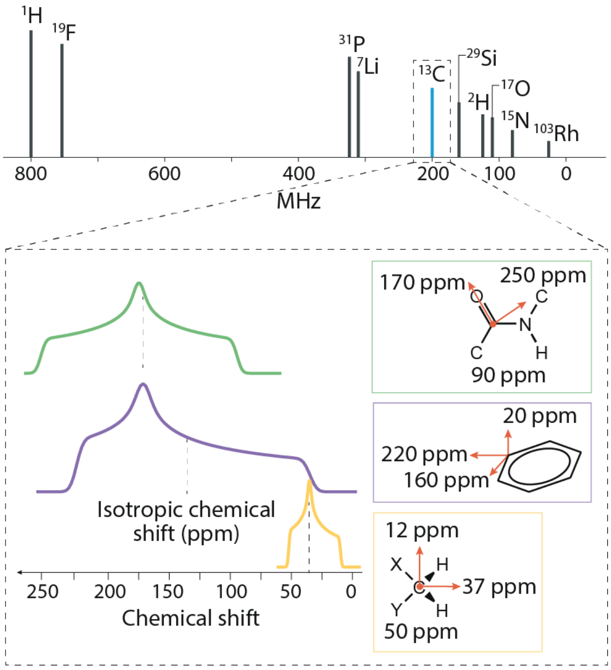

Figure 2.4. The NMR frequencies of different nuclear isotopes depend on their gyromagnetic ratios (γ) and the magnetic field (B0 = 18.8 T, in this example).

In addition, for spins of the same isotope, the frequency depends on the electronic environment of the individual nuclei. Schematic NMR spectra of a static powder containing three 13C nuclei report the chemical structure of the functional groups. The broad powder pattern reflects chemical shift anisotropy, whose geometric average corresponds to the isotropic chemical shift, which is detected when the sample undergoes magic angle spinning (MAS).[89] *This figure and subscript were taken from Reif et al. 2021 Nat Rev Methods Primers 1 with permission from Springer Nature.*

Ultimately, the three different principal components of the shielding tensors as described above with respect to the anisotropy δ_{aniso} and asymmetry η the equation can be reformulated as:

$$\delta(\alpha,\beta) = \delta_{\mathrm{iso}} + \frac{1}{2}\delta_{\mathrm{aniso}}(3\cos^2\beta - 1 - \eta\sin^2\beta\cos 2\alpha)$$

with β and α as the Euler angles which define the Z principal axis orientation of shielding in the magnetic field B_0. Different shielding thus can lead to an axially symmetric anisotropy (η=0), a negative or positive shielding anisotropy (η=0.5), or an asymmetric anisotropy (η=1) [73,90].[73,90]

2.4 Two-dimensional NMR experiments

The fundamental steps for two-dimensional NMR are 1) preparation, 2) evolution, 3) mixing time, and finally 4) detection (figure 2.5). Initially, during the preparation step, cross polarisation via a 90° pulse flips the spins in the xy plane. In the evolution period, magnetization is evolving over time (t_1). Subsequently, the following pulse flips the y-component to the z-axis. During the mixing time $t_{m,}$ the spins interact with each other, and dipolar coupling can take place. Depending on the pulse sequence set, this can be both home homonuclear and heteronuclear. Finally, the NMR signals are measured as a function of time (t_2). Together with the t_1 evolution time, the recorded FIDs can be Fourier transformed into a two-dimensional spectrum[64,73].

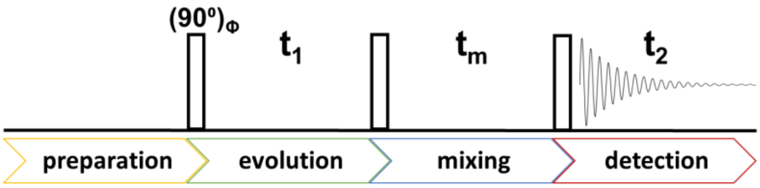

Figure 2.5 Basic schematic setup of an NMR experiment.

Homonuclear ^{13}C spin diffusion[91]

A frequently used homonuclear polarization NMR experiment is proton-driven spin diffusion (PDSD), the equivalent of heteronuclear single quantum coherence/correlation (HSQC) of liquid state NMR. The ^{1}H magnetization is transferred to the X (e.g., ^{13}C) nuclei which are in close proximity (figure 2.6). Dipolar-assisted rotational resonance (DARR) is used for longer mixing times between ^{1}H and X. The latter can be achieved by continuous wave (CW) irradiation, which allows more efficient magnetization transfer to obtain stronger cross peaks in comparison to PDSD. Here, the ^{1}H radio frequency should synchronize with the rotary resonance (RR) as:

$$\omega_H = \omega_X \pm n\omega_{RR}$$

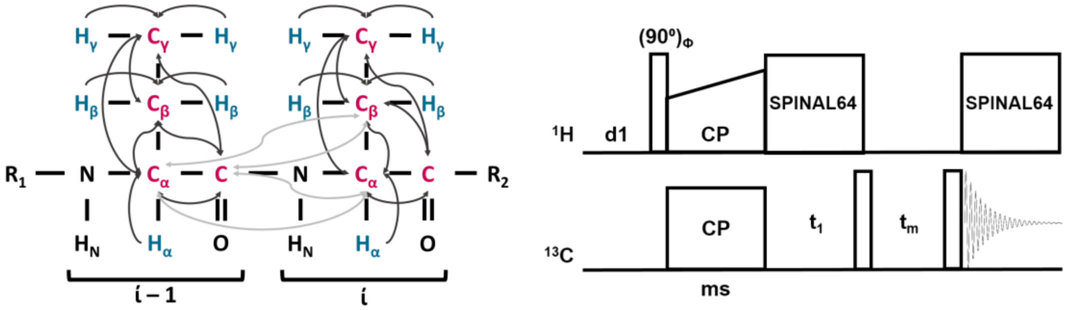

Figure 2.6. Proton-driven spin diffusion (PDSD). Left: ^{1}H magnetization is transferred to the ^{13}C nuclei which are close in space. Right: PDSD pulse sequence. During the experiment, a DARR pulse was introduced.

Heteronuclear polarization transfer[91]

Heteronuclear cross-polarization, or double cross-polarization (DCP) is achieved by the preparation between 1H and Y nuclei, followed by the mixing between nuclei X and Y (figure 2.7). The magnetisation is transferred from the H-N (i) of the amide to the Co (i-1) or Cα (i) under the following conditions:

$$\omega_Y = \omega_X \pm n\omega_{RR}$$

To determine the NCA conditions with respect to the Hartmann-Hahn condition:

$$\omega_Y = \frac{5}{2}\omega_{RR} \text{ and } \ \omega_X = \frac{3}{2}\omega_{RR}$$

For the NCO NCA conditions, this would then be:

$$\omega_{Y} = \frac{5}{2}\omega_{RR} \quad \text{and} \quad \omega_{X} = \frac{7}{2}\omega_{RR}$$

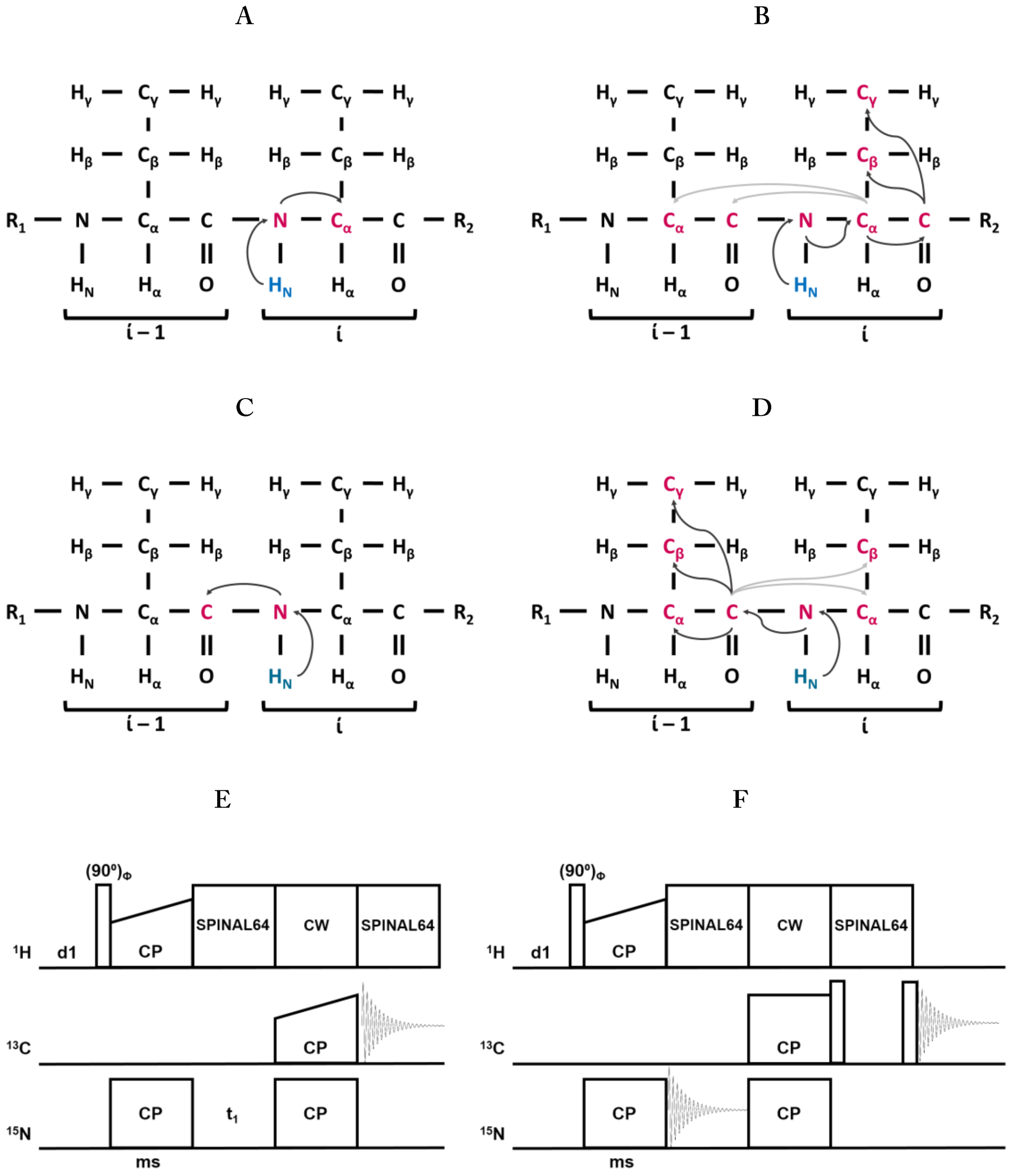

Figure 2.7. NCO(CX) and NCA(CX) experiments. A) Magnetisation transfer of an NCA experiment. B) Magnetisation transfer of an NCACX experiment. C) Magnetisation transfer of an NCO experiment. D) Magnetisation transfer of an NCOCX experiment. E) NCO/NCA pulse sequence. F) NCACX/NCOCX pulse sequence.

Nuclear Overhauser effect

In the nuclear Overhauser effect (NOE) the polarization of nuclear spins is transferred to other nuclei via cross-relaxation (figure 2.8). In NMR the cross-relaxation rates can be measured. This is done by using two-dimensional NOE spectroscopy (NOESY). The cross-relaxation is given by the proton dipolar coupling. Spins that undergo cross-relaxation are in proximity to one another. The resulting cross peaks give information about the protons in space. Here, the magnetization transfer via cross-relaxation takes place during the given mixing time which can be fixed experimentally. Build-up curves of the NOE can be obtained by increasing the NOE mixing time per experiment. The protons in close proximity will have the fasted build-up rates.[63,92,93] In solid-state NMR, NOE is normally not possible, but under some conditions such as anisotropic motions in lipid membranes, it can be observed.

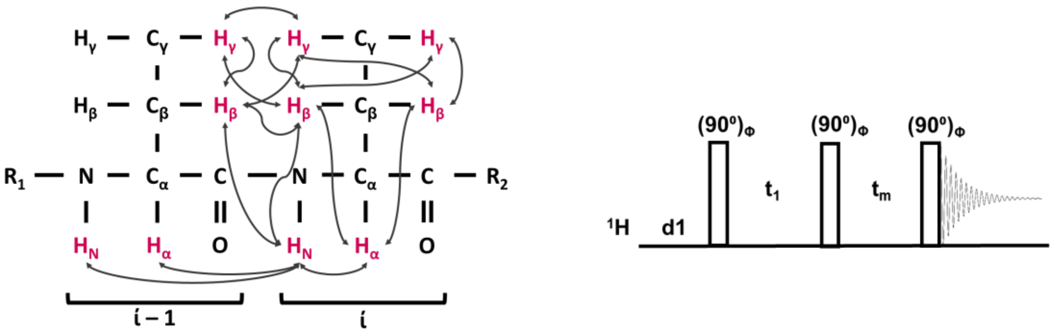

Figure 2.8. H-H nuclear Overhauser spectroscopy. Left: Magnetisation transfer of a NOESY experiment. Right: H-H NOESY pulse sequence.

2.5 Labelling strategies

Given that membrane proteins are generally large complexes, strategic labelling schemes are often required to make the NMR experiments more feasible. Protein expression in *E. coli* is an easy expression method to increase protein yield to overcome low NMR sensitivity. Isotope-labelled amino acids can be added to the growth media to incorporate isotope-labelled proteins. However, to label strategically is often required to know the bacterial metabolic pathway to avoid isotopic scrambling (figure 2.9). Moreover, precursors can be used to avoid isotope scrambling or to unlabel specific amino acids[19,94].[19,94] Furthermore, the UPLABEL algorithm is one of the many ways to strategic labelling schemes easier[20]. By selecting the right combinations of amino acids, unique pairs can be formed to assign distinct regions in the protein[43,45]. A good combination could gain a high yield of non-isotope scrambled protein samples and less ambiguous NMR data.

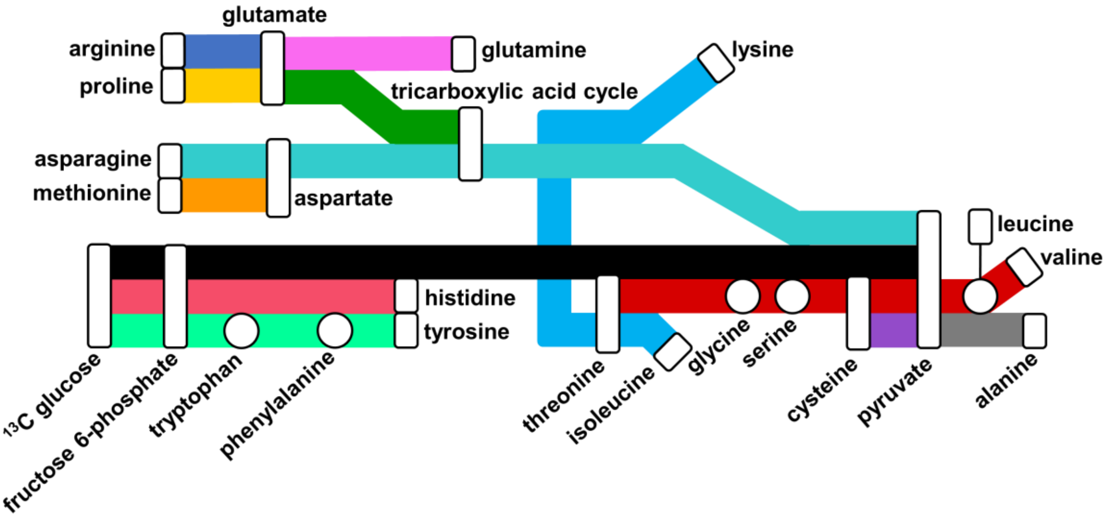

Figure 2.9. The metabolic pathway for isotopic labelling of proteins expressed bacterial cells. *Based on Lacabanne et al 2017 J. Biomol. NMR.*

Another way to overcome scrambling or overcrowded spectra is by introducing specific labelling. This can be done by site-specific labelling in combination with unique pair labelling as described above. In this way, a unique signal is introduced that is specific to a protein region e.g., drug binding sites. This can be done by adding specific isotope-labelled amino acids. Sparse labelling can be introduced to larger proteins to avoid a crowded spectrum by only labelling a few amino acids or by substituting the carbon source for glycerol[95]. Alternatively, deuterium labelling, fluorine labelling, or chemical labelling could be used[96-101]. Various combinations can be made from any of the strategies discussed above to create a tailored labelling scheme.

2.6 The application of real-time ^{31}P NMR on MsbA

A straightforward way to follow the most essential reaction for ABC transporters by NMR is time-resolved NMR. Time-resolved NMR is an excellent way to measure enzyme kinetics. This method has been used to study the hydrolysis of sucrose into glucose and fructose[8]. It has also been used to study RNA folding, photolysis, and phosphorylation[102-106]. Using real-time ^{31}P NMR the ATP hydrolysis of MsbA can be followed over time. This has been done in liquid-state and solid-state NMR. The latter has a minor limitation, that being the reaction of interest has a dead time due to the unpacking and repacking of the NMR rotor. In contrast to liquid-state NMR, this can be overcome by an automated injection program (figure 2.10). Thus, there is no dead time, and the entire reaction of interest can be followed over time. The original setup was designed by Mok et al. 2003[107].

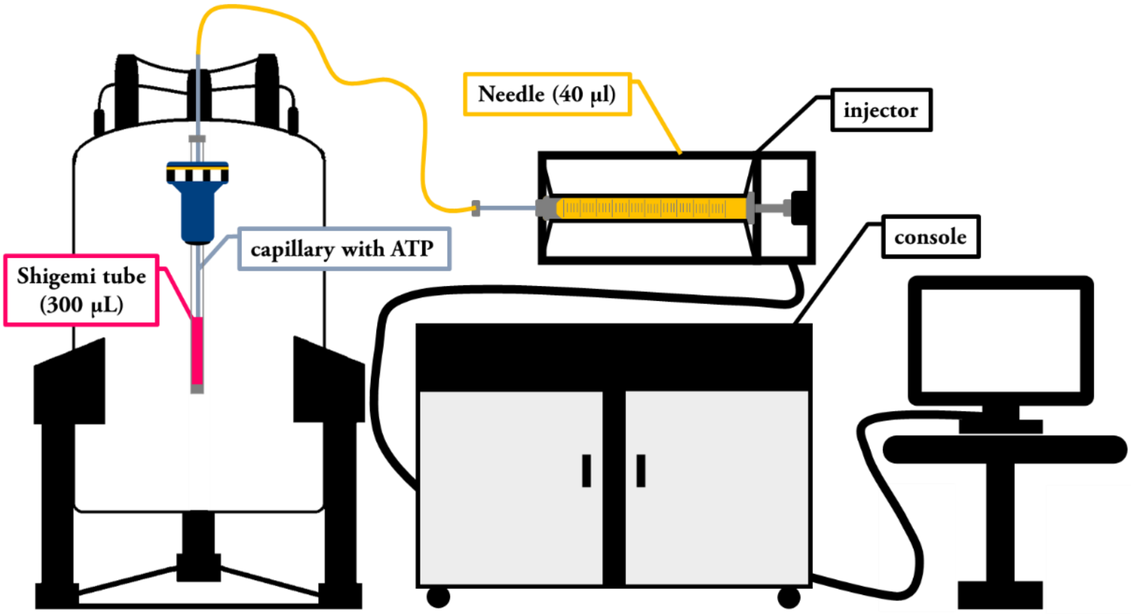

Figure 2.10. Liquid state NMR setup for time-resolved NMR. This setup allows a controlled and automated injection of compounds. *Based on Mok et al. 2003 J Am Chem Soc.*

References

1 Berman, H. M. *et al.* The Protein Data Bank. *Nucleic Acids Res* **28**, 235-242, doi:10.1093/nar/28.1.235 (2000).

2 Liang, B. & Tamm, L. K. NMR as a tool to investigate the structure, dynamics and function of membrane proteins. *Nat Struct Mol Biol* **23**, 468-474, doi:10.1038/nsmb.3226 (2016).

3 Hoglund, P. J., Nordstrom, K. J., Schioth, H. B. & Fredriksson, R. The solute carrier families have a remarkably long evolutionary history with the majority of the human families present before divergence of Bilaterian species. *Mol Biol Evol* **28**, 1531-1541, doi:10.1093/molbev/msq350 (2011).

4 Almen, M. S., Nordstrom, K. J., Fredriksson, R. & Schioth, H. B. Mapping the human membrane proteome: a majority of the human membrane proteins can be classified according to function and evolutionary origin. *BMC Biol* **7**, 50, doi:10.1186/1741-7007-7-50 (2009).

5 Liu, Y., Engelman, D. M. & Gerstein, M. Genomic analysis of membrane protein families: abundance and conserved motifs. *Genome Biol* **3**, research0054, doi:10.1186/gb-2002-3-10-research0054 (2002).

6 Opella, S. J. & Marassi, F. M. Applications of NMR to membrane proteins. *Arch Biochem Biophys* **628**, 92-101, doi:10.1016/j.abb.2017.05.011 (2017).

7 Hellmich, U. A. & Glaubitz, C. NMR and EPR studies of membrane transporters. *Biol Chem* **390**, 815-834, doi:10.1515/BC.2009.084 (2009).

8 Exnowitz, F., Meyer, B. & Hackl, T. NMR for direct determination of K(m) and V(max) of enzyme reactions based on the Lambert W function-analysis of progress curves. *Biochim Biophys Acta* **1824**, 443-449, doi:10.1016/j.bbapap.2011.10.011 (2012).

9 Furukawa, A., Konuma, T., Yanaka, S. & Sugase, K. Quantitative analysis of protein-ligand interactions by NMR. *Prog Nucl Magn Reson Spectrosc* **96**, 47-57, doi:10.1016/j.pnmrs.2016.02.002 (2016).

10 Hass, M. A. S. & Mulder, F. A. A. Contemporary NMR Studies of Protein Electrostatics. *Annual Review of Biophysics* **44**, 53-75, doi:10.1146/annurev-biophys-083012-130351 (2015).

11 Mineev, K. S. & Nadezhdin, K. D. Membrane mimetics for solution NMR studies of membrane proteins. *Nanotechnology Reviews* **6**, 15-32, doi:10.1515/ntrev-2016-0074 (2017).

12 Puthenveetil, R., Nguyen, K. & Vinogradova, O. Nanodiscs and Solution NMR: preparation, application and challenges. *Nanotechnol Rev* **6**, 111-126, doi:10.1515/ntrev-2016-0076 (2017).

13 Puthenveetil, R. & Vinogradova, O. Solution NMR: A powerful tool for structural and functional studies of membrane proteins in reconstituted environments. *J Biol Chem* **294**, 15914-15931, doi:10.1074/jbc.REV119.009178 (2019).

14 Carlson, J. W., Jonas, A. & Sligar, S. G. Imaging and manipulation of high-density lipoproteins. *Biophysical Journal* **73**, 1184-1189, doi:10.1016/s0006-3495(97)78150-5 (1997).

15 Bayburt, T. H., Grinkova, Y. V. & Sligar, S. G. Self-Assembly of Discoidal Phospholipid Bilayer Nanoparticles with Membrane Scaffold Proteins. *Nano Letters* **2**, 853-856, doi:10.1021/nl025623k (2002).

16 Sligar, S. G. Finding a single-molecule solution for membrane proteins. *Biochem Biophys Res Commun* **312**, 115-119, doi:10.1016/j.bbrc.2003.09.188 (2003).

17 Bayburt, T. H. & Sligar, S. G. Self-assembly of single integral membrane proteins into soluble nanoscale phospholipid bilayers. *Protein Sci* **12**, 2476-2481, doi:10.1110/ps.03267503 (2003).

18 Yu, H. Extending the size limit of protein nuclear magnetic resonance. *Proc Natl Acad Sci U S A* **96**, 332-334, doi:10.1073/pnas.96.2.332 (1999).

19 Lacabanne, D., Meier, B. H. & Bockmann, A. Selective labeling and unlabeling strategies in protein solid-state NMR spectroscopy. *J Biomol NMR* **71**, 141-150, doi:10.1007/s10858-017-0156-z (2018).

20 Hefke, F. *et al.* Optimization of amino acid type-specific 13C and 15N labeling for the backbone assignment of membrane proteins by solution- and solid-state NMR with the UPLABEL algorithm. *J Biomol NMR* **49**, 75-84, doi:10.1007/s10858-010-9462-4 (2011).

21 Renault, M. *et al.* Cellular solid-state nuclear magnetic resonance spectroscopy. *Proc Natl Acad Sci U S A* **109**, 4863-4868, doi:10.1073/pnas.1116478109 (2012).

22 Marszalek, R., Pisklak, M., Horsztynski, D. & Wawer, I. 1H, 13C and 31P MAS NMR studies of lyophilized brain tumors. *Solid State Nucl Magn Reson* **37**, 21-27, doi:10.1016/j.ssnmr.2010.01.001 (2010).

23 Nikel, O. *et al.* Solid state NMR investigation of intact human bone quality: balancing issues and insight into the structure at the organic-mineral interface. *J Phys Chem C Nanomater Interfaces* **116**, 6320-6331, doi:10.1021/jp2125312 (2012).

24 Bryant, P. L., Lukiw, W. J., Gan, Z., Hall, R. W. & Butler, L. G. High-field 19.6T 27Al solid-state MAS NMR of in vitro aluminated brain tissue. *J Magn Reson* **170**, 257-262, doi:10.1016/j.jmr.2003.12.013 (2004).

25 Warnet, X. L., Arnold, A. A., Marcotte, I. & Warschawski, D. E. In-Cell Solid-State NMR: An Emerging Technique for the Study of Biological Membranes. *Biophys J* **109**, 2461-2466, doi:10.1016/j.bpj.2015.10.041 (2015).

26 Separovic, F., Keizer, D. W. & Sani, M. A. In-cell Solid-State NMR Studies of Antimicrobial Peptides. *Front Med Technol* **2**, 610203, doi:10.3389/fmedt.2020.610203 (2020).

27 Basting, D., Lehner, I., Lorch, M. & Glaubitz, C. Investigating transport proteins by solid state NMR. *Naunyn Schmiedebergs Arch Pharmacol* **372**, 451-464, doi:10.1007/s00210-006-0039-4 (2006).

28 Shcherbakov, A. A. *et al.* Structure and dynamics of the drug-bound bacterial transporter EmrE in lipid bilayers. *Nat Commun* **12**, 172, doi:10.1038/s41467-020-20468-7 (2021).

29 Shcherbakov, A. A., Spreacker, P. J., Dregni, A. J., Henzler-Wildman, K. A. & Hong, M. High-pH structure of EmrE reveals the mechanism of proton-coupled substrate transport. *Nat Commun* **13**, 991, doi:10.1038/s41467-022-28556-6 (2022).

30 Duan, P., Dregni, A. J. & Hong, M. Solid-State NMR (19)F-(1)H-(15)N Correlation Experiments for Resonance Assignment and Distance Measurements of Multifluorinated Proteins. *J Phys Chem A* **126**, 7021-7032, doi:10.1021/acs.jpca.2c05154 (2022).

31 Kaplan, M. *et al.* EGFR Dynamics Change during Activation in Native Membranes as Revealed by NMR. *Cell* **167**, 1241-1251 e1211, doi:10.1016/j.cell.2016.10.038 (2016).

32 Ader, C., Pongs, O., Becker, S. & Baldus, M. Protein dynamics detected in a membrane-embedded potassium channel using two-dimensional solid-state NMR spectroscopy. *Biochim Biophys Acta* **1798**, 286-290, doi:10.1016/j.bbamem.2009.06.023 (2010).

33 Sun, Z., Xu, Y., Zhang, D. & McDermott, A. E. Probing allosteric coupling in a constitutively open mutant of the ion channel KcsA using solid-state NMR. *Proc Natl Acad Sci U S A* **117**, 7171-7175, doi:10.1073/pnas.1908828117 (2020).

34 Jakdetchai, O. *et al.* Probing the photointermediates of light-driven sodium ion pump KR2 by DNP-enhanced solid-state NMR. *Sci Adv* **7**, doi:10.1126/sciadv.abf4213 (2021).

35 Kaur, J. *et al.* Solid-state NMR analysis of the sodium pump Krokinobacter rhodopsin 2 and its H30A mutant. *J Struct Biol* **206**, 55-65, doi:10.1016/j.jsb.2018.06.001 (2019).

36 Maciejko, J., Kaur, J., Becker-Baldus, J. & Glaubitz, C. Photocycle-dependent conformational changes in the proteorhodopsin cross-protomer Asp-His-Trp triad revealed by DNP-enhanced MAS-NMR. *Proc Natl Acad Sci U S A* **116**, 8342-8349, doi:10.1073/pnas.1817665116 (2019).

37 Maciejko, J. *et al.* Visualizing Specific Cross-Protomer Interactions in the Homo-Oligomeric Membrane Protein Proteorhodopsin by Dynamic-Nuclear-Polarization-Enhanced Solid-State NMR. *J Am Chem Soc* **137**, 9032-9043, doi:10.1021/jacs.5b03606 (2015).

38 Hellmich, U. A., Monkemeyer, L., Velamakanni, S., van Veen, H. W. & Glaubitz, C. Effects of nucleotide binding to LmrA: A combined MAS-NMR and solution NMR study. *Biochim Biophys Acta* **1848**, 3158-3165, doi:10.1016/j.bbamem.2015.10.003 (2015).

39 Siarheyeva, A. *et al.* Probing the molecular dynamics of the ABC multidrug transporter LmrA by deuterium solid-state nuclear magnetic resonance. *Biochemistry* **46**, 3075-3083, doi:10.1021/bi062109a (2007).

40 Lacabanne, D. *et al.* Flexible-to-rigid transition is central for substrate transport in the ABC transporter BmrA from Bacillus subtilis. *Commun Biol* **2**, 149, doi:10.1038/s42003-019-0390-x (2019).

41 Kunert, B. *et al.* Efficient and stable reconstitution of the ABC transporter BmrA for solid-state NMR studies. *Front Mol Biosci* **1**, 5, doi:10.3389/fmolb.2014.00005 (2014).

42 Lacabanne, D. *et al.* Solid-State NMR Reveals Asymmetric ATP Hydrolysis in the Multidrug ABC Transporter BmrA. *J Am Chem Soc* **144**, 12431-12442, doi:10.1021/jacs.2c04287 (2022).

43 Kaur, H. *et al.* Unexplored Nucleotide Binding Modes for the ABC Exporter MsbA. *J Am Chem Soc* **140**, 14112-14125, doi:10.1021/jacs.8b06739 (2018).

44 Kaur, H. *et al.* Coupled ATPase-adenylate kinase activity in ABC transporters. *Nat Commun* **7**, 13864, doi:10.1038/ncomms13864 (2016).

45 Spadaccini, R., Kaur, H., Becker-Baldus, J. & Glaubitz, C. The effect of drug binding on specific sites in transmembrane helices 4 and 6 of the ABC exporter MsbA studied by DNP-enhanced solid-state NMR. *Biochim Biophys Acta Biomembr* **1860**, 833-840, doi:10.1016/j.bbamem.2017.10.017 (2018).

46 Lange, V. *et al.* A MAS NMR study of the bacterial ABC transporter ArtMP. *Chembiochem* **11**, 547-555, doi:10.1002/cbic.200900472 (2010).

47 Schwalbe, H. Editorial: New 1.2 GHz NMR Spectrometers- New Horizons? *Angew Chem Int Ed Engl* **56**, 10252-10253, doi:10.1002/anie.201705936 (2017).

48 Sperling, L. J., Nieuwkoop, A. J., Lipton, A. S., Berthold, D. A. & Rienstra, C. M. High resolution NMR spectroscopy of nanocrystalline proteins at ultra-high magnetic field. *J Biomol NMR* **46**, 149-155, doi:10.1007/s10858-009-9389-9 (2010).

49 Samoson, A., Tuherm, T. & Gan, Z. High-field high-speed MAS resolution enhancement in 1H NMR spectroscopy of solids. *Solid State Nucl Magn Reson* **20**, 130-136, doi:10.1006/snmr.2001.0037 (2001).

50 Schneider-Muntau, H. J. High field NMR magnets. *Solid State Nuclear Magnetic Resonance* **9**, 61-71, doi:10.1016/s0926-2040(97)00044-1 (1997).

51 Nimerovsky, E. *et al.* Proton Detected Solid-State NMR of Membrane Proteins at 28 Tesla (1.2 GHz) and 100 kHz Magic-Angle Spinning. *Biomolecules* **11**, doi:10.3390/biom11050752 (2021).

52 Luchinat, E., Barbieri, L., Cremonini, M. & Banci, L. Protein in-cell NMR spectroscopy at 1.2 GHz. *J Biomol NMR* **75**, 97-107, doi:10.1007/s10858-021-00358-w (2021).

53 Quinn, C. M., Wang, M. & Polenova, T. NMR of Macromolecular Assemblies and Machines at 1 GHz and Beyond: New Transformative Opportunities for Molecular Structural Biology. *Methods Mol Biol* **1688**, 1-35, doi:10.1007/978-1-4939-7386-6_1 (2018).

54 Singh, C., Rai, R. K., Kayastha, A. M. & Sinha, N. Ultra fast magic angle spinning solid - state NMR spectroscopy of intact bone. *Magn Reson Chem* **54**, 132-135, doi:10.1002/mrc.4331 (2016).

55 Ye, Y. Q., Malon, M., Martineau, C., Taulelle, F. & Nishiyama, Y. Rapid measurement of multidimensional 1H solid-state NMR spectra at ultra-fast MAS frequencies. *J Magn Reson* **239**, 75-80, doi:10.1016/j.jmr.2013.12.010 (2014).

56 Paluch, P., Pawlak, T., Amoureux, J. P. & Potrzebowski, M. J. Simple and accurate determination of X-H distances under ultra-fast MAS NMR. *J Magn Reson* **233**, 56-63, doi:10.1016/j.jmr.2013.05.005 (2013).

57 Wang, S., Matsuda, I., Long, F. & Ishii, Y. Spectral editing at ultra-fast magic-angle-spinning in solid-state NMR: facilitating protein sequential signal assignment by HIGHLIGHT approach. *J Biomol NMR* **64**, 131-141, doi:10.1007/s10858-016-0014-4 (2016).

58 Li, S. *et al.* Observation of 1H-13C and 1H-1H proximities in a paramagnetic solid by NMR at high magnetic field under ultra-fast MAS. *J Magn Reson* **251**, 36-42, doi:10.1016/j.jmr.2014.11.013 (2015).

59 Struppe, J., Quinn, C. M., Sarkar, S., Gronenborn, A. M. & Polenova, T. Ultrafast (1)H MAS NMR Crystallography for Natural Abundance Pharmaceutical Compounds. *Mol Pharm* **17**, 674-682, doi:10.1021/acs.molpharmaceut.9b01157 (2020).

60 Ishii, Y. *et al.* Progress in proton-detected solid-state NMR (SSNMR): Super-fast 2D SSNMR collection for nano-mole-scale proteins. *J Magn Reson* **286**, 99-109, doi:10.1016/j.jmr.2017.11.011 (2018).

61 Wickramasinghe, A. *et al.* Evolution of CPMAS under fast magic-angle-spinning at 100 kHz and beyond. *Solid State Nucl Magn Reson* **72**, 9-16, doi:10.1016/j.ssnmr.2015.10.002 (2015).

62 Bougault, C., Ayala, I., Vollmer, W., Simorre, J. P. & Schanda, P. Studying intact bacterial peptidoglycan by proton-detected NMR spectroscopy at 100kHz MAS frequency. *J Struct Biol* **206**, 66-72, doi:10.1016/j.jsb.2018.07.009 (2019).

63 Hore, P. J. *Nuclear Magnetic Resonance* 2edn, (Oxford University Press, 2015).

64 Hore, P. J., Jones, J. A. & Wimperis, S. *NMR: The Toolkit*. 2 edn, (Oxford University Press, 2015).

65 Trinh, E. H., Wolff, A. M. & Naumiec, G. R. T1 Measurement by NMR Inversion Recovery: An Upper-Division Undergraduate Experiment in Advanced NMR Techniques Demonstrating the Concept of Contrast-Enhanced MRI. *Journal of Chemical Education* **98**, 587-591, doi:10.1021/acs.jchemed.0c00663 (2020).

66 Wang, H., Zhao, M., Ackerman, J. L. & Song, Y. Saturation-inversion-recovery: A method for T1 measurement. *J Magn Reson* **274**, 137-143, doi:10.1016/j.jmr.2016.11.015 (2017).

67 Levitt, M. H. & Freeman, R. NMR population inversion using a composite pulse. *Journal of Magnetic Resonance (1969)* **33**, 473-476, doi:10.1016/0022-2364(79)90265-8 (1979).

68 Apperley, D. C., Harris, R. K. & Hodgkinson, P. in *Solid-State NMR: Basic Principles and Practice* Ch. 2, 17-38 (Momentum Press, 2012).

69 Hennig, J. Echoes—how to generate, recognize, use or avoid them in MR-imaging sequences. Part I: Fundamental and not so fundamental properties of spin echoes. *Concepts in Magnetic Resonance* **3**, 125-143, doi:10.1002/cmr.1820030302 (1991).

70 Hahn, E. L. Spin Echoes. *Physical Review* **80**, 580-594, doi:10.1103/PhysRev.80.580 (1950).

71 Weingarth, M. & Baldus, M. CHAPTER 1. Introduction to Biological Solid-State NMR. 1-17, doi:10.1039/9781782627449-00001 (2014).

72 Apperley, D. C., Harris, R. K. & Hodgkinson, P. in *Solid-State NMR: Basic Principles and Practice* Ch. 4, 17-38 (Momentum Press, 2012).

73 Apperley, D. C., Harris, R. K. & Hodgkinson, P. *Solid State NMR Basic Principles and Practice*. (Momentum Press, 2012).

74 Duer, M. J. *Solid-State NMR Spectroscopy: Principles and Applications*. (Blackwell Science Ltd, 2002).

75 Pines, A., Gibby, M. G. & Waugh, J. S. Proton-Enhanced Nuclear Induction Spectroscopy. A Method for High Resolution NMR of Dilute Spins in Solids. *The Journal of Chemical Physics* **56**, 1776-1777, doi:10.1063/1.1677439 (1972).

76 Hartmann, S. R. & Hahn, E. L. Nuclear Double Resonance in the Rotating Frame. *Physical Review* **128**, 2042-2053, doi:10.1103/PhysRev.128.2042 (1962).

77 Kolodziejski, W. & Klinowski, J. Kinetics of cross-polarization in solid-state NMR: a guide for chemists. *Chem Rev* **102**, 613-628, doi:10.1021/cr000060n (2002).

78 Gorter, C. J. Negative result of an attempt to detect nuclear magnetic spins. *Physica* **3**, 995-998, doi:10.1016/s0031-8914(36)80324-3 (1936).

79 Gorter, C. J. & Broer, L. J. F. Negative result of an attempt to observe nuclear magnetic resonance in solids. *Physica* **9**, 591-596, doi:10.1016/s0031-8914(42)80073-7 (1942).

80 Purcell, E. M., Torrey, H. C. & Pound, R. V. Resonance Absorption by Nuclear Magnetic Moments in a Solid. *Physical Review* **69**, 37-38, doi:10.1103/PhysRev.69.37 (1946).

81 Bloch, F., Hansen, W. W. & Packard, M. Nuclear Induction. *Physical Review* **69**, 127-127, doi:10.1103/PhysRev.69.127 (1946).

82 Andrew, E. R. The narrowing of NMR spectra of solids by high-speed specimen rotation and the resolution of chemical shift and spin multiplet structures for solids. *Progress in Nuclear Magnetic Resonance Spectroscopy* **8**, 1-39, doi:10.1016/0079-6565(71)80001-8 (1971).

83 Andrew, E. R., Bradbury, A. & Eades, R. G. Removal of Dipolar Broadening of Nuclear Magnetic Resonance Spectra of Solids by Specimen Rotation. *Nature* **183**, 1802-1803, doi:10.1038/1831802a0 (1959).

84 Andrew, E. R., Bradbury, A. & Eades, R. G. Nuclear Magnetic Resonance Spectra from a Crystal rotated at High Speed. *Nature* **182**, 1659-1659, doi:10.1038/1821659a0 (1958).

85 Andrew, E. R. & Szczesniak, E. A historical account of NMR in the solid state. *Progress in Nuclear Magnetic Resonance Spectroscopy* **28**, 11-36, doi:10.1016/0079-6565(95)01018-1 (1995).

86 Lowe, I. J. Free Induction Decays of Rotating Solids. *Physical Review Letters* **2**, 285-287, doi:10.1103/PhysRevLett.2.285 (1959).

87 Duer, M. J. in *Solid-State NMR Spectroscopy: Principles and Applications* Ch. 2, (Blackwell Science Ltd, 2002).

88 Polenova, T., Gupta, R. & Goldbourt, A. Magic angle spinning NMR spectroscopy: a versatile technique for structural and dynamic analysis of solid-phase systems. *Anal Chem* **87**, 5458-5469, doi:10.1021/ac504288u (2015).

89 Reif, B., Ashbrook, S. E., Emsley, L. & Hong, M. Solid-state NMR spectroscopy. *Nat Rev Methods Primers* **1**, doi:10.1038/s43586-020-00002-1 (2021).

90 Sun, H. *et al.* Enabling materials informatics for 29Si solid-state NMR of crystalline materials. *npj Computational Materials* **6**, doi:10.1038/s41524-020-0328-3 (2020).

91 Apperley, D. C., Harris, R. K. & Hodgkinson, P. in *Solid-State NMR: Basic Principles and Practice* Ch. 5, 17-38 (Momentum Press, 2012).

92 Muhtadi, F. J. & Afify, A. F. A. A. Vinblastine Sulfate (Supplement). **21**, 611-658, doi:10.1016/s0099-5428(08)60403-7 (1992).

93 Dutagaci, B., Becker-Baldus, J., Faraldo-Gomez, J. D. & Glaubitz, C. Ceramide-lipid interactions studied by MD simulations and solid-state NMR. *Biochim Biophys Acta* **1838**, 2511-2519, doi:10.1016/j.bbamem.2014.05.024 (2014).

94 Rasia, R. M., Brutscher, B. & Plevin, M. J. Selective isotopic unlabeling of proteins using metabolic precursors: application to NMR assignment of intrinsically disordered proteins. *Chembiochem* **13**, 732-739, doi:10.1002/cbic.201100678 (2012).

95 Higman, V. A. *et al.* Assigning large proteins in the solid state: a MAS NMR resonance assignment strategy using selectively and extensively 13C-labelled proteins. *J Biomol NMR* **44**, 245-260, doi:10.1007/s10858-009-9338-7 (2009).

96 Sattler, M. & Fesik, S. W. Use of deuterium labeling in NMR: overcoming a sizeable problem. *Structure* **4**, 1245-1249, doi:10.1016/s0969-2126(96)00133-5 (1996).

97 Gimenez, D., Phelan, A., Murphy, C. D. & Cobb, S. L. (19)F NMR as a tool in chemical biology. *Beilstein J Org Chem* **17**, 293-318, doi:10.3762/bjoc.17.28 (2021).

98 Arntson, K. E. & Pomerantz, W. C. Protein-Observed Fluorine NMR: A Bioorthogonal Approach for Small Molecule Discovery. *J Med Chem* **59**, 5158-5171, doi:10.1021/acs.jmedchem.5b01447 (2016).

99 Nussbaumer, F., Plangger, R., Roeck, M. & Kreutz, C. Aromatic (19) F-(13) C TROSY-[(19) F, (13) C]-Pyrimidine Labeling for NMR Spectroscopy of RNA. *Angew Chem Int Ed Engl* **59**, 17062-17069, doi:10.1002/anie.202006577 (2020).

100 Bourriquen, F., Rockstroh, N., Bartling, S., Junge, K. & Beller, M. Manganese-Catalysed Deuterium Labelling of Anilines and Electron-Rich (Hetero)Arenes. *Angew Chem Int Ed Engl* **61**, e202202423, doi:10.1002/anie.202202423 (2022).

101 Fernandez, I., Gonzalez, J. & Lopez-Ortiz, F. Deuterium-labeling and NMR study of the dearomatization of N-alkyl-N-benzyldiphenylphosphinamides through anionic cyclization: ortho and benzylic lithiation directed by complex-induced proximity effects. *J Am Chem Soc* **126**, 12551-12564, doi:10.1021/ja039863t (2004).

102 Lieblein, A. L., Furtig, B. & Schwalbe, H. Optimizing the kinetics and thermodynamics of DNA i-motif folding. *Chembiochem* **14**, 1226-1230, doi:10.1002/cbic.201300284 (2013).

103 Furtig, B. *et al.* Refolding through a Linear Transition State Enables Fast Temperature Adaptation of a Translational Riboswitch. *Biochemistry* **59**, 1081-1086, doi:10.1021/acs.biochem.9b01044 (2020).

104 Furtig, B. *et al.* Time-resolved NMR studies of RNA folding. *Biopolymers* **86**, 360-383, doi:10.1002/bip.20761 (2007).

105 Helmling, C. *et al.* Life times of metastable states guide regulatory signaling in transcriptional riboswitches. *Nat Commun* **9**, 944, doi:10.1038/s41467-018-03375-w (2018).

106 Gebel, J. *et al.* p63 uses a switch-like mechanism to set the threshold for induction of apoptosis. *Nat Chem Biol* **16**, 1078-1086, doi:10.1038/s41589-020-0600-3 (2020).

107 Mok, K. H. *et al.* Rapid sample-mixing technique for transient NMR and photo-CIDNP spectroscopy: applications to real-time protein folding. *J Am Chem Soc* **125**, 12484-12492, doi:10.1021/ja036357v (2003).

Chapter 3

The preparation of the bacterial membrane protein MsbA

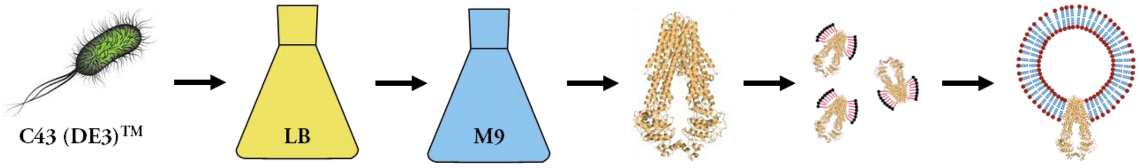

> “I cannot judge my work while I am doing it, I have to do as painters do,
> stand back and view it from a distance, but not too great a distance.”
>
> – *Blaise Pascal*

3.1 Membrane protein sample preparation

The native state of a protein is determined by the interatomic interactions and the amino acid sequence in a certain environment, as described by the thermodynamic hypothesis, which was reinforced by Anfinsen (1973) [1]. It is challenging to obtain a membrane-mimetic environment that supports the native structures, dynamics, and functions of a membrane protein. As a result, functional assays of membrane proteins may not be feasible in the chosen environment[2], which can also be described by the hydrophobic mismatching hypothesis, revised by Jensen et al. (2004) [3]. Moreover, membrane proteins represent a major challenge in protein biochemistry, as a result of the problems encountered when working outside the natural lipid environment[4].

In the past large molecules such as membrane proteins have made NMR measurements challenging because of overlapping individual spectra signals in solution NMR (figure 3.1). Furthermore, such large complexes are not suitable for solution NMR. To overcome these complications with membrane proteins in NMR, the use of selective labelling schemes, and 3D, or 4D NMR spectroscopy have been beneficial. Yet, solid-state NMR studies have shown that solid-state NMR is an extremely suitable method to study structural biology (**Chapter 2**) [5-9]. Specifically, membrane proteins are allowed to retain a more native environment, due to the mimicking of their native membranes with lipids compared to solution NMR.

Furthermore, using MAS at an angle of 54.7^0 allows equalization of anisotropic interactions, thereby allowing fast MAS to detect isotropic lines at high resolution, which results in an improved NMR spectra resolution of crystalline proteins[10]. Moreover, to overcome low sensitivity, the application of dipole-coupled electron spin pairs hyperpolarization of nearby protons, or cross-effect DNP under microwave irradiation, can enhance NMR sensitivity by orders of magnitude[7].

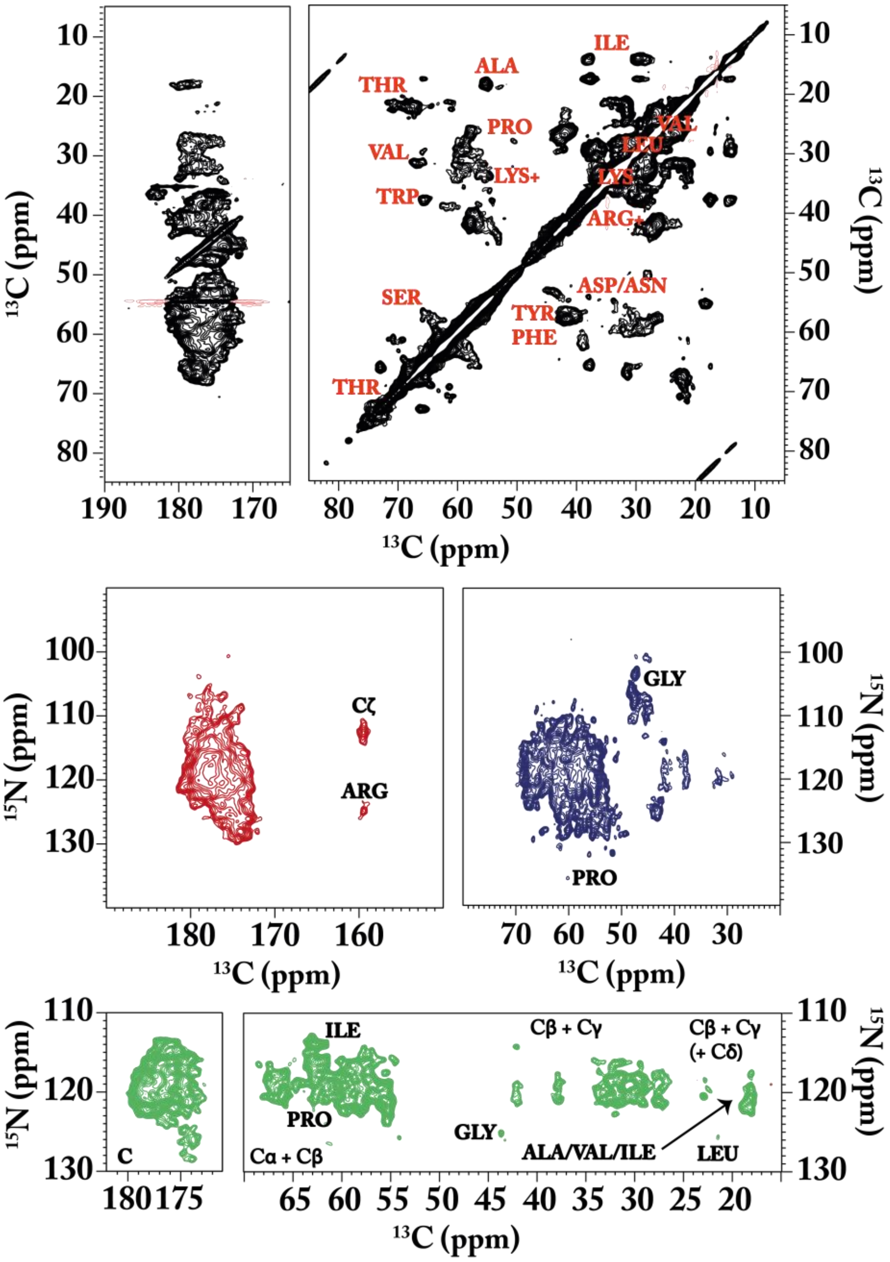

Figure 3.1. Fully labelled $^{13}C^{15}N$ wild-type MsbA. In black (top) is shown de PDSD of fully labelled $^{13}C^{15}N$ wild-type MsbA. Most amino acids can be found despite large overlaps of peaks. In red (middle) the NCO of fully labelled MsbA peaks are not separatable from each other, similarly for the NCA spectrum in blue (middle). In the NCACX (green, bottom) different regions along the ^{13}C chemical shift range can be found. However, the peaks are overlapping and are indistinguishable from one another.

3.2 Workflow

Expression

To carry out NMR experiments, MsbA is yielded in a high quantity. Therefore, MsbA was cloned with the pET19b expression vector and overexpressed in *E. coli* C43(DE3) cells (figure 3.2). The collective process from expression to sample reconstitution of MsbA is based on previous studies[8,9,11,12]. Additionally, the membrane protein contains a 10x His-tag at the N-terminal which is connected by an 11 amino acid peptide linker (Appendix). The plasmid is transformed on a Luria Broth (LB, 25 g/L) agar plate (270 µM ampicillin). Upon transformation, one colony is placed into 50 mL LB media (270 µM ampicillin) for an overnight preculture (17 hours, 220 rpm, 37 ^{0}C).

	HHHHHHHHHHSSGHIDDDDKH	
1	MHNDKDLSTWQTFRRLWPTIAPFKAGLIVAGVALILNAASDTFMLSLLKP	50
51	LLDDGFGKTDRSVLVWMPLVVIGLMILRGITSYVSSYCISWVSGKVVMTM	100
101	RRRLFGHMMGMPVSFFDKQSTGTLLSRITYDSEQVASSSSGALITVVREG	150
151	ASIIGLFIMMFYYSWQLSIILIVLAPIVSIAIRVVSKRFRNISKNMQNTM	200
201	GQVTTSAEQMLKGHKEVLIFGGQEVETKRFDKVSNRMRLQGMKMVSASSI	250
251	SDPIIQLIASLALAFVLYAASFPSVMDSLTAGTITVVFSSMIALMRPLKS	300
301	LTNVNAQFQRGMAACQTLFTILDSEQEKDEGKRVIERATGDVEFRNVTFT	350
351	YPGRDVPALRNINLKIPAGKTVALVGRSGSGKSTIASLITRFYDIDEGEI	400
401	LMDGHDLREYTLASLRNQVALVSQNVHLFNDTVANNIAYARTEQYSREQI	450
451	EEAARMAYAMDFINKMDNGLDTVIGENGVLLSGGQRQRIAIARALLRDSP	500
501	ILILDEATSALDTESERAIQAALDELQKNRTSLVIAHRLSTIEKADEIVV	550
551	VEDGVIVERGTHNDLLEHRGVYAQLHKMQFGQ	582

Figure 3.2. MsbA construct used in this dissertation.

Henceforth, 10 mL of the overnight culture is washed and further inoculated in 1L of LB medium (220 rpm, 37 ^{0}C). When the optical density at 600 nm (OD$_{600}$) reached 0.5-0.6, the cells were collected (6000 rpm, 10 minutes), washed and transferred to the minimal microbial growth medium (M9 medium) or M9+ media with additional supplements (600 mL). To reach a maximum oxygen level in the medium flasks, incubator rotation is increased to 260 rpm, allowing the cells to grow over an extended period. The cells are allowed to adapt to the new media and grow for 1 hour at 37 ^{0}C.

The minimal medium allows slow growth of the cells. Upon isopropyl β- d-1-thiogalactopyranoside (IPTG) induction (1 mM) the cells will express significantly more MsbA, giving a final amount of 10-15 mg MsbA/L M9 media. The M9 medium contains K_2HPO_4 (60.3 mM), KH_2PO_4 (33.1 mM), NaCl (8.6 mM), NH_4Cl (18.7 mM), $MgSO_4$ (2.0 mM), $FeCl_3$ (20 μM), glucose (11.1 mM), ampicillin (270 μM), and 10 mL of filter sterilized solution. The filter-sterilized solution contains $CaCl_2{\cdot}2H_2O$ (1.4 mM), $ZnSO_4{\cdot}7H_2O$ (0.7 mM), $MnSO_4{\cdot}H_2O$ (1.2 mM), thiamine (18.8 mM), niacin (40.6 mM), and biotin (0.4 mM) (**table 3.1-3.3**).

Table 3.1. M9 medium composition, pH 7.5

Buffer components	Concentration
K_2HPO_4	10.5 g/L
KH_2PO_4	4.5 g/L
NaCl	0.5 g/L
NH_4Cl	1 g/L
$MgSO_4$	2 mM
$FeCl_3$	10 μM
Vitamin solution	10 mL/L
Glucose	2 g/L
Ampicillin	100 mg/L
IPTG	1 mM

The M9+ medium with supplement allows the cells to grow longer and/or divide more, and eventually to express more MsbA, up to two- to three-fold (from 15-20 mg/L to 30-50 mg/L). The added supplements can be subdivided into two subgroups concerning the preparation. The autoclave-stable amino acids are alanine (5.6 mM), arginine (2.3 mM), glycine (7.3 mM), isoleucine (1.8 mM), leucine (1.8 mM), lysine (2.3 mM), methionine (1.7 mM), serine (1.9 mM), threonine (1.9 mM), and valine (2.0 mM). The remaining supplements are aspartic acid (3.0 mM), cysteine (412.7 μM), glutamine (2.9 mM), glutamic acid (4.4 mM), proline (868.8 μM), tryptophan (244.8 μM), histidine (644.5 μM), phenylalanine (787.0 μM), and tyrosine (938.2 μM) (**table 3.2**).

Table 3.2. M9$^+$ supplements

Buffer components	Concentration	Notes
Alanine	500 mg/L	Autoclavable
Arginine	400 mg/L	
Glycine	550 mg/L	
Isoleucine	230 mg/L	
Leucine	230 mg/L	
Lysine HCl	420 mg/L	
Methionine	250 mg/L	
Serine	2010 mg/L	
Threonine	230 mg/L	
Valine	230 mg/L	
Aspartic acid	400 mg/L	Non-autoclavable
Cysteine	50 mg/L	
Glutamine	417 mg/L	
Glutamic acid	650 mg/L	
Proline	100 mg/L	
Tryptophan	50 mg/L	
Histidine	100 mg/L	
Phenylalanine	103 mg/L	
Tyrosine	170 mg/L	

In the case of various specific labelled MsbA samples, M9+ medium can be used. The amino acids can be substituted in the same amount by isotope-labelled amino acids. For fully labelled MsbA preparations, only minimal M9 medium is used, where NH_4Cl and glucose are replaced for isotope labelled $^{15}NH_4Cl$ and ^{13}C-glucose. After the cells are induced with IPTG the cells are allowed to grow slowly overnight at 20 ^{0}C (17 hours, 260 rpm). For minimal M9 medium, a usual OD_{600} is reached between 2.2-2.3, while for the M9+ medium, an OD_{600} of 2.7-2.8 is reached. At this point, the cells can be collected for -80 ^{0}C storage or continuation of experiments (6000 rpm, 15 minutes).

Table 3.3. Vitamin solution

Components	Concentration
$CaCl_2.2H_2O$	200 mg/L
$ZnSO_4.7H_2O$	200 mg/L
$MnSO_4.H2O$	200 mg/L
Thiamine	5 g/L
Niacin	5 g/L
Biotin	100 mg/L

Solubilisation

Membrane protein solubilisation is carried out by extracting the membrane of the cells. Upon extraction, the membranes can be substituted for the solubilisation process. The cells are lysed with 5 mL lysis buffer/1 g wet cell by vortexing until the suspension becomes homogenous. The lysis buffer consists of tris (10 mM), sucrose (250 mM), NaCl (150 mM), $MgSO_4$ (2.5 mM), 1,4-dithiothreitol (DTT, 16 mM), and 2 tablets of cOmplete™, Mini, EDTA-free Protease Inhibitor Cocktail (Roche) per 100 mL lysis buffer (**appendix table 3.4**). The cells are ruptured by running the suspension through a French press at 1.7-1.8 kbar (180 MPa) 3 times (4 ^{0}C).

Table 3.4. Cell lysis buffer composition, pH 7.5

Components	Concentration
Tris	10 mM
Sucrose	250 mM
NaCl	150 mM
$MgSO_4$	2.5 mM
DTT	16 mM
cOmplete™ Protease Inhibitor Cocktail	20 tablets/L

Cell debris is removed by centrifugation at 8000 rpm for 15 minutes at 4 ^{0}C. Subsequently, the supernatant is ultra-centrifugated at 43.000 rpm for 1.5 hours (4 ^{0}C). The membranes can be collected for -80 ^{0}C storage or used for solubilisation and purification. Membranes are solubilised overnight (17 hours, 4 ^{0}C) in resuspension buffer (25 mL/g membranes) containing HEPES (50 mM), NaCl (300 mM), $MgMCl_2$ (5 mM), 10% glycerol (v/v or 136.8 mM), DTT (0.5 mM), imidazole (10 mM), and 1.25 % n-dodecyl-B-D-maltoside (DDM, w/v or 24.5 mM) (**table 3.5**).

Table 3.5. Resuspension buffer composition, pH 7.5

Components	Concentration
HEPES	50 mM
NaCl	300 mM
$MgCl_2$	5 mM
Glycerol (ρ=1.261 g/cm^3)	136.8 mM
DTT	0.5 mM
Imidazole	10 mM
DDM	24.5 mM

Purification

The purification of 10x His-tag MsbA is carried out with a nickel (Ni^{2+}) nitrilotriacetic acid (NTA) column. Prior to the purification the column is washed and treated with at least two column volumes of water and washing buffer, respectively. The washing buffer contains HEPES (50 mM), NaCl (300 mM), $MgMCl_2$ (5 mM), 10% glycerol (v/v or 136.8 mM), imidazole (50 mM), and 0.015% DDM (w/v or 0.3 mM). The solubilized protein fraction is collected with the ultracentrifuge (55.000 rpm, 1 hour) and the supernatant is transferred to the Ni-NTA beads (binding capacity <50 mg/mL beads) (**table 3.6**).

Table 3.6. Washing buffer composition, pH 7.5

Components	Concentration washing buffer	Concentration elution buffer
HEPES	50 mM	50 mM
NaCl	300 mM	300 mM
$MgCl_2$	5 mM	5 mM
Glycerol (ρ=1.261 g/cm^3)	136.8 mM	136.8 mM
Imidazole	50 mM	400 mM
DDM	0.3 mM	0.3 mM

After 1.0-1.5 hours of incubation at 4 ^{0}C, the column is washed (flow rate = 2 mL/minute) until an OD_{280} value of <0.05 is reached. Protein is eluted with elution buffer containing HEPES (50 mM), NaCl (300 mM), $MgMCl_2$ (5 mM), 10% glycerol (v/v or 136.8 mM), imidazole (400 mM), and 0.015 % DDM (w/v or 0.3 mM) and is monitored via the OD_{280} value (<0.05). Upon elution, the protein can be additionally purified in size-exclusion chromatography. The final protein concentration is determined with NanoDrop™. Lastly, the protein can be analysed by SDS PAGE (**table 3.7**), Blue Native PAGE (table 3.8 and figure 3.3), and Western Blot (table 3.9 and figure 3.4).

Table 3.7. SDS PAGE buffers compositions.

Components	Concentration	Buffer
Tris	1 M	Cathode buffer (10x)pH 8.3, room temperature
Tricine	1 M	
SDS	35 mM	
Tris	2.1 M	Anode buffer 10(x)pH 8.9, room temperature
Methanol	40% (v/v)	Coomassie brilliant blue R-250 staining solution
Acetic acid	10% (v/v)	
MilliQ H_2O	40% (v/v)	
Coomassie brilliant blue R-250	0.025 %(w/v)	
Methanol	50% (v/v)	Coomassie brilliant blue R-250 destaining solution
Acetic acid	10% (v/v)	
MilliQ H_2O	40% (v/v)	

Table 3.8. Blue Native PAGE buffers compositions.

Components	Concentration	Buffer
BisTris	1 M	Blue Native PAGE running buffer (20x)
Tricine	1 M	
Coomassie G250	0.4%	Cathode buffer (20x)
BisTris	200 mM	Native sample buffer, pH 7.2 (4x)
6 N HCl		
NaCl	200 mM	
Glycerol	40%	
Ponceau S	0.004%	

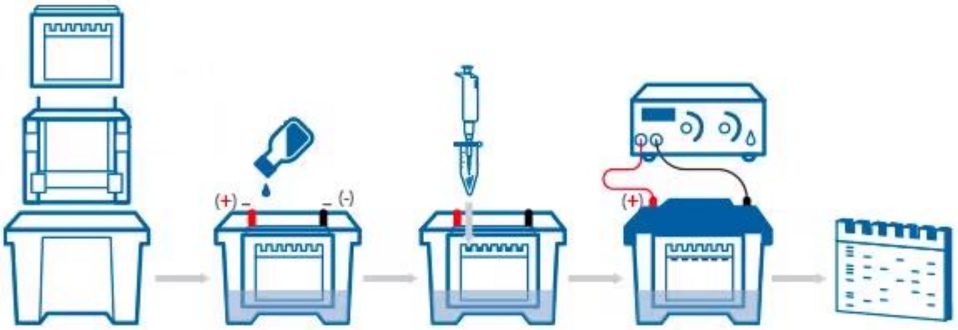

1. Treat the gel with fixing solution (40% EtOH, 10% acetic acid) in the microwave (high) for 45 seconds. Then incubate for 15 minutes.
2. Distain the gel (8% acetic acid) in the microwave (high) for 45 seconds. Incubate until the desired background is obtained.

Cathode buffer 1x	
BN PAGE running buffer 20x	10 mL
BN PAGE cathode buffer additive 20x	10mL
Deionized H20	180 mL
Total volume	200 mL

Anode buffer 1x	
BN PAGE running buffer 20x	30 mL
Deionized H20	570 mL
Total volume	600 mL

Sample	
4x sample buffer	5 µL
Sample (1 mg/mL)	10 µL
Deionized H20	4 µL
G250% additive	1 µL
Total volume	20 µL

Figure 3.3. Blue Native PAGE protocol.

Table 3.9. Western Blot buffers compositions.

Components	Concentration	Buffer
Tris	25 mM	Transfer buffer, pH 8.3 (10x)
Glycin	150 mM	
MeOH	10%	
Tris/HCl (pH 8)	10 mM	TBST (10x)
NaCl	150 mM	
Tween 20	0.05%	
Tris/HCl (pH 9.5)	100 mM	AP buffer
NaCl	100 mM	
MgCl2	5 mM	

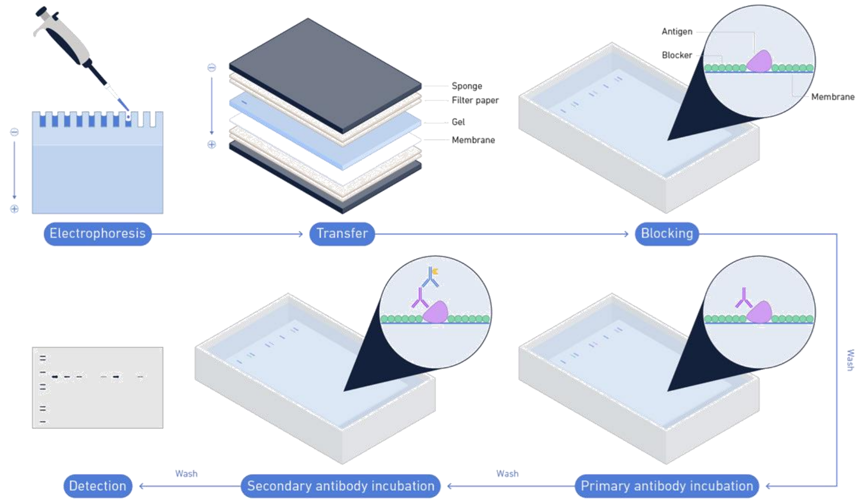

1. Block → TBST + 2% BSA → 1 hr (or overnight @4C)
2. Wash → 3x TBST → 5 minutes
3. Incubation → 1:2000 antibody + TBST + 0.5% BSA → 1 hr @RT
4. Wash → 3x TBST → 5 minutes
5. Wash → 3x AP-buffer → 5 minutes
6. Dye → 50 µL BCIP /10 mL AP-buffer (BCIP 50 mg/mL in DMF -20 degrees Celsius), 100 µL NBT /10 mL AP-buffer (NBT 50 mg/mL in 70% DMF -20 degrees Celsius)

Figure 3.4. Western Blot Protocol.

Reconstitution

After purification, the protein is reincorporated in a more native environment via a reconstitution process. For the reconstitution of MsbA, a mixture of 1,2-dimyristoyl-sn-glycero-3-phosphocholine (DMPC) and 1,2-dimyristoyl-sn-glycero-3-phosphate (DMPA) is used, with a 9 to 1 ratio, respectively. The lipids are dissolved in a 1:2 methanol/chloroform mixture, evaporated under a nitrogen air stream, and dried fully with an evaporator overnight. The fully dried lipids are then resuspended in lipid buffer (50 mM HEPES, 50 mM NaCl) to give a final liposome concentration of 4 mg/mL (**table 3.10**).

Table 3.10. Lipid buffer composition, pH 7.2, filtered.

Components	Concentration
HEPES	50 mM
NaCl	50 mM

The mixture is warmed up to 35 ^{0}C to form liposomes and to give a lipid suspension. The lipid suspension with small unilamellar vesicles (SUVs) is substituted to three freeze-thaw cycles in liquid nitrogen and then at 37 ^{0}C to form large multilamellar vesicles (LMVs). Upon this, the lipid suspension is then extruded (5-7 bar/0.5-0.7 MPa) 11-13 times through 400 nm, 200 nm and eventually 100 nm membranes to form large unilamellar vesicles (LUVs) for homogeneous reconstitution[13].

To probe the amount of detergent needed for the reconstitution of MsbA, a turbidity test at an optical density of 540 nm was performed[14]. DDM is titrated to the liposomes. Up to the determined R_{SAT} concentration of 5 mM DDM MsbA has been observed to aggregate easily during the reconstitution process. In this stage, the liposome vesicles are fully saturated with DDM. From this point on, the vesicles destabilise and slowly break open. After R_{SAT}, no aggregations have been observed during reconstitution. Therefore, a minimum amount of 7 mM DDM is used for the reconstitution of MsbA.

Initially, 9 mM DDM is added to the required amount of liposomes for a protein/lipid ratio of 75 moles/moles (based on previous studies[8]) and is mixed for 15 minutes at room temperature. Freshly eluted MsbA (< 1 mg/mL) is added dropwise to the liposomes. Finally, detergent is removed using Bio-Beads™ SM-2 Resins (80 wet beads mg/mL protein/lipid/detergent mixture). The protein/lipid/detergent mixture is immediately incubated for overnight end-over-end rotation. The remaining detergent is removed by adding new beads every 2 hours at room temperature until there is no remaining DDM. The reconstituted MsbA can be washed and collected by centrifugation (28.000 rpm). Prior to this, a sucrose gradient and an SDS-PAGE can be used to determine the homogeneity of the reconstitution. The ATPase activity was comparable to previously reconstituted MsbA in liposomes.

Reconstitution of MsbA in 1-palmitoyl-2-oleoyl-sn-glycero-3-phosphoethanolamine (POPE) and 1-Palmitoyl-2-Oleoyl-sn-Glycero-3-Phosphoglycerol (POPG) was done similarly as for MsbA in DMPC/DMPA. POPE/POPG (4:1) was dissolved in $CHCl_3$ and dried under nitrogen gas flow. Subsequently, liposomes were prepared in buffer (50 mM HEPES and 50 mM NaCl, pH 7.5) and extruded >10 times through membranes (100 nm) to form uniform vesicles. Upon detergent destabilisation (4 mM Triton X-100), MsbA was reconstituted in the liposomes with a final LPR ratio of 75:1 mol/mol. The protein/liposome mixture was allowed to equilibrate for 30 minutes at room temperature before the removal of detergent (80 mgL^{-1} biobeads, overnight, 4 °C). Reconstituted MsbA was washed and collected by ultracentrifugation (28,000 r.p.m., rotor Ti70, 20 minutes).

3.3 Biochemical assays

The detection of phosphate dates back to 1920, a phosphomolybdic acid-based method of Bell and Doisy, later succeeded by Briggs in 1922, and 1925 by Fiske and Subbarow[15]. The latter also discovered adenosine triphosphate, independently alongside Lohmann and Jendrassik. Many modifications have been made to determine inorganic phosphate using molybdate. Eventually, in 1988 Chifflet et al published a modernized version of the classical molybdate method to determine inorganic phosphate.[16] By 1997 Walker, Boyer, and Skou received the Nobel Prize in Chemistry *"for their elucidation of the enzymatic mechanism underlying the synthesis of adenosine triphosphate (ATP)"* and *"for the first discovery of an ion-transporting enzyme, Na+, K+ - ATPase"*[17].

In this dissertation, the colourimetric assay is based on the Chifflet et al molybdate assay to determine the catalytic activity of MsbA (**table 3.11, appendix tables A1-3**)[8]. MsbA is in an assay buffer (*50 mm HEPES, 50 mm NaCl, 10 mm $MgCl_2$, 0.015% DDM*) (**table 3.12**) [8,18]. The release of inorganic phosphate was followed by titration of ATP up to 5 mM at OD_{850}. The reaction is stopped after 20 minutes by using 12% w/v sodium dodecyl sulphate (SDS) and coloured in two consecutive steps. Firstly, incubation with a 1:1 mixture of 12% w/v ascorbic acid and 2% w/v ammonium molybdate in 1M HCl. Finally, after 5 minutes use a mixture of 2% w/v sodium citrate, 2% w/v sodium meta-arsenite, and 2% v/v acetic acid with an incubation time of 20 minutes. The activity is measured at OD_{850} and determined with a phosphate standard curve (**table 3.13**).

Table 3.11. Colourimetric assay solutions

Solutions	Components	Concentration	Storage
A	SDS	12% w/v	RT
B	ascorbic acid	12% w/v (1M HCl)	4 ^{0}C
C	ammonium molybdate	2% w/v (1M HCl)	4 ^{0}C
D	B+C	1:1	4 ^{0}C
E	sodium citrate sodium meta-arsenite acetic acid	2% w/v 2% w/v 2% v/v	RT

Table 3.12. ATPase buffer components, pH 7.5

Components	Concentration
HEPES	50 mM
NaCl	50 mM
$MgCl_2$	10 mM

Table 3.13. Phosphate standard curve.

KH2PO4	KH2PO4 (500 μM)	Buffer	A	B+C=D	E
0 μM	0 μL	30 μL	30 μL	60 μL	90 μL
25 μM	1.5 μL	28.5 μL	30 μL	60 μL	90 μL
50 μM	3 μL	27 μL	30 μL	60 μL	90 μL
100 μM	6 μL	24 μL	30 μL	60 μL	90 μL
200 μM	12 μL	18 μL	30 μL	60 μL	90 μL
300 μM	18 μL	12 μL	30 μL	60 μL	90 μL
400 μM	24 μL	6 μL	30 μL	60 μL	90 μL
500 μM	30 μL	0 μL	30 μL	60 μL	90 μL

3.4 Solid-state NMR methods

Expression of unique pairs in CH1 and CH2, and MsbA lysine fingerprint

For coupling, helix 1 [^{13}C,^{15}N-F]-MsbA 103 mgL^{-1} ^{13}C,^{15}N-phenylalaline and 800 mgL^{-1} 4-hydroxy phenyl pyruvic acid (Sigma Aldrich) were supplemented to 1 gL^{-1} ^{14}NH$_4$Cl and 2 gL^{-1} ^{12}C-glucose M9^{+} media. In the case of coupling helix 2 [^{13}C-H,^{15}N-K]-MsbA 100 mgL^{-1} ^{13}C-histidine or ^{13}C,^{15}N-histidine and 420 mgL^{-1} ^{15}N-Lysine added to the M9^{+} media. Lastly, the [^{13}C,^{15}N-K]-MsbA was expressed using 420 mgL^{-1} ^{13}C,^{15}N-Lysine (**figure 3.5**). To enrich the M9^{+} media for overexpression, natural abundance 500 mgL^{-1} alanine, 400 mgL^{-1} arginine, 550 mgL^{-1} glycine, 230 mgL^{-1} isoleucine, 230 mgL^{-1} leucine, 250 mgL^{-1} methionine, 2010 mgL^{-1} serine, 230 mgL^{-1} threonine, 230 mgL^{-1} valine, 400 mgL^{-1} aspartic acid, 50 mgL^{-1} cystine, 417 mgL^{-1} glutamine, 650 mgL^{-1} glutamic acid, 100 mgL^{-1} proline, 50mgL^{-1} tryptophan, 100 mgL^{-1}, and 170 mgL^{-1} tyrosine were supplemented.

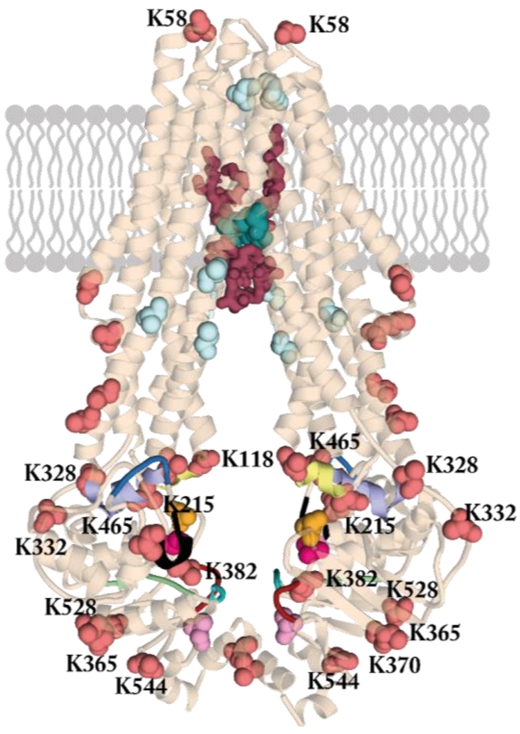

Figure 3.5: Location Lys residues assigned in NCA spectra of [^{13}C,^{15}N-K]-MsbA in[19]. The residues are highlighted salmon spheres in the structural cartoon based on the MsbA structure PDB 5TV4 [20]. Coupling helices 1 and 2 are highlighted in yellow (CH1) and purple (CH2). The X-loop, A-loop, Q-loop, and D-loop are indicated in blue, orange, magenta and cyan, respectively. The Walker A and B are represented by red and light green. Black and light pink are assigned to the signature loop and His switch. LPS is shown as raspberry spheres.

ADP vanadate, Hoechst 33342, and G907 trapping

Trapping of Hoechst 33342, ADP vanadate, and Hoechst 33342 + ADP vanadate in MsbA was achieved as previously described[9,12]. A protein mixture containing 50 mM HEPES, 10 mM ATP, 10 mM MgCl2 and 3 mM orthovanadate solution was subjected to freeze–thaw cycles to improve the MsbA accessibility in the proteoliposome sample at 37 °C for 20 minutes. Subsequently, the sample was washed with 20 mM HEPES to remove excess reagents, pelleted, and packed into a 3.2 mm or 4 mm MAS rotor. Trapping was confirmed by ^{31}P-CP MAS NMR[9]. MsbA was incubated with the G907 inhibitor (10 mol/mol MsbA) for 1 hour at room temperature. This inhibitor/protein ratio was determined by the ATPase activity (**Chapter 6**). The sample was pelleted and packed into a 3.2 mm or 4 mm MAS rotor for further measurements.

NOESY G907 in POPE/POPG sample preparation

The preparation of G907 in POPE/POPG was done as described before.[21] A total of 10 mg POPE and POPG was dissolved in $CHCl_3$ and G907 was added to the mixture to yield a drug/lipid ratio of 1:5 and dried under nitrogen gas flow. Multilamellar vesicles were then prepared by hydrating each sample with approximately 10 µL of D_2O (>97%). The sample was then freeze-thawed 10 times in liquid nitrogen and a 30-degree Celsius water bath. Finally, the gel-like sample was transferred into a 4 mm MAS rotor.

Solid-state NMR experiments

The NCO and NCA spectra were recorded using Bruker 600 MHz AVANCE NEO or Bruker 850 MHz AVANCE III with 3.2 mm Triple Resonance Probes. All NCO spectra are recorded with 20-25 mg reconstituted $\mathrm{MsbA_{DMPC/DMPA}}$ in a 3.2 mm rotor at 270 K with a MAS spinning speed of 11 kHz at 600 MHz or 14 kHz MAS at 850 MHz. ^{13}C and ^{15}N chemical shift referencing was carried out with respect to Alanine-CO (DSS) at 179.85 ppm.

In the case of NCA experiments, 10-15 mg of reconstituted $\mathrm{MsbA_{POPE/POPG}}$ was recorded in a 3.2 mm rotor at 260 K with a MAS spinning speed of 14 kHz MAS at 850 MHz. ^{13}C and ^{15}N chemical shift referencing was carried out the same way as for the NCO experiments.

PDSD spectra were recorded as control measurements for sample labelling (figure 3.6). Here, a mixing time of 20 ms was applied. Due to the varied amount of samples, the numbers of scans varied between 150-250 scans (500-100 increments) to obtain a good signal-to-noise. The spectral widths were 53 kHz in ω1.

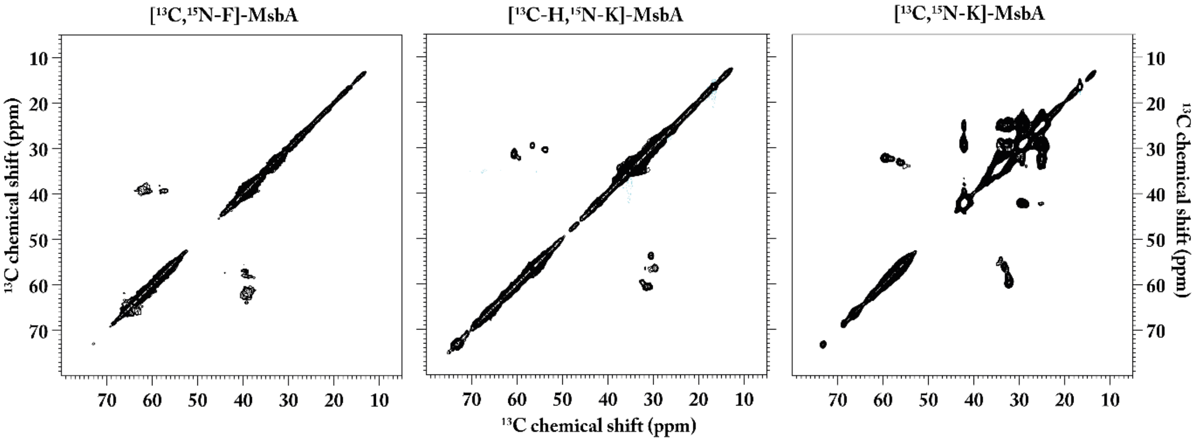

Figure 3.6: ^{13}C-^{13}C PDSD spectra of [^{13}C, ^{15}N-F]-MsbA (left), [^{13}C-H, ^{15}N-K]-MsbA (middle) and [^{13}C, ^{15}N-K]-MsbA (right). The expected ^{13}C-^{13}C correlations are observed in all three cases demonstrating only limited loss of labelling due to scrambling. Spectra were recorded at 600 MHz, 270K with a MAS rate of 11 kHz. A mixing time of 20 ms was used. All spectra were recorded on MsbA reconstituted into DMPC/DMPA lipid bilayers. ^{13}C chemical shift referencing was carried out indirectly to DSS using the C'-resonance of Alanine at 179.85 ppm.

^{31}P MAS spectra of ADP vanadate trapped states were recorded (4096 scans, 270 K) using CP with a 90° pulse of 4.5 ms and 62.5 kHz 1H SPINAL decoupling during 15 ms acquisition with a recycle delay of 3 s at 10 kHz MAS. ^{31}P chemical shift referencing was set to 58.62 ppm. with respect to H_3PO_4 of triethyl phosphine sulphide (TEPS).

Standard settings for cross-polarization (CP) and decoupling were applied for all experiments. ^{1}H 90° pulse had a duration of 3 µs with a chosen CP contact time between 0.5 and 1 ms and high-power proton decoupling of 70–100 kHz was applied using SPINAL64 during evolution and acquisition. 1H- and 13C-90°-pulses are set to 3 and 4.5 µs for ^{13}C and ^{15}N, respectively. NCO spectra were recorded with 5120 scans (30 increments) using a spectral width of 2 kHz in ω1. NCA spectra were recorded with 3720 scans (50 increments) using a spectral width of 2 kHz in ω1. Gd^{3+}-DOTA doping (3 mM) of MsbA reduced the recycle delay from 3 to 1 s. All spectra were processed with TOPSPIN 4.1 using an exponential window function applied to 1D spectra and a shifted cos2 function to 2D spectra.

The 2-dimensional ^{1}H MAS-NOESY spectra were recorded using Bruker 600 MHz AVANCE NEO with 4 mm Double Resonance Probes. Standard settings based on previous experiments have been used (Maier 2009) with 90° pulses of typically 3 µs. A total of 256 data points were collected in the indirect dimension, with 32 scans and a recycle delay of 2 s. All spectra were referenced with respect to D2O at 4.8 ppm or sodium trimethylsilyl propane sulfonate (DSS) at 0.00 ppm. Various NOESY spectra were obtained at 50, 100, 150, 200, 250, 300, 350, 400, 450, 500, 750, and 1000 ms to obtain the desired mixing time of 400 ms to study the G907-POPE/POPG interactions.

Liquid-state (solution) NMR experiments

Accordingly, MsbA was expressed and purified, and the sample was concentrated to a concentration of 20 mg/mL. The protein sample in DDM micelles was then transferred to a Shigemi tube of which 250 µL was 5 mg of MsbA and the volume was then adjusted to 300 µL after the addition of D_2O, $MgCl_2$ and substrates. The Shigemi tube was then closed with a plunger and calibrated (matching, tuning, and shimming) on the solution NMR before adding the injection capillary with the required 40 µL of ATP solution (Chapter 2). Upon the initiation of the pseudo-2D recordings of the time-resolved, 32 FIDs are allowed for the equilibration before the injection and the start of the intended reaction. Data was analysed in Originlab® and Matlab (**appendix Data analysis protocols 31P NMR progression curve and Matlab Script**).

3.5 Cellular assays

$_{WT}$MsbA gene was cloned and transformed into *E. coli* C43(DE3) and *E. coli* C43(DE3) ΔacrAB cells. The cells were grown in a preculture overnight (16 hrs, 37 °C, 220 r.p.m.), washed, and diluted to OD_{600} of 0.01 in 150 µL volume in a sterile microtiter plate in Luria Broth (25 gL^{-1}) and ampicillin (100 µg/mL). The growth of the cells was followed over a 12-hour timespan (20-minute intervals) using BMG LABTECH CLARIOstar at 37 °C. Initially, the *E. coli* C43(DE3) were optimized for a secondary stress factor. This was done by introducing SDS and IPTG to the cells. SDS and IPTG were titrated in matrices to the cells and growth was followed over time. Based on the results the experiments were carried on without a secondary stress factor (Chapter 4). After steady growth of 240 minutes, the G-compounds in DMSO (6 *µg/mL G907 and G247, 20 µg/mL G592, 40 µg/mL G593*) were added to the cells (minimum inhibitory concentration (MIC) literature values[22,23]). The same amount of DMSO was added to the control cells. The growth was followed for the remaining 720 minutes. The matrix data was then processed in Microsoft Excel and transformed into growth curves using OriginPro 2017. $^{*}p<0.05$, $^{**}p<0.01$, $^{***}p<0.001$ (ANOVA, Bonferroni test); n≥5.

References

1 Anfinsen, C. B. Principles that govern the folding of protein chains. *Science* **181**, 223-230, doi:10.1126/science.181.4096.223 (1973).

2 Cross, T. A., Sharma, M., Yi, M. & Zhou, H. X. Influence of solubilizing environments on membrane protein structures. *Trends Biochem Sci* **36**, 117-125, doi:10.1016/j.tibs.2010.07.005 (2011).

3 Jensen, M. O. & Mouritsen, O. G. Lipids do influence protein function-the hydrophobic matching hypothesis revisited. *Biochim Biophys Acta* **1666**, 205-226, doi:10.1016/j.bbamem.2004.06.009 (2004).

4 Seddon, A. M., Curnow, P. & Booth, P. J. Membrane proteins, lipids and detergents: not just a soap opera. *Biochim Biophys Acta* **1666**, 105-117, doi:10.1016/j.bbamem.2004.04.011 (2004).

5 Lehnert, E. *et al.* Antigenic Peptide Recognition on the Human ABC Transporter TAP Resolved by DNP-Enhanced Solid-State NMR Spectroscopy. *J Am Chem Soc*, doi:10.1021/jacs.6b07426 (2016).

6 Ong, Y. S., Lakatos, A., Becker-Baldus, J., Pos, K. M. & Glaubitz, C. Detecting substrates bound to the secondary multidrug efflux pump EmrE by DNP-enhanced solid-state NMR. *J Am Chem Soc* **135**, 15754-15762, doi:10.1021/ja402605s (2013).

7 Spadaccini, R., Kaur, H., Becker-Baldus, J. & Glaubitz, C. The effect of drug binding on specific sites in transmembrane helices 4 and 6 of the ABC exporter MsbA was studied by DNP-enhanced solid-state NMR. *Biochim Biophys Acta* **1860**, 833-840, doi:10.1016/j.bbamem.2017.10.017 (2018).

8 Kaur, H. *et al.* The ABC exporter MsbA probed by solid state NMR - challenges and opportunities. *Biol Chem* **396**, 1135-1149, doi:10.1515/hsz-2015-0119 (2015).

9 Kaur, H. *et al.* Coupled ATPase-adenylate kinase activity in ABC transporters. *Nat Commun* **7**, 13864, doi:10.1038/ncomms13864 (2016).

10 Hellmich, U. A. & Glaubitz, C. NMR and EPR studies of membrane transporters. *Biol Chem* **390**, 815-834, doi:10.1515/BC.2009.084 (2009).

11 Kaur, H. *et al.* Unexplored Nucleotide Binding Modes for the ABC Exporter MsbA. *J Am Chem Soc* **140**, 14112-14125, doi:10.1021/jacs.8b06739 (2018).

12 Spadaccini, R., Kaur, H., Becker-Baldus, J. & Glaubitz, C. The effect of drug binding on specific sites in transmembrane helices 4 and 6 of the ABC exporter MsbA studied by DNP-enhanced solid-state NMR. *Biochim Biophys Acta Biomembr* **1860**, 833-840, doi:10.1016/j.bbamem.2017.10.017 (2018).

13 Geertsma, E. R., Nik Mahmood, N. A., Schuurman-Wolters, G. K. & Poolman, B. Membrane reconstitution of ABC transporters and assays of translocator function. *Nat Protoc* **3**, 256-266, doi:10.1038/nprot.2007.519 (2008).

14 Simeonov, P., Werner, S., Haupt, C., Tanabe, M. & Bacia, K. Membrane protein reconstitution into liposomes guided by dual-color fluorescence cross-correlation spectroscopy. *Biophys Chem* **184**, 37-43, doi:10.1016/j.bpc.2013.08.003 (2013).

15 Fiske, C. H. & Subbarow, Y. The colorimetric determination of phosphorus. *J. Biol. Chem.* **66**, 375-400 (1925).

16 Chifflet, S., Torriglia, A., Chiesa, R. & Tolosa, S. A method for the determination of inorganic phosphate in the presence of labile organic phosphate and high concentrations of protein: application to lens ATPases. *Anal Biochem* **168**, 1-4, doi:10.1016/0003-2697(88)90002-4 (1988).

17 *The Nobel Prize in Chemistry 1997*, <https://www.nobelprize.org/prizes/chemistry/1997/summary/> (

18 Lammens, A. & Hopfner, K. P. Structural basis for adenylate kinase activity in ABC ATPases. *J Mol Biol* **401**, 265-273, doi:10.1016/j.jmb.2010.06.029 (2010).

19 Lakatos-Karoly, A. *et al.* Probing conformational changes in MsbA by selective chemical shift perturbations. *in preparation* (2023).

20 Mi, W. *et al.* Structural basis of MsbA-mediated lipopolysaccharide transport. *Nature* **549**, 233-237, doi:10.1038/nature23649 (2017).

21 Maier, T. J. *et al.* Cellular membranes function as a storage compartment for celecoxib. *J Mol Med (Berl)* **87**, 981-993, doi:10.1007/s00109-009-0506-8 (2009).

22 Ho, H. *et al.* Structural basis for dual-mode inhibition of the ABC transporter MsbA. *Nature* **557**, 196-201, doi:10.1038/s41586-018-0083-5 (2018).

23 Alexander, M. K. *et al.* Disrupting Gram-Negative Bacterial Outer Membrane Biosynthesis through Inhibition of the Lipopolysaccharide Transporter MsbA. *Antimicrob Agents Chemother* **62**, doi:10.1128/AAC.01142-18 (2018).

PART II

The influence of nucleotides and substrates on MsbA

Chapter 4

The characterization of the bacterial membrane protein MsbA

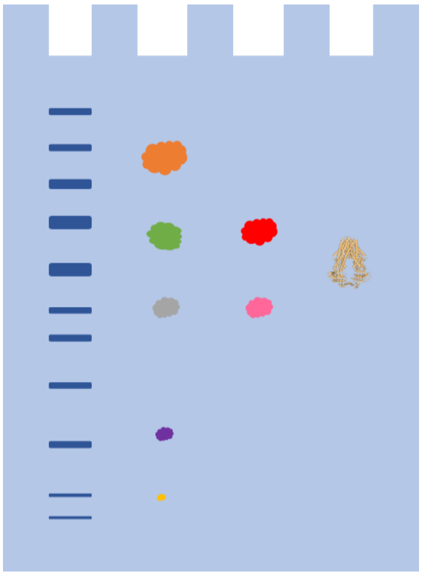

"Chasing meaning is better for your health than trying to avoid discomfort."

– *Kelly McGonigal*

4.1 Characterization by size

For the basic characterization of MsbA SDS-PAGE, blue native PAGE, Western blot, and size exclusion chromatography were used (figure 4.1). The size exclusion chromatogram of wild-type MsbA shows that the sample is homogenous, only one major peak has been eluted between 11-13 mL. The SDS-PAGE and western blot identified MsbA around 65 kDa. Similarly, for the blue native PAGE, the dimeric form of MsbA in DDM shows a maximum MsbA weight of 129 kDa with a 1.8x detergent factor, giving a total weight of approximately 232 kDa.

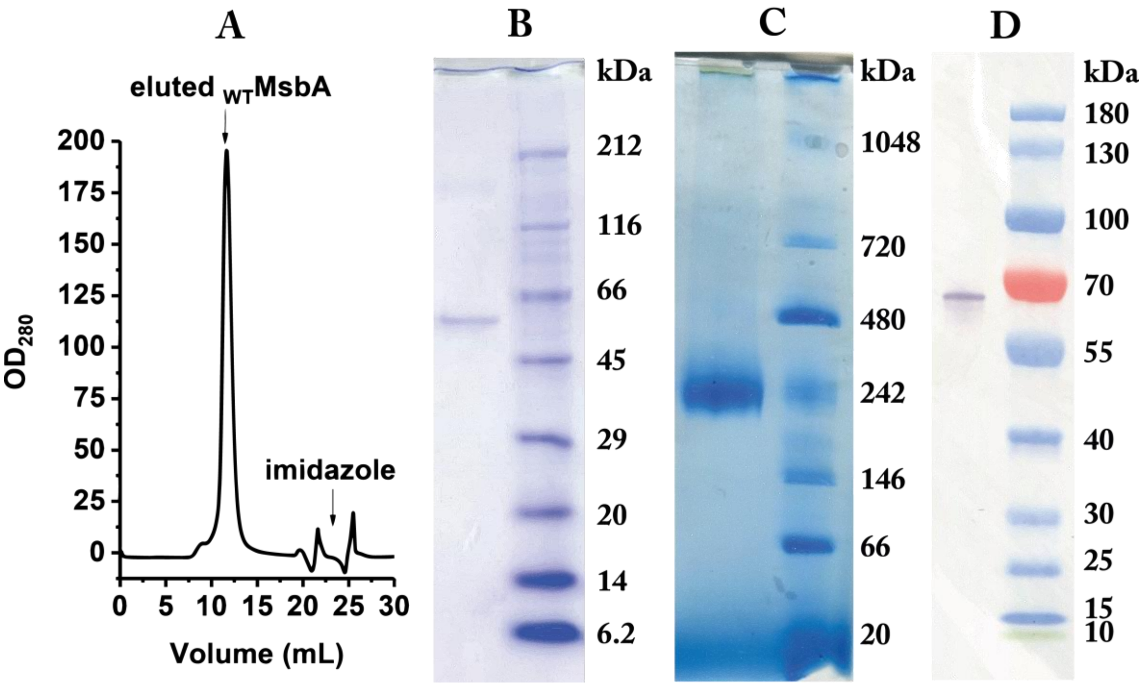

Figure 4.1. Purified MsbA visualized by SDS-PAGE and size exclusion chromatography. A) Size exclusion chromatography of freshly eluted MsbA (<24 hours), showing a homogenous protein sample between 11-13 mL, and imidazole (19-26 mL). B) SDS-PAGE (0.025% w/v Coomassie brilliant blue R-250 staining) of MsbA purification process after elution from Ni-NTA column in 0.015% DDM, and after reconstitution (in DPCA/DMPA, 9:1). C) Blue native PAGE ($MW_{DDM\text{-}MsbA} = W_{dimer} \times f1.8$). D) Western blot.

4.2 Characterization by sample homogeneity

Prior to the reconstitution of MsbA in both DMPC/DMPA and POPE/POPG, turbidity tests have been done for both conditions, by titrating DDM and Triton X-100 respectively (figure 4.2 and 4.3)[1]. To determine the homogeneity of the sample preparation, sucrose gradients were used for both conditions. The result in both cases appears to be homogenous. Furthermore, Arne Möller was so kind to provide us with cryo-EM of MsbA in detergent micelles (figure 4.4). Here, it is observed that MsbA is after purification.

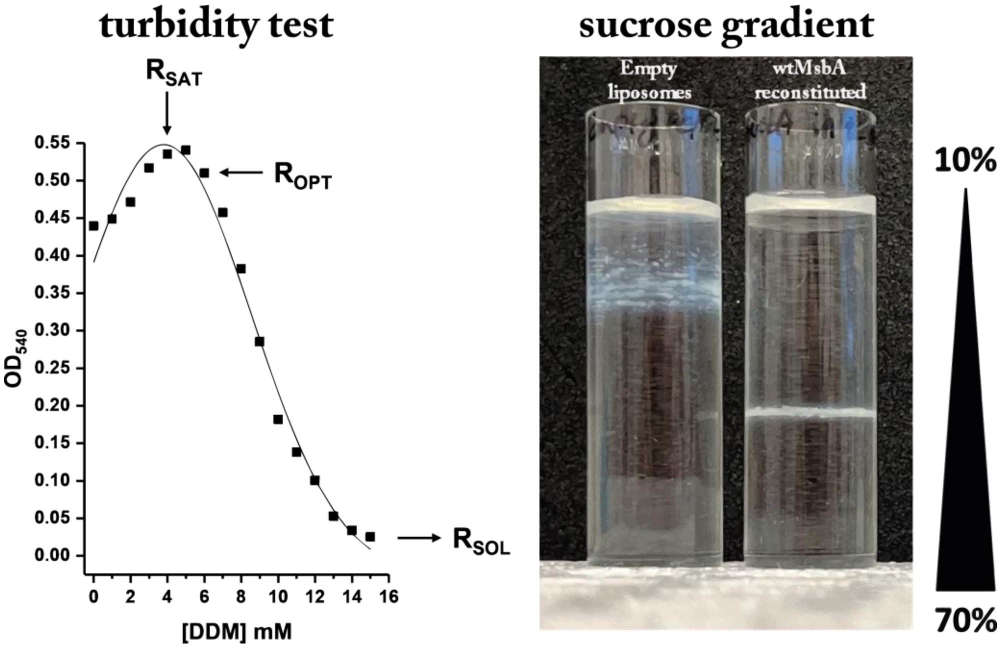

Figure 4.2. Reconstitution of MsbA in DMPC/DMPA. A) Turbidity test results in at least 7 mM DDM required for reconstitution without visible aggregations with a ratio of 1:75 MsbA to DMPC/DMPA 9:1. B) Sucrose gradient (70%, 50%, 30%, 10%) of reconstituted MsbA visualising no aggregations occurred during the reconstitution process.

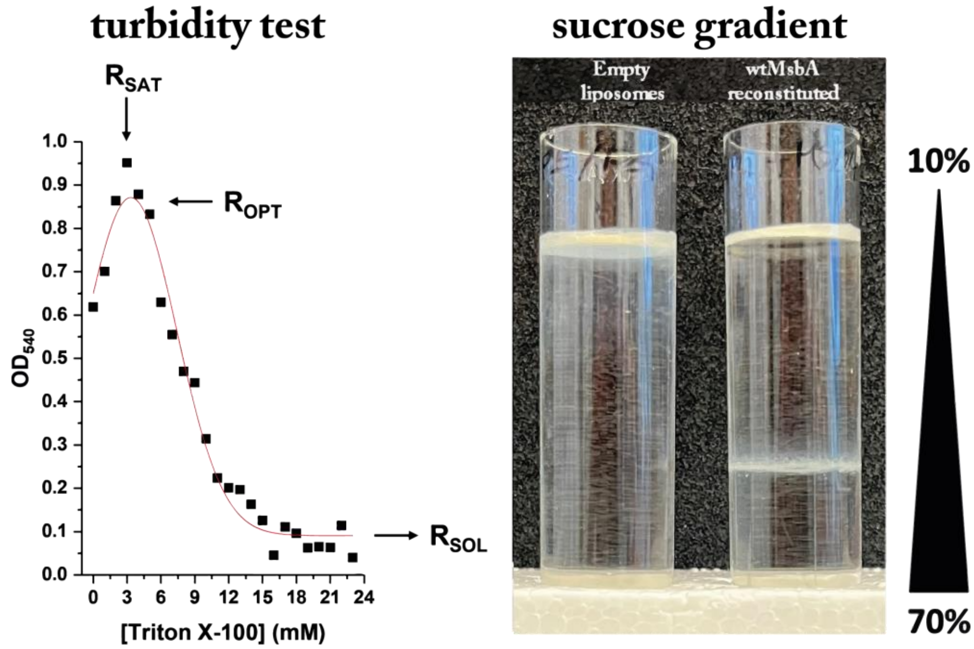

Figure 4.3. Reconstitution of MsbA in POPE/POPGE. A) Turbidity test results in at least 4 mM Triton X-100 required for reconstitution without visible aggregations with a ratio of 1:75 MsbA to DMPC/DMPA 9:1. B) Sucrose gradient (70%, 50%, 30%, 10%) of reconstituted MsbA visualising no aggregations occurred during the reconstitution process.

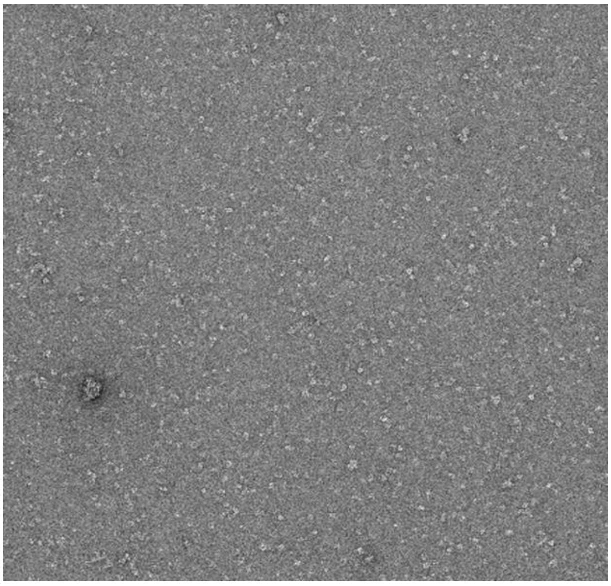

Figure 4.4. Cryo-EM of wild-type MsbA in DDM detergent micelles. *The Cryo-EM was done by Arne Moeller.*

4.3 Characterization by biochemical assays

MsbA was then further characterised with an ATPase assay. The resulting V_{MAX} values were 12.1, 8.5, and 13.9 µmol/min/mg, respectively for $_{WT}$MsbA$_{DDM,}$ $_{WT}$MsbA$_{DMPC/DPMA}$, and $_{WT}$MsbA$_{POPE/POPG}$ (**figure 4.5**). The K_M values were $4.1 \cdot 10^{-4}$, $3.5 \cdot 10^{-4}$, and $4.4 \cdot 10^{-4}$ M, respectively. Across the various batches, both the V_{MAX} and K_M values were in the same order of magnitude. Moreover, the values are comparable to previous studies[2]. Similarly, for the Hoechst 33342 stimulation assay (**figure 4.6**). Hoechst generally stimulates MsbA. However, at a significantly higher concentration, it can also act as an inhibitor.

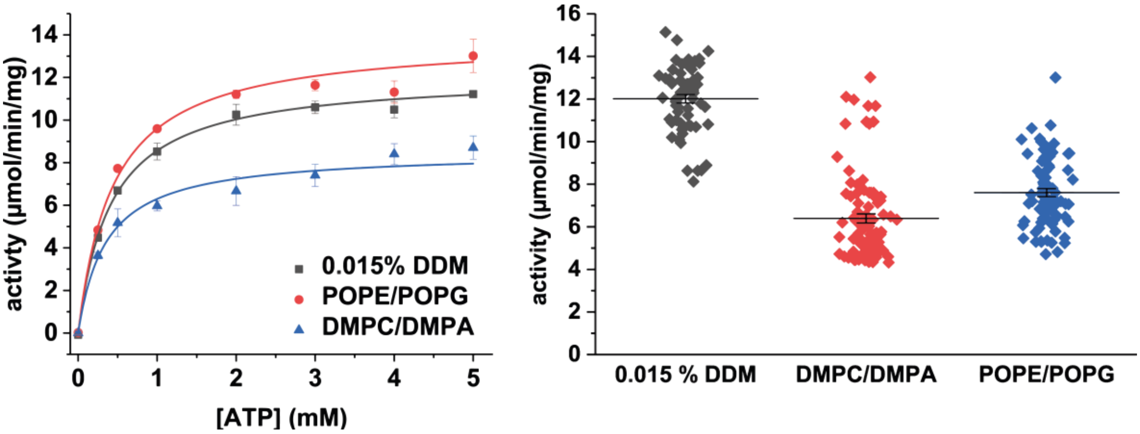

Figure 4.5. DMPC/DMPA vs POPE/POPG. Michaelis-Menten kinetics of $_{WT}$MsbA$_{DDM}$ compared to $_{WT}$MsbA$_{DMPC/DPMA}$ and $_{WT}$MsbA$_{POPE/POPG}$, with a V_{MAX} of 12.1, 8.5, and 13.9 µmol/min/mg, and a K_M of $4.1 \cdot 10^{-4}$, $3.5 \cdot 10^{-4}$, and $4.4 \cdot 10^{-4}$ M, respectively. Pulled V_{MAX} of $_{WT}$MsbA$_{DDM}$ compared to $_{WT}$MsbA$_{DMPC/DPMA}$ and $_{WT}$MsbA$_{POPE/POPG}$ across various batches showing V_{MAX} with the same order of magnitude across all samples.

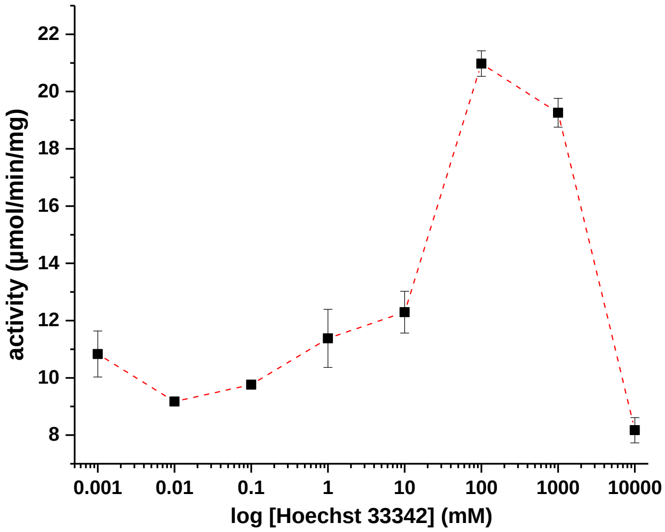

Figure 4.6. Stimulation of MsbA by Hoechst. At 100 µM Hoechst 33342 MsbA has the highest stimulated activity.

4.4 Characterization of MsbA mutants

With respect to the coupling helices of MsbA, alanine mutations were made to explore the biochemical side of the respective mutants. The mutants were made by Andrea Karoly-Lakatos (in-house)[3]. CH2 was more affected by mutations than CH1. Mutations in the conserved phenylalanine F115 and F116 to alanine in CH1 reduced the ATPase activity by 50%, whereas mutations of the aspartate D117 to alanine were not affected and retained more than 80% ATPase activity compared to the wild type (figure 4.7). F115A shows a reduced ATPase activity upon an increase in ATP concentration. Possibly at high levels of ATP, F115A-MsbA prohibits proper NBD dimerization thus resulting in a lower amount of ATP hydrolysed. H33342 stimulation did not take place after mutations in CH1. Along the CH2 stretch, G213A and E216A were the least affected mutants and had more than 50% ATPase activity compared to the wild type. H214A, K215A, V217A, and L218A were the most affected in CH2 and had less than 30% ATPase activity after the mutation to alanine. H33342 stimulation is most affected in H214A, K215A, and V217A.

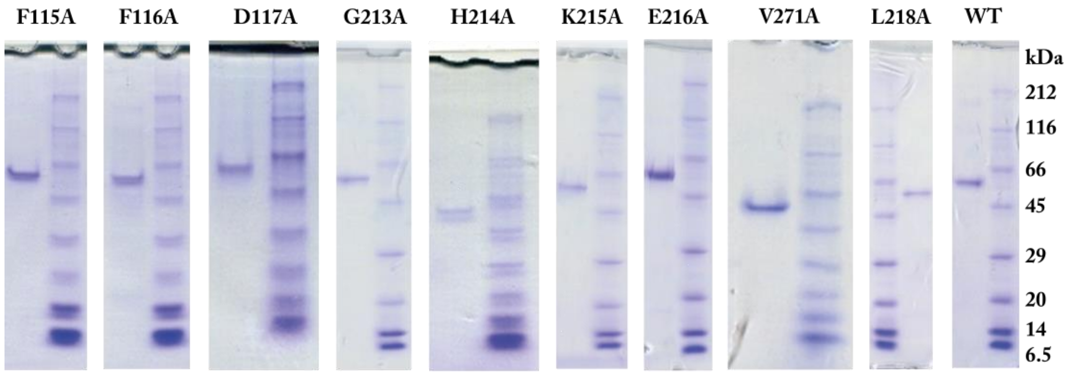

CH1 MsbA mutants

CH2 MsbA mutants

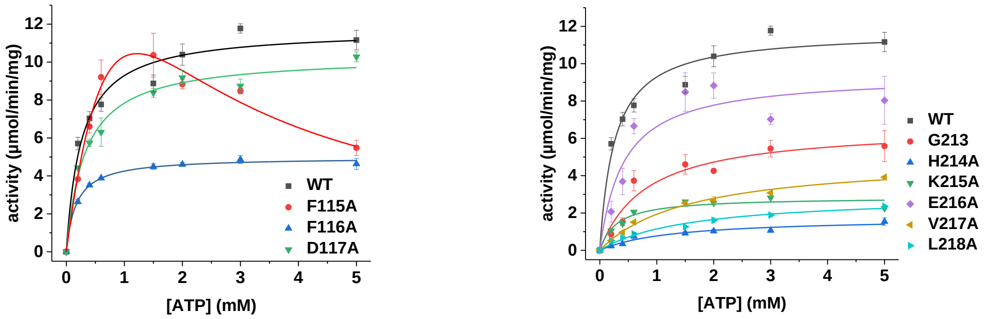

Hoechst stimulation CH1 mutants

Hoechst stimulation CH2 mutants

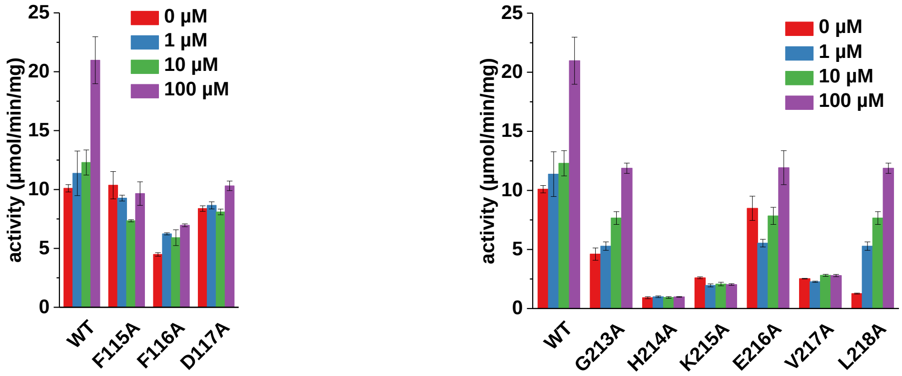

Figure 4.7. Characterization of alanine mutants by SDS PAGE, ATPase activity, and Hoechst 33342 simulation in coupling helix 1 (CH1) and coupling helix 2 (CH2). Stimulated ATPase activities of MsbA and coupling helix mutants in DDM. The activity reported here corresponds to [ATP] = 1.5 mM (n=3 of distinct samples with mean±SEM). The stimulated ATPase activity is strongly affected by mutations in both coupling helices. Positions F115, F116, and H214, K215 have then been selected for isotope labelling to serve as reporters within the coupling helices. (*Alanine mutations were generated by Andrea Karoly-Lakatos*)

4.5 Optimization of cellular assay conditions

Prior to the cellular assay to test the inhibition of the G-compounds, secondary stress factors were introduced to the C43 cells. This secondary stress factor could increase cellular sensitivity and minimize the amount of inhibitors required to achieve apoptosis. This test was based on previously published functional assays[4]. The maximum SDS concentration that allowed the C43 cells to grow was 0.125 mg/mL (**figure 4.8**). No optimal IPTG concentration was found as the highest concentration was stimulating growth beyond the control, but no significant differences were observed between the lower IPTG concentrations. Yet, upon replication, the cells could not reproduce the same growth curve at 0.125 mg/mL against the highest SDS concentration. No difference was observed in the control condition without ITPG or in the stimulating condition of 1 mM ITPG. Therefore, no secondary stress factor was introduced to the inhibition assay. Hence, no apoptosis was observed upon the addition of the G-compounds (**Chapter 6**). However, the C43 cells and the ΔAcrAB knockout control cells showed a significant reduction in cell growth.

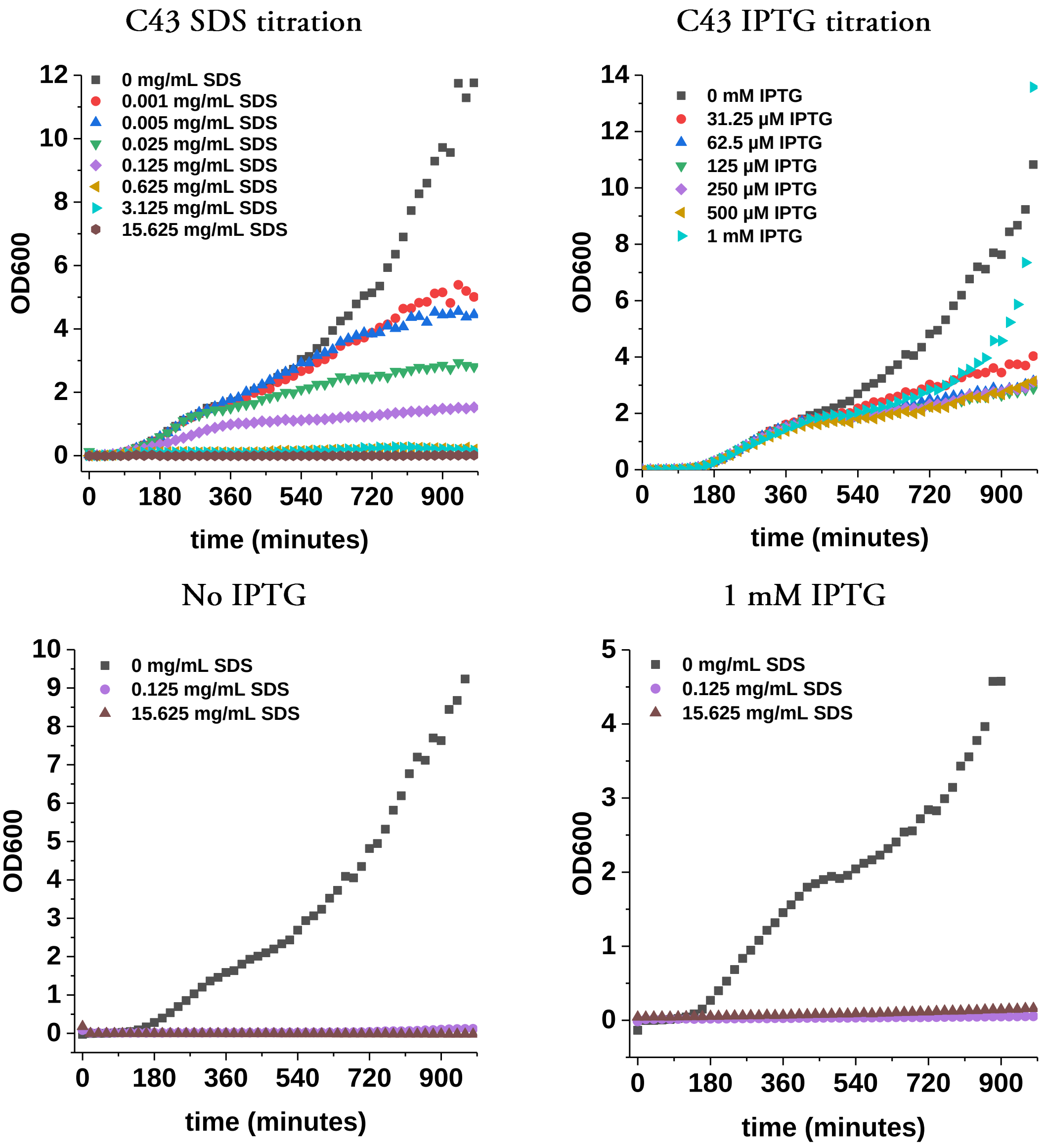
C43 SDS titration

C43 IPTG titration

No IPTG

1 mM IPTG

Figure 4.8. Optimization of a second stress factor for C43 cells prior to cellular inhibitor assay. SDS and IPTG were titrated to the C43 cells and growth was followed over time. To test for reproducibility, 0.125 and 15.625 mg/mL SDS was retested in 0 and 1 mM IPTG.

References

1 Geertsma, E. R., Nik Mahmood, N. A., Schuurman-Wolters, G. K. & Poolman, B. Membrane reconstitution of ABC transporters and assays of translocator function. *Nat Protoc* **3**, 256-266, doi:10.1038/nprot.2007.519 (2008).

2 Kaur, H. *et al.* The ABC exporter MsbA probed by solid state NMR - challenges and opportunities. *Biol Chem* **396**, 1135-1149, doi:10.1515/hsz-2015-0119 (2015).

3 Lakatos-Karoly, A. *et al.* Probing conformational changes in MsbA by selective chemical shift perturbations. *in preparation* (2023).

4 Cha, H. J., Muller, R. T. & Pos, K. M. Switch-loop flexibility affects transport of large drugs by the promiscuous AcrB multidrug efflux transporter. *Antimicrob Agents Chemother* **58**, 4767-4772, doi:10.1128/AAC.02733-13 (2014).

Chapter 5

Probing the allosteric NBD-TMD crosstalk in the ABC Transporter MsbA by solid-state NMR

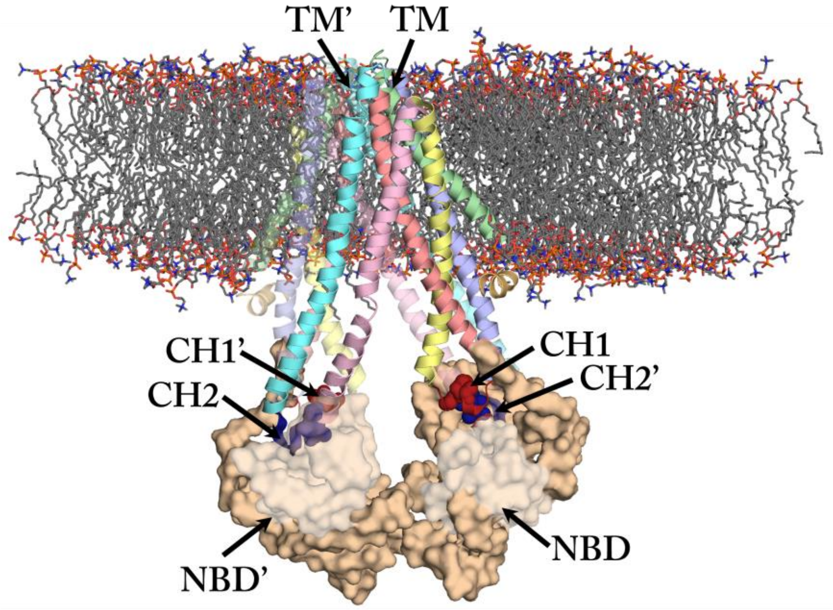

> "I have had my results for a long time, but I do not yet know how to arrive at them"
>
> *- Carl Gauss*

This chapter was taken from Novischi et al. Commun. Biol. 2023 (accepted).

5.1 The coupling helices of MsbA

Since ABC transporters have TMDs and NBDs, transporters also consist of the so-called coupling helices (CHs) and/or intracytoplasmic loops (ICLs) to couple the cross-talk between TMD and NBD. The universally located coupling helices that connect the TMD to the NBD, have been suggested to be responsible for the TMD-NBD coupling[1-11]. The NBD-TMD communication is mediated through long intracellular loops ICL1 and ICL2, which are extensions of transmembrane helices TMH2+3 and TMH4+5, respectively. Both ICLs contain short coupling helices CH1 and CH2, aligned parallel to the membrane, through which they interact with the NBD surface[2-14]. In the ABC homolog Sav1866 the coupling helices connect two antiparallel helices that are extensions of transmembrane helices, which form an intracellular loop[15]. Additionally, domain swapping of the coupling helices was observed, where the first coupling helix (CH1) binds at the NBD interface and interacts with both NBDs, and the second coupling helix (CH2) interacts with the opposite subunit only[13,14]. Notably, simulations have shown that F116 of CH1 is in direct contact with H214 of the opposing CH2 (**figure 5.1**)[9].

However, the sequence for CH2 is well-conserved, in contrast to CH1[16]. Some MD simulations showed highly cooperative NBD-TMD interaction during the transition state and a significant role of the coupling helices in the dynamic coupling of the full ABC transporters[9,17]. Moreover, CH1 and CH2 mutants have shown a decreased ATP binding affinity for both coupling helices, but CH2 has a stronger influence on the ATPase activity compared to CH1.[9] In MsbA, the inward-facing conformation seems to fluctuate in association with CH2. Nevertheless, CH2 fluctuation merely occurs minimally in its outward-facing state[18]. The mutations in CH1 and CH2 to alanine residues revealed that CH2 mutations lead to a significantly decreased ATPase activity (**Chapter 4 and Zou & McHaourab 2009[19]**).

MD simulations have shown that the outward-facing state is stabilized through ATP binding, and mutations in CH2 are changing the outward conformation to an inward conformation via an anticlockwise rotation, which indicates that CH2 mediates the conformation between the TMDs and the NBDs. Hence, this explains the strong influence on the ATPase activity in CH2 mutations in comparison to CH1. In addition, the MD simulation showed that the π-π stacking of the adenine of ATP and the aromatic residue of the A-loop is disrupted by the CH1 mutant. Also, the CH2 mutant weakened the electrostatic interaction between the H-loop and Walker A motif with ATP, and the Mg^{2+} ion between the Q-loop and Walker B motif. Lastly, the direct interaction between F116 of CH1 and H214 of CH2 was observed in all the systems[9].

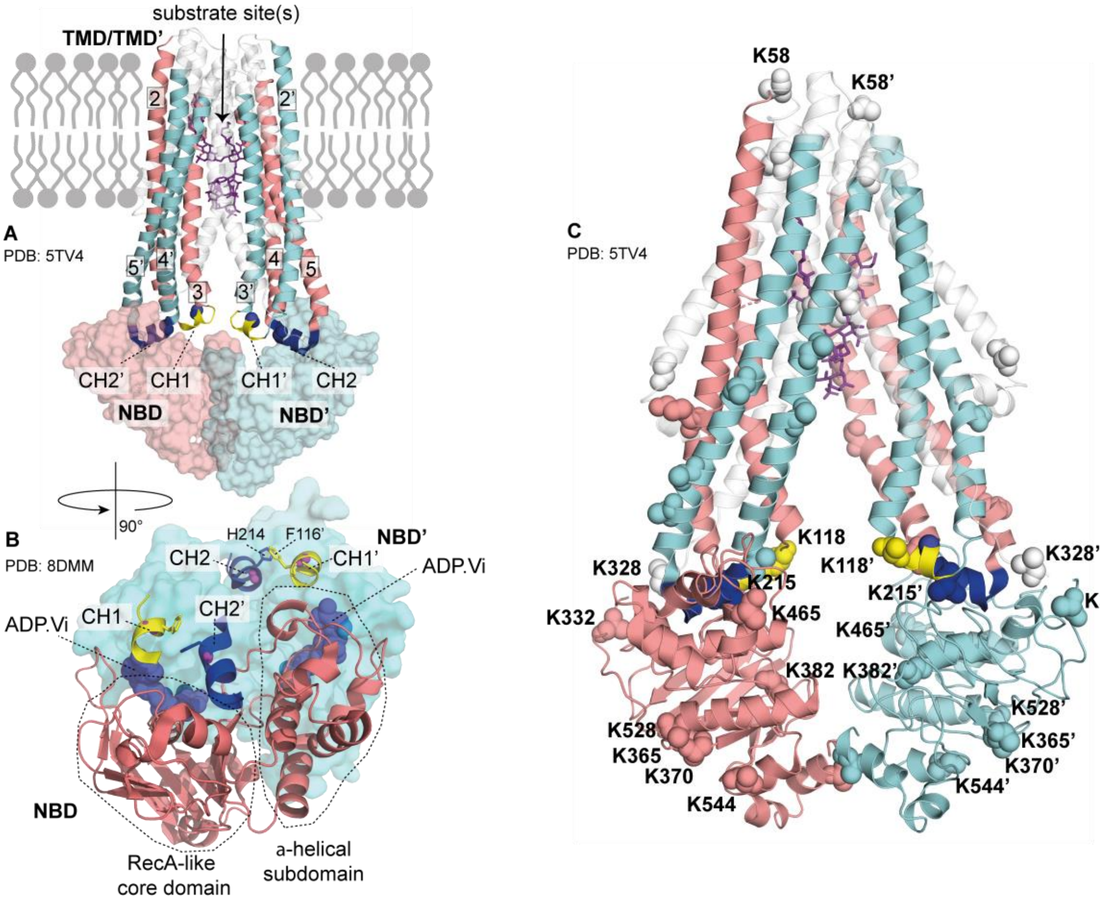

Figure 5.1: MsbA with substrate- and nucleotide binding sites, coupling helices, and unique pair labelling sites. (A) Apo-state MsbA with bound LPS in an inward-facing conformation (PDB 5TV4 [20]). CH1 is part of the intracellular loop formed by TMH2 and TMH3. It makes contact with the NBD of the same chain. In contrast, in CH2, the intracellular loop between TMH4 and TMH5 interacts with the opposing NBD'. The $^{13}C/^{15}N$-labelled sites in CH1 (F115-F116) and CH2 (H214-K215) are highlighted as blue spheres. The bound substrate is represented as sticks to schematically show the location of sites where LPS, small ligands, and inhibitors bind. For better visibility, TMHs 1, 1', 6, and 6' are only shown as gray transparent. (B) Location of CHs with respect to NBD structural segments based on an ADP•Vi bound MsbA structure (PDB: 8DMM [21]). For simplicity, NBD' is only indicated as a surface plot. CH1 binds to the NBD surface in the grooves of the RecA-like core domain and comes also in contact with NBD', while CH2' is located on the NBD surface in between the RecA-like and the a-helical subdomain. In most structures, F116 of CH1 and H215' of CH2' (as well as F116'-H215) point towards each other. (C) Location of Lys residues assigned in NCA spectra of [$^{13}C,^{15}N$-K]-MsbA[22]. The residues are highlighted as yellow spheres in the structural cartoon based on the MsbA structure PDB 5TV4 [20].

In other ABC transporters, such as McjD[23], LmrA[16], P-gp[16] (also known as multidrug resistance protein 1 (MDR1) or ABCB1[24]) and transporter associated with antigen processing (TAP1)[7] overlapping evidence with Sav1866 and MsbA were found, with respect to CH1 and CH2. In the case of TAP1, the mutations to cysteine residues in CH1 (residues 272- ETEFFQQNQT-281) have affected the transport activity of the protein, except for Q277C. However, mutations in CH2 (residues 373-AMPTVRSFA-381) compromise the peptide binding pocket. Here, R378C showed a significant decrease in substrate binding, while P375C had a strong influence on the peptide transport but substrate binding remained unaffected. Overall, CH1 is less lenient to mutagenesis compared to CH2. Additionally, the cross-linking of X-loop with CH1 or CH2 can respectively block substrate translocation or substrate binding[7].

Besides this, ABC exporters exclusively contain an X-loop, which was quoted by Roger J.P. Dawson and Kaspar P. Locher, to highlight its role in cross-linking the coupling helices[1,13,25]. Since the X-loops precede the signature loop, it was thought to undergo conformational changes upon ATP-binding and hydrolysis[5,13,26,27]. Hence, the X-loop might play an important role in the stability of NBD-NBD interaction in the outward-facing state.[28] Furthermore, X-loop mutations (i.e. E602) in TAP2 showed reduced transport activity, thus it is shown to play a critical role in substrate translocation but does not affect substrate binding. Mutation of E602C showed a reduced activity of 50%.

In the case of E602A or E602D, this is reduced to only 20% of transport activity. In E602R the transport activity is completely abolished[7]. Downstream mutations in the extension of the X-loop in MDR3 (Q1174E) showed basal activity, but no stimulation in ATPase activity, which indicates a role in the crosstalk between the TMD and NBD. In Q1181E (Q1174E isoform A) there are no large conformational rearrangements. However, the hydrogen bonding is no longer present. Nonetheless, the crosstalk between the TMDs and NBDs, and the inward- and outward-facing states of ABC transporters remains unclear. To this end, special attention is devoted to CH1 and CH2 to understand the conformational dynamics and crosstalk of the ATP-hydrolysis-mediated MsbA.

3D structures of MsbA in various membrane mimicking environments have been determined by X-ray crystallography and single particle cryo-electron microscopy covering conformations such as wide-open inward facing[29-31] or inward-facing (IF)[20,30,32,33] apo state and occluded[20] and outward-facing (OF)[30] nucleotide[20,30], LPS-bound[20,29,30,33] or inhibitor-bound states[31,33] (figure 5.2). The wide-open inward-facing conformation with well-separated NBDs was initially debated as artificial due to sample preparation conditions caused by the flat energy landscape of apo state MsbA but was recently confirmed by EPR spectroscopy in the native membrane directly within *E. coli* cells[34].

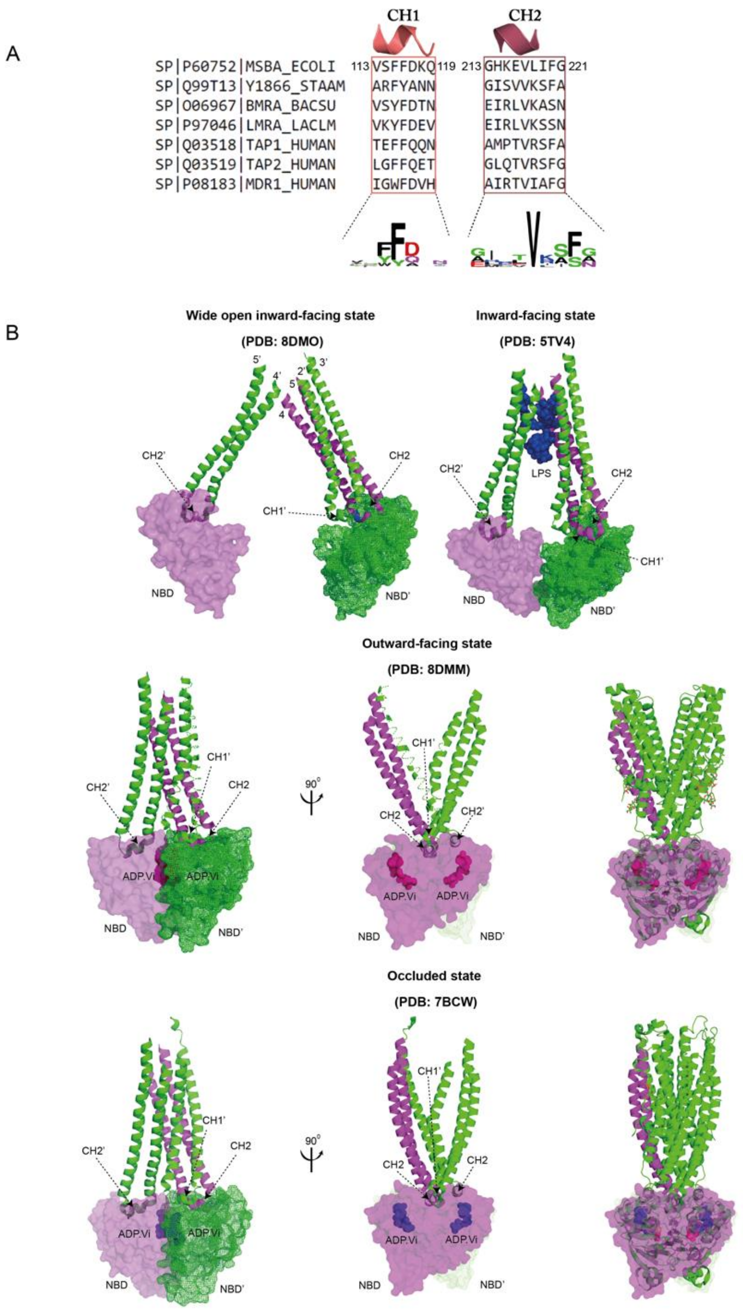

Figure 5.2: Coupling helix sequences and structural arrangement. (A) Sequence alignment of the coupling helices of MsbA and related homo-dimeric exporters Sav1855, BmrA, LmrA, MDR1 as well as hetero dimeric TAP1/2. The degree of conservation is illustrated by WebLogo (https://weblogo.berkeley.edu). **(B)** Arrangement of coupling helices in the wide-open inward-facing state of MsbA (PDB: 8DMO [21]), in the inward-facing conformation (PDB: 5TV4 [20]), in the outward-facing state (PDB: 8DMM [21]) and the occluded state (7BCW [35]). For simplification, all transmembrane helices have been omitted except for 4,5 of one protomer and 2', 3', 4', and 5' of the other. For the outward-facing and occluded states, a plot with all TMHs is shown (right).

In MsbA, as in all type IV exporters, two characteristic coupling helices are found. CH1 is part of ICL1, which extends from TMH3+4, and includes residues 113-119 (VSFFDKQ). Analogous, CH2 is found in ICL2 connecting TMH4+5 and is formed by residues 213-221 (GHKEVLIFG) (**figures 5.1 and 5.2**). CH1 of chain A lies within a groove on the surface of the RecA-like core domain of NBD A. In the NBD-dimerized occluded and OF states, it is also in contact with the surface of the opposite NBD (**figures 5.1 and 5.2**). In contrast, CH2 of chain A is domain-swapped which means it lies on the surface of NBD B within a groove at the boundary of the RecA-like core domain and the alpha-helical subdomain. CH2 of chain B then makes the same contact with NBD A (**figures 5.1 and 5.2**).

To date, the main evidence for the functional importance of CH1 and CH2 has come from biochemical and genetic data. A full alanine replacement of CH1 and CH2 probed by ATPase assays revealed similar effects on nucleotide binding but the CH2 mutant reduced basal ATPase activity much stronger than the CH1 mutant[9]. In the context of extensive EPR studies on MsbA, single-Cys mutations were introduced into CH1 and CH2[36]. Subsequent ATPase assays showed reduced activity for the CH1 mutants but a much stronger reduction and in some cases loss of protein stability for the CH2 mutants. A related picture emerges from studies on other ABC exporters. For TAP1/TAP2, cysteine cross-linking of CH1 with the X-loop inhibits substrate translocation, whereas cross-linking of CH2 inhibits substrate binding and translocation[7]. In the case of CFTR and P-glycoprotein, NBD mutations at the CH1 and CH2 contact sites also demonstrated their mechanistic importance[37,38].[37,38] These results suggest, at least for type IV exporters, that CH2 is functionally particularly important and mediates allosteric coupling between TMD and NBD.

The structural flexibility of the TMD/NBD interface in different conformational states was probed by hydrogen-deuterium exchange mass spectrometry (HDX-MS) experiments for P-glycoprotein and BmrA[39-41]. In the IF state, CH1, CH2, and their NBD counterparts appear more flexible than in the OF state, in which, however, CH2 exhibits a greater flexibility than CH1[39,41].[39,41] It was also shown that CH1 and CH2 are more rigid in the drug-bound and nucleotide-bound state compared to the post-hydrolysis state[40].

The available 3D structures of MsbA and other ABC exporters demonstrate how CH1 and CH2 are arranged with respect to both NBDs in distinct conformational states as illustrated in **figure 5.2**. Based on available P-glycoprotein structures, a 'ball and socket joint' model was proposed with CH2 as 'ball'[42]. However, no clear picture emerged with respect to structural changes within CH1 and CH2 in response to substrate and nucleotide binding.

Nucleotides bind at the canonical binding sites formed at the NBD dimerization interface. MsbA substrates core-LPS and amphipathic drugs as well as quinoline-inhibitors bind to different binding sites within the TMD (Fig, 1A) [20,33,43]. [20,33,43] A number of change-in-specificity mutations for small substrates were found in transmembrane helix 6[44]. which is also part of an inhibitor binding site. The distant nucleotide and substrate binding sites communicate allosterically through the NBD-TMD interface. To obtain experimental evidence for a structural response of CH1 and CH2 as part of this process is therefore essential for a mechanistic understanding of NBD-TMD crosstalk.

Here, we address this issue by solid-state NMR (ssNMR) spectroscopy. This NMR approach offers the opportunity to obtain data on the structure and dynamics of membrane proteins within liposomes, which offers a valuable complement to available 3D structures. So far, ssNMR has not been used extensively in the ABC transporter field, but previous studies for example on MsbA[45-47] and BmrA[48] have demonstrated its potential to obtain novel mechanistic insight[45,46] or to probe the conformational space during the catalytic cycle[47]. In the case of BmrA, solid-state NMR was also used to analyze the effect of mutations in the X-loop[49], which had been previously suggested to play a role for NBD-TMD cross-talk in ABC exporters[13], and to study the effect of nucleotide binding[50].

For our approach, we selected Hoechst 33342 from the group of amphipathic MsbA substrates because it has been shown to stimulate ATPase activity and is transported[46,51-55]. It is also a substrate of other ABC exporters with multidrug specificity[49,56-60] and has been used by us before for studying substrate-induced effects within MsbA TMH4 and 6[47]. It has also some practical advantages over the endogenous MsbA ligand core-LPS in terms of titratability and also in terms of preparing a clean substrate-free or substrate-bound state since multiple core-LPS species can bind to MsbA and get modulated differently by purification conditions[21,29].

As previously used for probing substrate binding in the TMD of MsbA[47], we utilized here a unique-pair labelling scheme by which CH1 (F115-F116) and CH2 (H214-K215) can be monitored in a highly site-resolved manner (figure 5.1). This approach is combined with a residue-selective Lys-labelling scheme based on known resonance assignments[22]. Substrate-, inhibitor- and nucleotide-dependent chemical shift changes are then a sensitive experimental readout for conformational changes. The data described below demonstrate that CH1 and CH2 undergo structural changes as part of the TMD-NBD cross-talk.

5.2 Results

5.2.1 Labelling scheme selection for CH1 and CH2

For the selective labelling approach used here, suitable residues at sensitive positions within the coupling helices must be identified. Ideally, these residues should also be part of a unique pair formed with the (i+1) or (i-1) residues for unambiguous assignment. Furthermore, not all amino acids can be labelled equally well due to isotope scrambling. To select appropriate residues at functionally sensitive sites suitable for labelling, we introduced single-point mutations in CH1 and CH2 and tested their effects using substrate-stimulated ATPase activity assays.

CH1 stretches from residue V113 to G119 (**figure 5.2A**). We have introduced Ala-mutations at positions F115, F116 and D117 in the middle of CH1. All three residues show a high degree of conservation. For all three mutations, a reduction in basal activity is observed, which was especially pronounced for F116A. None of them shows stimulated ATPase activity in the presence of substrate Hoechst-33342 (**figure 4.7**). The length of CH2 ranges from Gly-213 to Gly-221 (**figure 5.2A**). We probed residues G213, H214, K215, E216, V217 and L218 by Ala-mutations. Of these residues, V217 is especially highly conserved. Here, the strongest effects were observed for H214, K215 and V217 (**figure 4.7**).

A strong reduction in basal ATPase activity and lack of stimulation by the substrate is observed for H214A, K215A and V217A. For G213A, E216A and K218A, a reduction in basal activity is detected, but their activity can still be stimulated by H33342 (**figure 4.7**). Overall, these data allow the conclusion that mutations in CH2 have a stronger effect compared to CH1, which is in line with previous coupling helix studies on MsbA[9]. Based on these findings and taking known metabolic pathways for isotope scrambling into account [61], we selected F115-F116 in CH1 for isotope labelling as it is the only Phe–Phe pair in MsbA. For CH2, we choose H214-K215 for further studies, since only two His-Leu pairs occur in the MsbA sequence.

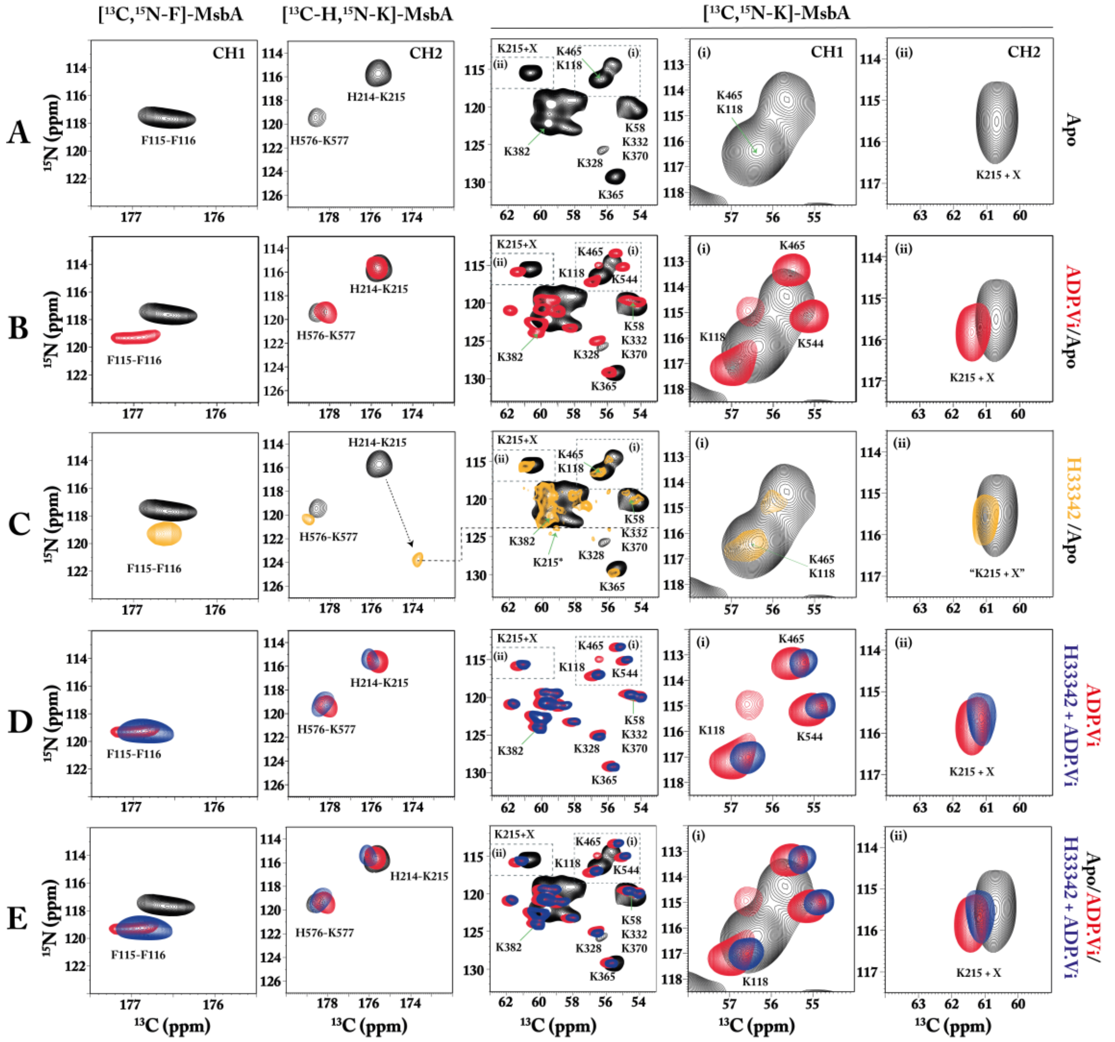

Figure 5.3: NCO and NCA spectra of residues in CH1 and CH2. NCO spectra of [^{13}C,^{15}N-F]-MsbA and [^{13}C-H,^{15}N-K]-MsbA visualize F115-F116 in CH1 and H214-K215 in CH2, respectively (left). In addition, NCA spectra of [^{13}C,^{15}N-K]-MsbA reveal cross peaks K118 in CH1 and K215 in CH2 (middle, right). (A) NCO and NCA spectra of apo-state MsbA. In MsbA, two H(i)-K(i+1) pairs occur resulting in two cross-peaks for [^{13}C-H,^{15}N-K]-MsbA. Some of the Lys in [^{13}C,^{15}N-K]-MsbA have been assigned in another study.[22] K118 in CH1 overlaps with K465 and K215 with one unassigned Lys (X). The apo state corresponds to an inward-facing conformation. (B) ADP•Vi-trapped MsbA. This state corresponds to an outward-facing conformation. (C) Apo-state MsbA with and without substrate Hoechst 33342. Here, a remarkable shift of the H214-K215 NCO cross peak is observed. The "K215+X" NCA cross peak (right) does not shift accordingly, which is because only residue X contributes. The K215 NCA cross peak has been tentatively assigned to a spectral intensity matching ^{15}N chemical shift (K215*, middle). (D) ADP•Vi-trapped MsbA with and without substrate Hoechst 33342. (E) Superposition of apo-, ADP•Vi- and ADP•Vi+Hoechst 33342 states. The experiments were performed using MsbA in DMPC/DMPA (9:1) with a lipid-to-protein ratio of 75:1. The NCO and NCA spectra were recorded at 600 MHz (270 K, 10 kHz MAS) and 850 MHz (270 K, 14 kHz MAS), respectively.

5.2.2 MsbA apo state spectra

Two labelled samples were then prepared namely [^{13}C,^{15}N-F]-MsbA for F115-F116 in CH1 and [^{13}C-H,^{15}N-K]-MsbA for H214-K215 in CH2. The ^{13}C(i-1)-^{15}N(i) correlation of the unique pairs can then be visualized in NCO spectra as shown for apo state MsbA (**figure 5.3A, left**). While only one cross peak occurs for the [^{13}C,^{15}N-F]-MsbA sample, two signals can be detected for [^{13}C-H,^{15}N-K]-MsbA corresponding to both His-Lys pairs H214-K215 and H576-K577. The H214-K215 peak can be unambiguously identified based on the known ^{15}N chemical shift of K215 from another ssNMR study on MsbA in which some of the lysines in MsbA have been assigned[22]. We, therefore, decided to use this data by preparing a third sample, [^{13}C,^{15}N-K]-MsbA, based on which NCA spectra can be recorded to complement the NCO spectra for CH1 and CH2. An NCA spectrum of apo state [^{13}C,^{15}N-K]-MsbA (**figure 5.3A, middle**) shows a number of resolved intra-residue lysine cross peaks including K118 in CH1 and K215 in CH2 (**figure 5.3A, right, insets i+ii**). In the apo state, the signals of K118 and K215 overlap with K465 and with an unassigned lysine (X), respectively. K465 is located prior to the X-loop. Other resolved and assigned residues are K328 (prior to A loop), K365 (between A loop and Walker A motif) and K382 (within Walker A motif). Residues K58, K332, and K370 have been assigned to one overlapping, unresolved cross peak. The location of the assigned lysines is illustrated in **figure 3.2**. The NCA spectrum of [^{13}C,^{15}N-K]-MsbA can serve as a ‘fingerprint’ for the nucleotide-free, inward-facing (IF) apo state of MsbA.

5.2.3 Effects of substrate and nucleotide binding

Subsequently, the effect of nucleotide binding on CH1 and CH2 was probed (**figure 5.3B**). Here, the apo state is compared with the ATP hydrolysis transition state, which is emulated by trapping MsbA with ADP•Vi resulting in a switch from an inward (IF) to an outward-facing (OF) conformation. As a result, the CH1 F115-F116 NCO cross peak shifts, while the CH2 NCO correlation of H214-K215 is not much affected (**figure 5.3B, left**). The NCA spectrum of [^{13}C-H,^{15}N-K]-MsbA (**figure 5.3B, middle**) shows many more changes including shifts of the K118 (CH1) and K215 (CH2) cross-peaks (**figure 5.3B, right**). All three spectra reveal substantial chemical shift increases (> 0.5 ppm) for F115 (C’), F116 (N), K118 (N, Ca) in CH1 and K215 (Ca) in CH2 upon trapping (**table 5.1**). In addition, the NCO peak of the H576-K577 pair in the NBD shifts (+1.2 ppm for H576-C’). It is noteworthy that the linewidth of the NCA cross peaks of [^{13}C,^{15}N-K]-MsbA is substantially reduced in the ADP•Vi state (**appendix Slices of 2D spectra**).

The effect of substrate binding was probed by the addition of H33342 to the apo sample. In CH1, the F115 nitrogen signal shifts by 1.6 ppm. Even larger changes are observed in CH2 for C' of H214 and N of K215, which shift by -1.8 and +8.0 ppm, respectively (**figure 5.3C, left**). In contrast to this observation, the "K215+X" NCA cross peak in the spectrum of [^{13}C,^{15}N-K]-MsbA does not seem to change (**figure 5.3C, right**). The reason is that in the apo state spectrum, K215 and one other Lys residue (X) overlap and contribute to this NCA signal intensity. If only K215 responds to substrate binding but not residue X, then an NCA cross peak will remain at this position. The new K215 NCA cross peak cannot be unambiguously identified but upon inspecting the full NCA spectrum, signal intensity matching the ^{15}N chemical shift of K215 as observed in the NCO spectrum can be found (**figure 5.3C, middle, "K215*"**).

Spectral changes are also observed for lysines in the NBDs, especially for K328 (close to the A-loop) and K365 (between A loop and Walker A motif), which could indicate that substrate binding prepares the protein for ATP uptake. One can speculate that the other observed changes arise from unassigned lysine in the TMD, which could be also influenced by substrate binding.

We then tested how ADP•Vi trapping affects the spectra of Hoechst 33342-bound MsbA. All substrate-affected peaks seem to shift towards their positions in a pure ADP•Vi trapped state, which is also illustrated in the overlap of all three states (figure 5.3E). Only small changes can be detected between ADP•Vi and ADP•Vi +Hoechst 33342, which are all below 0.5 ppm (figure 5.3D). ADP•Vi trapping in addition to Hoechst 33342 substrate binding seems to set the MsbA protein to an OF state (figure 5.3E).

5.3 Discussion

A fundamental question in understanding the functional mechanism of ABC transporters is the interplay between TMDs and NBDs. There are accumulating hints that the coupling helices mediate this crosstalk[1-9,13], but so far, the available 3D structures have not provided unambiguous evidence of a structural response during the transport cycle. Here, we tried to address this question in a highly specific way by creating isotope-labelled C(i)-(N+1) pairs within both helices so that chemical shift changes can be detected. Although the whole sequence of CH1 and CH2 cannot be probed in this way, the specific reporter sites provide a very sensitive readout for induced conformational changes during the transport cycle.

5.3.1 The effect of nucleotide binding

We first observed the response of CH1 and CH2 was probed towards nucleotide binding, which induces the transition from an IF- (apo) to an OF-state. The latter was created by trapping the catalytic transition state with ADP.Vi. This conformational switching is reflected by a number of spectral changes in the Lys-NCA spectrum of [^{13}C, ^{15}N-K]-MsbA (figure 5.3A-B), which involves mainly residues within the NBD (figure 5.1C) and reflects NBD dimerization and nucleotide binding. The observed narrowing of the NCA cross peaks shows that MsbA becomes less flexible upon ADP•Vi trapping. This finding is consistent with HDX studies on MsbA and other ABC exporters[39-41,62] and also agrees with EPR DEER experiments that showed a narrowing of the broad apo state distance distributions [19,34,63].

Both unique pairs within the coupling helices show backbone chemical shift changes, which are larger in CH1 (F115/F116) compared to CH2 (H214/K215) (table 5.1). Chemical shifts of nuclei in the protein backbone mainly reflect the local secondary structure, suggesting that greater structural changes occur within CH1 compared with CH2 during the transition from the IF to the OF state or at least nucleotide binding. Interestingly, ATPase assays (figure 4.7) show a much stronger reduction for H214A and K215A mutants compared to F115A and F116A, which also agrees with published data.[9,36] One might therefore expect a stronger response in CH2, especially when considering its domain-swapped interaction with the opposing NBD, which makes it sensitive to the IF→OF transition. On the other hand, CH2 is located on the surface in between RecA-like and a-helical subdomains, while CH1 lies on top of a groove of the RecA-like domain near the bound nucleotide (figure 5.1B and 5.2B). In the outward-facing state, the NBDs dimerize and CH1 also comes in contact with the surface of the opposite NBD. This could make CH1 more responsive to nucleotide binding and the IF→OF conversion.

Furthermore, the proposed 'ball and socket joint' model [42] does not require secondary structure changes but just rigid body movements of CH2 and alterations in sidechain interactions would not necessarily involve large backbone chemical shift changes. Interestingly, the sidechain of F116 in CH1 of MsbA chain A is oriented towards H214 in CH2 of chain B (figure 5.1B) and it has been suggested that they mediate cross-talk between both coupling helices.[9] They could interact via π-stacking interactions so that both respond to nucleotide binding in a cooperative way, which is compatible with our observation that F116 in CH1 shows large chemical shift changes but mutations in H214 in CH2 have a large impact on the ATPase activity. Both residues are highly conserved in MsbA and F116 is also fully conserved amongst other ABC exporters (figure 5.2A). Additional solid-state NMR experiments will be needed in the future to fully describe the interaction between both residues during the ATPase and transport cycle.

5.3.2 The effect of substrate binding

For MsbA, it was shown that residues along TM6 are important for binding substrates such as Hoechst 33342[44,47,64] and that transmembrane helices, in particular TM3 and TM4 which connect to CH1 and CH2 (**figure 5.1A**), mediate conformational changes between NBD and TMD[53]. Here, upon binding of the MsbA substrate Hoechst 33342, clear chemical shift changes occur in both reporter regions in both coupling helices but the effect for CH2 is especially pronounced with an 8 ppm change for K215-N (**figure 5.3C, table 5.1**). Such a large change of backbone chemical shifts is most likely caused by alterations in the local secondary structure and hydrogen bond formations around K215 in CH2, which will also affect the above-mentioned interaction with F116 in CH1. Our biochemical data show that mutations in CH1 abolish the ability to stimulate the ATPase activity of MsbA by Hoechst 33342, which underlines that both coupling helices play an important role in substrate-induced TMD-NBD cross talk. However, the larger effect on the domain-swapped CH2 indicates that substrate binding induces conformational changes at the TMD-NBD interface, which prepares the protein for ATP binding and subsequent hydrolysis. So far, no nucleotide-free MsbA structure with a bound small molecule ligand (except for inhibitors) has been reported and the LPS-bound forms of MsbA provide no clear conclusion about structural changes within the CHs. However, immobilization of CH1 and CH2 in the peptide exporter TAP1/TAP2 by crosslinking revealed a direct coupling between TMD-NBD crosstalk and substrate binding and translocation[7]. Recent computational studies on P-glycoprotein also suggested a substrate-induced displacement of CH2 which leads to NBD reorientation and pre-dimerization[65].

Beyond the reporter sites in CH1 and CH2, substrate binding also induces some changes in the Lys-NCA spectrum of [^{13}C, ^{15}N-K]-MsbA. Some of the peaks shift and the peak intensities change. The cross peaks of lysines in the NBD region adjacent to the A-loop (K328 and K332), Walker A motif (K365 and K370), X-loop (K465), and His-switch (K528 and K544) are affected. These regions normally interact with ATP, suggesting that MsbA is preparing for ATP uptake after substrate binding. But overall, this fingerprint spectrum is not identical to but appears more similar to the IF- (apo) rather than to the OF- (ADP.Vi) state. This observation is compatible with previous suggestions of the formation of a substrate-induced pre-translocation intermediate state[66], which represents the transition from the IF to the OF state.

Table 5.1: Chemical shift changes

Coupling Helix	**Nuclei**	**δ(ADP.Vi) -δ(apo)** [ppm]	**δ(H33342)- δ(apo)** [ppm]	**δ(H33342+ADP.Vi) -δ(ADP.Vi)** [ppm]	**NMR spectra and samples**
CH1	**F115- C'**	+0.55	+0.05	-0.3	NCO, [^{13}C,^{15}N-F]-MsbA
	F116-N	+1.65	+1.6	-0.04	NCO, [^{13}C,^{15}N-F]-MsbA
	K118-N	+0.83	+0.09	-0.02	NCA, [^{13}C,^{15}N-K]-MsbA
	K118-Ca	+0.6	+0.12	-0.04	NCA, [^{13}C,^{15}N-K]-MsbA
CH2	**H214-C'**	+0.08	-1.81	0.35	NCO, [^{13}C-H,^{15}N-K]-MsbA
	K215-N	+0.3	8.01	-0.23	NCO, [^{13}C-H,^{15}N-K]-MsbA
	K215X-N	+0.1	0.38	-0.2	NCA, [^{13}C,^{15}N-K]-MsbA
	K215X-Ca	+0.8	0.11	-0.3	NCA, [^{13}C,^{15}N-K]-MsbA

When substrate-bound MsbA is subjected to ADP.Vi trapping, all spectral features change again. The spectra of the coupling helix reporters as well as the NCA Lys-fingerprint spectrum approach the spectral signature obtained for the OF- (ADP.Vi) state. This means that MsbA switches into an OF-state and the substrate-induced changes within CH1 and especially CH2 are reverted. However, spectra are not identical to the pure ADP.Vi state, which has also been reported in previous solid-state NMR studies in the effect of substrate binding to TM6[47]. Small spectral changes could also be caused by the non-specific substrate binding or accumulation of Hoechst 33342 within the lipid bilayer.

5.3.3 Chemical shift predictions from known 3D structures

For an assessment of our findings in the context of known 3D structures, we used the software ShiftX2[67] to predict the chemical shifts of our unique pair labels in CH1 and CH2. We selected the wide-open IF state of MsbA (PDB: 8DMO [21]), the IF conformation (PDB: 5TV4 [20]), the OF state (PDB: 8DMM [21]) and the occluded state (7BCW [35]) as shown in figure 5.2B. The predicted cross peaks deviate substantially from our experimental observations (figure 5.4). Structural asymmetry leads to the prediction of peak doublets for CH1 in all states and for CH2 in two cases, which are however not observed experimentally in our proteoliposome preparations. We therefore exclude structural asymmetry for CH1 and CH2. Reasons for the deviation between our experimental observation and the structure-based predictions could be limitations in structural resolution and prediction accuracy, crystal packing effects and the different experimental conditions used for each structure, especially with respect to the membrane mimic and there is no Hoechst 33342 bound structure far.

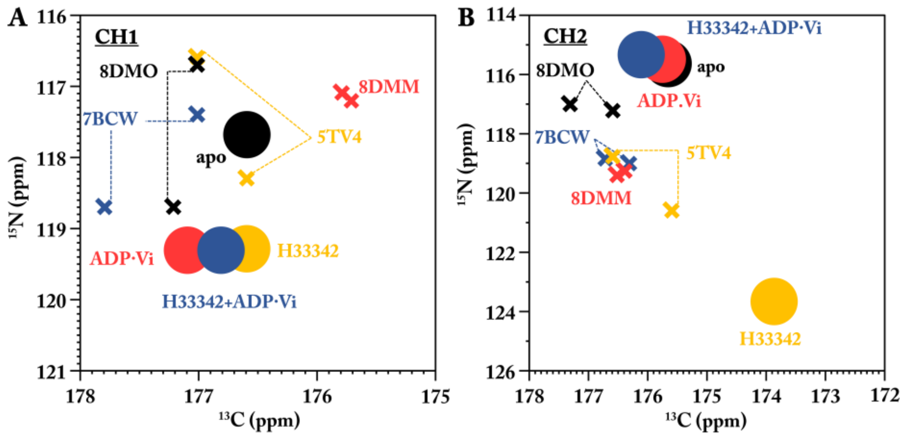

Figure 5.4: Chemical shift prediction for CH1 and CH2 from selected 3D structures. (A) Comparison between experimental chemical shifts for the F115-F116 unique pair in CH1 (circles) and predicted NCO cross peaks obtained by ShiftX2[67] (pH 7.5, 270 K) from the wide-open inward-facing state of MsbA (PDB: 8DMO [21]), the inward-facing conformation (PDB: 5TV4 [20]), in the outward-facing state (PDB: 8DMM [21]) and the occluded state (7BCW [35]). In the case of structural asymmetry, two cross-peaks are predicted connected by dotted lines. **(B)** As in (A) but for the H214-K215 unique pair in CH2.

5.3.4 Conclusions

The study presented here provides direct evidence for structural changes within the coupling helices of type IV ABC transporters during the transition from the IF to the OF state and during substrate and inhibitor binding. Our findings are summarized in figure 5.5. The data show that ADP.Vi binding and the IF→OF transition causes at the NBD-TMD interface a stronger response in CH1 while substrate binding has a stronger effect in CH2. It is noteworthy that the latter is based on a domain-swapped interaction with the NBD. Both cases are caused by stimuli with different vectoriality, namely nucleotide binding to the NBD and substrate binding to the TMD, which might then involve different pathways for NBD→TMD and TMD→NBD crosstalk. The observed spectral signatures are different compared to the substrate-bound state, which indicates a different interaction pathway. Our study provides selective data, which is highly complementary to the available 3D structures. Future solid-state NMR experiments will address the potential interaction between CH1 and CH2 and connect NMR data and 3D structures via computational approaches.

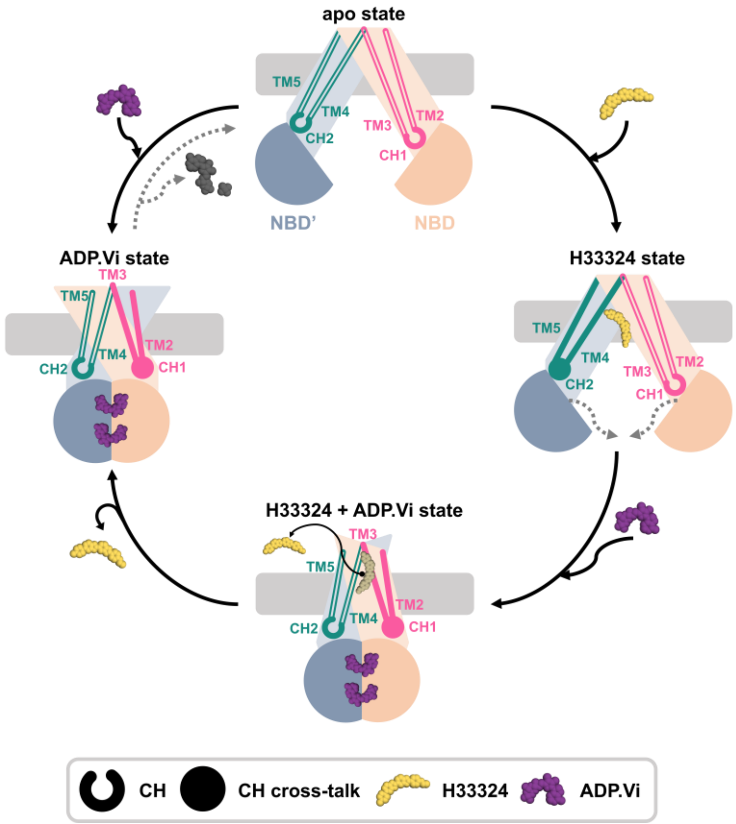

Figure 5.5. The response of CH1 and CH2 upon nucleotide and substrate binding. In the apo state, CH1 is solely interacting with the NBD of its own chain and CH2 with the other NBD'. Upon binding of Hoechst 33342, MsbA moves to an occluded conformation, and a large chemical shift change is observed within the domain-swapped CH2 (Hoechst 33342 state). It triggers conformational changes within the NBD which supports nucleotide binding. Trapping MsbA in an ATP hydrolysis transition state by ADP•Vi (ADP•Vi state), a conformational change from the inward- to the outward-facing conformation occurs. Here, a chemical shift change in CH1 is observed. ADP•Vi trapping of the Hoechst 33342 state converges towards the ADP•Vi state.

References

1 George, A. M. *ABC Transporters—40 Years on.* (Springer International Publishing AG, 2016).

2 Bukowska, M. A. *et al.* A Transporter Motor Taken Apart: Flexibility in the Nucleotide Binding Domains of a Heterodimeric ABC Exporter. *Biochemistry* **54**, 3086-3099, doi:10.1021/acs.biochem.5b00188 (2015).

3 Crow, A., Greene, N. P., Kaplan, E. & Koronakis, V. Structure and mechanotransmission mechanism of the MacB ABC transporter superfamily. *Proc Natl Acad Sci U S A* **114**, 12572-12577, doi:10.1073/pnas.1712153114 (2017).

4 Dawson, J. E., Farber, P. J. & Forman-Kay, J. D. Allosteric coupling between the intracellular coupling helix 4 and regulatory sites of the first nucleotide-binding domain of CFTR. *PLoS One* **8**, e74347, doi:10.1371/journal.pone.0074347 (2013).

5 He, L. *et al.* Multiple membrane-cytoplasmic domain contacts in the cystic fibrosis transmembrane conductance regulator (CFTR) mediate regulation of channel gating. *J Biol Chem* **283**, 26383-26390, doi:10.1074/jbc.M803894200 (2008).

6 Khunweeraphong, N., Stockner, T. & Kuchler, K. The structure of the human ABC transporter ABCG2 reveals a novel mechanism for drug extrusion. *Sci Rep* **7**, 13767, doi:10.1038/s41598-017-11794-w (2017).

7 Oancea, G. *et al.* Structural arrangement of the transmission interface in the antigen ABC transport complex TAP. *Proc Natl Acad Sci U S A* **106**, 5551-5556, doi:10.1073/pnas.0811260106 (2009).

8 Shah, A. H. *et al.* Mutational Analysis of Intracellular Loops Identify Cross Talk with Nucleotide Binding Domains of Yeast ABC Transporter Cdr1p. *Sci Rep* **5**, 11211, doi:10.1038/srep11211 (2015).

9 Furuta, T., Yamaguchi, T., Kato, H. & Sakurai, M. Analysis of the structural and functional roles of coupling helices in the ATP-binding cassette transporter MsbA through enzyme assays and molecular dynamics simulations. *Biochemistry* **53**, 4261-4272, doi:10.1021/bi500255j (2014).

10 Priess, M. & Schafer, L. V. Release of Entropic Spring Reveals Conformational Coupling Mechanism in the ABC Transporter BtuCD-F. *Biophys J* **110**, 2407-2418, doi:10.1016/j.bpj.2016.04.027 (2016).

11 Wen, P. C. & Tajkhorshid, E. Conformational coupling of the nucleotide-binding and the transmembrane domains in ABC transporters. *Biophys J* **101**, 680-690, doi:10.1016/j.bpj.2011.06.031 (2011).

12 George, A. M. *ABC Transporters - 40 Years on.* (Springer International Publishing AG, 2016).

13 Dawson, R. J. & Locher, K. P. Structure of a bacterial multidrug ABC transporter. *Nature* **443**, 180-185, doi:10.1038/nature05155 (2006).

14 Seeger, M. A. & van Veen, H. W. Molecular basis of multidrug transport by ABC transporters. *Biochim Biophys Acta* **1794**, 725-737, doi:10.1016/j.bbapap.2008.12.004 (2009).

15 Gyimesi, G. *et al.* ATP hydrolysis at one of the two sites in ABC transporters initiates transport related conformational transitions. *Biochim Biophys Acta* **1808**, 2954-2964, doi:10.1016/j.bbamem.2011.07.038 (2011).

16 DeGorter, M. K., Conseil, G., Deeley, R. G., Campbell, R. L. & Cole, S. P. Molecular modeling of the human multidrug resistance protein 1 (MRP1/ABCC1). *Biochem Biophys Res Commun* **365**, 29-34, doi:10.1016/j.bbrc.2007.10.141 (2008).

17 Xie, X. L. *et al.* Allosteric transitions of ATP-binding cassette transporter MsbA studied by the adaptive anisotropic network model. *Proteins* **83**, 1643-1653, doi:10.1002/prot.24850 (2015).

18 Moradi, M. & Tajkhorshid, E. Mechanistic picture for conformational transition of a membrane transporter at atomic resolution. *Proc Natl Acad Sci U S A* **110**, 18916-18921 (2013).

19 Zou, P. & McHaourab, H. S. Alternating access of the putative substrate-binding chamber in the ABC transporter MsbA. *J Mol Biol* **393**, 574-585, doi:10.1016/j.jmb.2009.08.051 (2009).

20 Mi, W. *et al.* Structural basis of MsbA-mediated lipopolysaccharide transport. *Nature* **549**, 233-237, doi:10.1038/nature23649 (2017).

21 Lyu, J. *et al.* Structural basis for lipid and copper regulation of the ABC transporter MsbA. *Nat Commun* **13**, 7291, doi:10.1038/s41467-022-34905-2 (2022).

22 Lakatos-Karoly, A. *et al.* Probing conformational changes in MsbA by selective chemical shift perturbations. *in preparation* (2023).

23 Choudhury, H. G. *et al.* Structure of an antibacterial peptide ATP-binding cassette transporter in a novel outward occluded state. *Proc Natl Acad Sci U S A* **111**, 9145-9150, doi:10.1073/pnas.1320506111 (2014).

24 Kluth, M. *et al.* A mutation within the extended X loop abolished substrate-induced ATPase activity of the human liver ATP-binding cassette (ABC) transporter MDR3. *J Biol Chem* **290**, 4896-4907, doi:10.1074/jbc.M114.588566 (2015).

25 Dawson, R. J. & Locher, K. P. Structure of the multidrug ABC transporter Sav1866 from Staphylococcus aureus in complex with AMP-PNP. *FEBS Lett* **581**, 935-938, doi:10.1016/j.febslet.2007.01.073 (2007).

26 Weng, J. W., Fan, K. N. & Wang, W. N. The conformational transition pathway of ATP binding cassette transporter MsbA revealed by atomistic simulations. *J Biol Chem* **285**, 3053-3063, doi:10.1074/jbc.M109.056432 (2010).

27 King, G. & Sharom, F. J. Proteins that bind and move lipids: MsbA and NPC1. *Crit Rev Biochem Mol Biol* **47**, 75-95, doi:10.3109/10409238.2011.636505 (2012).

28 Furukawa-Hagiya, T., Furuta, T., Chiba, S., Sohma, Y. & Sakurai, M. The power stroke driven by ATP binding in CFTR as studied by molecular dynamics simulations. *J Phys Chem B* **117**, 83-93, doi:10.1021/jp308315w (2013).

29 Padayatti, P. S. *et al.* Structural Insights into the Lipid A Transport Pathway in MsbA. *Structure* **27**, 1114-1123 e1113, doi:10.1016/j.str.2019.04.007 (2019).

30 Ward, A., Reyes, C. L., Yu, J., Roth, C. B. & Chang, G. Flexibility in the ABC transporter MsbA: Alternating access with a twist. *Proc Natl Acad Sci U S A* **104**, 19005-19010, doi:10.1073/pnas.0709388104 (2007).

31 Thelot, F. A. *et al.* Distinct allosteric mechanisms of first-generation MsbA inhibitors. *Science* **374**, 580-585, doi:10.1126/science.abi9009 (2021).

32 Angiulli, G. *et al.* New approach for membrane protein reconstitution into peptidiscs and basis for their adaptability to different proteins. *Elife* **9**, doi:10.7554/eLife.53530 (2020).

33 Ho, H. *et al.* Structural basis for dual-mode inhibition of the ABC transporter MsbA. *Nature* **557**, 196-201, doi:10.1038/s41586-018-0083-5 (2018).

34 Galazzo, L. *et al.* The ABC transporter MsbA adopts the wide inward-open conformation in E. coli cells. *Sci Adv* **8**, eabn6845, doi:10.1126/sciadv.abn6845 (2022).

35 Kehlenbeck, D. M. *et al.* Cryo-EM structure of MsbA in saposin-lipid nanoparticles (Salipro) provides insights into nucleotide coordination. *FEBS J* **289**, 2959-2970, doi:10.1111/febs.16327 (2022).

36 Zou, P. & McHaourab, H. S. Alternating Access of the Putative Substrate-Binding Chamber in the ABC Transporter MsbA. *Journal of Molecular Biology* **393**, 574-585, doi:10.1016/j.jmb.2009.08.051 (2009).

37 Loo, T. W., Bartlett, M. C. & Clarke, D. M. Human P-glycoprotein contains a greasy ball-and-socket joint at the second transmission interface. *J Biol Chem* **288**, 20326-20333, doi:10.1074/jbc.M113.484550 (2013).

38 Guggino, W. B. & Stanton, B. A. New insights into cystic fibrosis: molecular switches that regulate CFTR. *Nat Rev Mol Cell Biol* **7**, 426-436, doi:10.1038/nrm1949 (2006).

39 Kopcho, N., Chang, G. & Komives, E. A. Dynamics of ABC Transporter P-glycoprotein in Three Conformational States. *Sci Rep* **9**, 15092, doi:10.1038/s41598-019-50578-2 (2019).

40 Clouser, A. F. & Atkins, W. M. Long Range Communication between the Drug-Binding Sites and Nucleotide Binding Domains of the Efflux Transporter ABCB1. *Biochemistry* **61**, 730-740, doi:10.1021/acs.biochem.2c00056 (2022).

41 Mehmood, S., Domene, C., Forest, E. & Jault, J. M. Dynamics of a bacterial multidrug ABC transporter in the inward- and outward-facing conformations. *Proc Natl Acad Sci U S A* **109**, 10832-10836, doi:10.1073/pnas.1204067109 (2012).

42 Jin, M. S., Oldham, M. L., Zhang, Q. & Chen, J. Crystal structure of the multidrug transporter P-glycoprotein from Caenorhabditis elegans. *Nature* **490**, 566-569, doi:10.1038/nature11448 (2012).

43 Siarheyeva, A. & Sharom, F. J. The ABC transporter MsbA interacts with lipid A and amphipathic drugs at different sites. *Biochem J* **419**, 317-328, doi:10.1042/BJ20081364 (2009).

44 Woebking, B. *et al.* Functional role of transmembrane helix 6 in drug binding and transport by the ABC transporter MsbA. *Biochemistry* **47**, 10904-10914, doi:10.1021/bi800778d (2008).

45 Kaur, H. *et al.* Unexplored Nucleotide Binding Modes for the ABC Exporter MsbA. *J Am Chem Soc* **140**, 14112-14125, doi:10.1021/jacs.8b06739 (2018).

46 Kaur, H. *et al.* Coupled ATPase-adenylate kinase activity in ABC transporters. *Nat Commun* **7**, 13864, doi:10.1038/ncomms13864 (2016).

47 Spadaccini, R., Kaur, H., Becker-Baldus, J. & Glaubitz, C. The effect of drug binding on specific sites in transmembrane helices 4 and 6 of the ABC exporter MsbA studied by DNP-enhanced solid-state NMR. *Biochim Biophys Acta Biomembr* **1860**, 833-840, doi:10.1016/j.bbamem.2017.10.017 (2018).

48 Lacabanne, D. *et al.* Solid-State NMR Reveals Asymmetric ATP Hydrolysis in the Multidrug ABC Transporter BmrA. *Journal of the American Chemical Society* **144**, 12431-12442, doi:10.1021/jacs.2c04287 (2022).

49 Lacabanne, D. *et al.* Flexible-to-rigid transition is central for substrate transport in the ABC transporter BmrA from Bacillus subtilis. *Commun Biol* **2**, 149, doi:10.1038/s42003-019-0390-x (2019).

50 Lacabanne, D. *et al.* Solid-State NMR Reveals Asymmetric ATP Hydrolysis in the Multidrug ABC Transporter BmrA. *J Am Chem Soc* **144**, 12431-12442, doi:10.1021/jacs.2c04287 (2022).

51 Woebking, B. *et al.* Drug-lipid A interactions on the Escherichia coli ABC transporter MsbA. *J Bacteriol* **187**, 6363-6369, doi:10.1128/JB.187.18.6363-6369.2005 (2005).

52 Reuter, G. *et al.* The ATP binding cassette multidrug transporter LmrA and lipid transporter MsbA have overlapping substrate specificities. *J Biol Chem* **278**, 35193-35198, doi:10.1074/jbc.M306226200 (2003).

53 Doshi, R. *et al.* Molecular disruption of the power stroke in the ATP-binding cassette transport protein MsbA. *J Biol Chem* **288**, 6801-6813, doi:10.1074/jbc.M112.430074 (2013).

54 Eckford, P. D. & Sharom, F. J. Functional characterization of Escherichia coli MsbA: interaction with nucleotides and substrates. *J Biol Chem* **283**, 12840-12850, doi:10.1074/jbc.M708274200 (2008).

55 Velamakanni, S., Yao, Y., Gutmann, D. A. & van Veen, H. W. Multidrug transport by the ABC transporter Sav1866 from Staphylococcus aureus. *Biochemistry* **47**, 9300-9308, doi:10.1021/bi8006737 (2008).

56 Cherukuri, P. K., Songkiatisak, P., Ding, F., Jault, J. M. & Xu, X. N. Antibiotic Drug Nanocarriers for Probing of Multidrug ABC Membrane Transporter of Bacillus subtilis. *ACS Omega* **5**, 1625-1633, doi:10.1021/acsomega.9b03698 (2020).

57 Steinfels, E. *et al.* Characterization of YvcC (BmrA), a multidrug ABC transporter constitutively expressed in Bacillus subtilis. *Biochemistry* **43**, 7491-7502, doi:10.1021/bi0362018 (2004).

58 Oepen, K., Mater, V. & Schneider, D. Unfolding Individual Domains of BmrA, a Bacterial ABC Transporter Involved in Multidrug Resistance. *Int J Mol Sci* **24**, doi:10.3390/ijms24065239 (2023).

59 Orelle, C., Dalmas, O., Gros, P., Di Pietro, A. & Jault, J. M. The conserved glutamate residue adjacent to the Walker-B motif is the catalytic base for ATP hydrolysis in the ATP-binding cassette transporter BmrA. *J Biol Chem* **278**, 47002-47008, doi:10.1074/jbc.M308268200 (2003).

60 Oepen, K. *et al.* Myristic Acid Inhibits the Activity of the Bacterial ABC Transporter BmrA. *Int J Mol Sci* **22**, doi:10.3390/ijms222413565 (2021).

61 Lacabanne, D., Meier, B. H. & Bockmann, A. Selective labeling and unlabeling strategies in protein solid-state NMR spectroscopy. *J Biomol NMR* **71**, 141-150, doi:10.1007/s10858-017-0156-z (2018).

62 Javed, W. *et al.* Structural Insights into the Catalytic Cycle of a Bacterial Multidrug ABC Efflux Pump. *J Mol Biol* **434**, 167541, doi:10.1016/j.jmb.2022.167541 (2022).

63 Zou, P., Bortolus, M. & McHaourab, H. S. Conformational cycle of the ABC transporter MsbA in liposomes: detailed analysis using double electron-electron resonance spectroscopy. *J Mol Biol* **393**, 586-597, doi:10.1016/j.jmb.2009.08.050 (2009).

64 Smriti, Zou, P. & McHaourab, H. S. Mapping Daunorubicin-binding Sites in the ATP-binding Cassette Transporter MsbA Using Site-specific Quenching by Spin Labels. *Journal of Biological Chemistry* **284**, 13904-13913, doi:10.1074/jbc.M900837200 (2009).

65 Xing, J., Huang, S., Heng, Y., Mei, H. & Pan, X. Computational Insights into Allosteric Conformational Modulation of P-Glycoprotein by Substrate and Inhibitor Binding. *Molecules* **25**, doi:10.3390/molecules25246006 (2020).

66 Doshi, R. & van Veen, H. W. Substrate binding stabilizes a pre-translocation intermediate in the ATP-binding cassette transport protein MsbA. *J Biol Chem* **288**, 21638-21647, doi:10.1074/jbc.M113.485714 (2013).

67 Han, B., Liu, Y., Ginzinger, S. W. & Wishart, D. S. SHIFTX2: significantly improved protein chemical shift prediction. *J Biomol NMR* **50**, 43-57, doi:10.1007/s10858-011-9478-4 (2011).

Chapter 6

Inhibiting MsbA

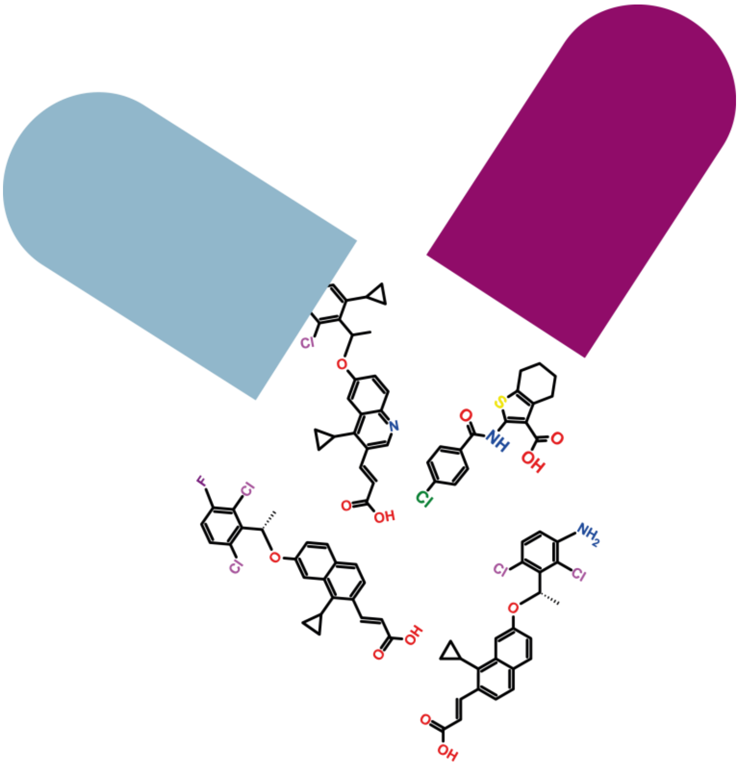

> “Simplicity is about subtracting the obvious and adding the meaningful.”
>
> – *John Maeda*

This chapter contains data from Novischi et al. Commun. Biol. 2023 (accepted).

6.1 MsbA is a potential target for a novel class of antibiotics

The bacterial ABC transporter MsbA is found in some of the ESKAPE pathogens strains (Enterococcus faecium, Staphylococcus aureus, Klebsiella pneumoniae, Acinetobacter baumannii, Pseudomonas aeruginosa, and Enterobacter species) [1,2]. The ESKAPE strains contribute to over 40% of the infections in the intensive care unit[3,4]. Thus, it has been estimated to surpass the mortality rates of cancer in the future[5-9]. Four out of six ESKAPE strains are Gram-negative bacteria. The outer membrane of Gram-negative bacteria consists of lipopolysaccharide (LPS) which makes the bacteria inherently resistant to environmental changes. The LPS prevents the permeability of many antibiotics in Gram-negative bacteria, consequently leading to antibiotic resistance[10]. MsbA is therefore a potential target for new antibiotics.

MsbA plays a critical role in the regulation of the bacterial outer membrane by flopping core LPS across the inner membrane in Gram-negative bacteria. Depletion of MsbA or loss of MsbA function results in the accumulation of LPS and phospholipids in the inner membrane of *E. coli* bacteria[11-14]. Additionally, this floppase acts as an efflux pump by translocating drugs through the inner membrane, hence making it an interesting drug target[15,16]. Recently, two different classes of MsbA inhibitors have been reported: Tetrahydrobenzothiophene (TBT)-based inhibitors block the LPS-binding site and thus transport, resulting in an inward-facing (IF) conformation[17], whereas quinoline derivatives inhibit LPS translocation by inducing an outward-facing (OF) state that prevents NBD dimerization and thus ATP hydrolysis[18].

The bacterial homologue MsbA is an excellent candidate to study the structural importance of the ABC protein family. Its export of amphiphilic substrates across the membrane in Gram-negative bacteria is mediated by ATP-hydrolysis and thereby coupled to a catalytic cycle in the NBDs. This 64.5 kDa homodimer is a homologue of the human multidrug-resistant protein 1 (MDR1) or P-glycoprotein and has been used as a model to study the human P-glycoprotein[19-21]. Moreover, the 3D structural determination of MsbA has revealed various interesting states of the floppase by X-ray and cryo-EM[1,17,22-24]. This part of the dissertation is focused on interactions of MsbA with G907 (**figure 6.1**), in particular, the role of the coupling helices to further understand the crosstalk of MsbA during ATP hydrolysis and substrate translocation.

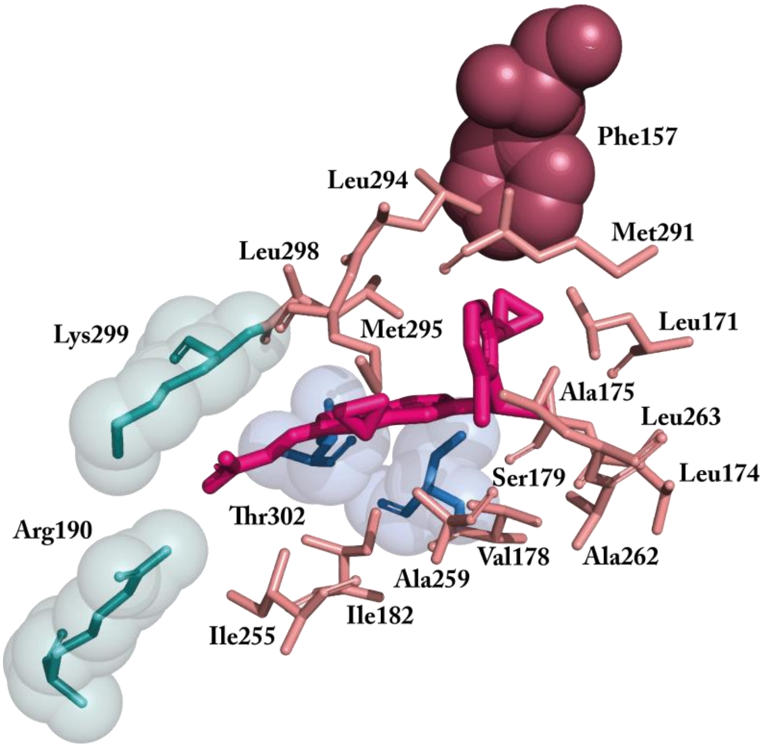

Figure 6.1. Interactions of G907 with MsbA. TM4 (L171, A175, V178), TM5 (A259 and L263), and TM6 (M291 and L294) make van der Waals interactions with G907. R190 in TM5 forms a salt bridge with G907. The olefin linker is surrounded by I182, I255, and K299, in TM4, TM5, and TM6 respectively[18]. pdb code: 6BPL

6.2 Results

Quinolone-based inhibitors bind to MsbA and have been shown to suppress ATP hydrolysis and significantly affect cell growth[18]. We have reproduced the effect of one of these inhibitors (*given by Genentech*), G907, based on cell growth assays using our *E. coli* MsbA expression strain. Initial biochemical data demonstrated that the G compounds can enter the bacterial cell wall and reduce cell growth (**figure 6.2**). The cell growth rate was reduced similarly as the inhibitor concentrations were adjusted to the minimum inhibitory concentration (MIC). The cell growth is significantly inhibited upon the addition of the G-compounds. The same effect was observed in the control ΔacrAB cells, which indicated that cell growth reduction is a result of MsbA inhibition. A previous study with hyperpermeable outer membrane mutation showed similar results of MsbA on-target cell inhibition of the quinoline-based compounds[25].

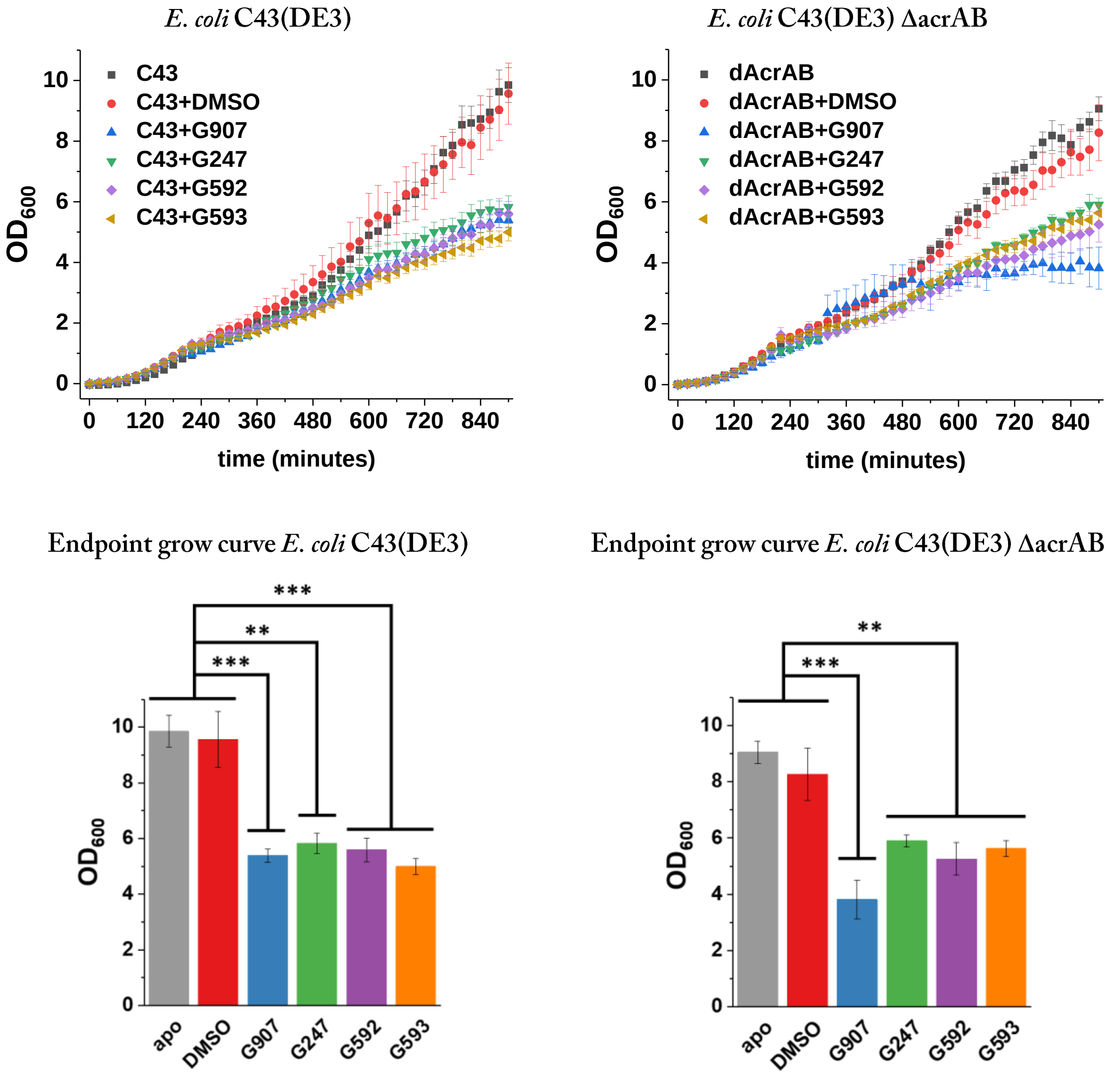

E. coli C43(DE3)

E. coli C43(DE3) ΔacrAB

Endpoint grow curve *E. coli* C43(DE3)

Endpoint grow curve *E. coli* C43(DE3) ΔacrAB

Figure 6.2. Cell growth assay of G-compounds in *E. coli* C43(DE3) and *E. coli* C43(DE3) ΔacrAB cells. After steady growth of 240 minutes, the G-compounds in DMSO (6 *μg/mL G907 and G247, 20 μg/mL G592, 40 μg/mL G593*) were added to the cells (minimum inhibitory concentration (MIC) literature values[18,25]). The growth was followed for the remaining 720 minutes. **p<0.05, **p<0.01, ***p<0.001* (ANOVA, Bonferroni test); n=5 of distinct samples with mean±SEM. *The inhibitors were given by Genentech (appendix Declarations).*

Previous studies have shown that these inhibitors prevent MsbA from going into the outward-facing state by keeping the NBDs separated[18]. However, their binding site is located within the transmembrane domain raising questions about how the TMD-NBD crosstalk mediated by CH1 and CH2 is affected. To address this question, we utilized the MsbA labelling schemes and the experimental outline described in **Chapter** 5. To find the best experimental conditions, the ATPase activity of MsbA in DMPC/DMPA liposomes was probed upon titration of G907. In these liposomes, a surprisingly high stoichiometry of 1:300 was needed to achieve a substantial ATPase reduction (**figure 6.3**). Since the binding pocket is within the TMD and accessible from the membrane phase, the reasons could be reduced accessibility and/or reduced G907 membrane penetration in these lipids. The selection of DMPC/DMPA as lipids for reconstitution was primarily driven by previously published studies in which it was shown that MsbA preparations are stable, active and provide well-resolved NMR spectra[26-29]. However, it was also shown that the G907 inhibitor affinity was affected by the detergent and lipid environment of MsbA[18]. We therefore reconstituted MsbA into POPE/POPG, which are the main components of the inner *E. coli* membrane and tested its ATPase activity. Here, we found that a much-reduced stoichiometry of 1:10 is already sufficient to inhibit MsbA (**figure 6.3**). Therefore, all further NMR experiments were conducted on POPE/POPG proteoliposomes. A comparison between NCA spectra of [^{13}C,^{15}N-K]-MsbA reconstituted into DMPC/DMPA and POPE/POPG shows no major chemical shift differences (**figure 6.4**). Furthermore, POPE/POPG is also closer to the native lipid composition of the inner *E. coli* membrane.

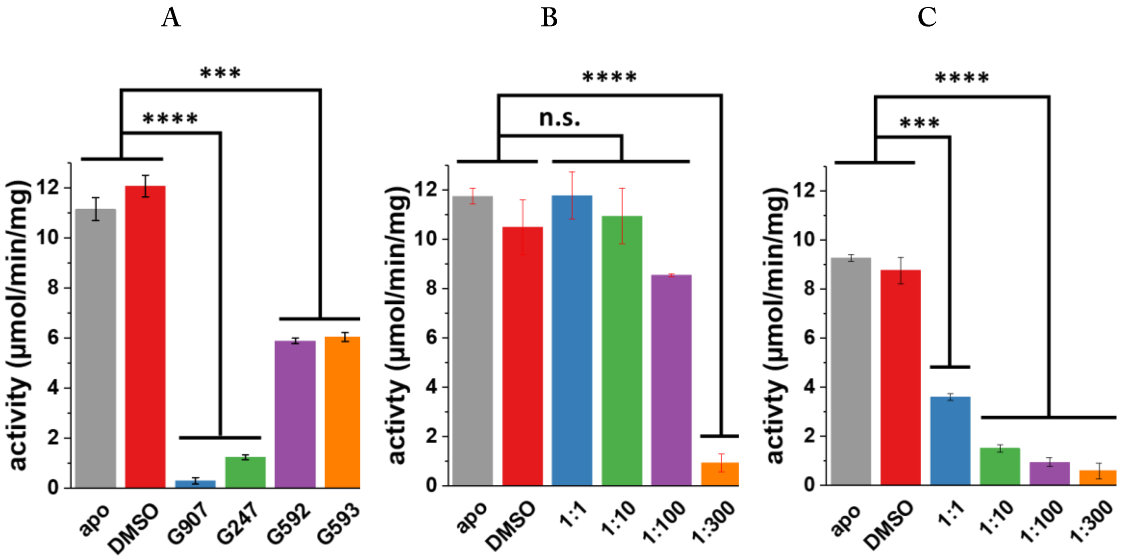

Figure 6.3. Determining G-compound concentrations for MAS-NMR. MsbA ATPase activity was determined based on previous studies using $_{\text{WT}}$MsbA proteoliposomes incubated with or without G-compounds. A) Inhibition of $_{\text{WT}}$MsbA in DMPC/DMPA (1:300). B) Titration of G907 to MsbA in DMPC/DMPA. C) Titration of G907 to MsbA in POPE/POPG. $^{*}p<0.01$, $^{**}p<0.001$, $^{***}p<0.0001$ (ANOVA, Bonferroni test); n=3 of distinct samples with mean±SEM. *The inhibitors were given by Genentech (appendix Declarations).*

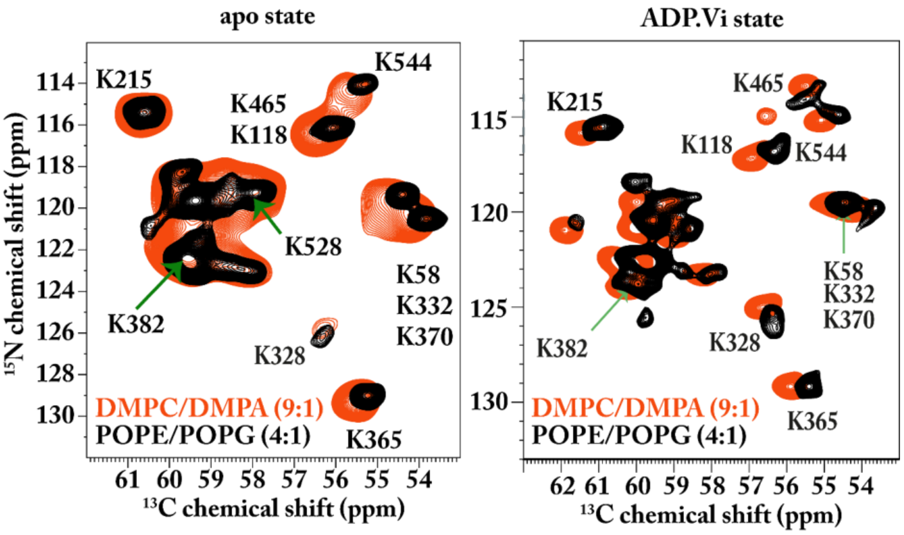

Figure 6.4. DMPC/DMPA vs POPE/POPG. NCA spectra of [13C,15N-K]-MsbA in DMPC/DMPA (red) and POPE/POPG (black). Chemical shifts appear mainly comparable in both cases, but cross peaks are sharper in POPE/POPG.

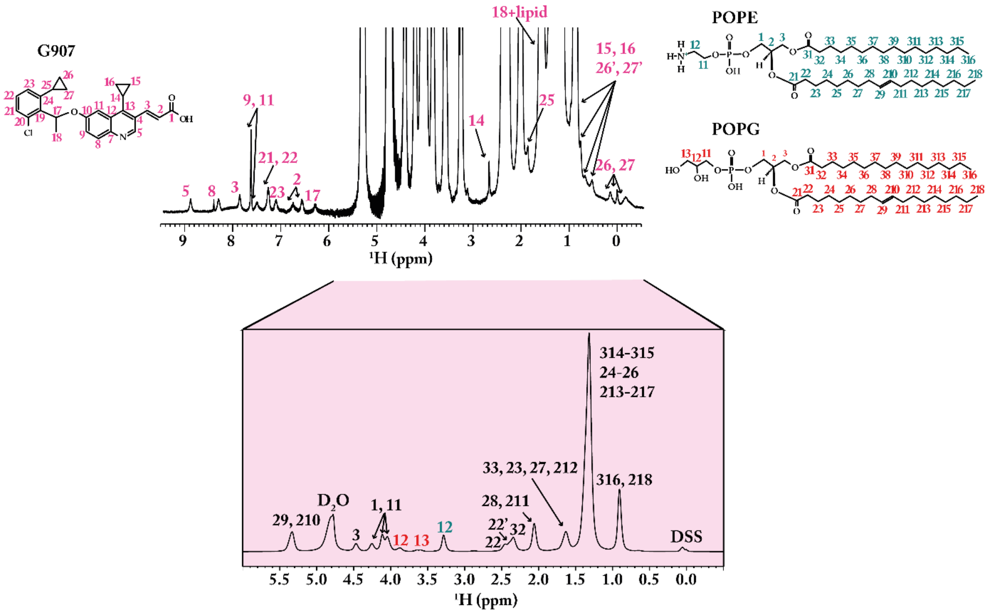

Figure 6.5. ^{1}H resonance assignments of G907 and POPE/POPG (4:1). One-dimension proton spectra were recorded on the 600 MHz (290 K, 10 KHz MAS). Assignments in black refer to peaks for both POPE and POPG. Assignments in green, red, and pink refer to POPE, POPG, and G907, respectively.

To reach MsbA and its binding site, G907 must be able to cross the outer membrane and penetrate the inner membrane. We, therefore, probed its lipid interactions by ^{1}H NOESY-MAS spectroscopy. Our data show strong NOEs between G907 protons and protons in the lipid acyl chains of POPE/POPG liposomes. In contrast, cross peaks are weaker in DMPC/DMPA model membranes indicating a lower degree of penetration, which could also explain the differences in the inhibitor efficiency between both lipid compositions (**figure 6.5-67, table 6.1**)

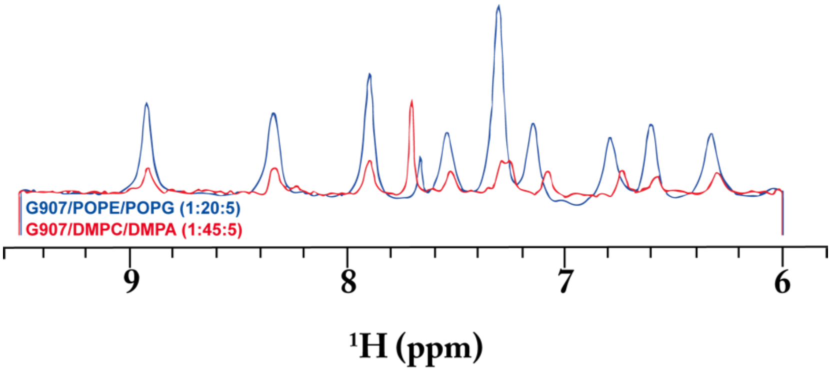

Figure 6.6: Slice along ω1 (1.2 ppm) of the spectrum in figure 6.7 in comparison with the same slice taken from the spectrum of G907 in DMPC/DMPC lipid bilayers. The spectra were normalized to the diagonal CH_2 resonance. Both samples contained the same G907:lipid ratio. The difference in NOE peak intensity is 3.4 times (scaling factor = 0.5513) higher for POPE/POPG compared to DMPC/DMPA.

The data here and previously published data[18], show that the MsbA inhibitors like G907 reduce cell growth (**figure 6.3**), which means that they must be able to cross the other membrane and penetrate the inner membrane. To further illustrate the membrane interaction of G907, ^{1}H-MAS-NOESY experiments on G907 in POPE/POPG lipid bilayers were carried out. POPE/POPG phospholipids are found mainly in the periplasmic leaflet of the asymmetric outer membrane and the symmetric inner membrane of *E. coli* bacteria[30]. ^{1}H resonances of the aromatic regions of G907 are well distinguished from the lipid acyl chains (**figure 6.5**).

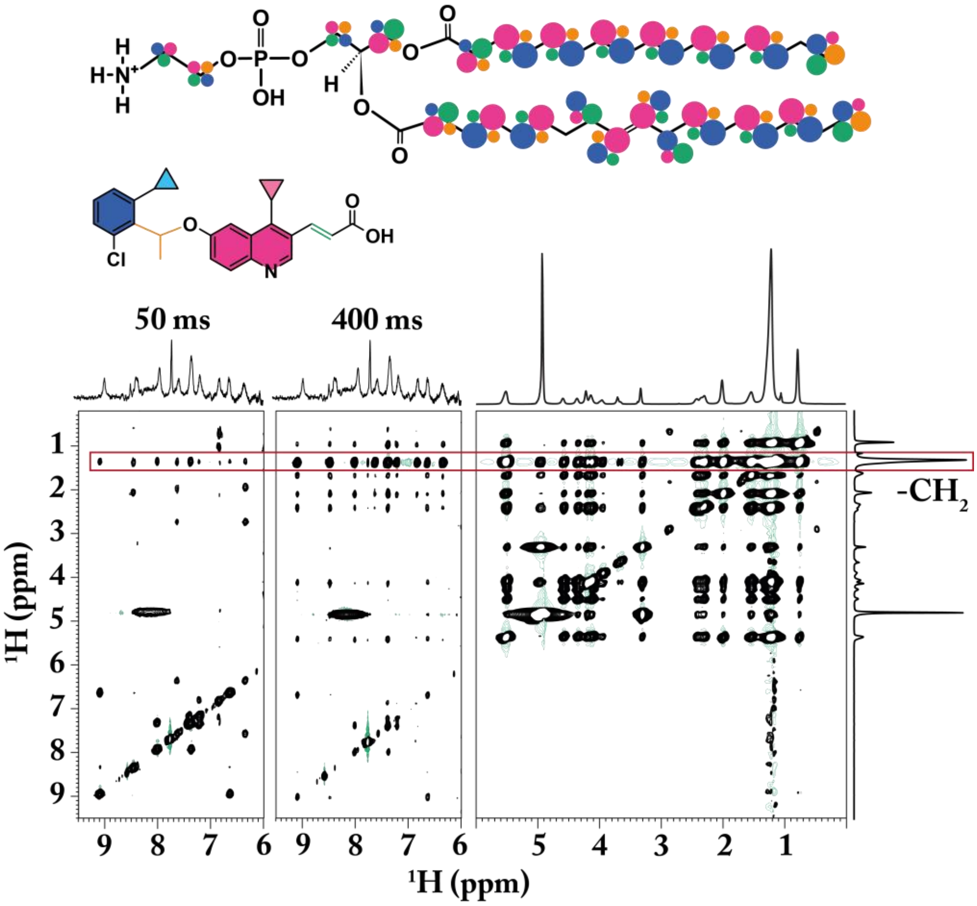

Figure 6.7. ^{1}H MAS NOESY spectra of POPE/POPG and G907 for a mixing time of 50 and 400 ms (mixing time for overall maximum cross-peak intensities). The aromatic signals of G907 occur between 7.5-9.5 ppm and are well separated from the lipid signals (below 6 ppm). Cross-peak intensities of G907 inside the lipid bilayer are indicated with the red box at 1.3 ppm. Colours in the POPE lipid structure indicate cross-peak intensities with the G907 drug region indicated in the same colours.

From the NOE cross-peak intensities of intermolecular lipid - G907 correlations (**figure 6.6**), a qualitative location of the inhibitor within the bilayer can be derived. With a NOESY mixing time of 50 ms, cross-peaks between G907 and the acyl chains of the POPE/POPG lipids are already visible and become much more pronounced at longer mixing times such as 400 ms (**figure 6.6-6.8, appendix build-up curves NOESY experiments**). Overall, these interactions are observed in all parts of the lipids, but the most pronounced signals are found in the acyl chains. The drug-lipid interactions are also observed in the lipid head groups but with lower NOESY peak intensities. These data underline the assumption, that G907 must be able to penetrate lipid bilayers to reach the MsbA binding site. A comparison between G907-lipid cross-peaks between DMPC and POPE/POPG is shown in **figure 6.9**. In DMPC, smaller NOEs are observed indicating weaker interactions which are in line with the observation that a higher G907 concentration is needed in DMPC compared to POPE/POPG to reach similar inhibitory effects (**figure 6.3**).

Table 6.1 Chemical shifts of POPE/POPG

Lipid	#	*Chemical shift*
choline	12 (13)	3.3-3.4ppm (3.6-3.7 ppm)
phosphate	1, 11	4.1-4.2 ppm
glycerol	3; 22, 32	4.5-4.6; 2.4 ppm
CH2	29, 210	5.3-5.4 ppm
CH2	28, 211	2.0-2.1 ppm
CH2	34-315, 24-26, 213-217	1.3-1.7 ppm
CH2	316, 218	0.95-1.05 ppm

Table 6.2 Chemical shifts of DMPC/DMPA

Lipid	#	*Chemical shift*
choline	12, 13-15	3.3-3.4ppm (3.6-3.7 ppm)
phosphate	1, 11	4.2, 4.4 ppm
glycerol	3; 22, 32	2.3-2.7 ppm
CH2	34-313, 24-213	1.3-1.7 ppm
CH2	214, 314	0.9 ppm
CH2	23, 33	1.9 ppm
CH2	2	5.3-5.4 ppm

With a mixing time of 50 ms cross peaks of G907 and the acyl chains of the POPE/POPG lipids is clearly visible. With increasing mixing time more G907-lipid cross-peaks appear as a result of long-range interactions (**figure 6.8**). The longer mixing time of 400 ms, allows the observation of intermolecular interactions, thus more cross peaks in other lipid regions compared to 50 ms. With increasing mixing time over 400 ms, weaker peaks and viewer cross-peaks are observed. Overall, these interactions are observed in all parts of the lipids, but the most pronounced signals are found in the acyl chains. The drug-lipid interactions are also observed in the lipid head groups, despite the weaker signal, which suggests that G907 has the ability to cross bacterial cell walls as observed in the growth assays (**figure 6.3**) which is in line with previous findings[18].

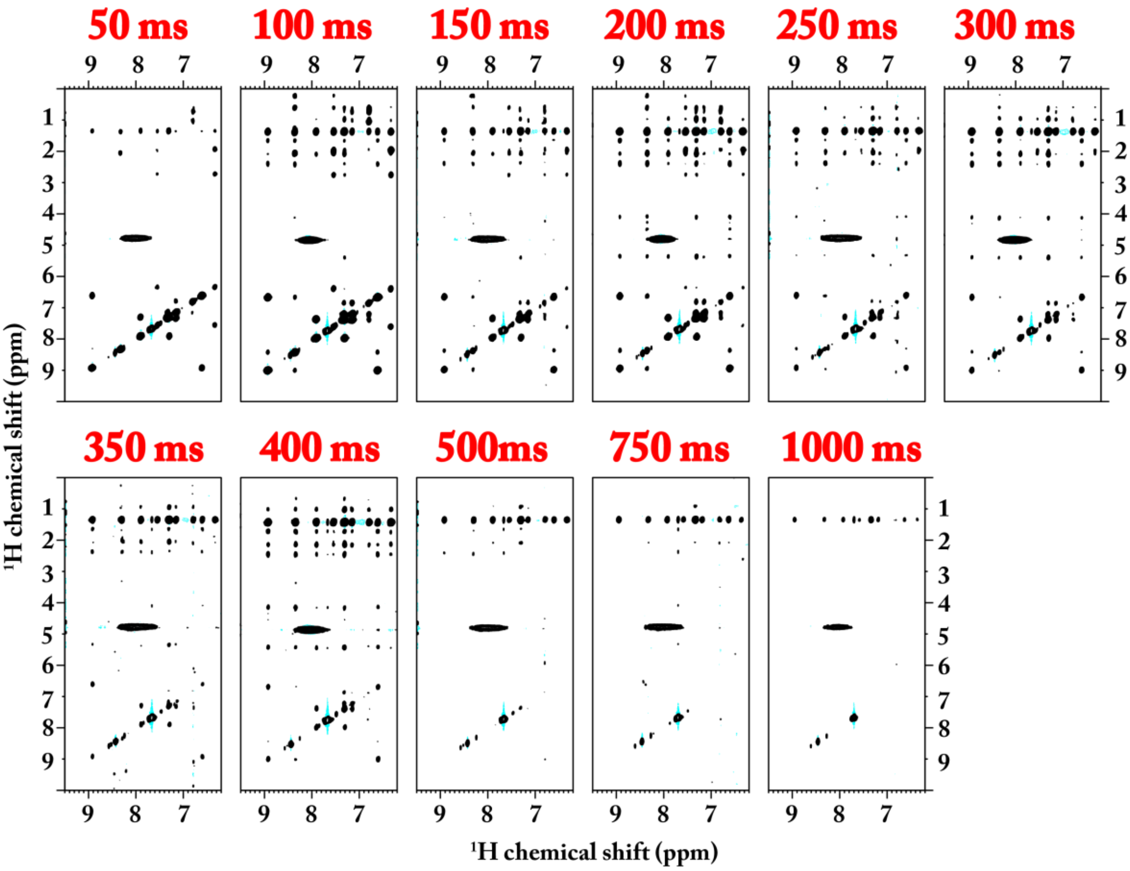

Figure 6.8. Various mixing times of G907 interactions with POPE/POPG lipids.

NOE cross peaks with other lipids such as DMPC/DMPA appear to be similar to the G907 interactions with POPE/POPG (**table 6.2 and figure 6.9**). However, the NOE signals in DMPC/DMPA appear to be much weaker than in POPE/POPG (**figure 6.10**).

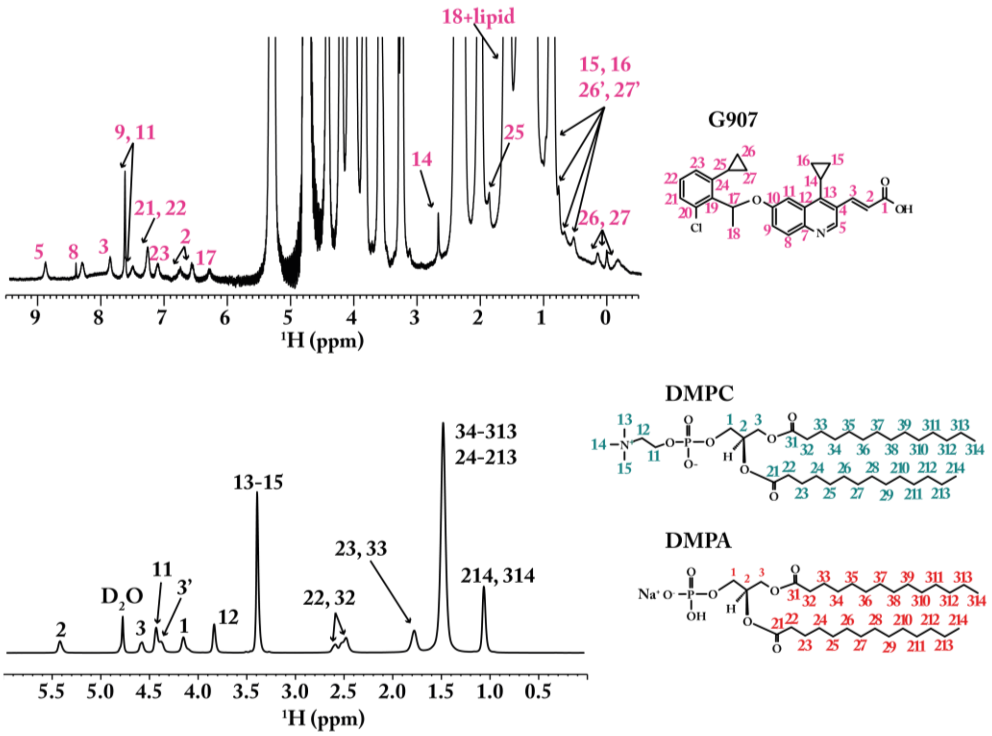

Figure 6.9. ^{1}H resonance assignments of G907 and DMPC.DMPA (9:1). One-dimension proton spectra were recorded on the 600 MHz (290 K, 10 KHz MAS). Assignments in black refer to peaks for both DMPC and DMPA. Assignments in pink refer to G907.

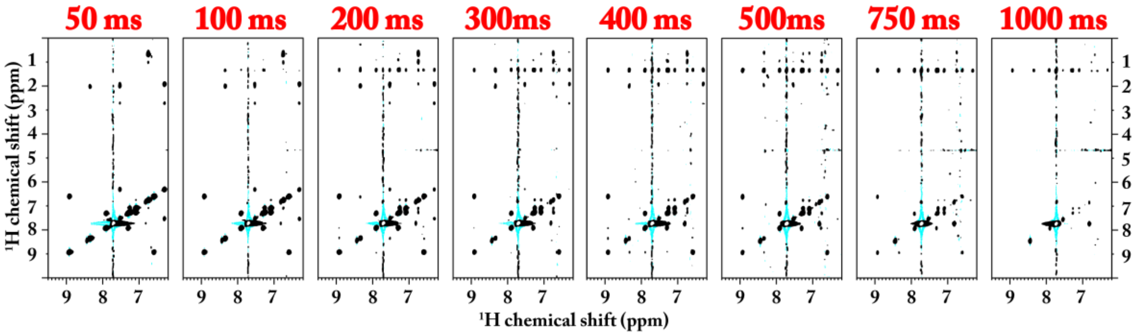

Figure 6.10 Various mixing times of G907 interactions with DMPC/DMPA lipids.

The effect of G907 on [^{13}C,^{15}N-F]-MsbA and [^{13}C,^{15}N-K]-MsbA was then probed by recording NCO and NCA spectra in the apo state and the presence of G907 (**figure 6.11**). In CH1 ([^{13}C,^{15}N-F]-MsbA), F115(C') shifts by 0.3 ppm and F116 (N) by -1.6 ppm (**figure 6.11, left**). Notably, the ^{15}N chemical shift in POPE/POPG lipid bilayer is slightly different from the CH1 of MsbA in DMPC/DMPA. Possibly, CH1 is located close to the interface of the TMD and the lipid bilayer and is more sensitive to these environmental changes. Inspecting the NCA spectrum of [^{13}C,^{15}N-K]-MsbA reveals also some small G907-induced changes (**figure 6.11, right**). Additional peaks occur around K118 in CH1, which overlaps with K465 in the apo state (**figure 6.11, inset (i)**). Peak "K215+X" shifts slightly by -0.23 ppm (N) (**figure 6.11, inset (ii)**), which contrasts with H33342 binding, where larger changes were observed (**figure 5.3C**). This means that K215 is not much affected by G907. In addition, K328 in the NBD shows a 1.5 ppm ^{15}N shift. Hence, the effect of G907 seems to affect mainly CH1 and indicates crosstalk. A separate spectrum of [^{13}C-H,^{15}N-K]-MsbA was not recorded as K215 was already detected in the NCA experiment.

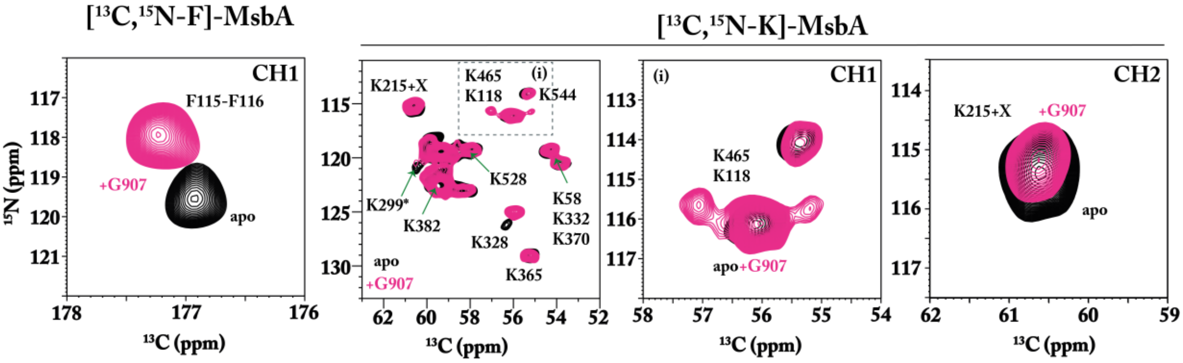

Figure 6.11: NCO and NCA spectra of residues in CH1 and CH2 upon binding of the allosteric MsbA inhibitor G907. NCO spectrum of [^{13}C,^{15}N-F]-MsbA (left) reveals a G907-induced shift of the F115-F116 NCO cross peak. The NCA spectrum of [^{13}C,^{15}N-K]-MsbA (middle, right). The signals of residues (i) K118 in CH1 and (ii) K215 in CH2 overlap with other resonances. Additional intensities occur around K118/K465 upon G907 binding while the K215 cross peak remains unaffected. The experiments were performed using MsbA in POPE/POPG (4:1) with a lipid-to-protein ratio of 75:1. The NCO (CH1) and NCA (13C15N-K + CH2) MAS-NMR spectra were recorded on the 600 MHz (260 K, 10 KHz MAS) and 850 MHz (260 K, 14 KHz MAS), respectively. The apo state is depicted in black. The G907-MsbA is shown in pink.

6.3 Discussion

In this short chapter, the effects of G-compounds or quinoline derivatives on MsbA and lipids were studied. The discussion above focused on the effect of binding of small ligands and nucleotides, which allosterically influence each other, and eventually lead to substrate translocation. The discovery of quinolone-based inhibitors such as G907 with a TMD binding site at TM6 therefore raises the question of how TMD-NBD crosstalk differs, because its mode of action involves disruption of NBD dimerization with subsequent inhibition of ATP hydrolysis[18].

Here, the binding of G907 resulted in substantial chemical shift changes for F115/F116 in CH1 (**figure 6.11, table 6.3**), while no change was detected for CH2. Interestingly, the X-ray structure of MsbA in complex with G907 in facial amphiphile–3 (FA-3) detergent shows binding-induced propagation of structural changes along TM4 resulting in a larger displacement of CH1 compared to CH2[18]. The proposed inhibition mechanism involves IF-state dependent binding of G907 which prevents transition to the OF state as well as asymmetric NBD-NBD uncoupling. Here, the NCA spectrum of [^{13}C, ^{15}N-K]-MsbA is similar to the IF- apo state spectrum but with some specific differences. For example, additional intensities occur around the K118/K465 cross peak and K328 appears shifted.

Table 6.3. Chemical shift changes.

Coupling Helix	Nuclei	δ(G907)-δ(apo) [ppm]	NMR spectra and samples
CH1	F115- C’	0.33	NCO, [^{13}C,^{15}N-F]-MsbA
	F116-N	-1.62	NCO, [^{13}C,^{15}N-F]-MsbA
	K118-N	-0.03	NCA, [^{13}C,^{15}N-K]-MsbA
	K118-Ca	-0.08	NCA, [^{13}C,^{15}N-K]-MsbA
CH2	H214-C’	-	NCO, [^{13}C-H,^{15}N-K]-MsbA
	K215-N	0.0	NCO, [^{13}C-H,^{15}N-K]-MsbA
	K215X-N	-0.23	NCA, [^{13}C,^{15}N-K]-MsbA
	K215X-Ca	0.0	NCA, [^{13}C,^{15}N-K]-MsbA

Overall, a general structural asymmetry cannot be concluded from this spectrum, but the additional peak intensities could be an indication. However, since these signals have not been assigned, a definitive statement cannot be made at this point. A recent cryo-EM study of MsbA in complex with a similar inhibitor G247 in nanodiscs proposed a symmetric NBD uncoupling but no specific conclusion on the coupling helices has been derived [17]. Our data also demonstrate that CH-mediated crosstalk plays a role in the mechanism of an allosteric MsbA inhibitor, which binds in the TMD but prevents ATP hydrolysis in the NBD. In summary, the data show that G907 binding in the NBDs triggers signalling into the NBDs involving at least CH1 and stabilizing an IF state.

References

1 Verma, V. A. *et al.* Discovery of Inhibitors of the Lipopolysaccharide Transporter MsbA: From a Screening Hit to Potent Wild-Type Gram-Negative Activity. *J Med Chem* **65**, 4085-4120, doi:10.1021/acs.jmedchem.1c01909 (2022).

2 Rice, L. B. Federal funding for the study of antimicrobial resistance in nosocomial pathogens: no ESKAPE. *J Infect Dis* **197**, 1079-1081, doi:10.1086/533452 (2008).

3 Rice, L. B. Progress and challenges in implementing the research on ESKAPE pathogens. *Infect Control Hosp Epidemiol* **31 Suppl 1**, S7-10, doi:10.1086/655995 (2010).

4 Hidron, A. I. *et al.* NHSN annual update: antimicrobial-resistant pathogens associated with healthcare-associated infections: annual summary of data reported to the National Healthcare Safety Network at the Centers for Disease Control and Prevention, 2006-2007. *Infect Control Hosp Epidemiol* **29**, 996-1011, doi:10.1086/591861 (2008).

5 Siegel, R. L., Miller, K. D., Fuchs, H. E. & Jemal, A. Cancer statistics, 2022. *CA Cancer J Clin* **72**, 7-33, doi:10.3322/caac.21708 (2022).

6 Sung, H. *et al.* Global Cancer Statistics 2020: GLOBOCAN Estimates of Incidence and Mortality Worldwide for 36 Cancers in 185 Countries. *CA Cancer J Clin* **71**, 209-249, doi:10.3322/caac.21660 (2021).

7 Nanayakkara, A. K. *et al.* Antibiotic resistance in the patient with cancer: Escalating challenges and paths forward. *CA Cancer J Clin* **71**, 488-504, doi:10.3322/caac.21697 (2021).

8 de Kraker, M. E., Stewardson, A. J. & Harbarth, S. Will 10 Million People Die a Year due to Antimicrobial Resistance by 2050? *PLoS Med* **13**, e1002184, doi:10.1371/journal.pmed.1002184 (2016).

9 Hollis, A. & Ahmed, Z. Preserving Antibiotics, Rationally. *N Engl J Med* **369**, 2474-2476, doi:10.1056/NEJMp1311479 (2013).

10 Bertani, P., Raya, J. & Bechinger, B. 15N chemical shift referencing in solid state NMR. *Solid State Nucl Magn Reson* **61-62**, 15-18, doi:10.1016/j.ssnmr.2014.03.003 (2014).

11 Doerrler, W. T. & Raetz, C. R. ATPase activity of the MsbA lipid flippase of Escherichia coli. *J Biol Chem* **277**, 36697-36705, doi:10.1074/jbc.M205857200 (2002).

12 Karow, M. & Georgopoulos, C. The essential Escherichia coli msbA gene, a multicopy suppressor of null mutations in the htrB gene, is related to the universally conserved family of ATP-dependent translocators. *Mol Microbiol* **7**, 69-79, doi:10.1111/j.1365-2958.1993.tb01098.x (1993).

13 Zhou, Z., White, K. A., Polissi, A., Georgopoulos, C. & Raetz, C. R. Function of Escherichia coli MsbA, an essential ABC family transporter, in lipid A and phospholipid biosynthesis. *J Biol Chem* **273**, 12466-12475, doi:10.1074/jbc.273.20.12466 (1998).

14 Polissi, A. & Georgopoulos, C. Mutational analysis and properties of the msbA gene of Escherichia coli, coding for an essential ABC family transporter. *Mol Microbiol* **20**, 1221-1233, doi:10.1111/j.1365-2958.1996.tb02642.x (1996).

15 Guo, D. *et al.* Energetics of lipid transport by the ABC transporter MsbA is lipid dependent. *Commun Biol* **4**, 1379, doi:10.1038/s42003-021-02902-8 (2021).

16 Bonifer, C. & Glaubitz, C. MsbA: an ABC transporter paradigm. *Biochem Soc Trans* **49**, 2917-2927, doi:10.1042/BST20211030 (2021).

17 Thelot, F. A. *et al.* Distinct allosteric mechanisms of first-generation MsbA inhibitors. *Science* **374**, 580-585, doi:10.1126/science.abi9009 (2021).

18 Ho, H. *et al.* Structural basis for dual-mode inhibition of the ABC transporter MsbA. *Nature* **557**, 196-201, doi:10.1038/s41586-018-0083-5 (2018).

19 Reyes, C. L., Ward, A., Yu, J. & Chang, G. The structures of MsbA: Insight into ABC transporter-mediated multidrug efflux. *FEBS Lett* **580**, 1042-1048, doi:10.1016/j.febslet.2005.11.033 (2006).

20 Seigneuret, M. & Garnier-Suillerot, A. A structural model for the open conformation of the mdr1 P-glycoprotein based on the MsbA crystal structure. *J Biol Chem* **278**, 30115-30124, doi:10.1074/jbc.M302443200 (2003).

21 Becker, J. P., Depret, G., Van Bambeke, F., Tulkens, P. M. & Prevost, M. Molecular models of human P-glycoprotein in two different catalytic states. *BMC Struct Biol* **9**, 3, doi:10.1186/1472-6807-9-3 (2009).

22 Ward, A., Reyes, C. L., Yu, J., Roth, C. B. & Chang, G. Flexibility in the ABC transporter MsbA: Alternating access with a twist. *Proc Natl Acad Sci U S A* **104**, 19005-19010, doi:10.1073/pnas.0709388104 (2007).

23 Mi, W. *et al.* Structural basis of MsbA-mediated lipopolysaccharide transport. *Nature* **549**, 233-237, doi:10.1038/nature23649 (2017).

24 Padayatti, P. S. *et al.* Structural Insights into the Lipid A Transport Pathway in MsbA. *Structure* **27**, 1114-1123 e1113, doi:10.1016/j.str.2019.04.007 (2019).

25 Alexander, M. K. *et al.* Disrupting Gram-Negative Bacterial Outer Membrane Biosynthesis through Inhibition of the Lipopolysaccharide Transporter MsbA. *Antimicrob Agents Chemother* **62**, doi:10.1128/AAC.01142-18 (2018).

26 Kaur, H. *et al.* Unexplored Nucleotide Binding Modes for the ABC Exporter MsbA. *J Am Chem Soc* **140**, 14112-14125, doi:10.1021/jacs.8b06739 (2018).

27 Kaur, H. *et al.* The ABC exporter MsbA probed by solid state NMR - challenges and opportunities. *Biol Chem* **396**, 1135-1149, doi:10.1515/hsz-2015-0119 (2015).

28 Kaur, H. *et al.* Coupled ATPase-adenylate kinase activity in ABC transporters. *Nat Commun* **7**, 13864, doi:10.1038/ncomms13864 (2016).

29 Spadaccini, R., Kaur, H., Becker-Baldus, J. & Glaubitz, C. The effect of drug binding on specific sites in transmembrane helices 4 and 6 of the ABC exporter MsbA studied by DNP-enhanced solid-state NMR. *Biochim Biophys Acta Biomembr* **1860**, 833-840, doi:10.1016/j.bbamem.2017.10.017 (2018).

30 Wang, J., Ma, W. & Wang, X. Insights into the structure of Escherichia coli outer membrane as the target for engineering microbial cell factories. *Microb Cell Fact* **20**, 73, doi:10.1186/s12934-021-01565-8 (2021).

Chapter 7

Exploring the coupling between the ATPase and reverse adenylate kinase mechanism and the effects of substrates in MsbA

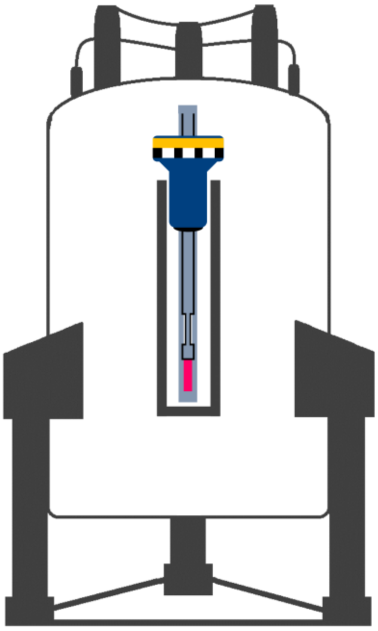

“Great ideas are the ones that lie in the intersection of the Venn diagram of ‘is a good idea’ and ‘looks like a bad idea’.”

– *Sam Altman*

This chapter contains data from S. Y. Phoebe Novischi et al. 2023 (manuscript in preparation).

7.1 The diverse mechanisms of ABC transporters

The first simple allosteric model for ATP-driven transporters was described in 1966 by Oleg Jardetzky, a pioneer in nuclear magnetic resonance and its use in the study of protein structure and dynamics. His model suggested alternating access with two substrate affinities between the inward-facing state – the stable form of the unphosphorylated state, and the outward-facing state – the stable form of the phosphorylated state. Upon substrate binding the protein alternates from the inward to the outward-facing mode, and returns to inward facing state after dephosphorylation[1].

The inward and outward-facing model described by Oleg Jardetzky for the P-type ATPase is an extensively discussed model, not only amongst the ABC transporters but also for the major facilitator superfamily (MFS) which belongs to the largest known superfamily of secondary carriers[2,3]. The two most often discussed models concerning ABC transporters are the continuous or constant NBD-NBD contact and the NBD separation model (figure 7.1) [4]. The tweezer-like, ATP switch and processive clamp models are examples of models where the NBD have separation during the ATP hydrolysis cycle[5-9]. The constant contact and nucleotide occlusion models are thought to have a continuous NBD-NBD contact throughout the hydrolysis cycle[10-14].

Naturally, ABC transporters have their primary reaction where energy is obtained via ATP hydrolysis where ATP is converted into ADP and inorganic phosphate. However, recent NMR studies have shown that for MsbA under ATP depletion, a secondary reaction can take place. This secondary reaction is also known as the adenylate kinase reaction[15-32]:

ATP hydrolysis: **ATP → ADP + Pi**		primary reaction

Adenylate kinase: **2 ADP → ATP + AMP**

Here ATP (+ AMP) is regenerated via two ADP molecules (figure 7.2). This *de novo* adenine nucleotide synthesis was described previously as a function of a sufficient cellular energy regulation of nucleotide synthesis and nucleotide ratio in various cell compartments[15-32].

The adenylate kinase reaction has been found among other ABC proteins such as Rad50, ABCC7, LmrA, TmrAB, CFTR, and $\mathrm{LptB_2FG}$[30,33-38]. It appears that in MsbA the second reaction is coupled with the primary ATP hydrolysis. This process could be important for the cell when ATP is exhausted[33,39].[33,39] Therefore, the adenylate kinase reaction in MsbA was further explored using time-resolved ^{31}P NMR.

Here, the effect of substrates is on the adenylate kinase reaction is probed to gain more insight on the coupled kinase mechanism in MsbA.

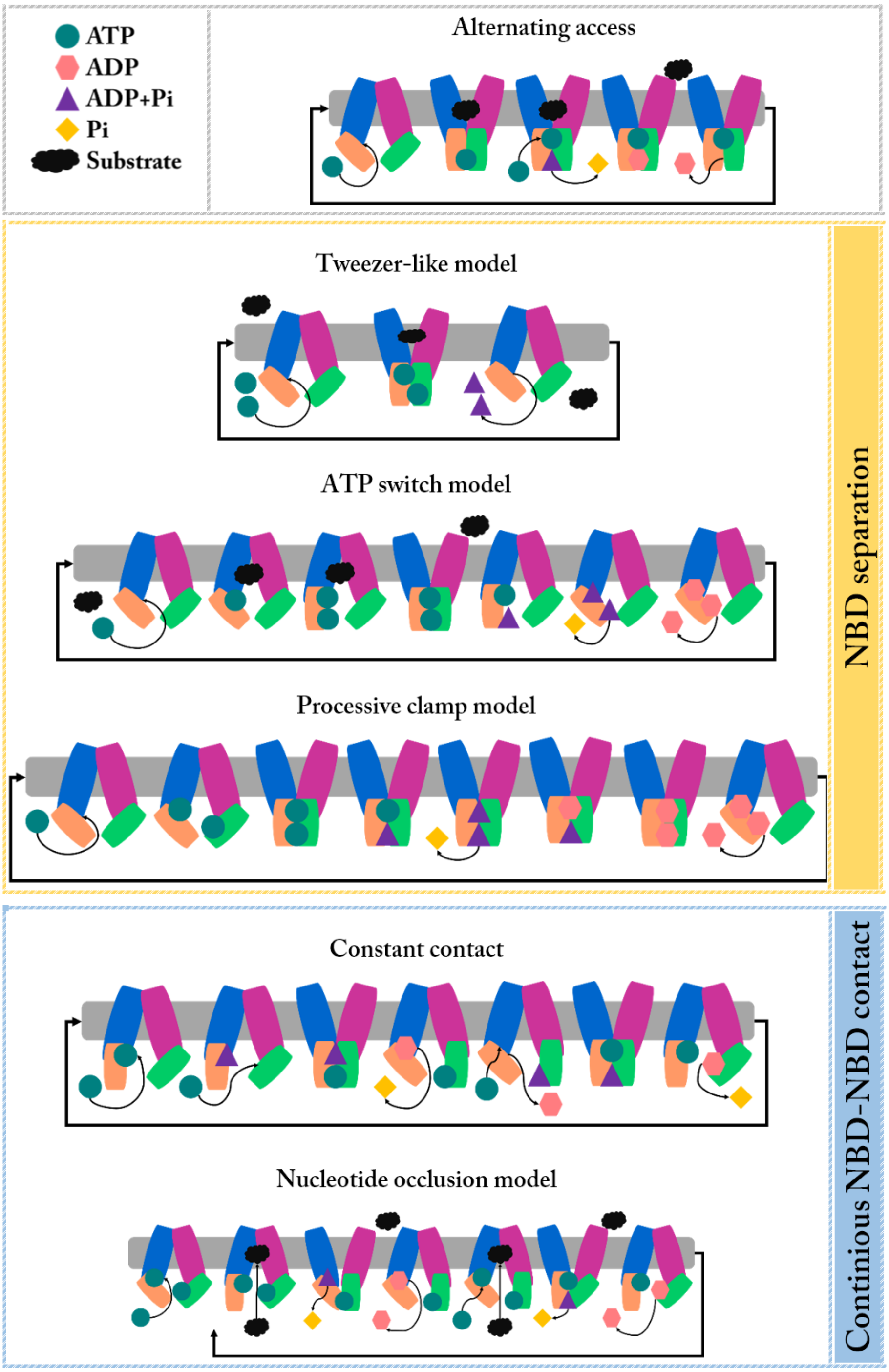

Figure 7.1. Overview of the most discussed ABC transporter models[5-14].

In this chapter a range of substrates were tested based on their physicochemical properties in detergent micelles and liposomes were probed through the analysis of 31P NMR progress curves. The first readout-parameter was the final AMP/Pi ratio after completion of the reaction because it serves as a parameter to estimate the extent of interplay between both activities. Under standard conditions (apo MsbA) the AMP/Pi ratio is 2:1. Furthermore, ^{31}P progress curves were analysed to obtain the ATP hydrolysis, Pi buildup, and AMP buildup rates of the kinase reaction.

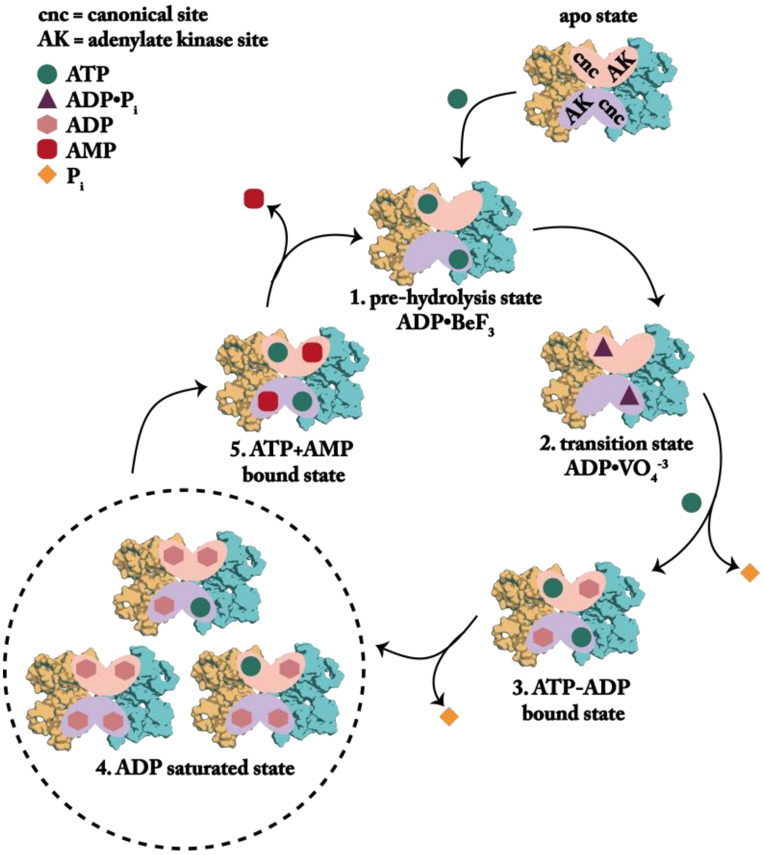

Figure 7.2. The primary and coupled secondary reaction of MsbA. This cartoon is based on Kaur et al 2018[39].

7.2 Progress curve analysis

Time-resolved ^{31}P NMR of ATP hydrolysis by MsbA results in the progress curves of ATP, ADP, AMP, and inorganic phosphate plotted in concentration versus time (figure 7.3). While the Michaelis-Menten kinetic approach can provide the enzymatic steady-state conditions, NMR progress curves also reveal side reactions that are otherwise not observed in the classical Michaelis-Menten kinetics. For instance, the biochemical reactions give valuable information of the inorganic phosphate turnover of MsbA early on in the reaction. Time-resolved ^{31}P NMR provides additional information of the ATP hydrolysis reactions in MsbA from beginning until the end, and can follow all the side reactions, such as the consumption of ATP and ADP, and the turnover of inorganic phosphate as well as the buildup of ADP and AMP.

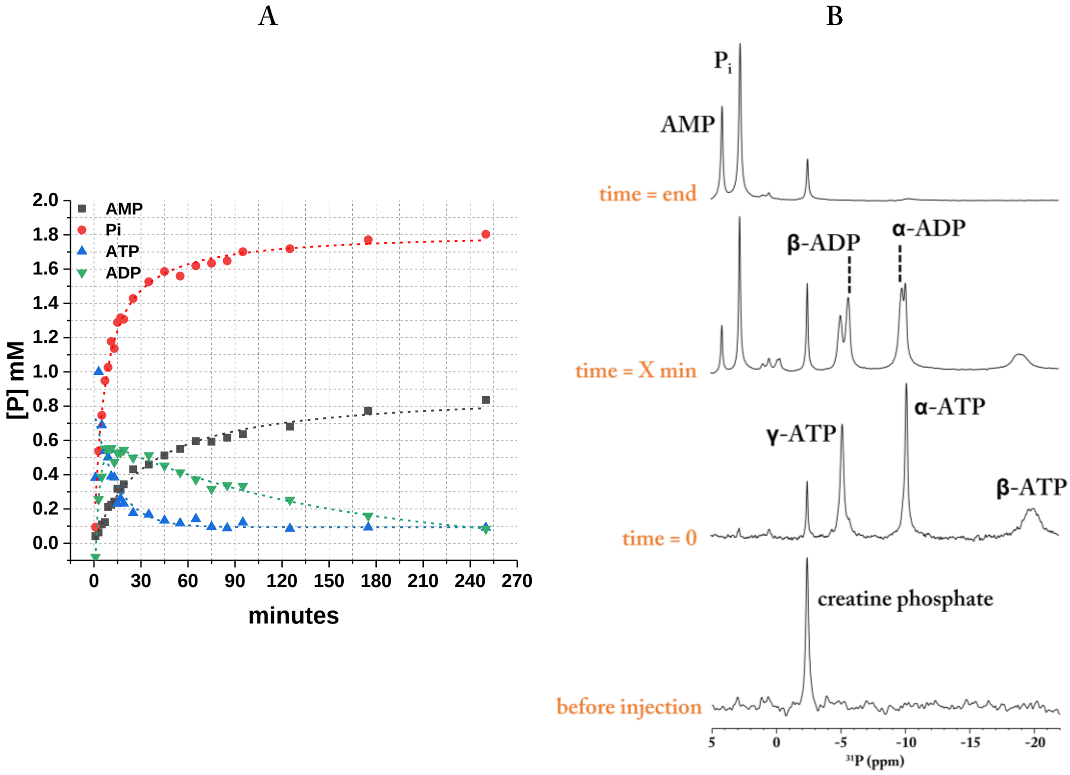

Figure 7.3. Example of a progress curve of ATP hydrolysis by MsbA. A) Typical example of a processed progress curves. The Y-axis was obtained from the 31P peak intensities after calibrating them to the [P] concentration B) Examples of processed pseudo 2D spectra of experimental parameters [ATP], [ADP], [AMP], and [Pi] at various time points. Time = 0 is right after the injection of ATP, time = X min is any time point during the reaction where consumption and buildup of all the parameters can be observed, and time = end is at the end of the reaction.

By analysing the progress curves enzymatic reactions can be characterized. This can be done in several ways. The first and straightforward progress curve analysis is by determination of the reaction velocity. This type of progress curve analysis is based on the initial velocity of the reaction by estimating the initial slope and is not always accurate. Furthermore, the enzymatic reaction is required to respect the Michaelis-Menten kinetics or first-order reactions (figure 7.4) and a (quasi) steady-state conditions according to Briggs-Haldane and useful framework that reduces the reaction scheme to 2 enzyme species (i.e., free and bound). Thus, the higher n^th^ order of reactions can no longer be determined by the initial velocity.

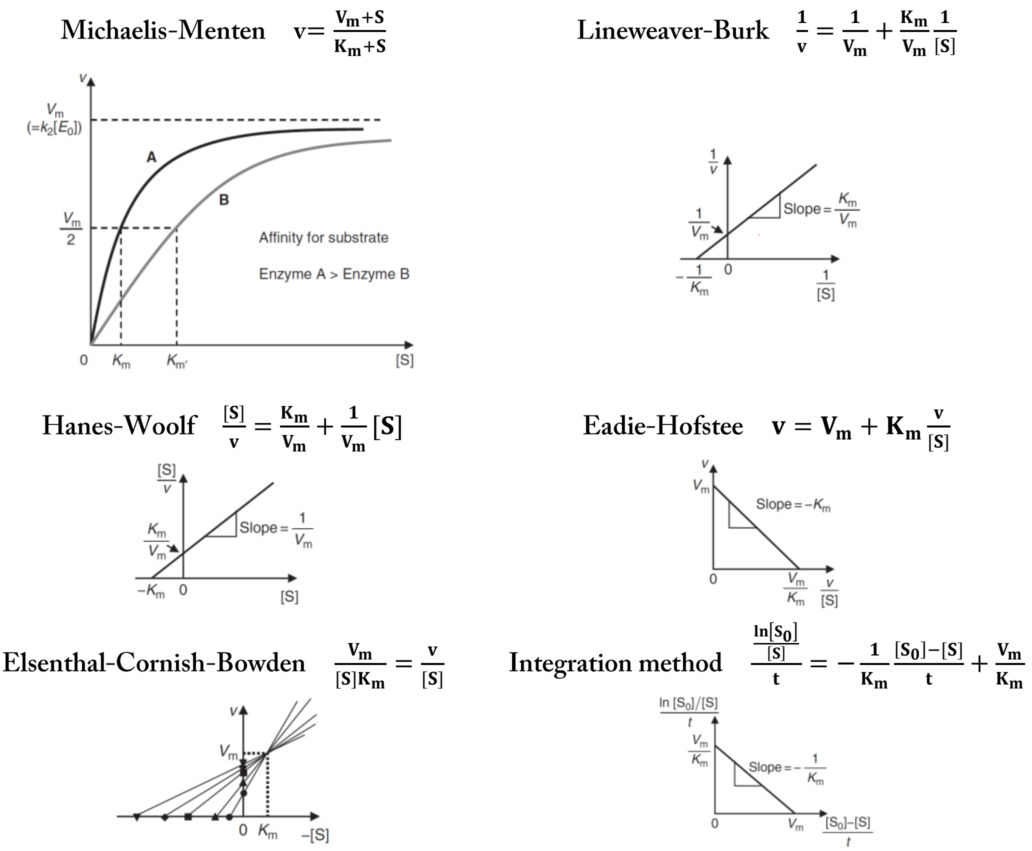

Figure 7.4. Various types of plots for determination of kinetic parameters in the Michaelis–Menten type enzyme reactions[40]. *With permission from ©Elsevier*

Second, progress curve analysis of higher n^th^ order of reactions can be done using numerical integrations. Analysis by numerical integrations does not require a steady-state approach. Yet, numerical integration required prespecified and appropriately conditioned kinetic model. In other words, the n^th^ order of the reaction(s) and the type of reaction(s) need(s) to be known. For instance, for $nA \overset{k_r}{\rightarrow}$ products the nth order reaction rate equation would be $\frac{d[A]}{dt} = -k_r[A]^n$, with integration $\int_{A_0}^{A_t} \frac{d[A]}{[A]^n} = -\,k_r \int_{A_0}^{A_t} dt$ and integrated rate equations:

$$\frac{1}{(n-1)[A_t]^{-1}} = \frac{1}{(n-1)[A_0]^{n-1}} + k_r t \qquad \text{or} \qquad [A_t] = \frac{[A_0]}{\sqrt[n-1]{1+(n-1)[A_0]^{n-1}k_r t}}$$

where the slope k_r can be obtained using $\frac{1}{[(n-1)A_t{}^{n-1}]}$ plotted against time. Rate equations of higher order reactions are given in **table 7.1** as an example[41].

Table 7.1 Overview of numerical integration of nth order reaction[41].

nth order reaction	n=1	n=2	n=3
Rate equation	$\frac{d[A]}{dt} = -k_r[A]$	$\frac{d[A]}{dt} = -k_r[A]^2$	$\frac{d[A]}{dt} = -k_r[A]^3$
Integration	$\int_{A_0}^{A_t} \frac{d[A]}{[A]} = -\,k_r \int_{A_0}^{A_t} dt$	$\int_{A_0}^{A_t} \frac{d[A]}{[A]^2} = -\,k_r \int_{A_0}^{A_t} dt$	$\int_{A_0}^{A_t} \frac{d[A]}{[A]^3} = -\,k_r \int_{A_0}^{A_t} dt$
Integrated rate equation	$\ln\frac{A_t}{A_0} = -k_r t$ or $[A_t] = [A_0]e^{-k_r t}$	$\frac{1}{A_t} = \frac{1}{A_0} + k_r t$ or $[A_t] = \frac{[A_0]}{1+[A_0]k_r t}$	$\frac{1}{2[A_t]^2} = \frac{1}{2[A_0]^2} + k_r t$ or $[A_t] = \frac{[A_0]}{\sqrt{1+2[A_0]^2 k_r t}}e^{-k_r t}$
Slope	$-k_r \rightarrow \ln\frac{A_t}{A_0}$ vs. time	$k_r \rightarrow \frac{1}{A_t}$ vs. time	$k_r \rightarrow \frac{1}{2[A_t]^2}$ vs. time

In the case of $A + B \overset{k_r}{\rightarrow} P$ (products) the rate equation would be described as $\frac{d[P]}{dt} = -k_r\ [A_0 - P][B_0 - P]$ with integration $\frac{1}{[A_0]-[B_0]}\int_0^{P_t}\left(\frac{dP}{[B_0-P]} - \frac{dP}{[A_0-P]}\right) = -k_r \int_0^t dt$ and integrated rate equation:

$$\frac{1}{[A_0]-[B_0]}\ln\frac{[B_0][A_t]}{[A_0][B_t]} = k_r t$$

$$[A_t] = [A_0 - P_t] \text{ and } \qquad [B_t] = [B_0 - P_t]$$

where the slope k_r can be obtained using $\frac{1}{[A_0]-[B_0]}\ln\frac{[B_0][A_t]}{[A_0][B_t]} = k_r t$ plotted against time.[41]

Nevertheless, enzymatic reactions can have multiple layers of complexity:

$$\begin{tikzcd}
\mathrm{SE'I'} \arrow[r, leftarrow, "a'k_I"] \arrow[d, leftrightarrow] & \mathrm{SEI} \arrow[r, leftrightarrow] \arrow[d, leftrightarrow, "k_2"] & \mathrm{SE} \arrow[r, leftrightarrow] \arrow[d, leftrightarrow, "k_3"] & \mathrm{SES} \arrow[r, "ak"] \arrow[d, leftrightarrow, "k_4"] & \mathrm{SE} + \mathrm{P} \\
\mathrm{E'I'} \arrow[r, leftarrow, "k_I"] & \mathrm{EI} \arrow[r, leftrightarrow, "k_I"] & \mathrm{E} \arrow[r, leftrightarrow, "k_S"] & \mathrm{ES} \arrow[r, "k"] & \mathrm{E} + \mathrm{P}
\end{tikzcd}$$

where E is the free enzyme, S is the substrate, I is the inhibitor, and P is the product of decomposition. Imagine the following where ES, SE, SES, EI, and SEI are the enzyme-substrate, enzyme-inhibitor, and enzyme-substrate-inhibitor complexes and E'I' and SE'I' are the irreversible enzyme-inhibitor and substrate-enzyme-inhibitor complexes.

Multiple mechanistic models can be derived from the system given above, namely (1) enzyme-single substrate-single slow binding irreversible modifier system, (2) enzyme-single substrate-single slow binding reversible modifier system, (3) enzyme-single substrate-single slow binding irreversible modifier system which include the enzyme activity modulation by the second molecule of the same substrate, and (4) enzyme-single substrate-single slow binding reversible modifier system which include the enzyme activity modulation by the second molecule of the same substrate. An overview of progress curves and the significance of the corresponding kinetic parameters can be found in *Jure Stojan (1998), Journal of Enzyme Inhibition, 13:3, 161-176*[42].

Generally, as previously described, the Michaelis-Menten approach is an easy and straightforward way to extract parameters such as the V_{max} and K_m. This is a simplified case where a stable enzyme that catalyses an irreversible one-substrate reaction where the products are non-inhibitory. This linear approach can lead to biases when determining parameters such as the V_{max} and K_m. Moreover, the theoretical disadvantage is, that the V_{max} and K_m would be obtained via a substrate titration, while in principle a single progress curve could provide these data directly. Third, to minimize this potential bias in progress curve analysis the Lambert ω function (figure 7.5) can be introduced:

$$\mathrm{f(W) = We^W}$$

where W is any complex number $(a + bi,\ i^2 = -1)$ and e^W is the exponential function and

$$\mathrm{W(x) + \ln\{W(x)\} = \ln(x)}$$

$$x \geq -\exp(-1)\,;\ -1 \ \geq \mathrm{W}_{-1}\,;\ -1 \ \leq \ \mathrm{W}_0^- \ \leq 0\,;\ 0 \ \leq \ \mathrm{W}_0^+$$

In 1758, Johann Heinrich Lambert solved the equation $\mathrm{x = q +\ x^m}$. In 1783, Leonard Euler transformed this equation into a more symmetrical form and eventually leading to:

$$\mathrm{x^\alpha + x^\beta = (\alpha - \beta)vx^{\alpha+\beta}}$$

$$\mathrm{\log x = vx^\alpha}$$

$$\log x = v + \frac{2^1}{2!}v^2 + \frac{3^2}{3!}v^3 + \text{etc.}, \ |v| < 1/e$$

$$\mathbf{W(z)e^{W(z)} = z}$$

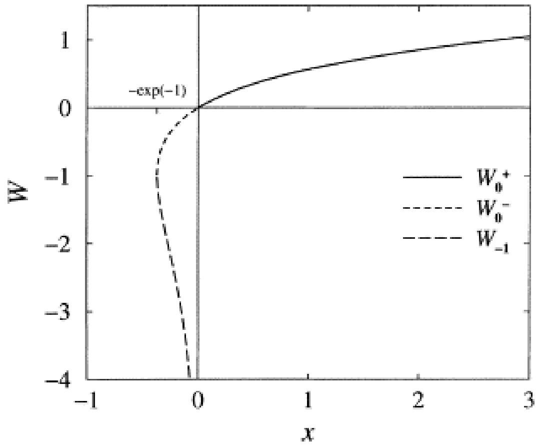

Figure 7.5 Branches of the W -function, showing the division into W_{-1}, W^-_0, and W^+_0.

The Lambert ω function can be integrated in Michaelis-Menten kinetics as a closed-form analytical solution for single progress curves for mathematical computing:

$$[S]_t = K_M W \left\{ \frac{[S]_0}{K_M} \exp\left(\frac{[S]_0 - V_M t}{K_M}\right) \right\}$$

The rate equations are not only the functions of substrates, but also as functions of time. The function has been applied by several studies in enzyme kinetics.[43-49] As a results, more precise values can be obtained, e.g., maximum given error is only 2% and can be further reduced to 0.2% (table 7.2).[50] Furthermore, linearization of the integrated form of Michaelis–Menten equation of the equation given above, results in V_{max} and K_m estimates[47]:

$$\frac{t}{\ln(\frac{[S]_0}{[S]})} = \frac{1}{V_M}\frac{[S]_0-[S]}{\ln(\frac{[S]_0}{[S]})} + \frac{K_M}{V_M} \quad \text{and} \quad \frac{t}{[S]_0-[S]} = \frac{K_M}{V_M}\frac{\ln(\frac{[S]_0}{[S]})}{[S]_0-[S]} + \frac{1}{V_M}$$

A fourth way to determine kinetic parameters is by modelling or simulations. There are several free software and platforms available, such as FITSIM, DYNAFIT, ENZO, PCAT, and BioCatNet[51-56]. The advantage of modelling or simulations is the possibility of everyday application of computer intensive procedures. An example of a modelling or simulation workflow is shown in figure 7.6. The downside is that it requires assumptions or estimations which can lead to unreliable parameters, misinterpretation, and major errors.

Table 7.2 Parameter calculations from *Goličnik, Marko (2010)* on closed form Michaelis-Menten solution using the Lambert W function with approximation functions if given[50].

Fitted parameter	[S] (μM)	[S] (μM)	V_M (μM/s)	K_M (μM)	SSQ
Theoretical value	1.000	3.000	1.00	1.00	-
$[S]_t = K_M W \left\{\frac{[S]_0}{K_M} \exp\left(\frac{[S]_0 - V_M t}{K_M}\right)\right\}$ $W(x) \approx \ln(1+x)\{1 - \frac{\ln(1+\ln(1+X))}{2+\ln(1+x)}$	0.994 ± 0.007	3.00 ± 0.01	0.97 ± 0.02	0.96 ± 0.06	0.1500
$[S]_t = K_M W \left\{\frac{[S]_0}{K_M} \exp\left(\frac{[S]_0 - V_M t}{K_M}\right)\right\}$ $W(x) \approx \ln \frac{6x}{5\ln[(\frac{12}{5})(x/\ln(1+\left(\frac{12}{5}\right)x))]}$	0.997 ± 0.008	2.99 ± 0.01	1.05 ± 0.04	1.09 ± 0.09	0.1818
$[S]_t = K_M W \left\{\frac{[S]_0}{K_M} \exp\left(\frac{[S]_0 - V_M t}{K_M}\right)\right\}$ $W(x) \approx (1+\epsilon) \ln\left\{\frac{6x}{5\ln[(\frac{12}{5})(x/\ln(1+\left(\frac{12}{5}\right)x))]}\right\} - \epsilon \ln\{\frac{2x}{\ln(1+2x)}\}$ with ε=0.4586887	0.993 ± 0.007	3.00 ± 0.01	0.98 ± 0.03	0.95 ± 0.08	0.1497
$[S]_t^{(2)} = K_M \frac{\{1 + \frac{[S]_0}{K_M}\left(\frac{[S]_0}{K_M} + 2\right)\}^{\left(\frac{1+\frac{[S]_0}{K_M}}{2+\frac{[S]_0}{K_M}}\right)} e^{-\frac{K_M t}{V_M}}}{\{1 + \frac{[S]_0}{K_M}\left(\frac{[S]_0}{K_M} + 2\right)\} e^{-\frac{K_M t}{V_M}\left(\frac{1+\frac{[S]_0}{K_M}}{2+\frac{[S]_0}{K_M}}\right)}}$	1.012 ± 0.008	3.00 ± 0.01	1.45 ± 0.16	1.21 ± 0.09	0.1508
$[S]_t = K_M \ln\{1 - \left[1 - \exp\left(\frac{[S]_0}{K_M}\right)\right] \exp\left(-\frac{V_M t}{K_M}\right)\}$	0.999 ± 0.008	3.00 ± 0.01	0.74 ± 0.01	0.84 ± 0.05	0.1823

This table was taken with the permission from © Elsevier

Moreover, numerical integration simulates progress curves according to user-defined mechanism and most platforms are insensitive to differences, e.g., different kinetics rates. Multiple iterations of the model parameters are required to minimize SSD between the points of the simulated and experimental curves. Monto Carlo simulation could be used to automate the optimizations. This would eliminate any potential bias originating from the small number of the manually initiated iterations, hidden shortcomings of the user-defined model, and reduces the risk of misuses in progress curve analysis. However, it does not eliminate the necessity for careful expert inspection of the final analytic output[57].

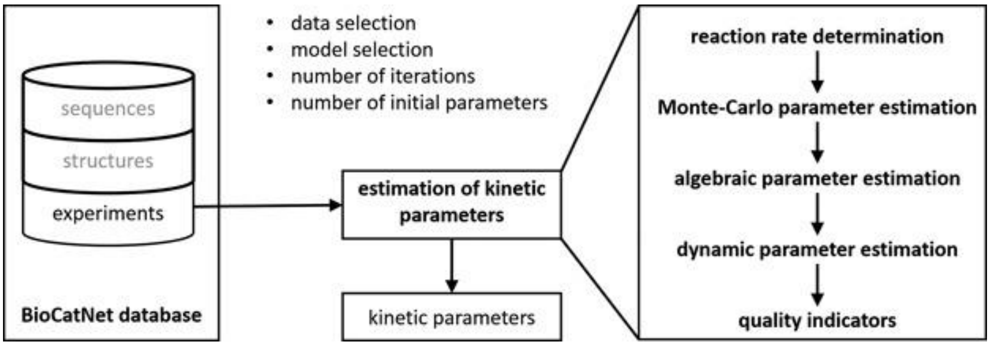

Figure 7.6. Simplified scheme of the workflow that combines experimental data retrieved from the BioCatNet database with routines for the estimation of kinetic parameters. In each repetition of the kinetic parameter estimation, three subsequent steps of parameter estimation are performed as a trade-off between accuracy and performance, using previously interpolated reaction rates (Monte-Carlo and algebraic parameter estimation) and finally using progress curves of concentrations over time (dynamic parameter estimation). Quality indicators comprise standard deviations of kinetic parameters and the residual sum of squares (RSS) with respect to the full data set. *This figure and subscript were taken from Buchholz, P. C. et al. (2019). Biotechnology Journal, 14(3), 1800183. with the permission of Wiley and Sons.*

The integration of the Lambert ω function is a good way to reduce the maximum error range for known models and functions. However, complex reactions such as the coupled adenylate kinase reaction in MsbA would require correct assumptions to provide meaningful kinetic values. As outlined above, progress curve analysis offers potentially a powerful approach to extract enzymatic parameter. However, especially in case of more complex enzymatic reactions, assumptions are needed which cause ambiguities. After initial trails, it was therefore decided to focus on an empirical description of the experimentally obtained MsbA progress curves by assuming a simple single-exponential curve[58]:

$$[S](t) = [S]_0\exp(-kt)$$

These values could provide initial estimates for future in-depth analysis using a more established model for coupled MsbA kinetic reactions.

7.3 Substrate stimulated ATPase activity

7.3.1 H33342 stimulated ATPase activity

Previously, it has been known that H33342 stimulates MsbA. As described in chapter 5, H33342 generally stimulates ATP hydrolysis in MsbA, but in higher concentration it can also inhibit ATP hydrolysis[59]. The maximum stimulated activity for MsbA of 2.5-fold or 250% activity is similar to previous studies[60]. Here, a H33342 stimulation matrix assay was carried out to determine additional kinetics. Various H33342 concentrations are plotted against different ATP concentrations, showing the (1) kinetics and the (2) stimulations at various concentrations (figure 7.7 and table 7.3).

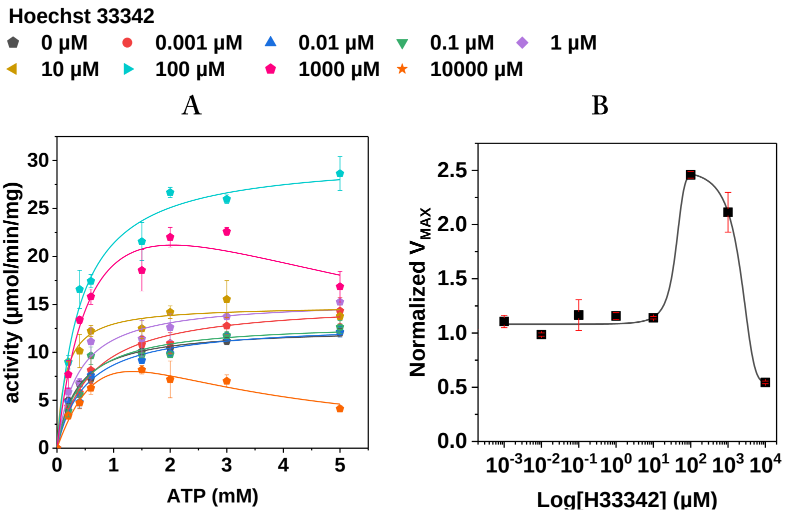

Figure 7.7. The effect of various H33342 concentration on the substrate stimulation of MsbA in DDM micelles. A) Michaelis-Menten fitting. B) Biphasic dose-response curve of H33342 for MsbA (n=3).

The V_{MAX} and (apparent) K_M values are not significantly affected by the addition of H33342 between 0 and 10 μM. Between 0.1 and 10 mM of H33342 the V_{MAX} is increased nearly 2.5-fold. At 10 mM of H33342 the K_M has decreased by 2-fold. The K_i of H33342 is $5.97 \cdot 10^{-4} \pm 3.6 \cdot 10^{-4}$ and $9.5 \cdot 10^{-4} \pm 7.2 \cdot 10^{-5}$ M for 1 and 10 mM H33342, respectively.

Table 7.3 Various H33342 concentrations were tested against different ATP concentrations, showing the (1) kinetics and the (2) stimulations at various concentrations.

H33342 (µM)	V_{MAX} (µmol/min/mg)	Apparent K_M (M)	K_i (M)
0	12.07±0.4	$3.6 \cdot 10^{-4} \pm 3.6 \cdot 10^{-5}$	-
0.001	13.36±0.7	$6.0 \cdot 10^{-4} \pm 7.0 \cdot 10^{-5}$	-
0.01	11.90±0.2	$5.0 \cdot 10^{-4} \pm 1.0 \cdot 10^{-4}$	-
0.1	14.07±1.7	$4.2 \cdot 10^{-4} \pm 1.1 \cdot 10^{-4}$	-
1	13.97±0.4	$3.7 \cdot 10^{-4} \pm 8.3 \cdot 10^{-5}$	-
10	13.76±0.1	$1.5 \cdot 10^{-4} \pm 3.4 \cdot 10^{-5}$	-
100	29.68±0.4	$4.2 \cdot 10^{-4} \pm 6.9 \cdot 10^{-5}$	-
1000	25.52±2.2	$7.0 \cdot 10^{-4} \pm 2.9 \cdot 10^{-5}$	$5.97 \cdot 10^{-4} \pm 3.6 \cdot 10^{-4}$
10.000	6.57±0.1	$1.9 \cdot 10^{-3} \pm 1.3 \cdot 10^{-4}$	$9.5 \cdot 10^{-4} \pm 7.2 \cdot 10^{-5}$

Given in pink is the standard ATP concentration used in MsbA stimulation assays, in blue is the standard substrate concentration used in MsbA stimulation assays, in pink is the standard MsbA activity in the apo state, and in grey highlighted the conditions resulted in MsbA inhibition. The K_M and K_i were fitted in Origin® and the V_{MAX} was determined by Lineweaver-Burk fittings.

7.3.2 Substrate stimulated ATPase activity

In addition to H33342, a series of substates with different physicochemical properties have been analysed (figure 7.8). Substrates where initially screened with the ATPase assays for stimulation or inhibition effects and later on used to carried out NMR experiments. As a control for substrate dissolved in DMSO, an assay was carried out to determine the effect of DMSO on the MsbA activity (figure 7.9C). Up to the used amount of 3% DMSO concentration in the substrate stimulation assays, no significant decrease in protein activity has been observed.

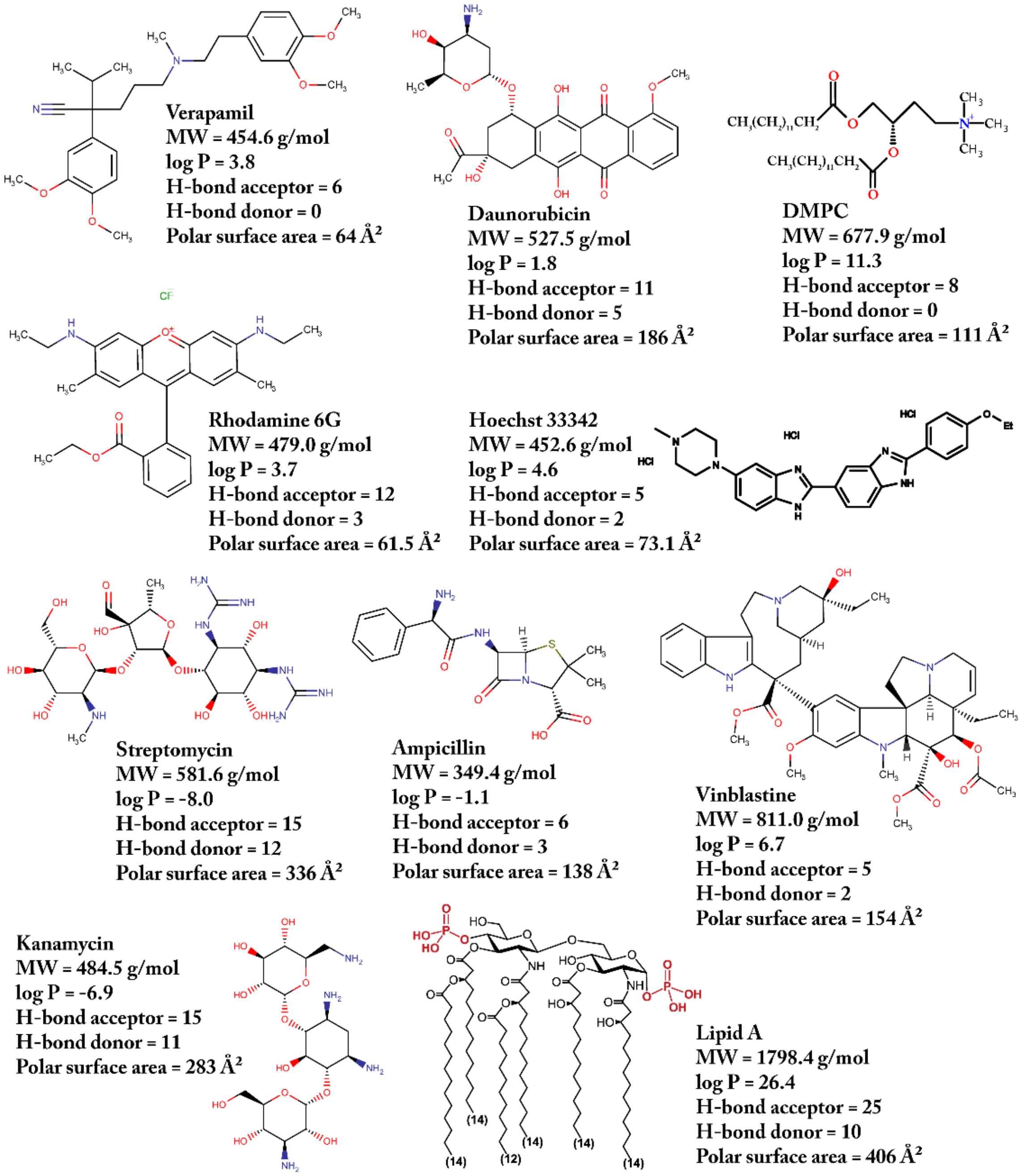

Verapamil
MW = 454.6 g/mol
log P = 3.8
H-bond acceptor = 6
H-bond donor = 0
Polar surface area = 64 Å^2

Daunorubicin
MW = 527.5 g/mol
log P = 1.8
H-bond acceptor = 11
H-bond donor = 5
Polar surface area = 186 Å^2

DMPC
MW = 677.9 g/mol
log P = 11.3
H-bond acceptor = 8
H-bond donor = 0
Polar surface area = 111 Å^2

Rhodamine 6G
MW = 479.0 g/mol
log P = 3.7
H-bond acceptor = 12
H-bond donor = 3
Polar surface area = 61.5 Å^2

Hoechst 33342
MW = 452.6 g/mol
log P = 4.6
H-bond acceptor = 5
H-bond donor = 2
Polar surface area = 73.1 Å^2

Streptomycin
MW = 581.6 g/mol
log P = -8.0
H-bond acceptor = 15
H-bond donor = 12
Polar surface area = 336 Å^2

Ampicillin
MW = 349.4 g/mol
log P = -1.1
H-bond acceptor = 6
H-bond donor = 3
Polar surface area = 138 Å^2

Vinblastine
MW = 811.0 g/mol
log P = 6.7
H-bond acceptor = 5
H-bond donor = 2
Polar surface area = 154 Å^2

Kanamycin
MW = 484.5 g/mol
log P = -6.9
H-bond acceptor = 15
H-bond donor = 11
Polar surface area = 283 Å^2

Lipid A
MW = 1798.4 g/mol
log P = 26.4
H-bond acceptor = 25
H-bond donor = 10
Polar surface area = 406 Å^2

Figure 7.8. Overview of substrates with their physicochemical properties.

Lipid A, kanamycin, and ampicillin showed no significant increase in stimulated activity. Lipid A does not appear to affect the ATP hydrolysis of MsbA in contrast to what has previously been reported. Daunorubicin showed stimulated activity in MsbA, which is consistent with previous research[60,61]. Rhodamine 6G, Vinblastine, DMPC, Verapamil and streptomycin showed a decrease in the MsbA activity (figure 7.9b). In contrast to a previous study, Verapamil did not show stimulation but rather it appeared to be inhibiting MsbA DMPC was probed to study the possible influence on MsbA as it is used throughout this dissertation for reconstitution. Possibly, DMPC in the detergent micelle buffer is too large to be transported by MsbA and is interrupting the ATP hydrolysis. Similar to previous studies, the effect of Vinblastine on MsbA was inhibitory[62]. However, some studies reported Vinblastine to have no effect on MsbA[60,63]. Here the activity was reduced by 50% at a concentration of 10 mM.

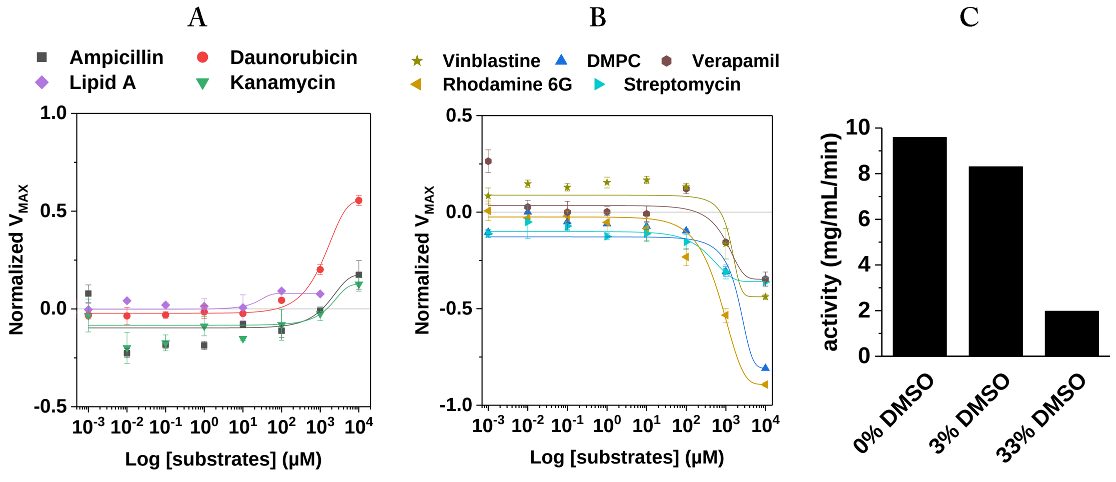

Figure 7.9. The effect of substrates on MsbA in DDM micelles. Dose-response curves of various substrates for MsbA (n=3) with stimulating effects (A) and inhibiting effects (B). C) The effect of DMSO on the ATP hydrolysis for MsbA in DDM micelles. MsbA kinase activity in the apo state is normalized to zero.

7.4 ATPase kinetics by real-time ^{31}P NMR

To further explore the effect of substrates on the MsbA activity, substrates were further analysed by ^{31}P solution (liquid-state) NMR (lsNMR). For this a fixed amount of ATP was used throughout all samples *(unless stated otherwise)*. The ATP hydrolysis was followed over time at 290K. For the analysis of the resulting progress curves, calibration curves have been carried out to determine the real phosphate concentration from the NMR intensities (figure 7.10A). The correction factor is determined by titration of ATP with creatine phosphate as an internal reference. By correcting for the internal reference results in the correct NMR intensities per mol of ATP. In turn, the slope can be used to calculate the absolute ATP concentration from the NMR intensities.

Additionally, the relaxation delay d1 was reduced from 3.0 to 1.5 seconds to gain double the number of data points and resolution in the same amount of time. However, to obtain the correct signal intensity for inorganic phosphate, a correction factor was introduced. This was done by determining the NMR signals at a relaxation delay d1 of 3.0 and 1.5 seconds across time. Inorganic phosphate intensities across time at d1=3.0s were plotted against the inorganic phosphate intensities under the same reaction conditions at d1=1.5s. As the trend of the inorganic phosphate signals across time appears to be linear, a linear correction factor was introduced of 1.35194x and was used to correct the inorganic phosphate signal at a d1 of 1.5 seconds (figure 7.10b).

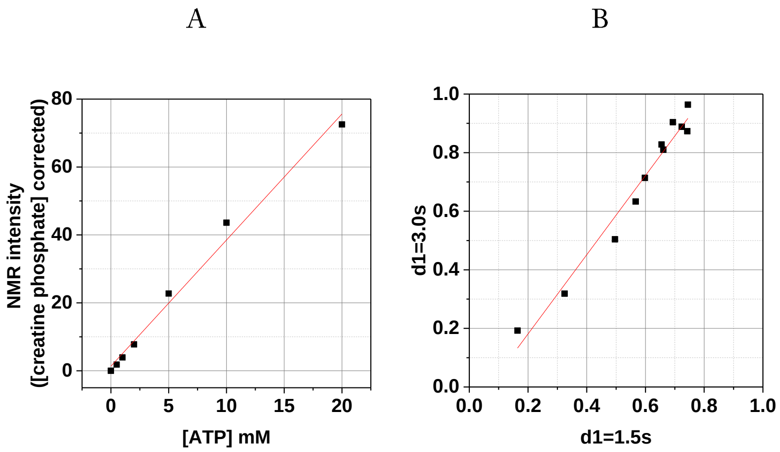

Figure 7.10. Calibration curves for ^{31}P lsNMR. A) Concentration calibration curve corrected by creatine phosphate as an internal reference, giving a correction factor of 3.71367x and an R^2 of 0.99. B) The relaxation delay d1 correction factor for inorganic phosphate is 1.35194x with an R^2 of 0.97.

7.4.1 ATP hydrolysis of MsbA in DDM micelle

The enzymatic reaction of MsbA was followed over time using ^{31}P liquid-state NMR (290K). For this, a range of substrates with various physicochemical properties have been tested on MsbA in DDM micelles (figure 7.12). MsbA in DDM detergent micelles were concentrated to 20 mg/mL protein to reach a final MsbA amount of 5 mg (250 μL, 78 nmoles). The standard ATP concentration to determine the effect of substrates was set on 1 mM. These amounts were determined by the reaction MsbA would take to hydrolyse the ATP and the NMR sensitivity. To prevent a pH shift during the ATP hydrolysis, the samples and ATP solutions were buffered. No shift has been at the standard amount of 1 mM ATP (figure 7.11). At a very high concentration of 16 mM of ATP a slight pH shift was observed.

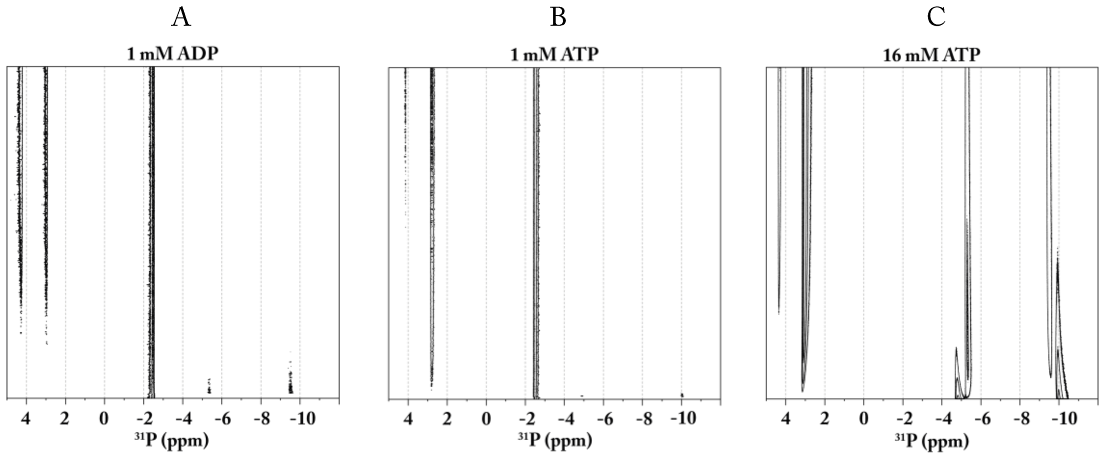

Figure 7.11. Buffered NMR conditions to prevent pH shifts during ATP hydrolysis across time. No shift has been at 1 mM ATP. At 16 mM of ATP a slight pH shift was observed.

As a control, ATP hydrolysis by MsbA was first carried out by ^{31}P liquid-state NMR at various ATP concentrations. Pseudo 2D were analysed and plotted as progress curves (figure 7.12 A-C, G, appendix pages IV-VIII, MATLAB Script, Determination of ATP hydrolysis rates). The ATP, ADP, AMP, and inorganic phosphate P_i stoichiometry nor the AMP/P_i ratio was not affected by the ATP concentration (figure 7.12D). Subsequently, progress curve analysis was done determining the initial velocity (figure 7.12 E, F, and H). As a result, the K_M value of P_i was $8.5 \cdot 10^{-4} \pm 2.2 \cdot 10^{-5}$ M, which is in the similar order of magnitude to the biochemical assay (Chapter 4). The V_{MAX} was 22.26±1.45 μM/min/mg. For AMP the V_{MAX} and K_M values were 2.2±0.25 μM/min/mg and $1.0 \cdot 10^{-4} \pm 2.6 \cdot 10^{-3}$ M, respectively. However, the Michaelis-Menten fit of AMP was unsatisfied due to the low signal-to-noise.

Finally, the ADP resulted in a V_{MAX} and K_M of 29.0±3.5 μM/min/mg and $1.65 \cdot 10^{-3} \pm 6.5 \cdot 10^{-4}$ M, respectively. The overall k_{ATP}, k_{Pi}, and k_{AMP} appears to decrease with increasing concentrations of ATP (table 7.5). This is due to the amount of time it takes to hydrolyse higher concentrations of ATP. At the standard 1 mM ATP amount in this study the k_{ATP} was $1.0 \cdot 10^{-1} \pm 1.0 \cdot 10^{-2}$ min^{-1}, and the k_{Pi}, and k_{AMP} were $7.3 \cdot 10^{-2} \pm 1.0 \cdot 10^{-2}$ and $2.6 \cdot 10^{-2} \pm 2.0 \cdot 10^{-3}$ min^{-1}, respectively.

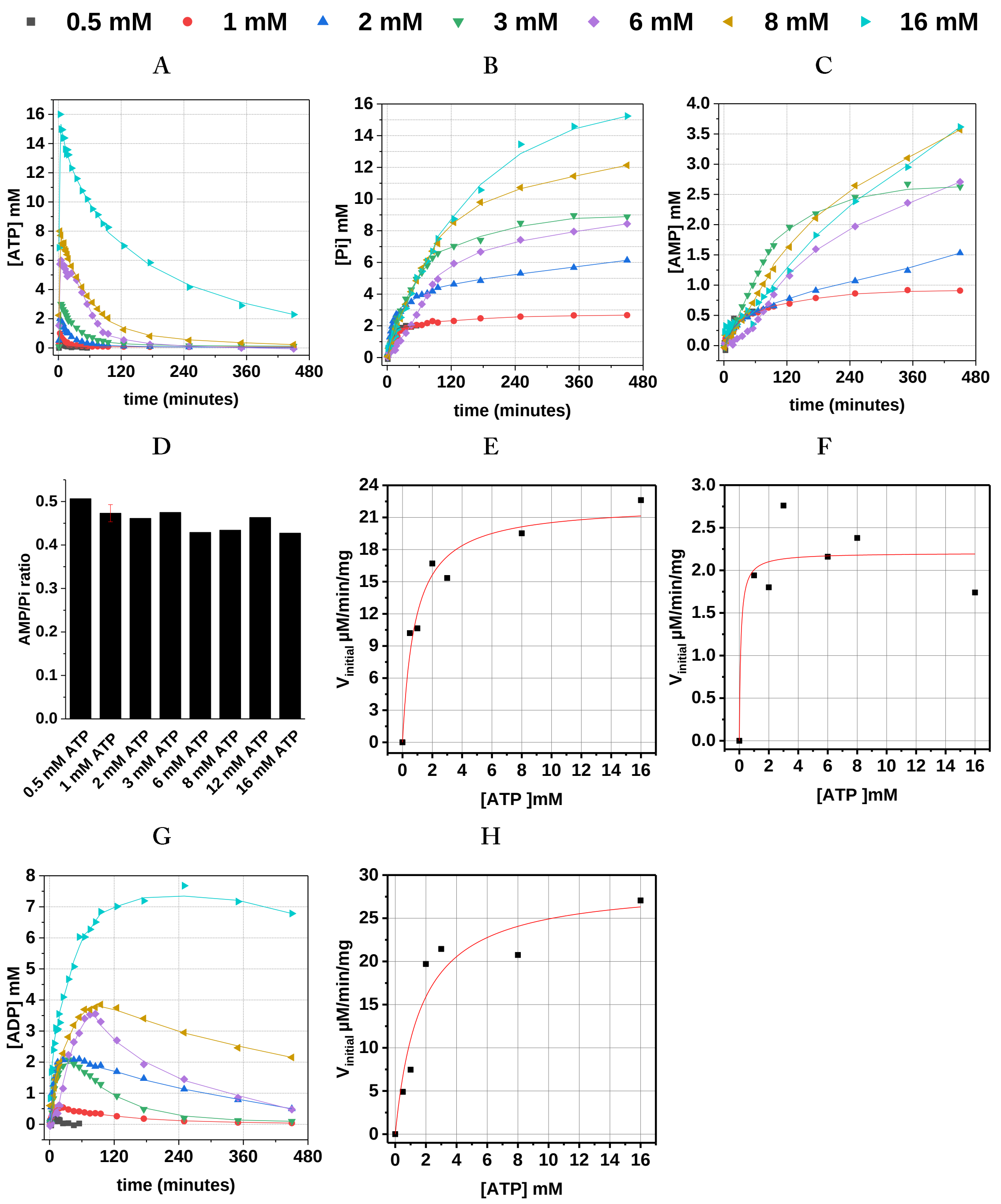

Figure 7.12. ATP hydrolysis (0.5 mM to 16 mM) of MsbA in DDM micelles in ^{31}P lsNMR. Progress curves of ATP (A), Pi (B), AMP (C), and ADP (G). The curve trend is shown by the moving averages as lines. Overview of the AMP/Pi ratio at $t_{ATP>90\%}$ (D) at various ATP concentrations (*apo state n=3*). Reaction velocity of Pi (E) with a V_{MAX} 22.26±1.45 µM/min/mg and K_M $8.5\cdot 10^{-4}\pm2.2\cdot 10^{-5}$ M, AMP (F) with a V_{MAX} 2.2±0.25 µM/min/mg and K_M $1.0\cdot 10^{-4}\pm2.6\cdot 10^{-3}$ M, and ADP (H) with a V_{MAX} 29.0±3.5 µM/min/mg and K_M $1.65\cdot 10^{-3}\pm6.5\cdot 10^{-4}$ M.

7.4.2 The effect of H33342 on the ATP hydrolysis of MsbA in DDM micelle

Accordingly, the effect of H33342 was studied using a similar range of H33342 concentration as in the H33342 stimulation assay on MsbA (**figure 7.13**). The high amount of MsbA (78 nmoles) used in the liquid state ^{31}P NMR, does not appear to affect the P_i and AMP build up, with the exception of the 0.025 µM H33342. This low concentration of H33342 did not affect the ATP hydrolysis and seems to be similar to the apo state. What appears to be most affected is the ADP consumption (**figure 7.13G-H**). Additionally, the AMP/Pi ratio, [Pi] and [AMP] at $t_{ATP50\%}$, [ADP] at $t_{ADP100\%}$ k_{ATP}, k_{Pi}, and k_{AMP}, were analysed.

The analysis of the AMP/Pi ratio showed that the various H33342 concentration did not affected the AMP/P_i ratio significantly (**figure 7.13D**). Minor differences could be observed at 100 µM H33342 where the Pi buildup appeared to be slightly higher compared to the H33342 concentrations, following the trend observed stimulation in the biochemical assays. At 10 µM of H33342 the AMP/Pi ratio and ADP buildup (0.63 mM) appears to be slightly higher compared to the other H33342 concentrations (~0.5 mM), while generally the AMP appears to increase with increasing H33342 concentrations (**figure 7.13F and H**). Despite that the local H33342 concentration at 100 µM (300 nmol/mL) and 1000 µM (3.0 µmol/mL) to MsbA (230 nmol/mL) were still the saturation range, it appears that the MsbA:H33342 is important to reproduce a clear stimulation as observed in the biochemical assays (**figure 7.7**).

Furthermore, dose-response curves of tested H33342 concentration (**figure 7.14**) show H33342 stimulation within the first five minutes of the ATP reaction. After one minute of the ATP hydrolysis the Pi buildup appears to be 12-fold higher compared to the apo states (**figure 7.14A**). After three and five minutes there is still H33342 stimulation (**figure 7.14B**). This is comparable to the biochemical assay which only provide the initial rates (maximum 20 minutes). The Pi buildup is then significantly reduced by H33342 after 15, 45, and 95 minutes.

Moreover, the analysis of the k_{ATP}, k_{Pi}, and k_{AMP} showed that k_{ATP} (**table 7.5**) appear to be highest at 0.025 µM, which is very similar to apo MsbA. This is expected as the amount of H33342 is too low to reveal an observable effect. The k_{Pi} with a rate of $6.9 \cdot 10^{-2}$ min^{-1} was also highest at 0.025 µM. Interestingly, at 10 µM H33342 the k_{AMP} ($4.0 \cdot 10^{-2}$ min^{-1}) appears to not only be the highest, but also higher than apo MsbA. Possibly, the ADP turnover at this amount of H33342 is still most effective as previously shown in the biochemical assay (**figure 7.7**).

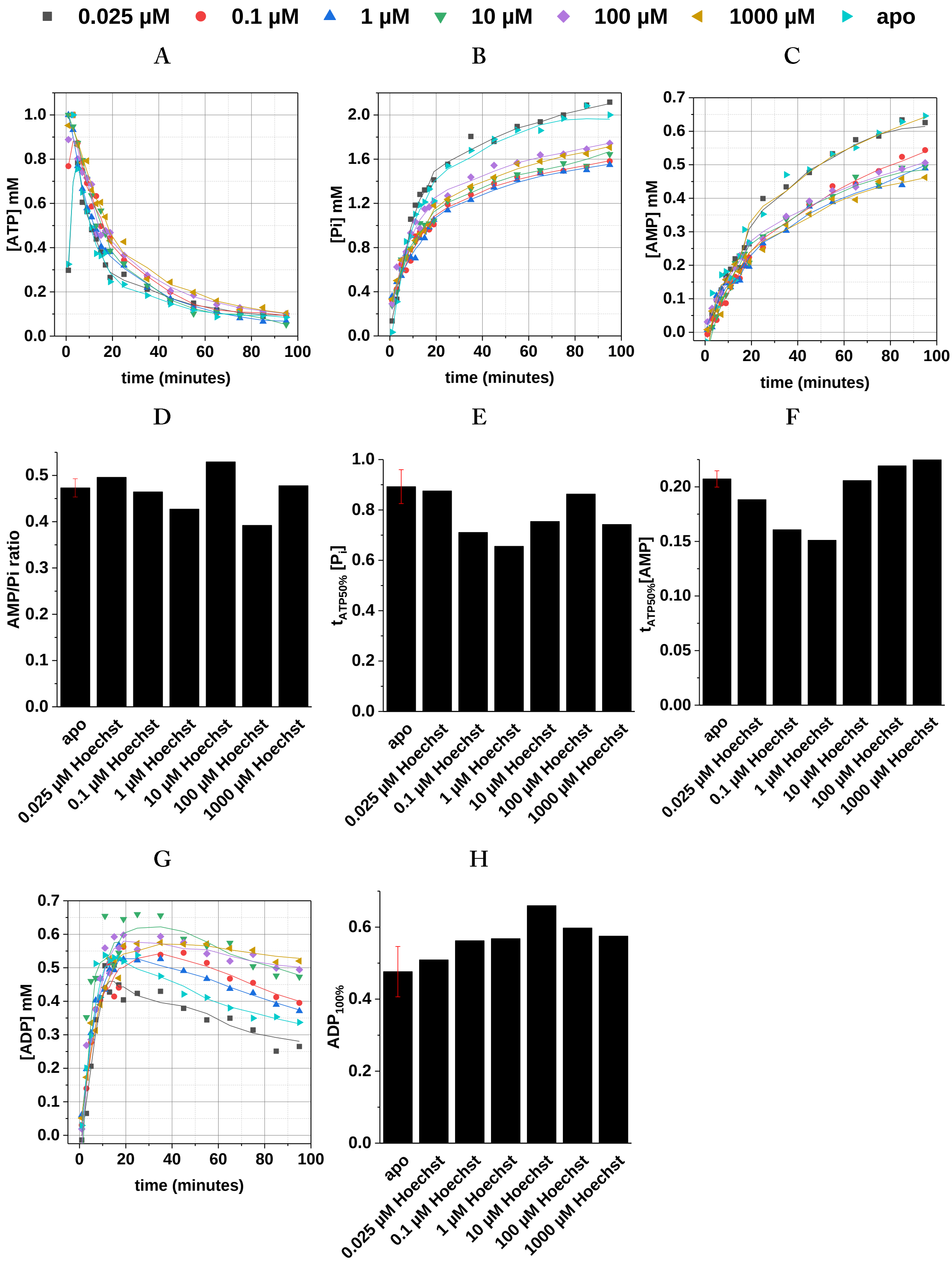

Figure 7.13. The effect of H33342 on the ATP hydrolysis of MsbA in DDM micelles in lsNMR. Progress curves of ATP (A), Pi (B), AMP (C), and ADP (G) from 0.025 µM to 1000 µM H33342 with 1 mM ATP. The curve trend is shown by the moving averages as lines. AMP/Pi ratio (D) at $t_{ATP>90\%}$, Pi (E), AMP (F), and ADP (H) buildup at $t_{ATP50\%}$ at various H33342 concentrations (*apo state n=3*).

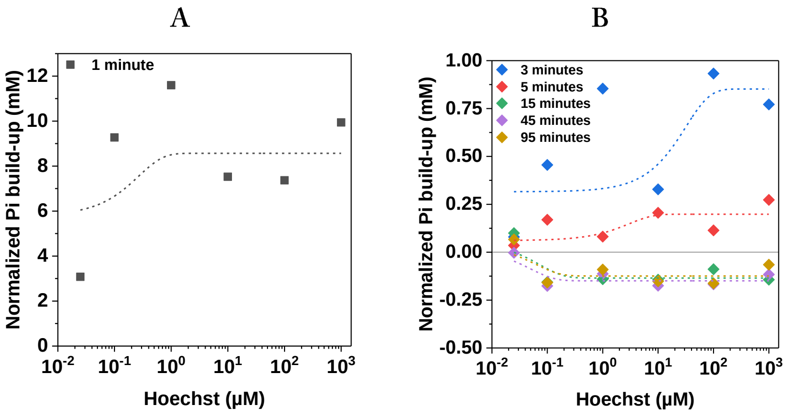

Figure 7.14. The effect of H33342 on the ATP hydrolysis of MsbA in DDM micelles in lsNMR across time. Normalized Pi buildup (apo state normalized to zero) across time plotted as dose-response curves. A) Dose-response curve at 1 minute of the reaction showing a 12-fold Pi buildup compared to the apo state (normalized to zero). B) At 3 and 5 minutes H33342 still show stimulation of ATP hydrolysis. After 15 minutes H33342 seems to inhibit the Pi buildup.

7.4.3 The effect of substrates on the ATP hydrolysis in DDM micelle MsbA

Additionally, other substrates were compared to each other (figure 7.15). Here, the concentration of the substrates was set on 100 µM, with the exception of 3 mM orthovanadate (VO_4). The VO_4 was used as a control, as can be seen, by adding VO4 the ADP consumption is inhibited due to the formation of ADP vanadate (ADP•Vi). Furthermore, the AMP/P_i ratio appears to be the affected by the molecular weight, log D, log P, the number of hydrogen bond (H-bond) acceptors and donors, and the polar surface area of the substrates (**table 7.4 and figure 7.16**). The correlations are negative with increasing the molecular weight, number of H-bond donors and acceptors, and polar surface area. Positive correlations were found for increasing log D and log P. While the ADP, AMP, and Pi buildup ($t_{ATP50\%}$) did not show a direct correlation with the physicochemical properties, clear differences could still be observed (**figures 7.15E, F, and H**). H33342, Verapamil, and Daunorubicin have the highest AMP buildup at $t_{ATP50\%}$.

Similarly, to H33342, the k_{ATP} appears to be slower with substrates compared to the apo state of MsbA (table 7.5). However, differences can still be observed between the different substrates. Progress curve analysis showed that synthetic lipid A and ADP•Vi have the lowest ATP hydrolysis rate (table 7.5). Despite a very high k_{AMP} in the ADP•Vi sample, AMP buildup is inhibited (figure 7.15C). The MsbA sample after one hour solubilisation has the high ATP hydrolysis, Pi buildup, and AMP buildup rates, which is similar to previous publication[59]. In addition, Verapamil, streptomycin, and Daunorubicin also have very high k_{ATP}, k_{Pi}, and k_{AMP} compared to other substrates.

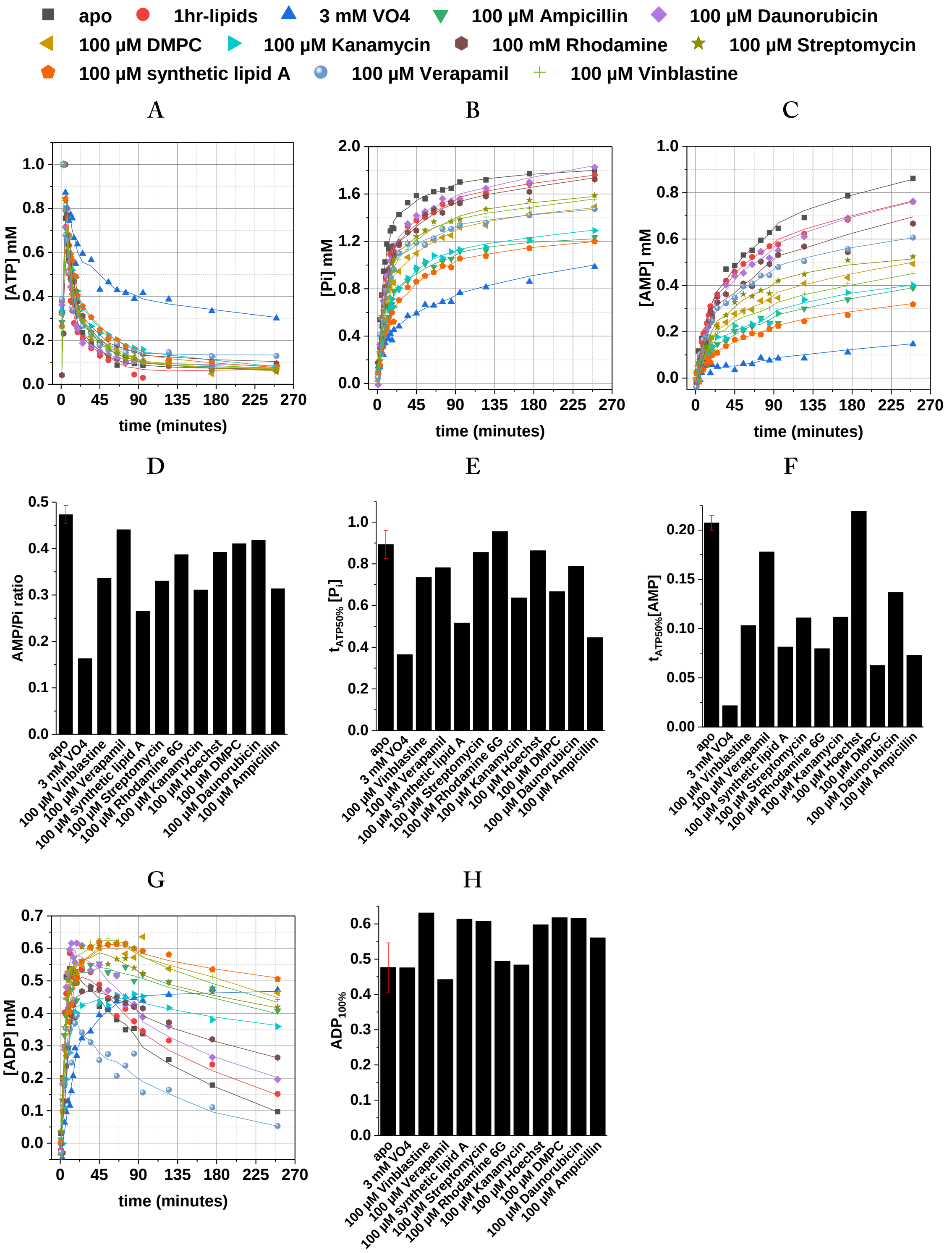

Figure 7.15. The effect substrates (100 µM) on the ATP (1 mM) hydrolysis of MsbA in DDM micelles in ^{31}P lsNMR. Progress curves of ATP (A), Pi (B), AMP (C), and ADP (G). The curve trend is shown by the moving averages as lines. Overview of the AMP/Pi ratio (D) at $t_{ATP>90\%}$, Pi (E), AMP (F), and ADP (H) buildup at $t_{ATP50\%}$ of various substrates (*apo state n=3*).

Table 7.4 Correlations of the MsbA AMP/Pi ratio between different substrate physicochemical properties.

	Pearson
Molecular weight	-0.6664*
Log D	0.715*
log P	0.737*
H-bond acceptor	-0.792*
H-bond donor	-0.7453*
polar surface area Å²	-0.816*

**Significant Pearson correlation*

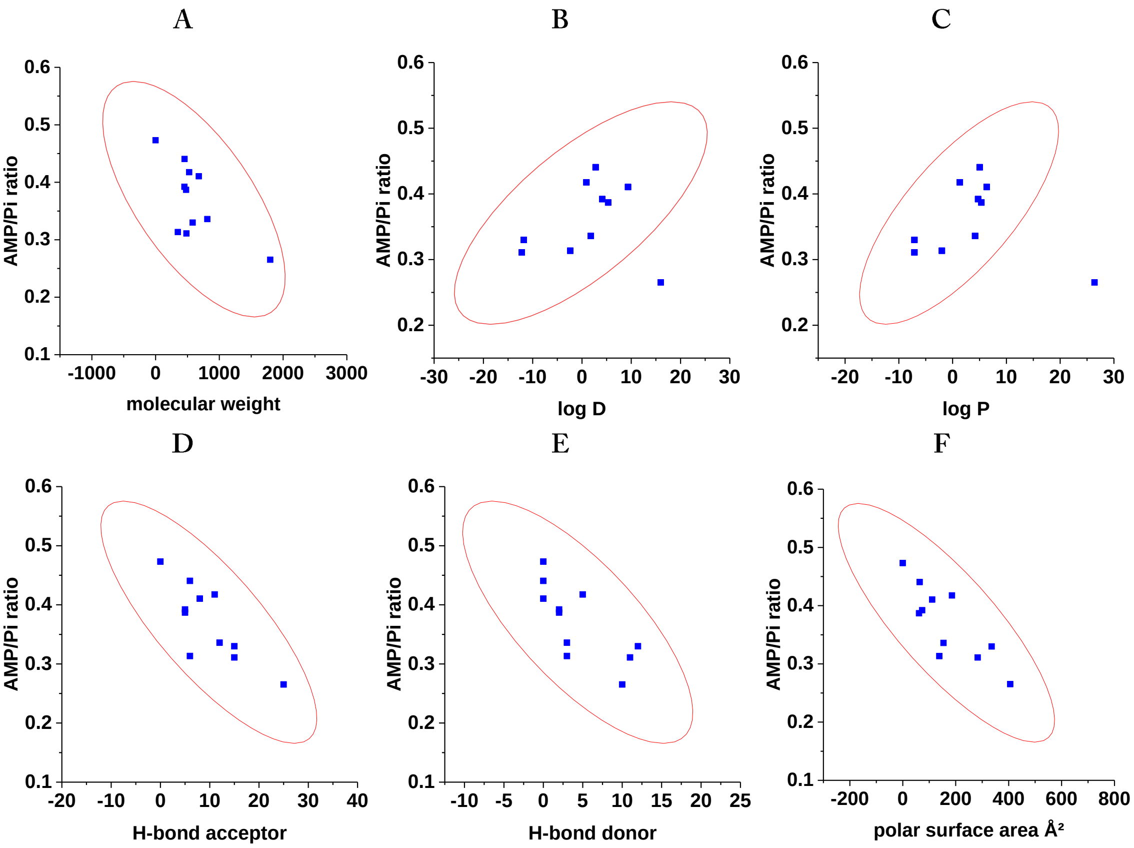

Figure 7.16. Covariance matrix with 95% confidence ellipses. AMP/Pi ratio (**figure 7.15F**) is plotted against the molecular weight (A), log D (B), log P (C), number of H-bond acceptors (D) and donors (E), and polar surface area (F) of the substrates (**figure 7.8**).

Table 7.5 ^{31}P liquid state NMR analysis of MsbA in DDM micelles of k_{ATP}, k_{Pi}, and k_{AMP}.

Substrate	[ATP]	k_{ATP} (min^{-1})	R^2	k_{Pi} (min^{-1})	R^2	k_{AMP} (min^{-1})	R^2
Apo	0.5 mM	$1.7\cdot 10^{-1}$	0.889	$1.1\cdot 10^{-1}$	0.983	$5.3\cdot 10^{-2}$	0.941
Apo (n≥5)	1 mM	$1.0\cdot 10^{-1}$ $\pm 1.0\cdot 10^{-2}$	0.986	$7.3\cdot 10^{-2}$ $\pm 1.0\cdot 10^{-2}$	0.984	$2.6\cdot 10^{-2}$ $\pm 2.0\cdot 10^{-3}$	0.983
Apo	2 mM	$4.6\cdot 10^{-2}$	0.992	$1.9\cdot 10^{-2}$	0.943	$5.5\cdot 10^{-3}$	0.974
Apo	3 mM	$2.9\cdot 10^{-2}$	0.997	$1.5\cdot 10^{-2}$	0.995	$1.0\cdot 10^{-2}$	0.997
Apo	6 mM	$1.5\cdot 10^{-2}$	0.977	$8.1\cdot 10^{-3}$	0.992	$2.8\cdot 10^{-3}$	0.990
Apo	8 mM	$1.6\cdot 10^{-2}$	0.999	$7.8\cdot 10^{-3}$	0.993	$2.7\cdot 10^{-3}$	0.997
Apo	12 mM	$1.9\cdot 10^{-2}$	0.985	$1.1\cdot 10^{-2}$	0.998	$6.9\cdot 10^{-3}$	0.996
Apo	16 mM	$7.5\cdot 10^{-3}$	0.992	$5.0\cdot 10^{-3}$	0.994	$1.3\cdot 10^{-3}$	0.996
H33342 0.025 μM	1 mM	$9.1\cdot 10^{-2}$	0.982	$6.9\cdot 10^{-2}$	0.983	$3.2\cdot 10^{-2}$	0.989
H33342 0.1 μM	1 mM	$5.5\cdot 10^{-2}$	0.991	$4.9\cdot 10^{-2}$	0.986	$2.5\cdot 10^{-2}$	0.994
H33342 1 μM	1 mM	$6.9\cdot 10^{-2}$	0.990	$4.3\cdot 10^{-2}$	0.990	$2.9\cdot 10^{-2}$	0.982
H33342 10 μM	1 mM	$5.5\cdot 10^{-2}$	0.992	$5.4\cdot 10^{-2}$	0.983	$4.0\cdot 10^{-2}$	0.985
H33342 100 μM	1 mM	$5.3\cdot 10^{-2}$	0.969	$5.6\cdot 10^{-2}$	0.982	$3.6\cdot 10^{-2}$	0.991
H33342 1000 μM	1 mM	$4.7\cdot 10^{-2}$	0.987	$4.4\cdot 10^{-2}$	0.991	$3.2\cdot 10^{-2}$	0.981
1hr solubilisation	1 mM	$7.2\cdot 10^{-2}$	0.977	$7.2\cdot 10^{-2}$	0.963	$2.9\cdot 10^{-2}$	0.973
VO_4 3 mM	1 mM	$4.5\cdot 10^{-2}$	0.946	$4.5\cdot 10^{-2}$	0.958	$1.1\cdot 10^{-1}$	0.644
Ampicillin 100 μM	1 mM	$5.4\cdot 10^{-2}$	0.981	$5.4\cdot 10^{-2}$	0.973	$1.7\cdot 10^{-2}$	0.964
Daunorubicin 100 μM	1 mM	$7.0\cdot 10^{-2}$	0.987	$7.0\cdot 10^{-2}$	0.965	$2.3\cdot 10^{-2}$	0.975
DMPC 100 μM	1 mM	$6.0\cdot 10^{-2}$	0.977	$6.0\cdot 10^{-2}$	0.967	$1.9\cdot 10^{-2}$	0.955
Kanamycin 100 μM	1 mM	$5.4\cdot 10^{-2}$	0.985	$5.4\cdot 10^{-2}$	0.980	$2.0\cdot 10^{-2}$	0.922
Rhodamine 100 μM	1 mM	$6.4\cdot 10^{-2}$	0.981	$6.4\cdot 10^{-2}$	0.968	$2.6\cdot 10^{-2}$	0.946
Streptomycin 100 μM	1 mM	$7.6\cdot 10^{-2}$	0.974	$7.6\cdot 10^{-2}$	0.960	$2.5\cdot 10^{-2}$	0.970
Lipid A 100 μM	1 mM	$4.4\cdot 10^{-2}$	0.984	$4.4\cdot 10^{-2}$	0.978	$1.7\cdot 10^{-2}$	0.970
Verapamil 100 μM	1 mM	$7.9\cdot 10^{-2}$	0.965	$7.9\cdot 10^{-2}$	0.966	$2.9\cdot 10^{-2}$	0.964
Vinblastine 100 μM	1 mM	$6.5\cdot 10^{-2}$	0.976	$6.5\cdot 10^{-2}$	0.967	$2.2\cdot 10^{-2}$	0.933

In the 1-hour solubilisation, MsbA contains the natural co-purified lipids of C43DE3 E. coli cells [59].

7.4.4 The effect of substrates on the ADP consumption of MsbA in DDM micelle

The changes observed in the Pi and AMP buildup, and thus the AMP/P_i ratio is reflecting from the ADP consumption (k_{ADP}), which appears to be much slower than the ATP hydrolysis (k_{ATP}). The progress curve analysis showed that the ADP consumption rate is at least ten times slower compared to the ATP hydrolysis rate (table 7.6). This is also reflected by the Pi and AMP buildup of the ADP consumption. MsbA seems to prefer ATP hydrolysis over ADP consumption when its engaging with a substrate. To further investigate this, the hydrolysis was studied using ADP (figure 7.17).

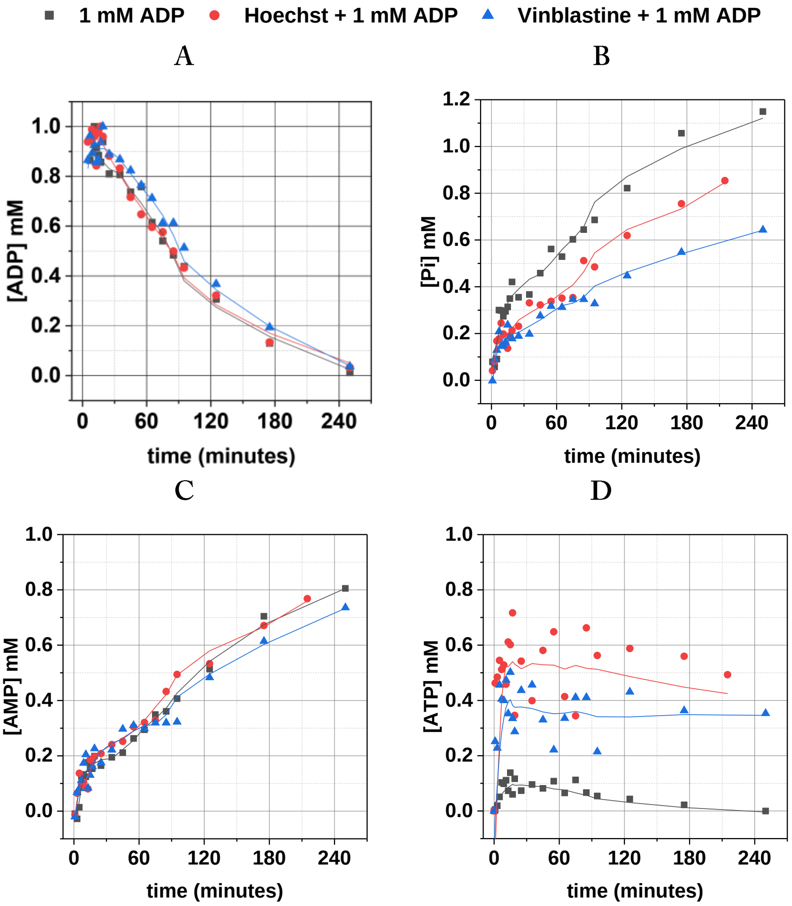

Figure 7.17. ADP consumption of MsbA in DDM micelles in ^{31}P lsNMR. The apo state is compared with H33342 and Vinblastine. Progress curves of ADP (A), Pi (B), AMP (C), and ATP (D). The curve trend is shown by the moving averages as lines.

H33342 and Vinblastine were selected as substrates, as both are known MsbA substrates[69,70].[64,65] Interestingly, the k_{ADP} is nearly 3-fold slower in the Vinblastine sample compared to apo MsbA, and the k_{AMP} is about 2-fold slower (table 7.6). In the case of H33342, the k_{Pi} is 3-fold slower. This is possible due the adenylate kinase reaction as nearly 50% ATP was regenerated during the ADP consumption reaction (figure 7.17D).

Table 7.6 ^{31}P solid-state NMR analysis of MsbA in liposomes of ADP consumption, AMP buildup, and Pi buildup rates.

Substrate	[ADP]	k_{ADP} (min^{-1})	R^2	k_{AMP} (min^{-1})	R^2	k_{Pi} (min^{-1})	R^2
Apo	1 mM	$7.3 \cdot 10^{-3}$	0.980	$6.1 \cdot 10^{-3}$	0.969	$8.2 \cdot 10^{-3}$	0.963
Apo	16 mM	$1.2 \cdot 10^{-3}$	0.905	$2.1 \cdot 10^{-3}$	0.441	$6.1 \cdot 10^{-4}$	0.803
H33342	1 mM	$4.8 \cdot 10^{-3}$	0.979	$4.5 \cdot 10^{-3}$	0.971	$2.8 \cdot 10^{-3}$	0.961
Vinblastine	1 mM	$2.0 \cdot 10^{-3}$	0.962	$3.1 \cdot 10^{-3}$	0.936	$4.8 \cdot 10^{-3}$	0.932

7.4.5 The ATP hydrolysis of MsbA in lipids

To further validate the effect of substrates on the MsbA activity, substrates were further analysed by ^{31}P solid-state NMR (ssNMR) in a more native environment. For this a fixed amount of ATP (1µmol) was used throughout all samples, which is equal to the absolute ATP amount used in the lsNMR experiments. The ATP hydrolysis was followed over time at 280K + ~10K MAS, comparable to the temperature in solution NMR (290K). The amount of MsbA was doubled (10 mg /rotor) to compensate for (1) inaccessibility of reconstituted MsbA protein orientation and (2) the accessibility in the NMR rotor as the nucleotides are added in the centre of the NMR rotor. Similar to the lsNMR experiments, to prevent a pH shift during the ATP hydrolysis, the samples and ATP solutions were buffered. Even though a slight shift was observed here (**figure 7.18**), the peaks where still clearly defined for the progress curve analysis.

Both ATP and ADP consumption by MsbA appear to be similar for both solution and solid-state NMR. The ATP hydrolysis in the NMR rotor is slightly slower than the solution state NMR sample, approximately 50%-time duration (**figure 7.19**). Due to the longer hydrolysis time the ATP hydrolysis rate is nearly 10-fold slower compared to MsbA in DDM micelles (table 7.7). The ATP hydrolysis rates of MsbA in liposomes follow the same trend as MsbA in DDM micelles, with decreasing rates with increasing ATP concentration as an effect of the longer hydrolysis time. To compare the activity of reconstituted MsbA with substrates with poor water solubility such as Daunorubicin, a control hydrolysis was carried out with DMSO (figure 7.19C). The ATP hydrolysis rate appears to be similar for the DMSO sample.

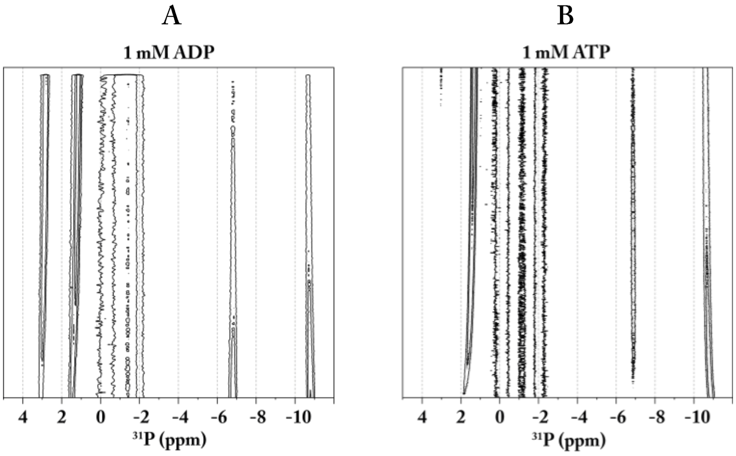

Figure 7.18. Buffered ssNMR conditions to prevent pH shifts during ATP hydrolysis across time. Slight shifts have been at 1 mM ATP.

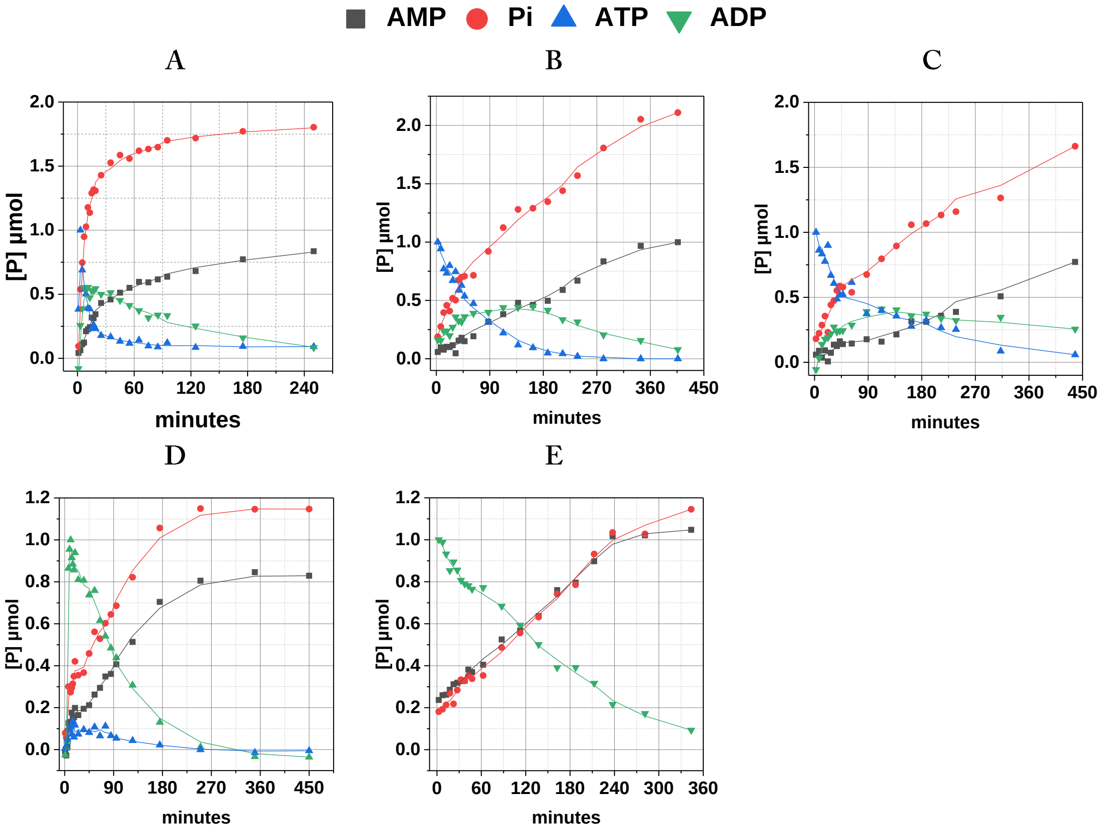

Figure 7.19. ATP and ADP of MsbA in DDM micelles versus lipids. A) MsbA in DDM (0.015%) micelles (lsNMR) 1 µmol ATP. B) MsbA in DMPC/DMPA liposomes (9:1) (ssNMR) 1 µmol ATP. C) MsbA in DMPC/DMPA liposomes (9:1) (ssNMR) 1 µmol ATP control with DMSO. D) MsbA in DDM (0.015%) micelles (lsNMR) 1 µmol ADP. E) MsbA in DMPC/DMPA liposomes (9:1) (ssNMR) 1 µmol ADP. The curve trend is shown by the moving averages as lines. *Lipid-to-protein ratio LPR=75:1.*

The substrates Daunorubicin, H33342, and Vinblastine at various concentrations showed small differences in their progress curves (figure 7.20-22). The AMP/Pi ratio of Daunorubicin, H33342, and Vinblastine appeared to not be affected by the substrates or the different concentrations (figure 7.23D). However, clear differences are observed for the buildup of the different nucleotides at different substrate concentrations.

At 1.6 µmol Daunorubicin the k_{ATP} (2.6· 10^{-2} min^{-1}) was twice as high compared the apo MsbA (1.2·10^{-2} min^{-1}) (table 7.7 and figure 7.20A). Furthermore, the k_{Pi} was nearly 10-fold higher at 1.6 µmoles compared to the DMSO control (table 7.7 and figure 7.19C), respectively 3.5· 10^{-2} and 3.6· 10^{-3} min^{-1}. In the case of the k_{AMP}, the rate was also 10-fold higher compared to apo MsbA respectively, 7.4· 10^{-3} and 7.5· 10^{-4} min^{-1} (table 7.7 and figure 7.20D). This fast buildup of AMP is reflected by the k_{ADP} and progress curve (figure 7.20C and 7.23F and G). Generally, the ADP buildup is higher at 70 nmoles and 160 nmoles Daunorubicin with a slower k_{ADP}.

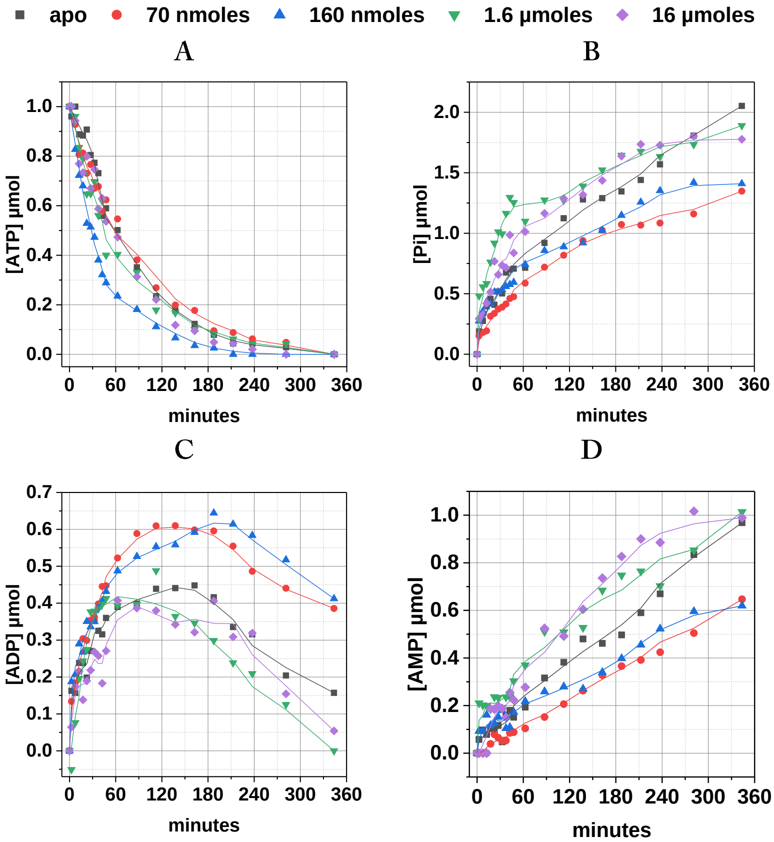

Figure 7.20. The effect of Daunorubicin on the ATP hydrolysis of MsbA in lipids using ^{31}P ssNMR. Progress curves of ATP hydrolysis (A), Pi buildup (B), AMP buildup (C), and ADP consumption (D) of 0.07, 0.16, 1.6, and 16 µmoles substrate with 1 mM ATP. The curve trend is shown by the moving averages as lines.

At 70 nmoles, 160 nmoles, and 1.6 nmoles of H33342, no significant changes were observed in the ATP hydrolysis or the Pi buildup rates (**table 7.7 and figure 7.21A and B**). However, at $ATP_{50\%}$, the Pi buildup was significantly higher at 1.6 μmoles compared to the apo state and the other H33342 concentrations (**figure 7.23E**). A higher concentration of 16 μmoles of H33342 significantly reduced the kinase reaction by approximately 10-fold in k_{ATP} and k_{Pi} (**table 7.7**) compared to apo MsbA, $8.4 \cdot 10^{-4}$ and $1.2 \cdot 10^{-2}$ min^{-1}), respectively. This is further reflected in the progress curves (**figure 7.21A-D**). Moreover, the AMP buildup appears to be affected by all H33342 samples, ranging from 2- to 6-fold higher in k_{AMP} compared to the apo state (**table 7.7**). The ADP consumption appears to be faster at 1.6 μmoles H33342 (**figure 7.21C**).

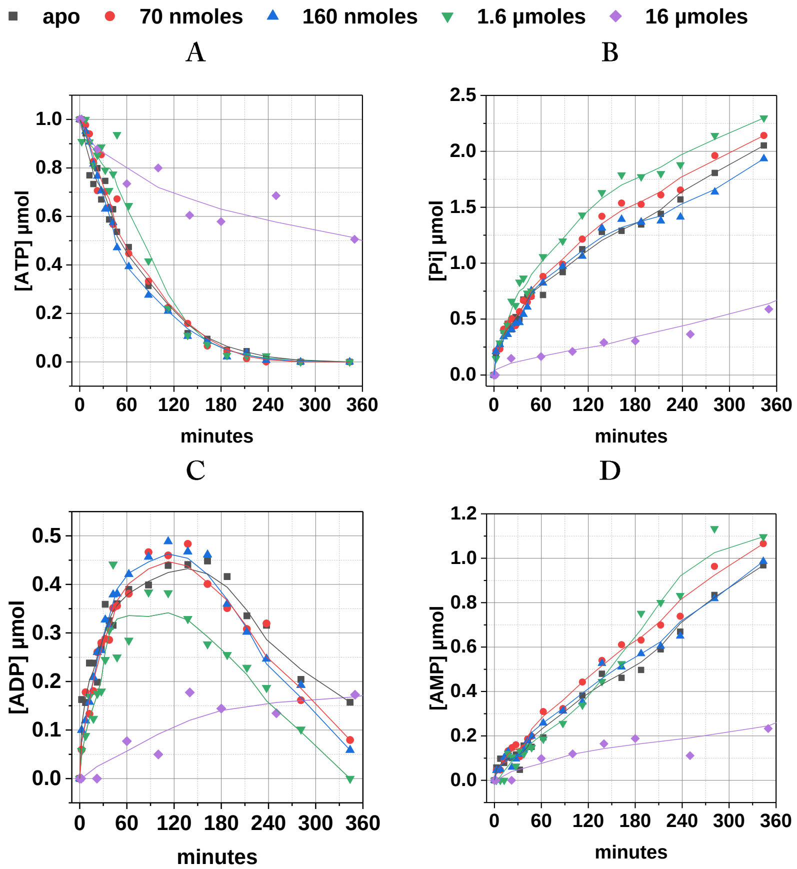

Figure 7.21. The effect of H33342 on the ATP hydrolysis of MsbA in lipids using ^{31}P ssNMR. Progress curves of ATP hydrolysis (A), Pi buildup (B), AMP buildup (C), and ADP consumption (D) of 0.07, 0.16, 1.6, and 16 μmoles substrate with 1 mM ATP. The curve trend is shown by the moving averages as lines.

The latter was similar for Vinblastine where the k_{AMP} were 2.5- to 4.5-fold higher compared to MsbA in the apo state (table 7.7 and figure 7.23F and G). No significant differences were observed for the k_{ATP} or k_{Pi}. Furthermore, at 70 nmoles of Vinblastine, the ADP buildup is higher compared to the other concentrations (figure 7.22A). The k_{ADP} is significantly slower, which is further reflected by the Pi and AMP buildup (figure 7.22B-D and figure 7.23F and G). Overall, the ATP hydrolysis in the samples with Vinblastine were not affected compared to H33342 or Daunorubicin (figure 7.23C and table 7.7).

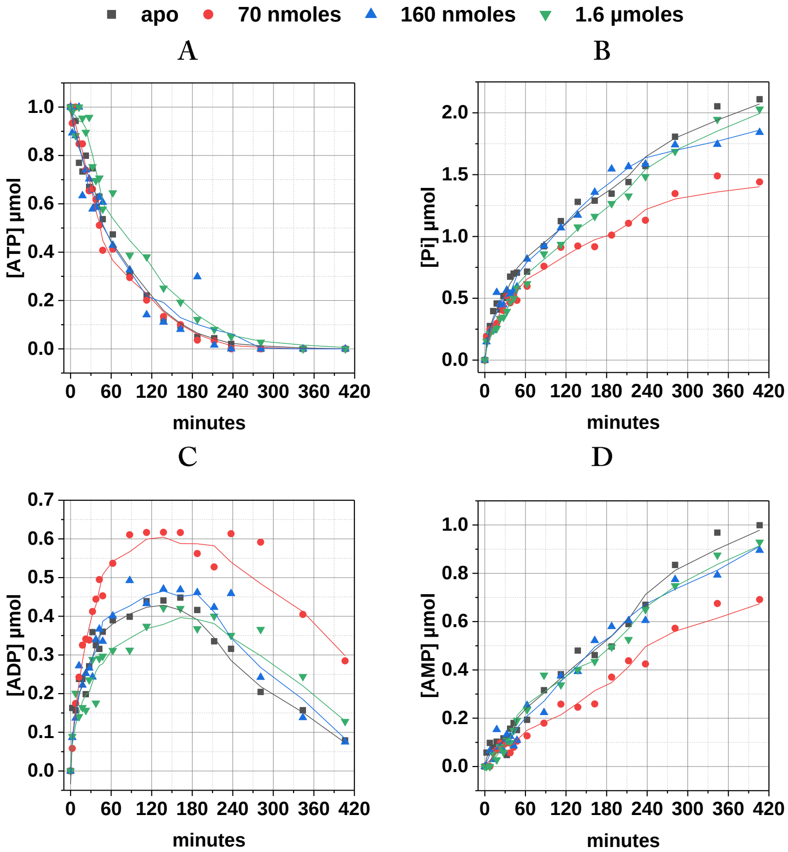

Figure 7.22. The effect of Vinblastine on the ATP hydrolysis of MsbA in lipids using ^{31}P ssNMR. Progress curves of ATP hydrolysis (A), Pi buildup (B), AMP buildup (C), and ADP consumption (D)of 0.07, 0.16, 1.6, and 16 µmoles substrate with 1 mM ATP. The curve trend is shown by the moving averages as lines.

Interestingly, the stimulation effect of H33342 in MsbA in DDM micelles was only observed within the first 15 minutes (figure 7.14), but in liposomes the effect was observed after approximately 30 minutes and lasted for more than 300 minutes (figure 7.23B). This is possibly due to the rebinding of H33342 in the lipid membranes, which allows H33342 to rebind to MsbA. Additionally, the inhibition effect of H33342 in MsbA in liposomes is 3-fold higher, from -0.25 in DDM to -0.75 in liposomes, compared to that in DDM micelles (figure 7.14 and 7.23B). The 12-fold increase in Pi buildup in DDM micelles is not observed in liposomes.

The maximum stimulation of Daunorubicin in MsbA in liposomes at 2.5 minutes (figure 7.23A) is three times higher compared to the biochemical assay (20 minutes reaction time), is similar to H33342 (figure 7.9A), increasing from 0.5 in DDM to 1.5 in liposomes. After 30 minutes the Pi buildup is still twice a high compared to the conditions in DDM micelles. Inhibition by Vinblastine was similar to the biochemical assay, around -0.4 in both DDM and liposomes (figure 7.9B and 7.23C) for the entire reaction time.

Table 7.7 ^{31}P solid-state NMR analysis of MsbA in liposomes of k_{ATP}, k_{AMP}, and k_{Pi}.

Substrate	**[ATP]**	**k_{ATP} (min^{-1})**	**R^2**	**k_{Pi} (min^{-1})**	**R^2**	**k_{AMP} (min^{-1})**	**R^2**
Apo	0.5 µmol	$2.9\cdot 10^{-2}$	0.943	$1.7\cdot 10^{-2}$	0.997	$2.8\cdot 10^{-3}$	0.990
Apo	1 µmol	$1.2\cdot 10^{-2}$	0.984	$7.4\cdot 10^{-3}$	0.987	$1.0\cdot 10^{-3}$	0.985
Apo	2 µmol	$6.3\cdot 10^{-3}$	0.994	$1.5\cdot 10^{-3}$	0.996	$6.1\cdot 10^{-5}$	0.996
Apo	4 µmol	$2.2\cdot 10^{-3}$	0.995	$8.1\cdot 10^{-4}$	0.997	$3.8\cdot 10^{-6}$	0.956
Apo	6 µmol	$1.3\cdot 10^{-3}$	0.994	$5.5\cdot 10^{-3}$	0.977	$6.6\cdot 10^{-6}$	0.946
DMSO	1 µmol	$9.2\cdot 10^{-3}$	0.919	$3.6\cdot 10^{-3}$	0.983	$7.5\cdot 10^{-4}$	0.992
H33342 70 nmol	1 µmol	$1.2\cdot 10^{-2}$	0.986	$8.8\cdot 10^{-3}$	0.985	$5.9\cdot 10^{-3}$	0.989
H33342 160 nmol	1 µmol	$1.4\cdot 10^{-2}$	0.996	$1.0\cdot 10^{-2}$	0.977	$4.9\cdot 10^{-3}$	0.985
H33342 1.6 µmol	1 µmol	$8.1\cdot 10^{-3}$	0.947	$1.1\cdot 10^{-2}$	0.982	$6.4\cdot 10^{-3}$	0.969
H33342 16 µmol	1 µmol	$8.4\cdot 10^{-4}$	0.928	$6.1\cdot 10^{-4}$	0.880	$1.8\cdot 10^{-3}$	0.719
Daunorubicin 70 nmol	1 µmol	$1.1\cdot 10^{-2}$	0.987	$1.1\cdot 10^{-2}$	0.989	$2.6\cdot 10^{-3}$	0.990
Daunorubicin 160 nmol	1 µmol	$1.1\cdot 10^{-2}$	0.993	$1.4\cdot 10^{-2}$	0.963	$4.4\cdot 10^{-3}$	0.956
Daunorubicin 1.6 µmol	1 µmol	$2.6\cdot 10^{-2}$	0.993	$3.5\cdot 10^{-2}$	0.907	$7.4\cdot 10^{-3}$	0.962
Daunorubicin 16 µmol	1 µmol	$1.5\cdot 10^{-2}$	0.985	$1.6\cdot 10^{-2}$	0.971	$8.0\cdot 10^{-3}$	0.980
Vinblastine 70 nmol	1 µmol	$1.5\cdot 10^{-2}$	0.990	$9.7\cdot 10^{-3}$	0.973	$2.7\cdot 10^{-3}$	0.971
Vinblastine 160 nmol	1 µmol	$1.3\cdot 10^{-2}$	0.951	$9.0\cdot 10^{-3}$	0.986	$4.4\cdot 10^{-3}$	0.980
Vinblastine 1.6 µmol	1 µmol	$8.8\cdot 10^{-3}$	0.977	$5.0\cdot 10^{-3}$	0.993	$4.5\cdot 10^{-3}$	0.986

The ATP and substrate amount were adjusted to the same absolute amount of ATP in solution NMR for comparison.

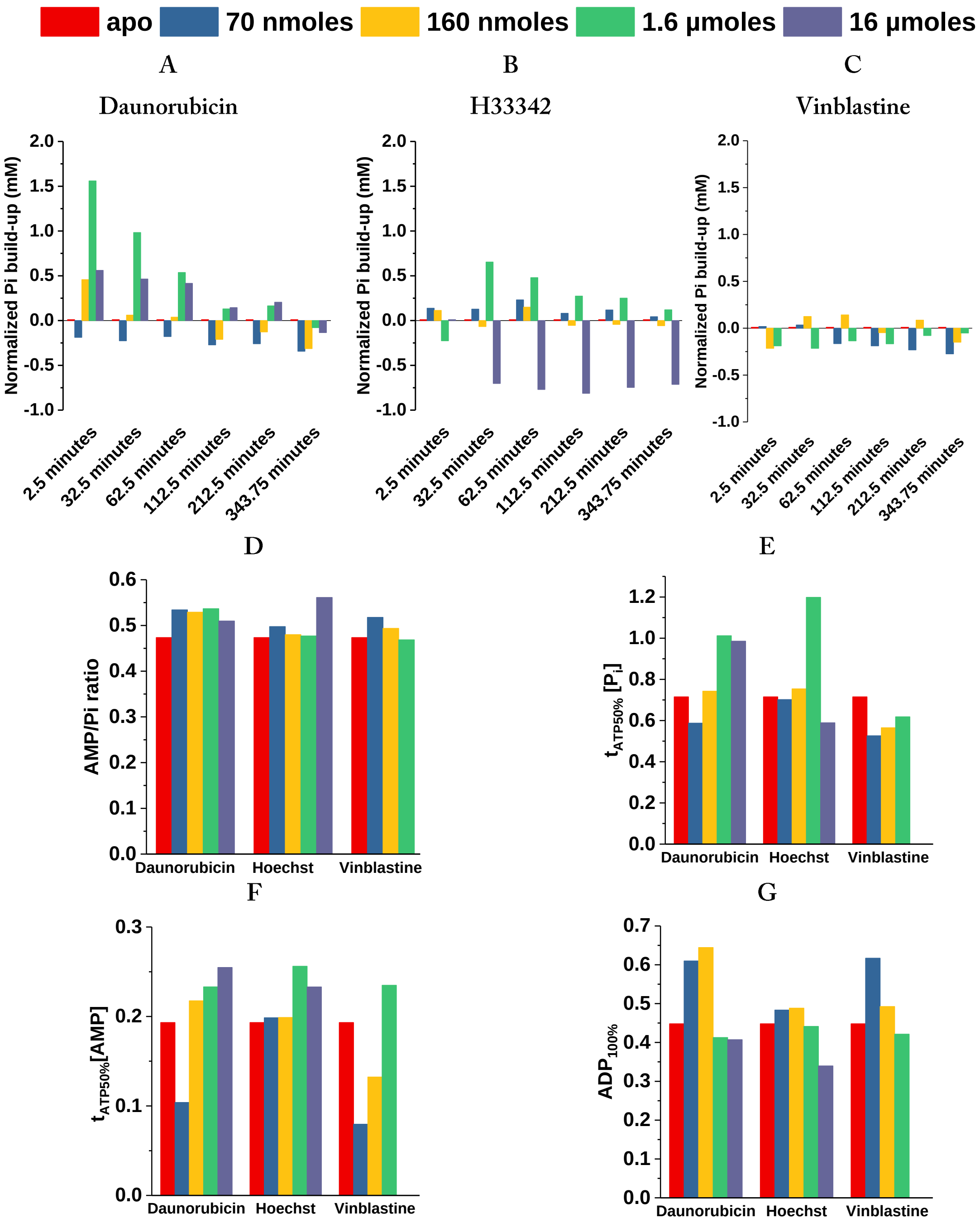

Figure 7.23. The effect of Daunorubicin, H33342, and Vinblastine on the ATP hydrolysis of MsbA in lipids at substrates concentrations. Normalized Pi buildup (apo state normalized to zero) was compared across time for Daunorubicin (A), H33342 (B), and Vinblastine (C). Overview of the AMP/Pi ratio (D) at $t_{ATP>90\%}$, ADP buildup (G), and Pi (E) and AMP (F) buildup at $t_{ATP50\%}$. MsbA kinase activity in the apo state is normalized to zero.

7.4.6 The effect of substrates on the ADP consumption of MsbA in lipids

Based on the analysis above, the effect of substrate on the ADP consumption was studied below. The substrate concentration was set to 1.6 µmoles, similar to the solution NMR samples. The ADP consumption of MsbA in liposomes is three times slower compared to the primary ATP hydrolysis reaction (table 7.8). Interestingly, the addition of substrate reduces the ADP consumption further (table 7.8 and figure 7.24). The addition of H33342 reduced the ADP consumption rate by 5-fold (table 7.8). In the case of Daunorubicin, the consumption rate reduced with 3-fold, but the AMP buildup rate reduced significantly by 20-fold. Vinblastine did not appear to affect the ADP consumption, but the overall effect was four times slower than in ATP consumption.

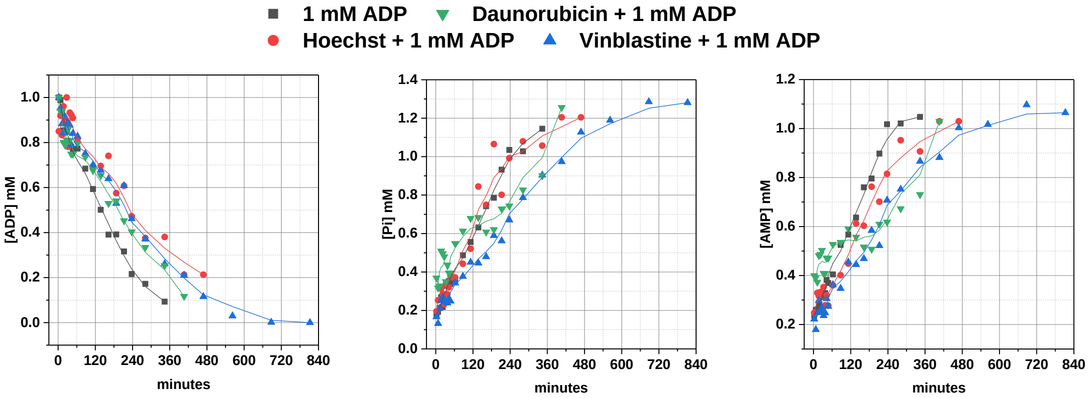

Figure 7.24. The effect of Daunorubicin, H33342, and Vinblastine on the ADP consumption of MsbA in lipids using ^{31}P ssNMR. Progress curve of 1.6 µmoles substrate with 1 mM ADP. The curve trend is shown by the moving averages as lines.

Table 7.8 ^{31}P solid-state NMR analysis of 1.6 µmoles H33342, Daunorubicin, and Vinblastine in MsbA in liposomes of k_{ADP}, k_{AMP}, and k_{Pi}.

Substrate	[ADP]	k_{ADP} (min^{-1})	R^2	k_{AMP} (min^{-1})	R^2	k_{Pi} (min^{-1})	R^2
Apo	1 mM	$3.4 \cdot 10^{-3}$	0.986	$2.8 \cdot 10^{-3}$	0.986	$2.2 \cdot 10^{-3}$	0.986
H33342	1 mM	$6.6 \cdot 10^{-4}$	0.936	$2.5 \cdot 10^{-3}$	0.963	$4.1 \cdot 10^{-3}$	0.947
Daunorubicin	1 mM	$1.1 \cdot 10^{-3}$	0.966	$1.2 \cdot 10^{-4}$	0.814	$1.9 \cdot 10^{-4}$	0.883
Vinblastine	1 mM	$2.2 \cdot 10^{-3}$	0.982	$2.4 \cdot 10^{-3}$	0.978	$1.7 \cdot 10^{-3}$	0.988

Furthermore, the ADP consumption rate in the H33342 sample was more than 120-fold slower than the ATP consumption rate. For Daunorubicin and Vinblastine this >20 and 4 times, respectively. This is possibly because (1) MsbA prefers the primary reaction to transport the substrates. Moreover, as discussed above (figure 7.17D), (2) the addition of substrate stimulates the production of ATP in the MsbA DDM micelles experiments. However, due to the low signal-to-noise level, this was not possible to conclude from the ssNMR experiments. Nevertheless, previous MsbA studies already showed the ATP buildup in the apo state using ADPβS in ssNMR.[33]

7.4.7 The effect of substrates on the ATP hydrolysis of MsbA in POPE/POPG/cardiolipin

When MsbA is in a more native environment MsbA like POPE/POPG membranes or POPE/POPG/cardiolipin membranes, the k_{ATP} is significantly higher rather in POPE/POPG and POPE/POPG/cardiolipin membranes, 3- and 17-fold respectively. The ATP hydrolysis in POPE/POPG was still two times slower compared to DDM micelles, but in POPE/POPG/CL it was twice as fast compared to MsbA in DDM micelles. The total ADP buildup appears to be similar to MsbA in DDM micelles. Yet, the ADP consumption appears to be very slow in both MsbA in DDM micelles and in DMPC/DMPA membranes despite that.

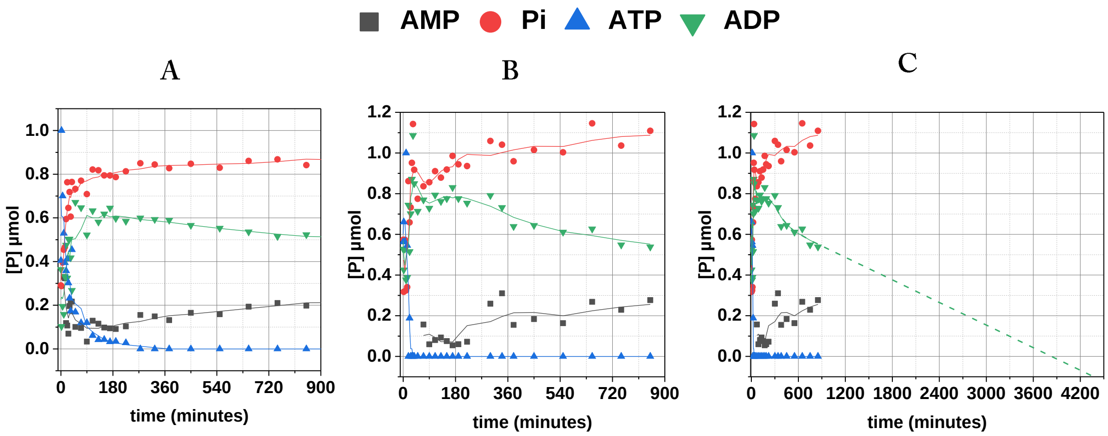

Figure 7.25. ATP hydrolysis of MsbA in POPE/POPG lipids versus POPE/POPG/cardiolipin lipids in ^{31}P ssNMR. A) MsbA in POPE/POPG (4:1) lipids with rates of $4.5\cdot 10^{-2}$ (R^2=0.919), $4.5\cdot 10^{-2}$ (R^2=0.923), and $6.2\cdot 10^{-6}$ (R^2=0.783) for ATP, Pi, and AMP, respectively. B) MsbA in POPE/POPG/CL (8:2:1) lipids rates of $2.1\cdot 10^{-1}$ (R^2=0.950), $3.8\cdot 10^{-2}$ (R^2=0.677), and $4.0\cdot 10^{-3}$ (R^2=0.639) for ATP, Pi, and AMP, respectively. The curve trend is shown by the moving averages as lines. C) Figure B with ADP progress curve extrapolated. *Lipid-to-protein ratio LPR=75:1.*

To roughly compare the two conditions, the ADP progress curve was extrapolated to estimate the time needed to fully hydrolyse ADP. Based on these results, the time needed to fully hydrolyse ADP would be roughly 10 times as long when compared to MsbA in DDM micelles or MsbA in DMPC/DMPA membranes.

7.5 Discussion

In this chapter the MsbA ATP hydrolysis and the adenylate kinase reaction was studied using ^{31}P real-time NMR. Progress curves were obtained from the reactions in the NMR spectroscopy and where further analysed using a closed form of Michaelis-Menten kinetics to obtain reaction rates. This single-exponential curve[58] form of Michaelis-Menten kinetics method in progress curve analysis allowed a good way to obtain useful information from progress curves without further complications compared to the other progress curve analysis methods discussed above.

7.5.1 Effect of substrate on the ATPase activity

It is known that H33342 stimulates MsbA, but in higher concentration it can also inhibit ATP hydrolysis[59]. It is possible that MsbA has multiple binding site where H33342 molecules, similar to the binding of Vinblastine to P-glycoprotein[66]. At the maximum H33342 stimulation (250%), the ATPase activity resulted in an increase in the affinity by 2-fold (K_M) (**figure 7.7 and table 7.3**). Lipid A, kanamycin, and ampicillin showed no significant increase in stimulated activity. As described above, lipid A does not appear to affect the ATP hydrolysis of MsbA in contrast to what has previously been reported. As Lipid A only increase ATPase activity by 20%, it is most likely that under the conditions used in this dissertation, MsbA possibly has co-purified Lipid A. Hence, MsbA cannot be further stimulated by the additional synthetic Lipid A (**figure 7.9a**). Potential causes would be the use of lipid A variants as substrate and the difficulty to control the amount of copurified core-LPS bound to MsbA upon purification. It has been shown in the literature that multiple core-LPS species can possibly bind to MsbA and get modulated differently by purification conditions[67,68]. Also, some of the available cryo-EM and X-ray structures contain lipid A substrates but others not, which is not correlated with the conformational state in which MsbA was trapped but seems to depend on the sample preparation conditions.[69] This observation is also in line with the degree of lipid A stimulated ATPase activity reported throughout the literature, which varies remarkably indicating varying amounts of pre-bound substrate[63,67,70].

7.5.2 The effect of substrates on the ATP hydrolysis in DDM micelles

Probing MsbA in ^{31}P lsNMR, reconfirmed that MsbA undergoes the adenylate kinase reaction when ATP is depleted as previous studies have shown[30,33,39]. Sharp transitions due to averaging of anisotropic NMR interactions by rapid tumbling allowed visible buildups of ATP signals as a result of the adenylate kinase reaction after the initial ATP consumption, which is normally harder to observe in ssNMR due to line-broadening. Whereas ssNMR allowed a good control of the reactions with MsbA in its more native protein state and compliments the lsNMR data. As shown in figure 7.17, the addition of ADP to MsbA resulted in ATP buildup even though no initial ATP was added to the reaction.

This is in agreement with previous MsbA study in DMPC/DMPA membranes where non-hydrolysable ATPβS was synthesized via the adenylate kinase reaction from ADPβS[33]. Furthermore, with the addition of substrates such as Vinblastine and H33342, MsbA appears to have undergo the adenylate kinase reaction, which resulted in a clear ATP buildup. The maximum ATP buildup in the MsbA apo state was approximately 10% based on the initially added ADP in the reaction (figure 7.17D). The buildup with substrates was particularly higher, approximately 4-6-fold (40-60%) when compared to the apo state. Possibly, in this way MsbA can transport the substrates using the primary ATP hydrolysis.

In addition, other parameters such as the AMP/Pi ratio, Pi and AMP buildup ($t_{ATP50\%}$), and the maximum ADP buildup ($t_{AD100\%}$) could also be used for additional analysis of the data sets. Moreover, the AMP/P$_i$ ratio was significantly affected by the molecular weight, log D, log P, the number of hydrogen bond (H-bond) acceptors and donors, and the polar surface area of the substrates (table 7.4 and figure 7.16). The negative correlations with increasing the molecular weight, number of H-bond donors and acceptors, and polar surface area, suggest that MsbA requires more energy for substrate transport of large molecules, therefore is highly dependent on its primary ATP hydrolysis. The positive correlation for log D indicates that the MsbA binding pockets are more lipophilic to accommodate large lipophilic substrates such as its endogenous lipid A. Despite that increasing number of H-bond donors and acceptors, and the polar surface area, increasing log P often leads to an increased binding potency or target engagement when lipophilic ligand–receptor interactions are important, thus leading to a positive log P correlation[71].

7.5.3 The ATP hydrolysis of MsbA in lipids

A more native lipid environment seems to prolong the effect of substrates in MsbA (**figure 7.14 and 7.23**). This has been clearly observed for H33342. However, no clear differences were observed in AMP/Pi ratio in reconstituted MsbA compared to MsbA in detergent micelles. Furthermore, due to the lower resolution in ssNMR, no ATP buildup was observed as result of the adenylate kinase reaction during ADP consumption. Although the reconstitution efficiency is similar in DMPC/DMPA compared to POPE/POPG (**Kaur et al 2015**[59] **and** chapter 4, figure 4.5). when MsbA is in a more native environment MsbA like POPE/POPG membranes or POPE/POPG/cardiolipin membranes, the ATP consumption is much faster than in DMPC/DMPA.

The ADP consumption is compared to MsbA in DDM micelles significantly slower than ATP hydrolysis only. In the POPE/POPG/cardiolipin membranes, the ADP consumption is ten times longer compared to MsbA in DDM micelles or MsbA in DMPC/DMPA membranes. Additionally, previous EPR study showed that in presence of ADP, MsbA shifts from an outward-facing to an inward-facing state, similarly to TmrAB[72,73].[72,73] Interestingly, ADP binding in the MsbA NBD region is shown to be very similar to ATP binding in a Fourier transform infrared spectroscopy study. This indicates that MsbA favours its primary ATP hydrolysis reaction over the ADP nucleotide[74]. Nevertheless, it appears to be highly dependent on the protein environment[68,75,76].

7.5.4 Outlook

Depending on the substrates or depletion conditions MsbA has the ability to (re)generate ATP via the adenylate kinase reaction, which has already been indicated by the ADP consumption using various substrates. To further investigate the adenylate kinase reaction in a more native lipid environment such as POPE or *E. coli* polar lipids and the effects of different substrates, ADPβS could be used to study ATPβS buildup in ssNMR to overcome low signal-to-noise[33]. As different substrates seem to influence this process, further studies could provide more insight into the physiological relevance of this process. Furthermore, a more in-depth progress curve analysis could provide more information in addition to the rate analysis given in this chapter. As discussed on section 7.2, the Lambert Omega function could provide a more precise fitting of the progress curves with K_M and V_{MAX} values. This would require a model that assumes a reverse adenylate kinase mechanism, thus resulting in more accurate kinetic values[50].

References

1 Jardetzky, O. Simple allosteric model for membrane pumps. *Nature* **211**, 969-970, doi:10.1038/211969a0 (1966).

2 Wilkens, S. Structure and mechanism of ABC transporters. *F1000Prime Rep* **7**, 14, doi:10.12703/P7-14 (2015).

3 Reddy, V. S., Shlykov, M. A., Castillo, R., Sun, E. I. & Saier, M. H., Jr. The major facilitator superfamily (MFS) revisited. *FEBS J* **279**, 2022-2035, doi:10.1111/j.1742-4658.2012.08588.x (2012).

4 Szollosi, D., Rose-Sperling, D., Hellmich, U. A. & Stockner, T. Comparison of mechanistic transport cycle models of ABC exporters. *Biochim Biophys Acta Biomembr* **1860**, 818-832, doi:10.1016/j.bbamem.2017.10.028 (2018).

5 van der Does, C. & Tampe, R. How do ABC transporters drive transport? *Biol Chem* **385**, 927-933, doi:10.1515/BC.2004.121 (2004).

6 Higgins, C. F. & Linton, K. J. The ATP switch model for ABC transporters. *Nat Struct Mol Biol* **11**, 918-926, doi:10.1038/nsmb836 (2004).

7 Janas, E. *et al.* The ATP hydrolysis cycle of the nucleotide-binding domain of the mitochondrial ATP-binding cassette transporter Mdl1p. *J Biol Chem* **278**, 26862-26869, doi:10.1074/jbc.M301227200 (2003).

8 Chen, J., Lu, G., Lin, J., Davidson, A. L. & Quiocho, F. A. A tweezers-like motion of the ATP-binding cassette dimer in an ABC transport cycle. *Mol Cell* **12**, 651-661, doi:10.1016/j.molcel.2003.08.004 (2003).

9 Smith, P. C. *et al.* ATP Binding to the Motor Domain from an ABC Transporter Drives Formation of a Nucleotide Sandwich Dimer. *Molecular Cell* **10**, 139-149, doi:10.1016/s1097-2765(02)00576-2 (2002).

10 Sauna, Z. E. & Ambudkar, S. V. About a switch: how P-glycoprotein (ABCB1) harnesses the energy of ATP binding and hydrolysis to do mechanical work. *Mol Cancer Ther* **6**, 13-23, doi:10.1158/1535-7163.MCT-06-0155 (2007).

11 Sauna, Z. E. *et al.* Catalytic cycle of ATP hydrolysis by P-glycoprotein: evidence for formation of the E.S reaction intermediate with ATP-gamma-S, a nonhydrolyzable analogue of ATP. *Biochemistry* **46**, 13787-13799, doi:10.1021/bi701385t (2007).

12 Siarheyeva, A., Liu, R. & Sharom, F. J. Characterization of an asymmetric occluded state of P-glycoprotein with two bound nucleotides: implications for catalysis. *J Biol Chem* **285**, 7575-7586, doi:10.1074/jbc.M109.047290 (2010).

13 Jones, P. M. & George, A. M. Opening of the ADP-bound active site in the ABC transporter ATPase dimer: evidence for a constant contact, alternating sites model for the catalytic cycle. *Proteins* **75**, 387-396, doi:10.1002/prot.22250 (2009).

14 Senior, A. E., al-Shawi, M. K. & Urbatsch, I. L. The catalytic cycle of P-glycoprotein. *FEBS Lett* **377**, 285-289, doi:10.1016/0014-5793(95)01345-8 (1995).

15 Dzeja, P. P., Zeleznikar, R. J. & Goldberg, N. D. Adenylate kinase: Kinetic behavior in intact cells indicates it is integral to multiple cellular processes. *Molecular and Cellular Biochemistry* **184**, 169-182, doi:10.1023/a:1006859632730 (1998).

16 Janssen, E. *et al.* Adenylate kinase 1 gene deletion disrupts muscle energetic economy despite metabolic rearrangement. *EMBO J* **19**, 6371-6381, doi:10.1093/emboj/19.23.6371 (2000).

17 Dzeja, P. & Terzic, A. Adenylate kinase and AMP signaling networks: metabolic monitoring, signal communication and body energy sensing. *Int J Mol Sci* **10**, 1729-1772, doi:10.3390/ijms10041729 (2009).

18 Dzeja, P. P., Bast, P., Pucar, D., Wieringa, B. & Terzic, A. Defective metabolic signaling in adenylate kinase AK1 gene knock-out hearts compromises post-ischemic coronary reflow. *J Biol Chem* **282**, 31366-31372, doi:10.1074/jbc.M705268200 (2007).

19 Dzeja, P. P. & Terzic, A. Phosphotransfer networks and cellular energetics. *J Exp Biol* **206**, 2039-2047, doi:10.1242/jeb.00426 (2003).

20 Abrusci, P. *et al.* Erythrocyte adenylate kinase deficiency: characterization of recombinant mutant forms and relationship with nonspherocytic hemolytic anemia. *Exp Hematol* **35**, 1182-1189, doi:10.1016/j.exphem.2007.05.004 (2007).

21 Noma, T. Dynamics of nucleotide metabolism as a supporter of life phenomena. *J Med Invest* **52**, 127-136, doi:10.2152/jmi.52.127 (2005).

22 Rahlfs, S. *et al.* Myristoylated adenylate kinase-2 of Plasmodium falciparum forms a heterodimer with myristoyltransferase. *Mol Biochem Parasitol* **163**, 77-84, doi:10.1016/j.molbiopara.2008.09.008 (2009).

23 van Horssen, R. *et al.* Modulation of cell motility by spatial repositioning of enzymatic ATP/ADP exchange capacity. *J Biol Chem* **284**, 1620-1627, doi:10.1074/jbc.M806974200 (2009).

24 Fernandez-Gonzalez, A., Kourembanas, S., Wyatt, T. A. & Mitsialis, S. A. Mutation of murine adenylate kinase 7 underlies a primary ciliary dyskinesia phenotype. *Am J Respir Cell Mol Biol* **40**, 305-313, doi:10.1165/rcmb.2008-0102OC (2009).

25 Savabi, F., Geiger, P. J. & Bessman, S. P. Myokinase and contractile function of glycerinated muscle fibers. *Biochem Med Metab Biol* **35**, 227-238, doi:10.1016/0885-4505(86)90078-2 (1986).

26 Walker, E. J. & Dow, J. W. Location and properties of two isoenzymes of cardiac adenylate kinase. *Biochem J* **203**, 361-369, doi:10.1042/bj2030361 (1982).

27 Criss, W. E. Relationship of ATP:AMP phosphotransferase isozymes to tissue respiration. *Arch Biochem Biophys* **144**, 138-142, doi:10.1016/0003-9861(71)90463-2 (1971).

28 Tanabe, T., Yamada, M., Noma, T., Kajii, T. & Nakazawa, A. Tissue-specific and developmentally regulated expression of the genes encoding adenylate kinase isozymes. *J Biochem* **113**, 200-207, doi:10.1093/oxfordjournals.jbchem.a124026 (1993).

29 Lee, H. J. *et al.* AK2 activates a novel apoptotic pathway through formation of a complex with FADD and caspase-10. *Nat Cell Biol* **9**, 1303-1310, doi:10.1038/ncb1650 (2007).

30 Baeta, T. *et al.* LptB2FG is an ABC transporter with Adenylate Kinase activity regulated by LptC/A recruitment. *bioRxiv*, doi:10.1101/2021.07.08.451440 (2021).

31 Pannicke, U. *et al.* Reticular dysgenesis (aleukocytosis) is caused by mutations in the gene encoding mitochondrial adenylate kinase 2. *Nat Genet* **41**, 101-105, doi:10.1038/ng.265 (2009).

32 Lagresle-Peyrou, C. *et al.* Human adenylate kinase 2 deficiency causes a profound hematopoietic defect associated with sensorineural deafness. *Nat Genet* **41**, 106-111, doi:10.1038/ng.278 (2009).

33 Kaur, H. *et al.* Coupled ATPase-adenylate kinase activity in ABC transporters. *Nat Commun* **7**, 13864, doi:10.1038/ncomms13864 (2016).

34 Williams, R. S. & Tainer, J. A. Learning our ABCs: Rad50 directs MRN repair functions via adenylate kinase activity from the conserved ATP binding cassette. *Mol Cell* **25**, 789-791, doi:10.1016/j.molcel.2007.03.004 (2007).

35 Randak, C. O., Dong, Q., Ver Heul, A. R., Elcock, A. H. & Welsh, M. J. ATP and AMP mutually influence their interaction with the ATP-binding cassette (ABC) adenylate kinase cystic fibrosis transmembrane conductance regulator (CFTR) at separate binding sites. *J Biol Chem* **288**, 27692-27701, doi:10.1074/jbc.M113.479675 (2013).

36 Randak, C. & Welsh, M. J. An Intrinsic Adenylate Kinase Activity Regulates Gating of the ABC Transporter CFTR. *Cell* **115**, 837-850, doi:10.1016/s0092-8674(03)00983-8 (2003).

37 Lammens, A. & Hopfner, K. P. Structural basis for adenylate kinase activity in ABC ATPases. *J Mol Biol* **401**, 265-273, doi:10.1016/j.jmb.2010.06.029 (2010).

38 Bhaskara, V. *et al.* Rad50 adenylate kinase activity regulates DNA tethering by Mre11/Rad50 complexes. *Mol Cell* **25**, 647-661, doi:10.1016/j.molcel.2007.01.028 (2007).

39 Kaur, H. *et al.* Unexplored Nucleotide Binding Modes for the ABC Exporter MsbA. *J Am Chem Soc* **140**, 14112-14125, doi:10.1021/jacs.8b06739 (2018).

40 Miyanaga, K. & Unno, H. Reaction Kinetics and Stoichiometry. 33-46, doi:10.1016/b978-0-08-088504-9.00085-4 (2011).

41 Marangoni, A. G. *Enzyme Kinetics: A Modern Approach.* (JOHN WILEY & SONS, INC., 2003).

42 Stojan, J. Equations for progress curves of some kinetic models of enzyme-single substrate-single slow binding modifier system. *J Enzyme Inhib* **13**, 161-176, doi:10.3109/14756369809028338 (1998).

43 Goudar, C. T., Sonnad, J. R. & Duggleby, R. G. Parameter estimation using a direct solution of the integrated Michaelis-Menten equation. *Biochim Biophys Acta* **1429**, 377-383, doi:10.1016/s0167-4838(98)00247-7 (1999).

44 Goudar, C. T., Harris, S. K., McInerney, M. J. & Suflita, J. M. Progress curve analysis for enzyme and microbial kinetic reactions using explicit solutions based on the Lambert W function. *J Microbiol Methods* **59**, 317-326, doi:10.1016/j.mimet.2004.06.013 (2004).

45 Lehtonen, J. & Rees, M. The Lambert W function in ecological and evolutionary models. *Methods in Ecology and Evolution* **7**, 1110-1118, doi:10.1111/2041-210x.12568 (2016).

46 Corless, R. M., Gonnet, G. H., Hare, D. E. G., Jeffrey, D. J. & Knuth, D. E. On the LambertW function. *Advances in Computational Mathematics* **5**, 329-359, doi:10.1007/bf02124750 (1996).

47 Exnowitz, F., Meyer, B. & Hackl, T. NMR for direct determination of K(m) and V(max) of enzyme reactions based on the Lambert W function-analysis of progress curves. *Biochim Biophys Acta* **1824**, 443-449, doi:10.1016/j.bbapap.2011.10.011 (2012).

48 Schnell, S. & Mendoza, C. Closed Form Solution for Time-dependent Enzyme Kinetics. *Journal of Theoretical Biology* **187**, 207-212, doi:10.1006/jtbi.1997.0425 (1997).

49 Schnell, S. & Mendoza, C. Enzyme kinetics of multiple alternative substrates. *Journal of Mathematical Chemistry* **27**, 155-170, doi:10.1023/a:1019139423811 (2000).

50 Golicnik, M. Explicit reformulations of time-dependent solution for a Michaelis-Menten enzyme reaction model. *Anal Biochem* **406**, 94-96, doi:10.1016/j.ab.2010.06.041 (2010).

51 De La Cruz, E. M. & Ostap, E. M. Kinetic and equilibrium analysis of the myosin ATPase. *Methods Enzymol* **455**, 157-192, doi:10.1016/S0076-6879(08)04206-7 (2009).

52 Golicnik, M. Progress-curve analysis through integrated rate equations and its use to study cholinesterase reaction dynamics. *J Mol Neurosci* **53**, 330-334, doi:10.1007/s12031-013-0129-y (2014).

53 Stojan, J. Rapid Mechanistic Evaluation and Parameter Estimation of Putative Inhibitors in a Single-Step Progress-Curve Analysis: The Case of Horse Butyrylcholinesterase. *Molecules* **22**, 1248, doi:10.3390/molecules22081248 (2017).

54 Bauerle, F., Zotter, A. & Schreiber, G. Direct determination of enzyme kinetic parameters from single reactions using a new progress curve analysis tool. *Protein Eng Des Sel* **30**, 149-156, doi:10.1093/protein/gzw053 (2017).

55 Buchholz, P. C. F., Ohs, R., Spiess, A. C. & Pleiss, J. Progress Curve Analysis Within BioCatNet: Comparing Kinetic Models for Enzyme-Catalyzed Self-Ligation. *Biotechnol J* **14**, e1800183, doi:10.1002/biot.201800183 (2019).

56 Buchholz, P. C. *et al.* BioCatNet: A Database System for the Integration of Enzyme Sequences and Biocatalytic Experiments. *Chembiochem* **17**, 2093-2098, doi:10.1002/cbic.201600462 (2016).

57 Nikolova, N., Tenekedjiev, K. & Kolev, K. Uses and misuses of progress curve analysis in enzyme kinetics. *Cent Eur J Biol* **3**, 345-350, doi:10.2478/s11535-008-0035-4 (2008).

58 Golicnik, M. Exact and approximate solutions for the decades-old Michaelis-Menten equation: Progress-curve analysis through integrated rate equations. *Biochem Mol Biol Educ* **39**, 117-125, doi:10.1002/bmb.20479 (2011).

59 Kaur, H. *et al.* The ABC exporter MsbA probed by solid state NMR - challenges and opportunities. *Biol Chem* **396**, 1135-1149, doi:10.1515/hsz-2015-0119 (2015).

60 Eckford, P. D. & Sharom, F. J. Functional characterization of Escherichia coli MsbA: interaction with nucleotides and substrates. *J Biol Chem* **283**, 12840-12850, doi:10.1074/jbc.M708274200 (2008).

61 Smriti, Zou, P. & McHaourab, H. S. Mapping daunorubicin-binding Sites in the ATP-binding cassette transporter MsbA using site-specific quenching by spin labels. *J Biol Chem* **284**, 13904-13913, doi:10.1074/jbc.M900837200 (2009).

62 Woebking, B. *et al.* Drug-lipid A interactions on the Escherichia coli ABC transporter MsbA. *J Bacteriol* **187**, 6363-6369, doi:10.1128/JB.187.18.6363-6369.2005 (2005).

63 Doerrler, W. T. & Raetz, C. R. ATPase activity of the MsbA lipid flippase of Escherichia coli. *J Biol Chem* **277**, 36697-36705, doi:10.1074/jbc.M205857200 (2002).

64 Reuter, G. *et al.* The ATP binding cassette multidrug transporter LmrA and lipid transporter MsbA have overlapping substrate specificities. *J Biol Chem* **278**, 35193-35198, doi:10.1074/jbc.M306226200 (2003).

65 Reyes, C. L., Ward, A., Yu, J. & Chang, G. The structures of MsbA: Insight into ABC transporter-mediated multidrug efflux. *FEBS Lett* **580**, 1042-1048, doi:10.1016/j.febslet.2005.11.033 (2006).

66 Clouser, A. F. & Atkins, W. M. Long Range Communication between the Drug-Binding Sites and Nucleotide Binding Domains of the Efflux Transporter ABCB1. *Biochemistry* **61**, 730-740, doi:10.1021/acs.biochem.2c00056 (2022).

67 Padayatti, P. S. *et al.* Structural Insights into the Lipid A Transport Pathway in MsbA. *Structure* **27**, 1114-1123 e1113, doi:10.1016/j.str.2019.04.007 (2019).

68 Lyu, J. *et al.* Structural basis for lipid and copper regulation of the ABC transporter MsbA. *Nat Commun* **13**, 7291, doi:10.1038/s41467-022-34905-2 (2022).

69 Bonifer, C. & Glaubitz, C. MsbA: an ABC transporter paradigm. *Biochem Soc Trans* **49**, 2917-2927, doi:10.1042/BST20211030 (2021).

70 Mi, W. *et al.* Structural basis of MsbA-mediated lipopolysaccharide transport. *Nature* **549**, 233-237, doi:10.1038/nature23649 (2017).

71 Lindsley, C. W. Lipophilicity. 1-6, doi:10.1007/978-3-642-27772-6_7015-1 (2014).

72 Galazzo, L. *et al.* The ABC transporter MsbA adopts the wide inward-open conformation in E. coli cells. *Sci Adv* **8**, eabn6845, doi:10.1126/sciadv.abn6845 (2022).

73 Stefan, E., Hofmann, S. & Tampe, R. A single power stroke by ATP binding drives substrate translocation in a heterodimeric ABC transporter. *Elife* **9**, doi:10.7554/eLife.55943 (2020).

74 Mann, D. *et al.* ATP binding and ATP hydrolysis in full-length MsbA monitored via time-resolved Fourier transform infrared spectroscopy. *Biol Chem* **404**, 727-737, doi:10.1515/hsz-2023-0122 (2023).

75 Siarheyeva, A. & Sharom, F. J. The ABC transporter MsbA interacts with lipid A and amphipathic drugs at different sites. *Biochem J* **419**, 317-328, doi:10.1042/BJ20081364 (2009).

76 Guo, D. *et al.* Energetics of lipid transport by the ABC transporter MsbA is lipid dependent. *Commun Biol* **4**, 1379, doi:10.1038/s42003-021-02902-8 (2021).

Conclusion

MsbA plays a vital role in the multidrug resistance of Gram-negative bacteria in some harmful ESKAPE pathogens strains. It does this by flopping core LPS across the inner membrane in Gram-negative bacteria as part of the LPS protection pathway to the outer Gram-negative bacterial cell wall. Additionally, this floppase acts as an efflux pump by translocating drugs through the inner membrane, hence making it an interesting drug target to further explore novel antibiotics in ESKAPE pathogen strains.

Over the past two decades, there have been many crystal structures of MsbA showing various conformations. A wider apo or inward-facing conformation has been debated, possibly due to a detergent micelle environment of the membrane protein rather than a more native lipid bilayer environment. Thus, MsbA has been used to study human ABC transporter homologues such as P-glycoprotein.

MsbA has been captured in many different states by X-ray, cryo-EM, and NMR spectroscopy. The latter showed different states, such as the ADP.Vi+ADPβS and ADP.Vi+AMP, which previously were not observed in X-ray or cryo-EM structures of MsbA. Hence, MsbA appears to have a *de novo* adenine nucleotide synthesis mechanism, which is referred to as the adenylate kinase reaction. Real-time ^{31}P solution and solid-state NMR are good methods to study these reactions closely. These hydrolysis reactions are said to be coupled with the MsbA transport of LPS and other substrates via the coupling helices. Unique pair labelling in ssNMR resulted in specific peaks with good resolution and enabled a more detailed look at the conformational dynamics and crosstalk of the coupling helices of MsbA in DMPC/DPMA (9:1) and POPE/POPG (4:1) membranes.

The allosteric interplay between substrate binding in the transmembrane domains (TMDs) and ATP binding and turnover in the nucleotide-binding domains must be mediated via the NBD/TMD interface. Biochemical data suggest the involvement of two intracellular loops called coupling helix 1 and 2 (CH1, CH2). Here, it is demonstrated by solid-state NMR spectroscopy, that substantial chemical shift changes within both CH1 and CH2 occur upon substrate binding, during ATP hydrolysis and upon inhibitor binding. CH2 is domain-swapped within the MsbA structure, and it is noteworthy that substrate binding induces a much larger response in CH2 compared to CH1. The data demonstrated that CH1 and CH2 undergo structural changes as part of the TMD-NBD cross-talk.

The study presented here shows the first direct evidence of structural changes within the coupling helices of type IV ABC transporters upon switching from the IF to the OF state and upon substrate and inhibitor binding. The data show that ADP.Vi binding and the IF→OF transition causes at the NBD-TMD interface a stronger response in CH1 while substrate binding has a stronger effect in CH2. Notably, the latter is based on a domain-swapped interaction with the NBD. Both cases are caused by stimuli with different vectoriality, namely nucleotide binding to the NBD and substrate binding to the TMD, which might then involve different pathways for NBD→TMD and TMD→NBD crosstalk. The results also show that CH-mediated crosstalk plays a role in the mechanism of an allosteric MsbA inhibitor, which binds in the TMD but prevents ATP hydrolysis in the NBD. The observed spectral signatures are different compared to the substrate-bound state, which indicates a different interaction pathway.

Probing MsbA in ^{31}P lsNMR, reconfirmed that MsbA undergoes the adenylate kinase reaction when ATP is depleted as previous studies have shown. Furthermore, with the addition of substrates such as Vinblastine and H33342, MsbA appears to have undergone the adenylate kinase reaction, which resulted in a clear ATP build-up. Moreover, it is shown that the molecular weight, the number of hydrogen bond acceptors and donors, polar surface area, log D and log P of the substrates are correlated with the AMP/P_i ratio. Generally, the ATP hydrolysis is rather fast under the different tested conditions (DDM micelles, DMPC/DMPA, POPE/POPG(/CL)).

On the other hand, ADP consumption appears to depend more on the protein environment. When MsbA is in a more native environment e.g., POPE/POPG or POPE/POPG/cardiolipin membranes, the ADP consumption appears to be very slow compared to both MsbA in DDM micelles and in DMPC/DMPA membranes. Depending on the substrates or depletion conditions MsbA has the ability to (re)generate ATP via the adenylate kinase reaction, which has already been indicated by the ADP consumption using various substrates. MsbA appears to favour its primary ATP hydrolysis reaction over the ADP nucleotide, which was also indicated by the ADP consumption using various substrates.

This dissertation provided selective data, which are highly complementary to the available 3D structures. Future solid-state NMR experiments will address the potential interaction between CH1 and CH2 and connect NMR data and 3D structures via computational approaches. Furthermore, a more in-depth progress curve analysis could provide more information in addition to the rate analysis. Together, the observations here indicate that MsbA can (re)generate ATP via the adenylate kinase reaction under certain conditions (i.e., ATP depletion, substrates, and substrate physicochemical properties) and this appears to be coupled to the substrate transport.

Appendix

Colourimetric assay

Table A1. Colourimetric assay pipetting scheme

[ATP]	MsbA	ATP (6 mM)	Buffer	A	B+C=D	E
0.2 mM	1 µg	0 µL	30 µL	30 µL	60 µL	90 µL
0.25 mM	1 µg	1.25 µL	23.75 µL	30 µL	60 µL	90 µL
0.5 mM	1 µg	2.5 µL	22.5 µL	30 µL	60 µL	90 µL
1.0 mM	1 µg	5 µL	20 µL	30 µL	60 µL	90 µL
2.0 mM	1 µg	10 µL	15 µL	30 µL	60 µL	90 µL
3.0 mM	1 µg	15 µL	10 µL	30 µL	60 µL	90 µL
4.0 mM	1 µg	20 µL	5 µL	30 µL	60 µL	90 µL
5.0 mM	1 µg	25 µL	0 µL	30 µL	60 µL	90 µL

Table A2. Substrate stimulation assay pipetting scheme

Substrate	MsbA	ATP 10 mM	Substrate	Buffer
0 µM	1 µg	4.5 µL	0 µL	20.5 µL
0.001 µM	1 µg	4.5 µL	1 µL (30 nM)	19.5 µL
0.01 µM	1 µg	4.5 µL	10 µL (30 nM)	10.5 µL
0.1 µM	1 µg	4.5 µL	1 µL (3 µM)	19.5 µL
1 µM	1 µg	4.5 µL	10 µL (3 µM)	10.5 µL
10 µM	1 µg	4.5 µL	1 µL (300 µM)	19.5 µL
100 µM	1 µg	4.5 µL	10 µL (300 µM)	10.5 µL
1 mM	1 µg	4.5 µL	1 µL (30 mM)	19.5 µL
10 mM	1 µg	4.5 µL	10 µL (30 mM)	10.5 µL

Table A3. Substrate stimulation assay matrix pipetting scheme

		ATP mM	**0.2**	**0.4**	**0.6**	**1.5**	**2.0**	**3.0**	**5.0**
		ATP 10 mM (µL)	0.6	1.2	1.8	4.5	6.0	9.0	15.0
Substrate	**Substrate (µL)**								
0 µM	0		1 µg MsbA + buffer (total volume 30 µL)						
0.001 µM	1	30 nM							
0.01 µM	10	30 nM							
0.1 µM	1	3 µM							
1 µM	10	3 µM							
10 µM	1	300 µM							
100 µM	10	300 µM							
1 mM	1	30 mM							
10 mM	10	30 mM							

Data analysis protocols 31P NMR progression curve

- For one standard real-time 31P measurement the ns=8 unless mentioned otherwise
- The number of increments depends on the desired duration of the measurement
- d1 is 1.5 seconds (solution NMR), d1 is 3.0 seconds (ssNMR)

1. To standardize the number of increments as time, the increments are converted into minutes by calculation. As the integrated peaks are the average between two-time points, the time assigned for each peak is the time point in the middle between the preceding and the following peak. For the analysis of the progression curve, initially, more points are taken across a smaller time distance. The number of increments is projected as time with the function *proj* (figure A1). The projected 1D spectra are exported from Topspin® into Originlab® (figure A2). As the projected spectra are sum averages, the final indicated time point between each projection (and the first time point is the average between time point 0 and the first projection).

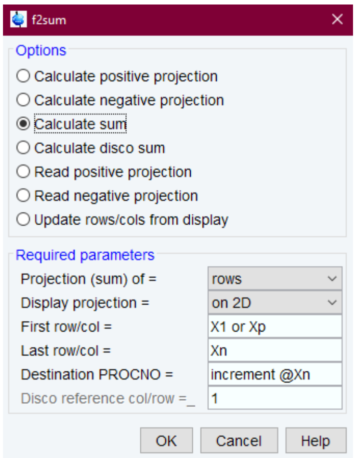

○ Calculate positive projection
○ Calculate negative projection
● Calculate sum
○ Calculate disco sum
○ Read positive projection
○ Read negative projection
○ Update rows/cols from display

Required parameters
Projection (sum) of = rows
Display projection = on 2D
First row/col = X1 or Xp
Last row/col = Xn
Destination PROCNO = increment @Xn
Disco reference col/row = 1

Figure A1. The *proj* function is used to extract increments per time unit. The sum of rows is projected in 1D spectra of the given parameters. The sum of rows is a rescaled sum of X_n-X_p, therefore the provided spectra are an average of the sum. In the First row/col X_1 = first increment for the first time point, in the last row/col X_n = the last increment of the chosen time point, X_{P+1} = the increment of the previous time point.

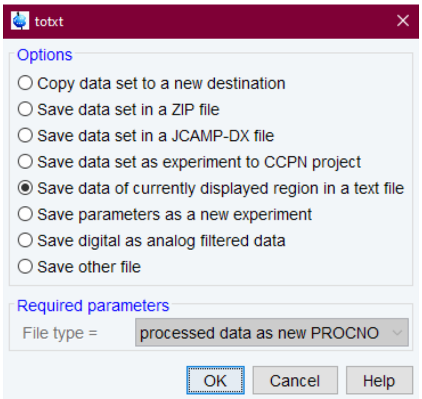

○ Copy data set to a new destination
○ Save data set in a ZIP file
○ Save data set in a JCAMP-DX file
○ Save data set as experiment to CCPN project
● Save data of currently displayed region in a text file
○ Save parameters as a new experiment
○ Save digital as analog filtered data
○ Save other file

Required parameters
File type = processed data as new PROCNO

Figure A2. The projections are saved as text files. Saved text files can be imported in Originlab®. (In Windows command *ctrl+S*, in MacOS command *cmd+S*, or directly in Topspin® under *files* and *save as*).

2. Initial fitting in Originlab® is done by using the spectra with the highest intensity, this can be acquired by adding up the projected spectra between time points where all peaks are visible in Topspin® to ensure a good fitting model, where the cumulative fit in Originlab® should resemble the original plot of sum exported from Topspin® (figure A3).

Model	Lorentz					
Equation	y = y0 + (2*A/pi)*(w/(4*(x-xc)^2 + w^2))					
Plot	Peak1(sum-ref)	Peak2(sum-ref)	Peak3(sum-ref)	Peak4(sum-ref)	Peak5(sum-ref)	Peak6(sum-ref)
y0	-112.49 ± 4.27	-112.49 ± 4.27	-112.49 ± 4.27	-112.49 ± 4.27	-112.49 ± 4.27	-112.49 ± 4.27
xc	3.15 ± 0.00	1.81 ± 0.00	-6.00 ± 0.00	-6.58 ± 0.00	-10.75 ± 0.00	-11.14 ± 0.00
w	0.18 ± 0.00	0.16 ± 0.00	0.29 ± 0.00	0.25 ± 0.00	0.37 ± 0.00	0.19 ± 0.00
A	761.48 ± 14.86	2625.89 ± 13.84	2996.71 ± 19.17	2259.88 ± 17.54	3240.47 ± 22.27	2312.88 ± 15.70
Plot	Peak7(sum-ref)	Peak8(sum-ref)	Peak9(sum-ref)	Peak10(sum-ref)	Peak11(sum-ref)	
y0	-112.49 ± 4.27	-112.49 ± 4.27	-112.49 ± 4.27	-112.49 ± 4.27	-112.49 ± 4.27	
xc	-19.94 ± 0.00	-3.53 ± 0.00	-0.10 ± 0.00	-0.57 ± 0.00	-1.39 ± 0.00	
w	1.08 ± 0.00	0.14 ± 0.00	0.30 ± 0.00	0.23 ± 0.00	0.26 ± 0.00	
A	3170.65 ± 38.13	1085.94 ± 12.77	167.85 ± 19.74	248.53 ± 17.24	429.74 ± 17.81	
Reduced Chi-Sqr	12880.680					
R-Square(COD)	0.993					
Adj. R-Square	0.993					

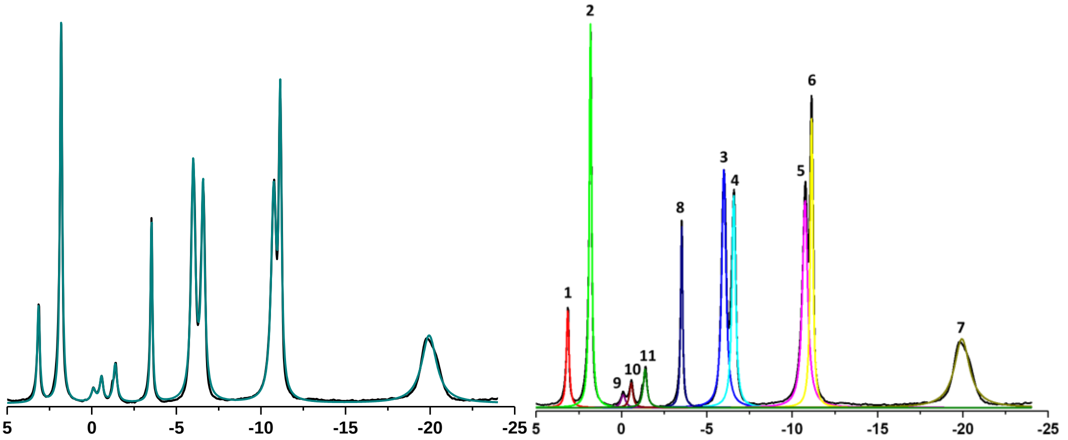

Figure A3. Example of an imported sum model with Lorentz fit. Top: the cumulative fit of the sum model (R^2=0.99). Bottom: fit of individual peaks; 1=AMP, 2=P_i, 3=γ-ATP, 4=β-ADP, 5=α-ADP, 6=α-ATP, and 7=β-ATP, 8=creatine phosphate, 9-11= endogenous Lipid A.

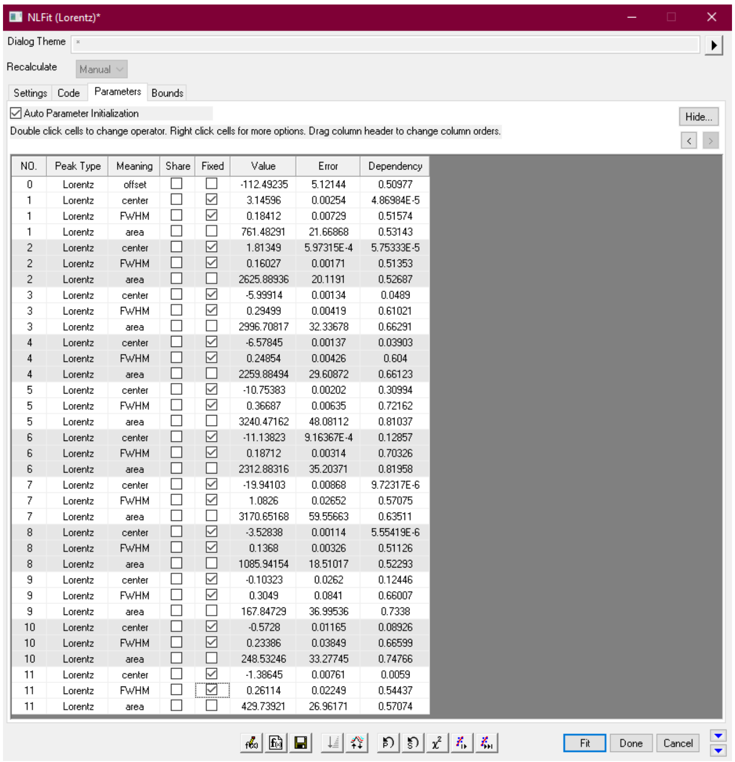

☑ Auto Parameter Initialization

Double click cells to change operator. Right click cells for more options. Drag column header to change column orders.

NO.	Peak Type	Meaning	Share	Fixed	Value	Error	Dependency
0	Lorentz	offset	☐	☐	-112.49235	5.12144	0.50977
1	Lorentz	center	☐	☑	3.14596	0.00254	4.86984E-5
1	Lorentz	FWHM	☐	☑	0.18412	0.00729	0.51574
1	Lorentz	area	☐	☐	761.48291	21.66868	0.53143
2	Lorentz	center	☐	☑	1.81349	5.97315E-4	5.75333E-5
2	Lorentz	FWHM	☐	☑	0.16027	0.00171	0.51353
2	Lorentz	area	☐	☐	2625.88936	20.1191	0.52687
3	Lorentz	center	☐	☑	-5.99914	0.00134	0.0489
3	Lorentz	FWHM	☐	☑	0.29499	0.00419	0.61021
3	Lorentz	area	☐	☐	2996.70817	32.33678	0.66291
4	Lorentz	center	☐	☑	-6.57845	0.00137	0.03903
4	Lorentz	FWHM	☐	☑	0.24854	0.00426	0.604
4	Lorentz	area	☐	☐	2259.88494	29.60872	0.66123
5	Lorentz	center	☐	☑	-10.75383	0.00202	0.30994
5	Lorentz	FWHM	☐	☑	0.36687	0.00635	0.72162
5	Lorentz	area	☐	☐	3240.47162	48.08112	0.81037
6	Lorentz	center	☐	☑	-11.13823	9.16367E-4	0.12857
6	Lorentz	FWHM	☐	☑	0.18712	0.00314	0.70326
6	Lorentz	area	☐	☐	2312.88316	35.20371	0.81958
7	Lorentz	center	☐	☑	-19.94103	0.00868	9.72317E-6
7	Lorentz	FWHM	☐	☑	1.0826	0.02652	0.57075
7	Lorentz	area	☐	☐	3170.65168	59.55663	0.63511
8	Lorentz	center	☐	☑	-3.52838	0.00114	5.55419E-6
8	Lorentz	FWHM	☐	☑	0.1368	0.00326	0.51126
8	Lorentz	area	☐	☐	1085.94154	18.51017	0.52293
9	Lorentz	center	☐	☑	-0.10323	0.0262	0.12446
9	Lorentz	FWHM	☐	☑	0.3049	0.0841	0.66007
9	Lorentz	area	☐	☐	167.84729	36.99536	0.7338
10	Lorentz	center	☐	☑	-0.5728	0.01165	0.08926
10	Lorentz	FWHM	☐	☑	0.23386	0.03849	0.66599
10	Lorentz	area	☐	☐	248.53246	33.27745	0.74766
11	Lorentz	center	☐	☑	-1.38645	0.00761	0.0059
11	Lorentz	FWHM	☐	☑	0.26114	0.02249	0.54437
11	Lorentz	area	☐	☐	429.73921	26.96171	0.57074

Figure A4. Example of parameters used for the fitting in Originlab®.

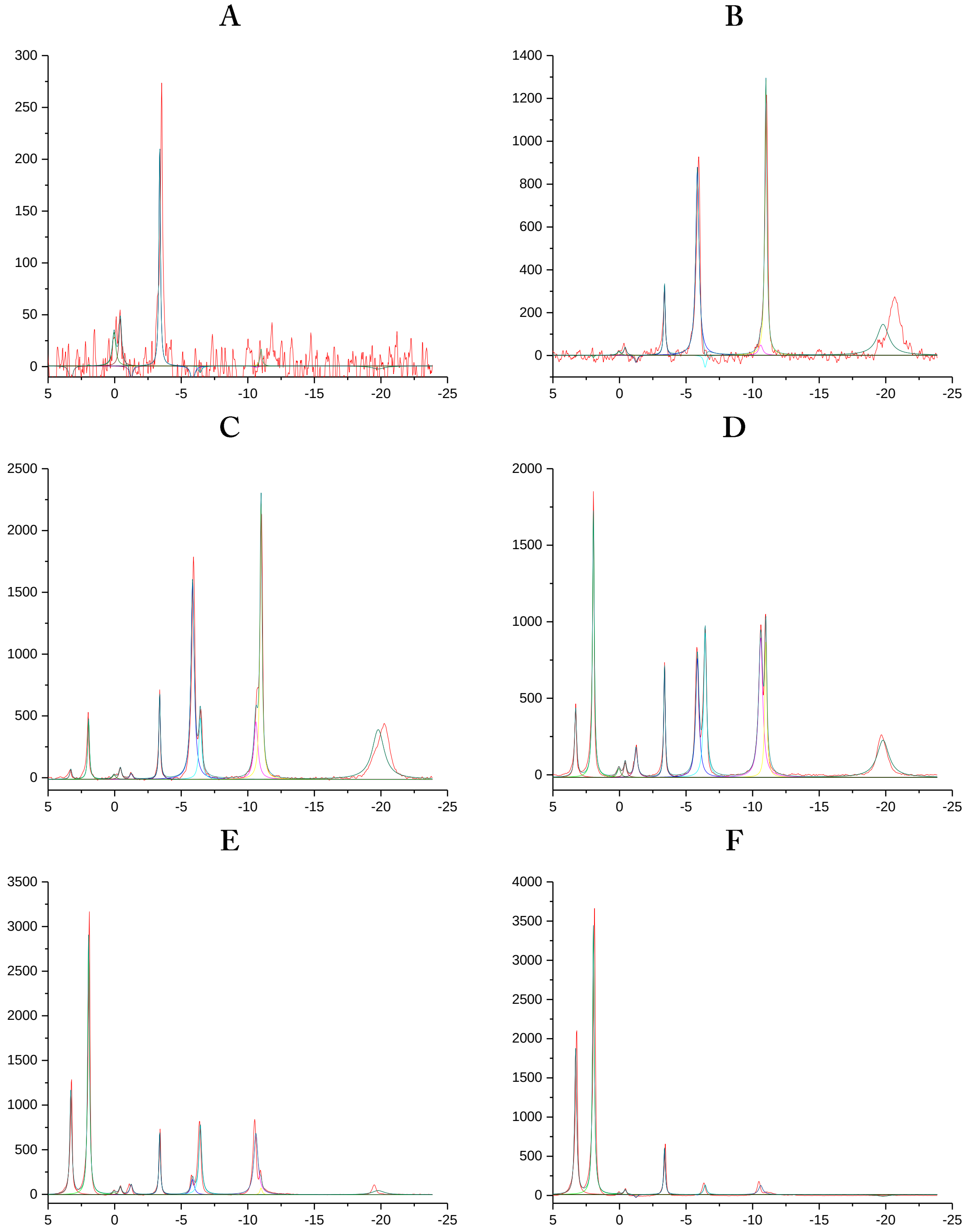

Figure A5. Example of parameters used for the fitting in Originlab® at time points 0.5, 1.5, 17.5, 75, 270, >>1000 minutes, prior to injection, where (A) creatine phosphate and endogenous lipid A, (B) initial ATP signals, (C) ADP and inorganic phosphate formation, (D) the ATP and ADP are nearly equal, and the formation of inorganic phosphate and AMP, (E) ATP is nearly fully hydrolysed with increasing inorganic phosphate and AMP concentrations, and (F) ADP is nearly fully turned over.

3. For the peak integration Lorentz function is used to integrate the peaks and to calculate the intensities for the progression curves. In the sum model, the fit should be at least >>95% (or p=0.05). In addition, to calculate the peak intensities all parameters are fixed (under *change parameters*), with the exception of the

offset (y0) and the area (A) (figure A4). Fixing the parameters allows the chemical shifts of the peaks to be fixed, and only the peak intensity or area under the curve to be calculated. The fit of the sum model can later be used for all the projected plots.

4. Subsequently each chosen time point can be integrated with the standard model. Initially, the lower concentration provides a less accurate integration. Over time, the integration improves with the signal-to-noise of the spectra (figure A5, examples of an integration for 8 mM ATP/5 mg (230 µM) $_{WT}$MsbA = 35.000 mole/mole ATP:MsbA).
5. The peak intensities can be taken from the fit plotted against time to make a progression curve (figure A6).

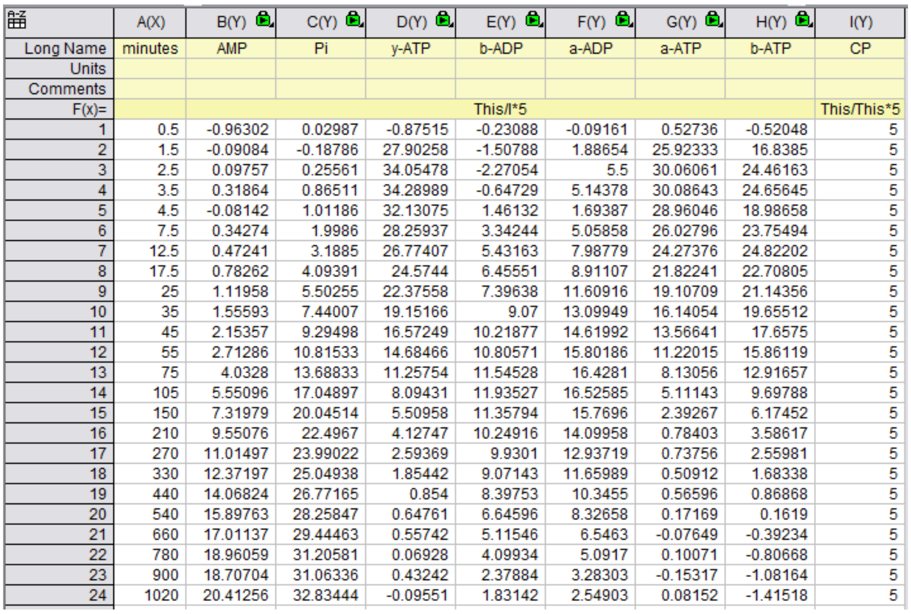

	A(X)	B(Y)	C(Y)	D(Y)	E(Y)	F(Y)	G(Y)	H(Y)	I(Y)
Long Name	minutes	AMP	Pi	y-ATP	b-ADP	a-ADP	a-ATP	b-ATP	CP
Units									
Comments									
F(x)=		This/I*5							This/This*5
1	0.5	-0.96302	0.02987	-0.87515	-0.23088	-0.09161	0.52736	-0.52048	5
2	1.5	-0.09084	-0.18786	27.90258	-1.50788	1.88654	25.92333	16.8385	5
3	2.5	0.09757	0.25561	34.05478	-2.27054	5.5	30.06061	24.46163	5
4	3.5	0.31864	0.86511	34.28989	-0.64729	5.14378	30.08643	24.65645	5
5	4.5	-0.08142	1.01186	32.13075	1.46132	1.69387	28.96046	18.98658	5
6	7.5	0.34274	1.9986	28.25937	3.34244	5.05858	26.02796	23.75494	5
7	12.5	0.47241	3.1885	26.77407	5.43163	7.98779	24.27376	24.82202	5
8	17.5	0.78262	4.09391	24.5744	6.45551	8.91107	21.82241	22.70805	5
9	25	1.11958	5.50255	22.37558	7.39638	11.60916	19.10709	21.14356	5
10	35	1.55593	7.44007	19.15166	9.07	13.09949	16.14054	19.65512	5
11	45	2.15357	9.29498	16.57249	10.21877	14.61992	13.56641	17.6575	5
12	55	2.71286	10.81533	14.68466	10.80571	15.80186	11.22015	15.86119	5
13	75	4.0328	13.68833	11.25754	11.54528	16.4281	8.13056	12.91657	5
14	105	5.55096	17.04897	8.09431	11.93527	16.52585	5.11143	9.69788	5
15	150	7.31979	20.04514	5.50958	11.35794	15.7696	2.39267	6.17452	5
16	210	9.55076	22.4967	4.12747	10.24916	14.09958	0.78403	3.58617	5
17	270	11.01497	23.99022	2.59369	9.9301	12.93719	0.73756	2.55981	5
18	330	12.37197	25.04938	1.85442	9.07143	11.65989	0.50912	1.68338	5
19	440	14.06824	26.77165	0.854	8.39753	10.3455	0.56596	0.86868	5
20	540	15.89763	28.25847	0.64761	6.64596	8.32658	0.17169	0.1619	5
21	660	17.01137	29.44463	0.55742	5.11546	6.5463	-0.07649	-0.39234	5
22	780	18.96059	31.20581	0.06928	4.09934	5.0917	0.10071	-0.80668	5
23	900	18.70704	31.06336	0.43242	2.37884	3.28303	-0.15317	-1.08164	5
24	1020	20.41256	32.83444	-0.09551	1.83142	2.54903	0.08152	-1.41518	5

Figure A6. Example of extracted peak intensities plotted against time.

6. Prior to this, the peak intensities are first corrected with the internal reference creatine phosphate peak. The intensity of every projection is corrected (e.g. all the peak intensities at time point X are corrected by the creatine phosphate intensity at time point X). This is done by normalizing creatine phosphate (e.g., 5 for 5 mM creatine phosphate) as creatine phosphate is a reference that remains stable over a long period of time or by calibration (**figure A7A**).
7. In the case of solution NMR, the d1 time was 1.5s instead of 3.0s. For this, a correction factor for the inorganic phosphate (Pi) peak has been applied for the final data transformation to determine the real concentration (**figure A7B**).
8. To improve the ADP and ATP signals for modelling and extraction of kinetic data, the ADP and ATP signals can also be averaged (figure A8).

Averaging ADP signal: $$\frac{\alpha\text{ADP} + \beta\text{ ADP}}{2}$$

Averaging ATP signal: $$\frac{\alpha\text{ADP} + \beta\text{ ADP} + \gamma\text{ATP}}{3}$$

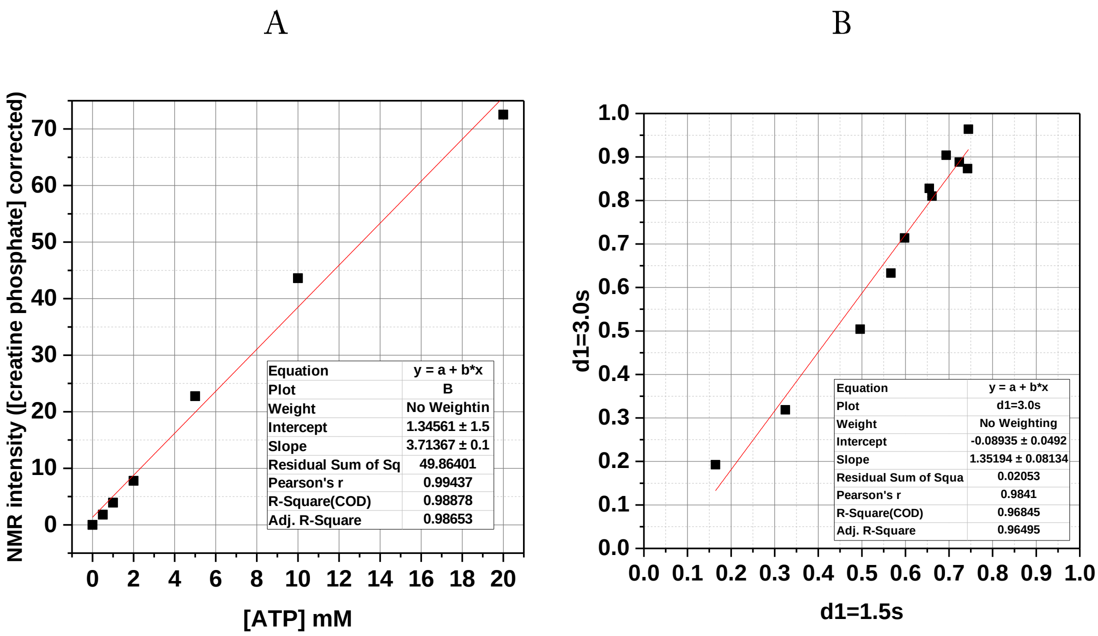

Figure A7. Calibration curves. A) Concentration calibration curve. B) d1 correction factor for inorganic phosphate.

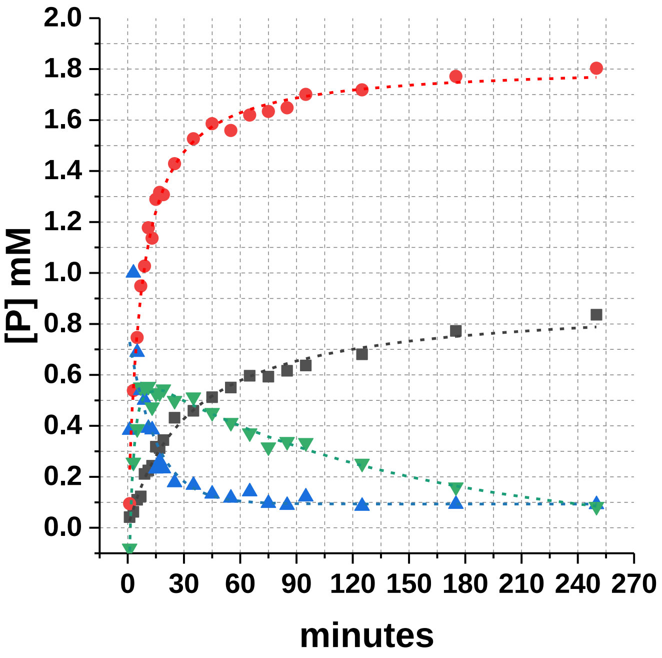

Figure A8. Example of a final progression curve with averaged ADP and ATP signals.

Slices of 2D spectra

CH1 (NCO)

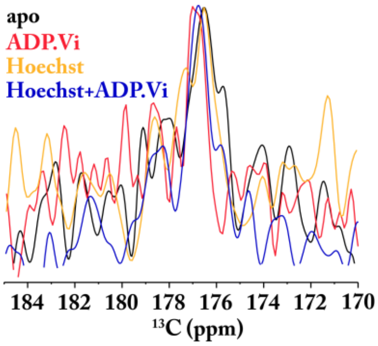

CH2 (NCO)

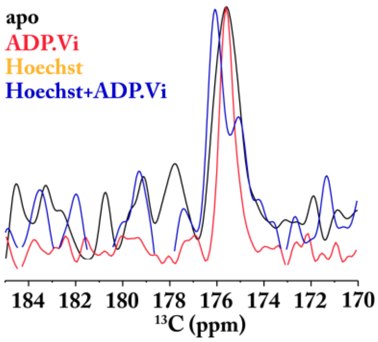

K118 (NCA)

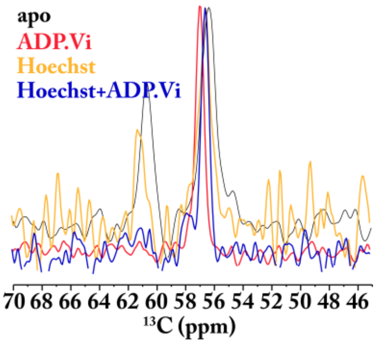

K215 (NCA)

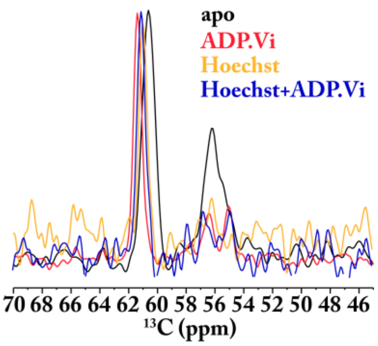

K328 (NCA)

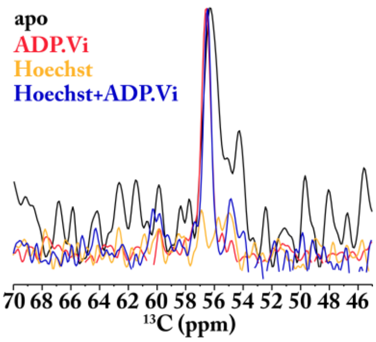

CH1 (NCO)

POPE/POPG

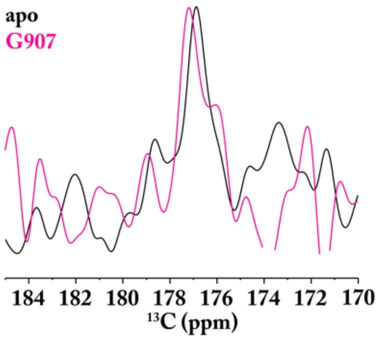

K118 (NCA)

POPE/POPG

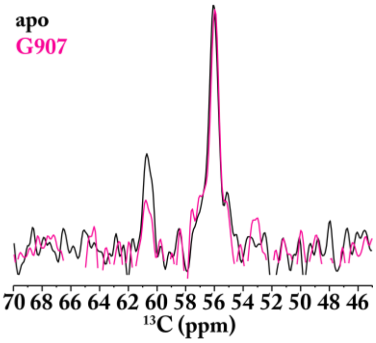

K215 (NCA)

POPE/POPG

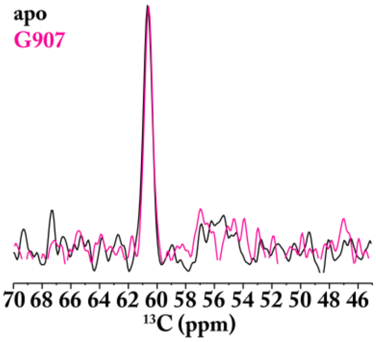

Build-up curves NOESY experiments G907+POPE/POPG

Table A4. Build-up curves choline interactions

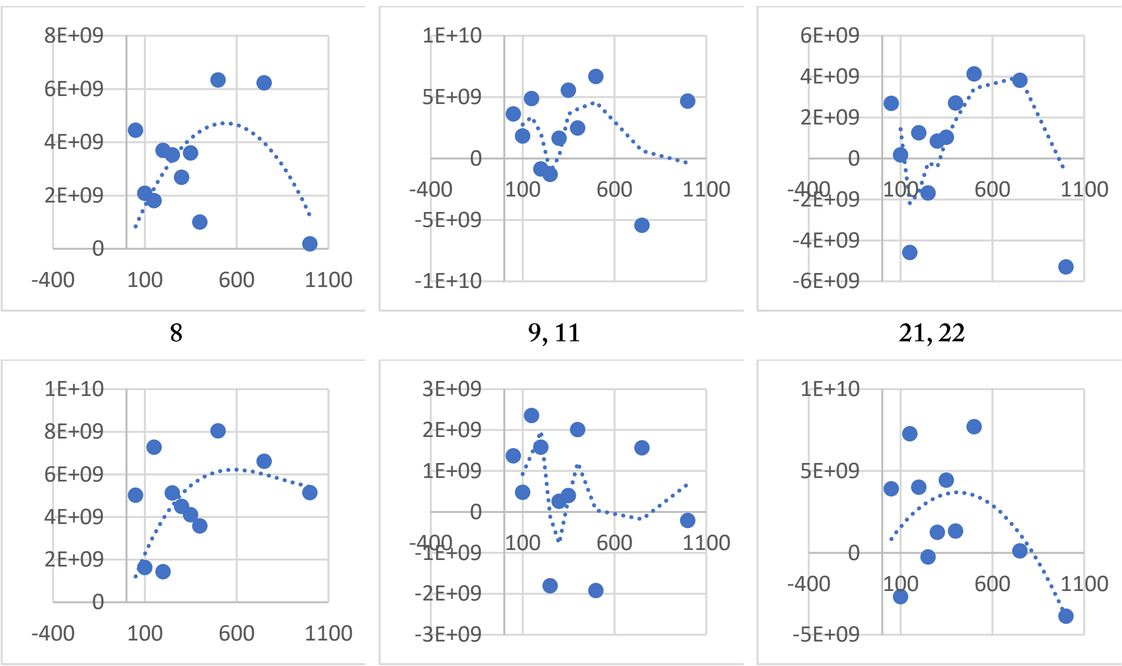
2 3 5

8 9, 11 21, 22

Table A5. Build-up curves phosphate headgroup interactions

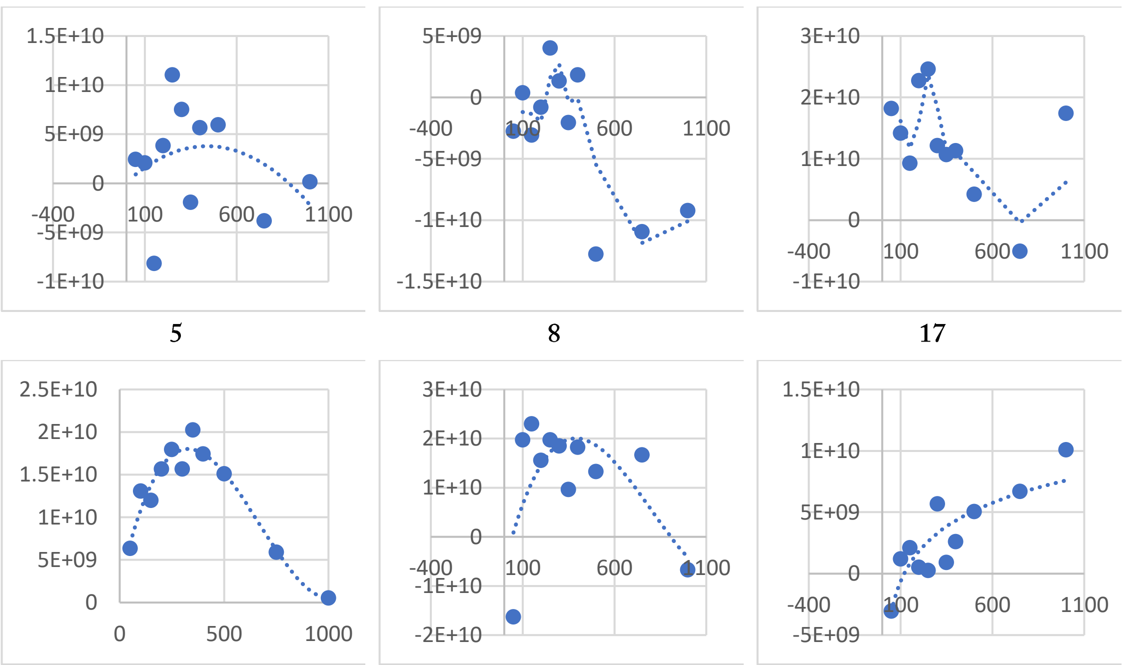
2 3 3

5 8 17

9, 11

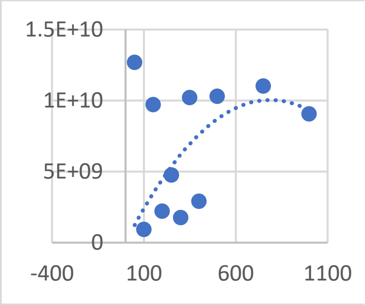

9, 11

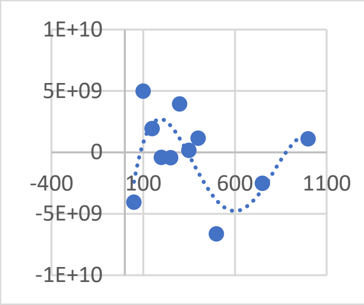

21, 22

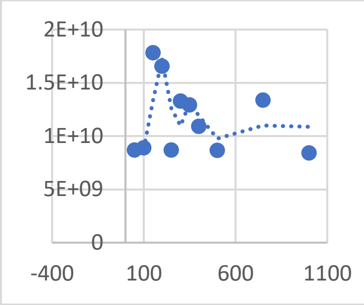

23

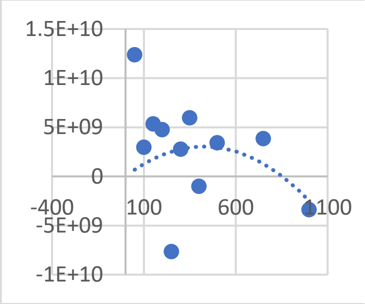

Table A6. Build-up curves glycerol interactions

2

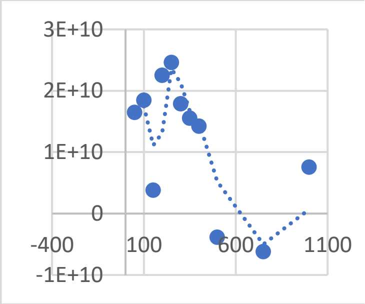

2

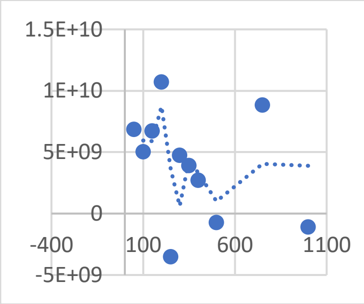

2

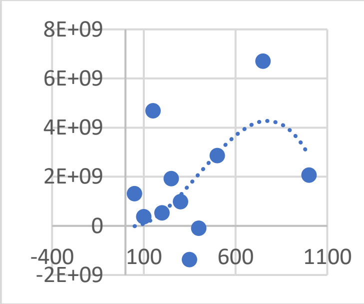

2

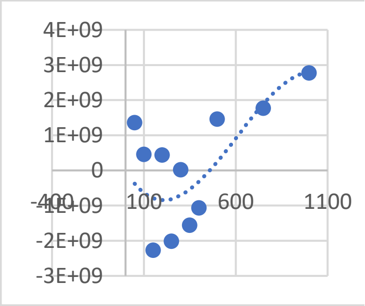

3

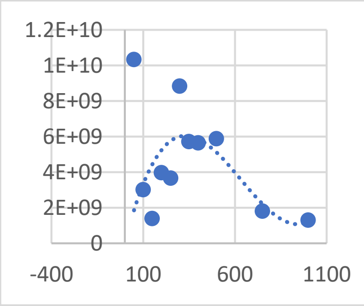

3

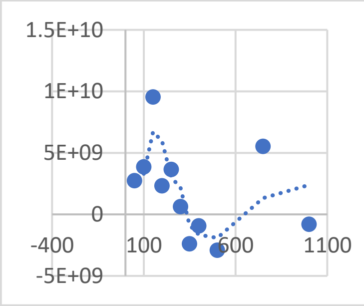

3

5

8

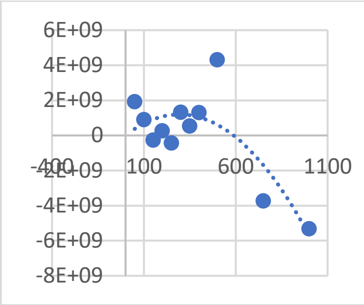

8

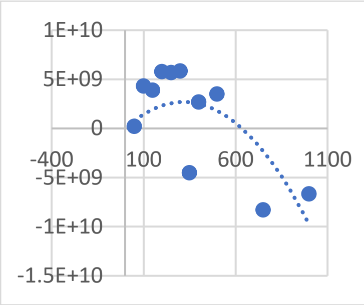

8

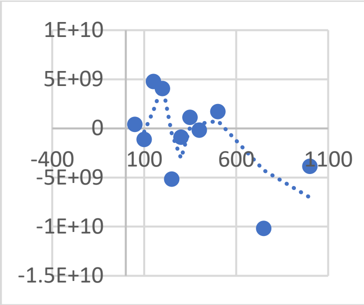

9, 11

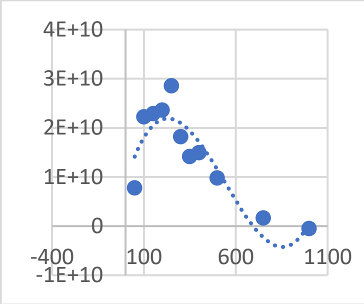

9, 11

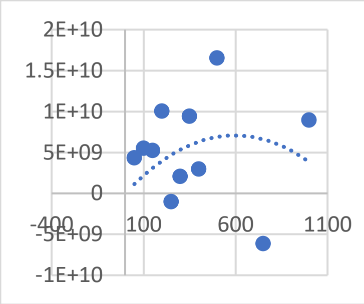

9, 11

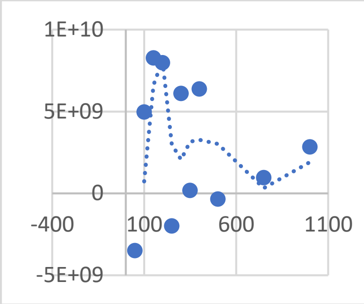

9, 11

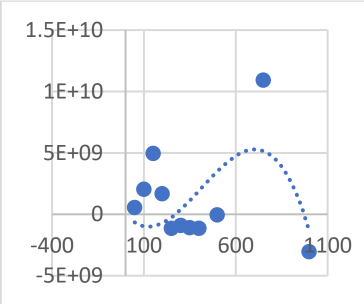

17

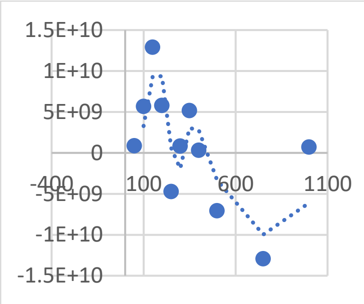

21, 22

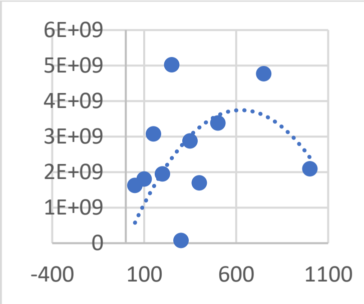

21, 22

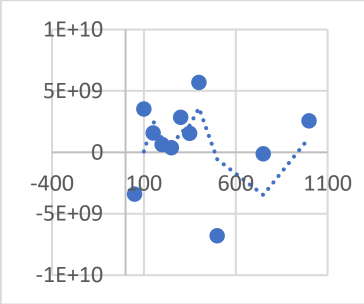

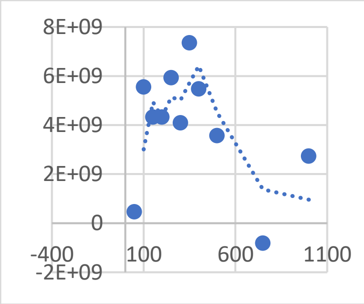

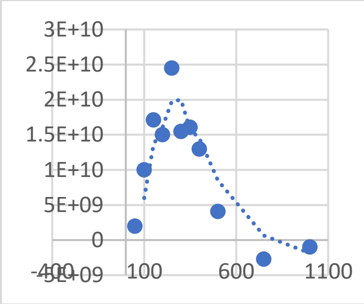

Table A7. Build-up curves CH2 29, 210 interactions

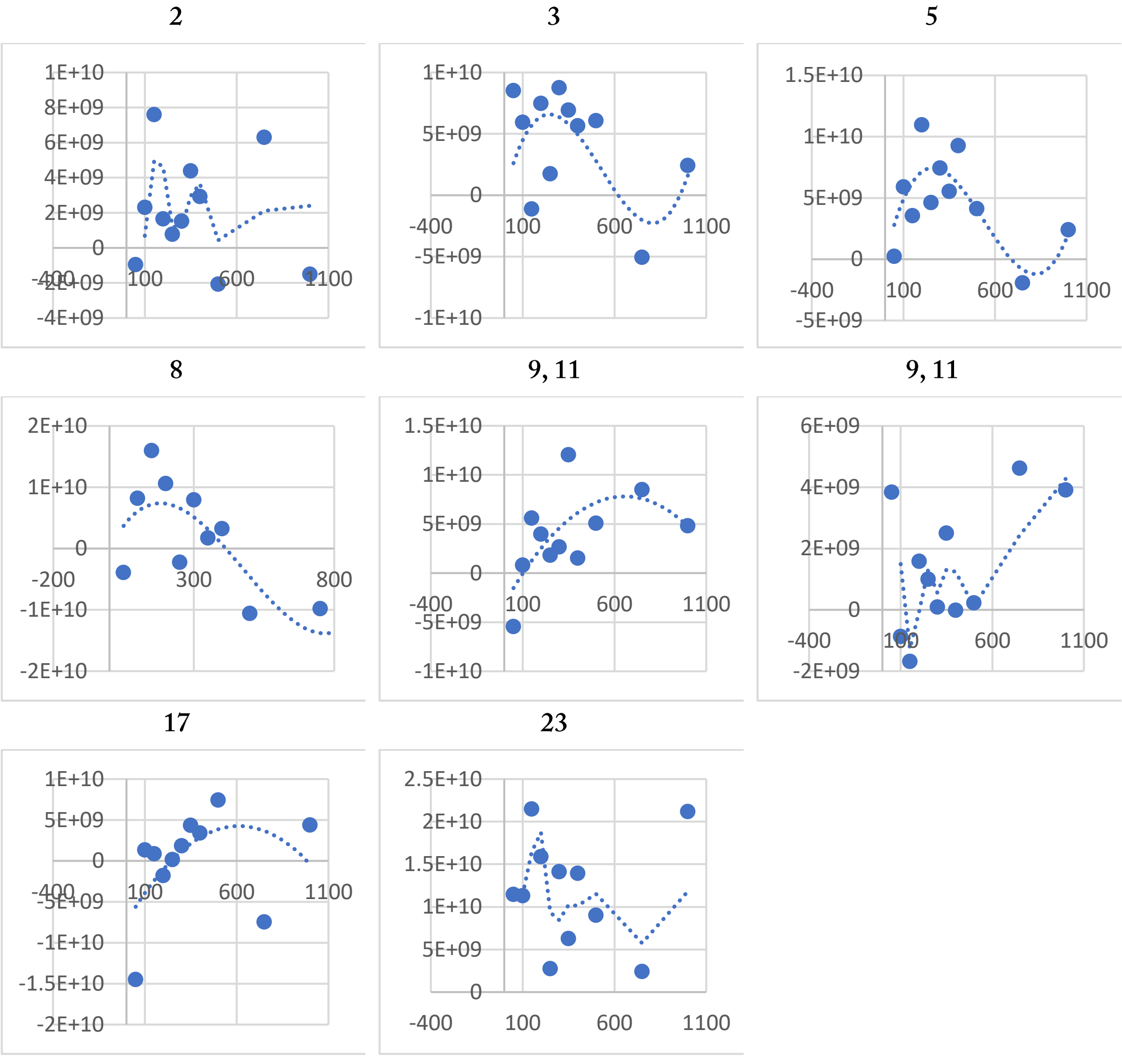
2 3 5 8 9, 11 9, 11 17 23

Table A8. Build-up curves CH2 28, 211 interactions

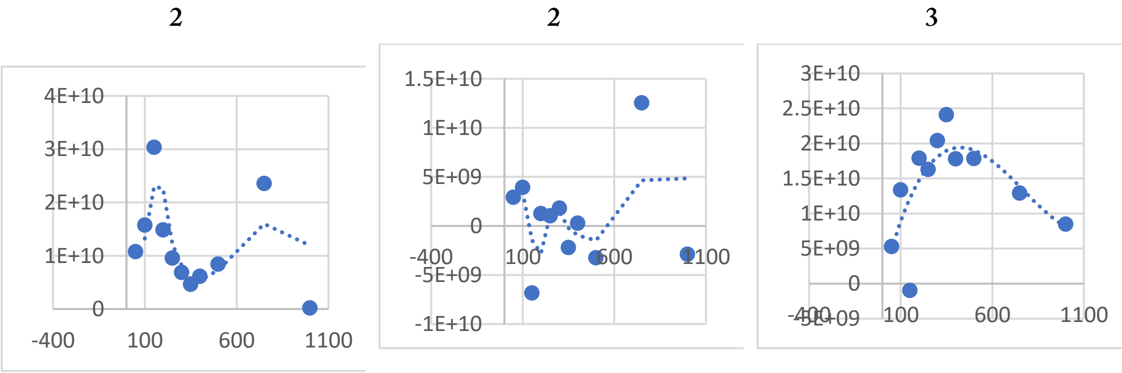
2 2 3

5

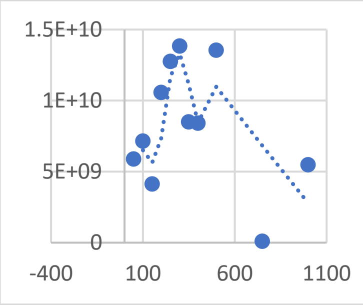

21, 22

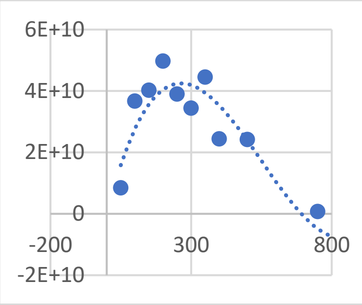

23

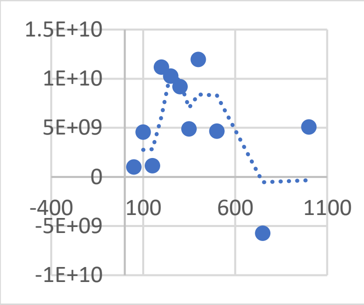

Table A9. Build-up curves CH2 316, 218 interactions

2

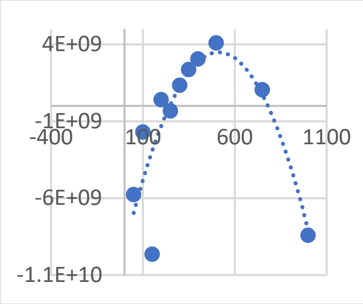

3

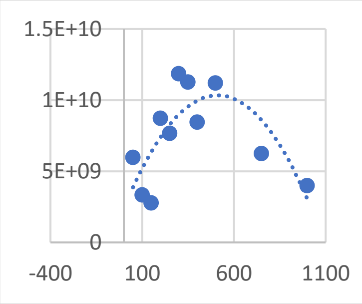

5

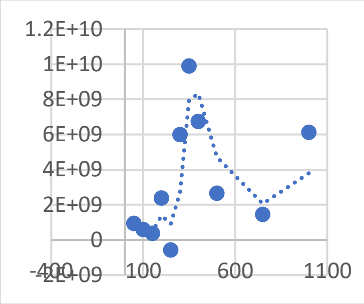

8

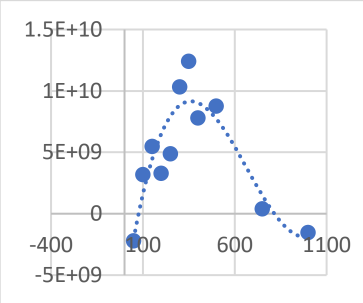

9, 11

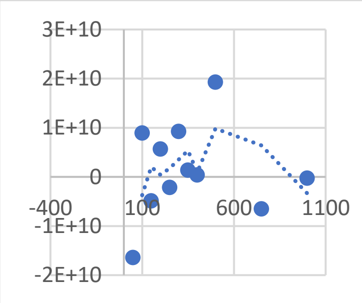

17

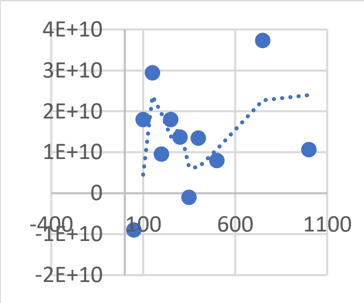

21, 22

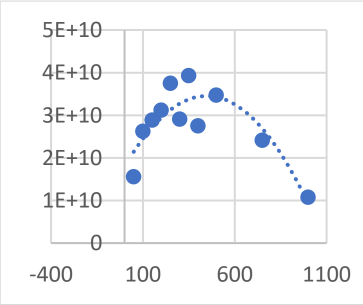

23

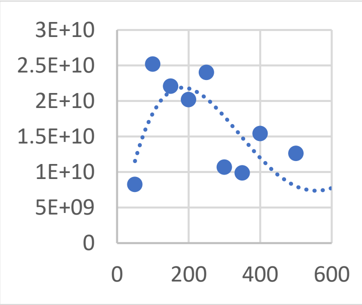

Table A10. Build-up curves CH2 interactions

2

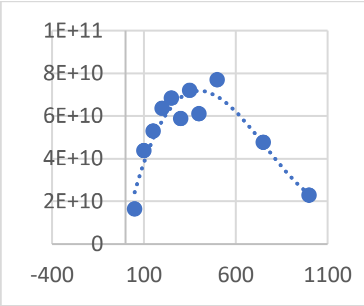

2

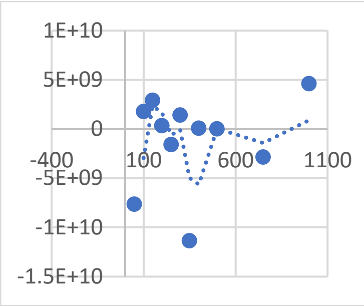

2

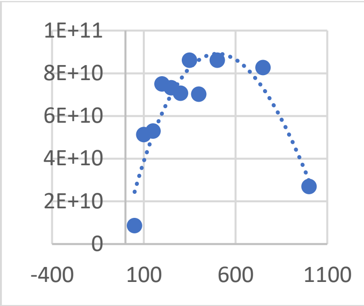

2

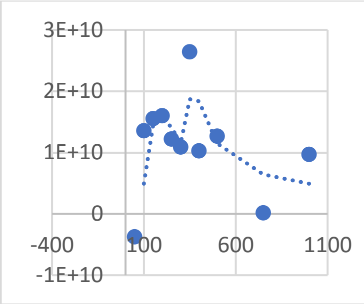

3

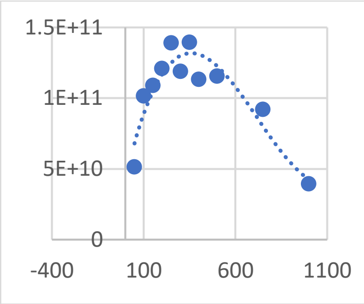

5

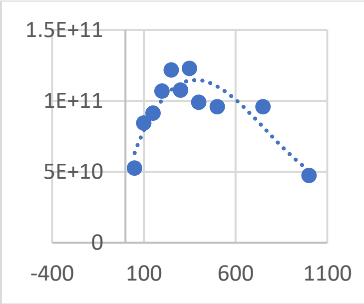

8

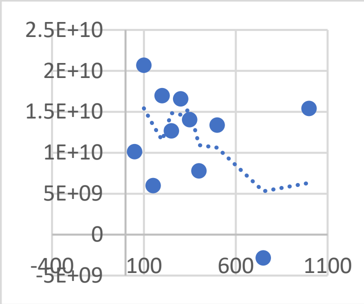

8

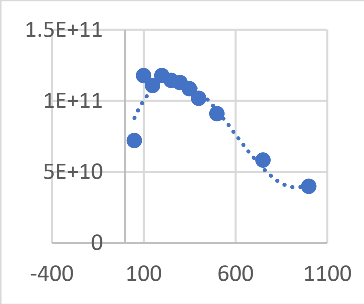

9, 11

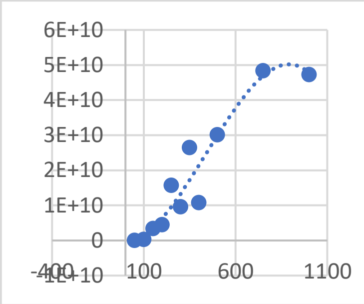

9, 11

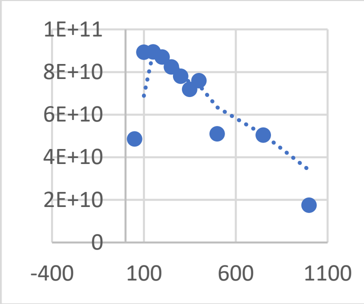

9, 11

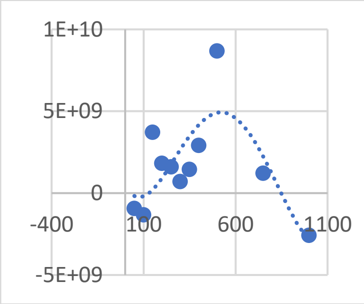

17

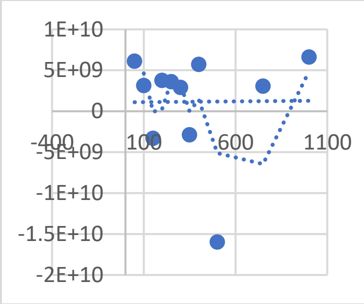

17

21, 22

21, 22

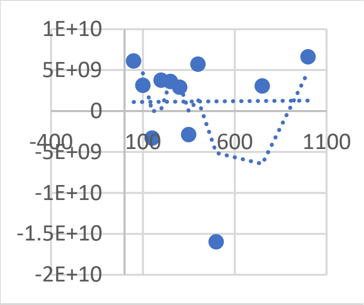
1E+10
5E+09
0
-5E+09
-1E+10
-1.5E+10
-2E+10
-400
100
600
1100

23

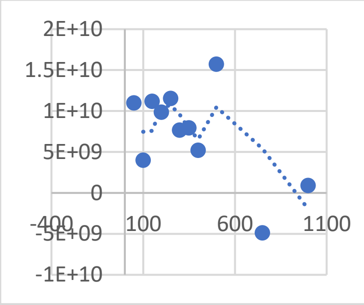
2E+10
1.5E+10
1E+10
5E+09
0
-5E+09
-1E+10
-400
100
600
1100

23

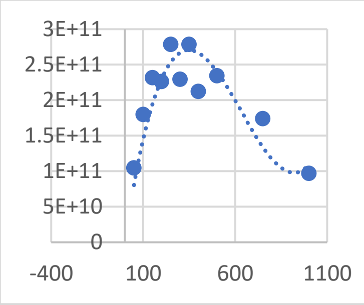
3E+11
2.5E+11
2E+11
1.5E+11
1E+11
5E+10
0
-400
100
600
1100

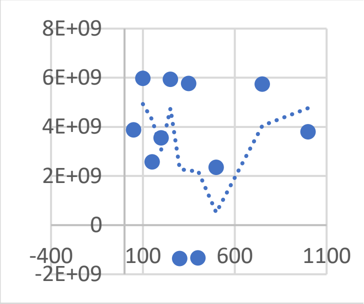
8E+09
6E+09
4E+09
2E+09
0
-2E+09
-400
100
600
1100

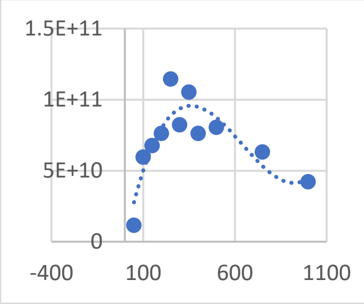
1.5E+11
1E+11
5E+10
0
-400
100
600
1100

Build-up curves NOESY experiments G907+DMPC/DPMA

Table A11. Build-up curves choline interactions

5

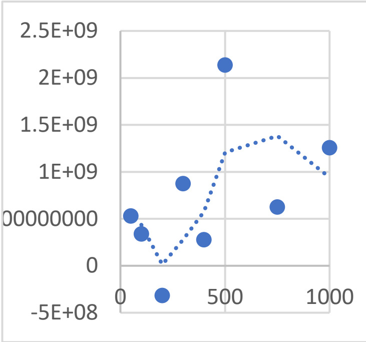

8

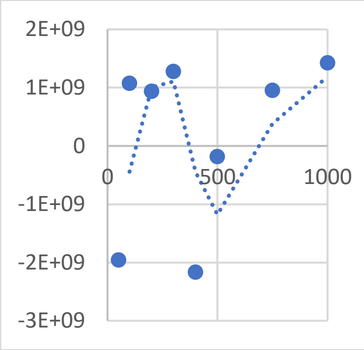

9, 11

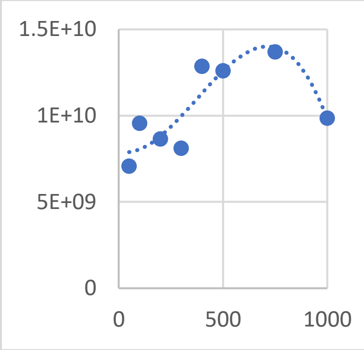

9, 11

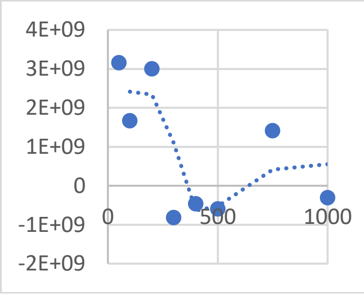

Table A12. Build-up curves glycerol interactions

2

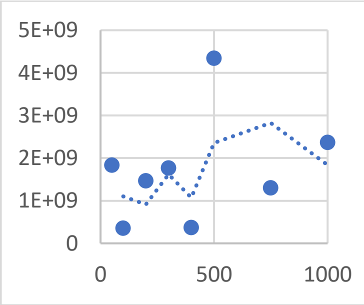

2

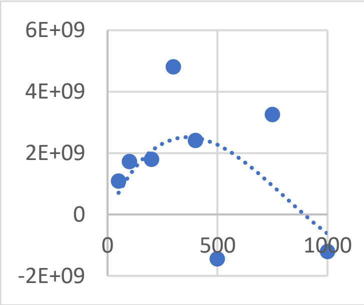

5

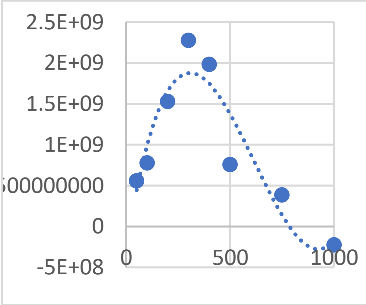

8

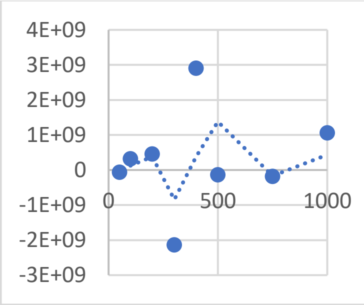

9, 11

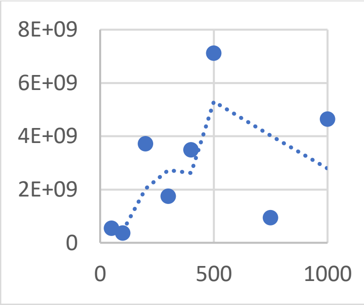

23

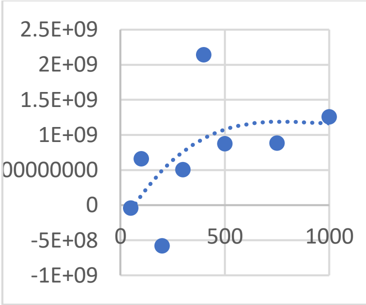

Table A13. Build-up curves CH2 23, 33 interactions

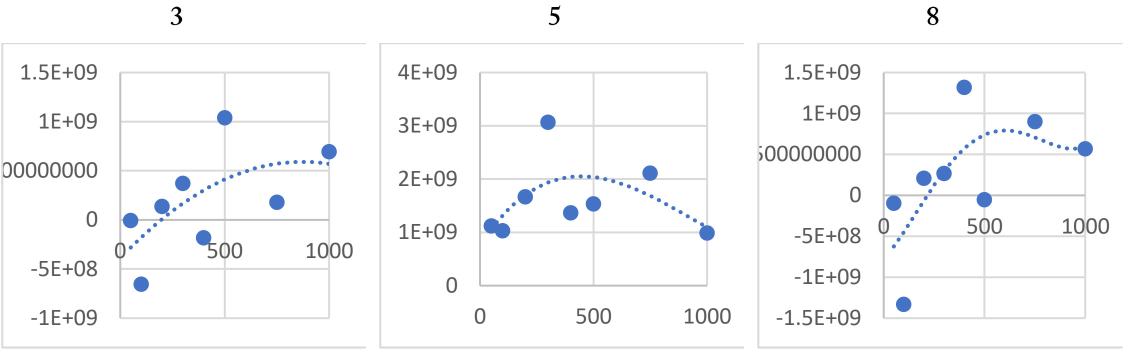

Table A14. Build-up curves CH2 214, 314 interactions

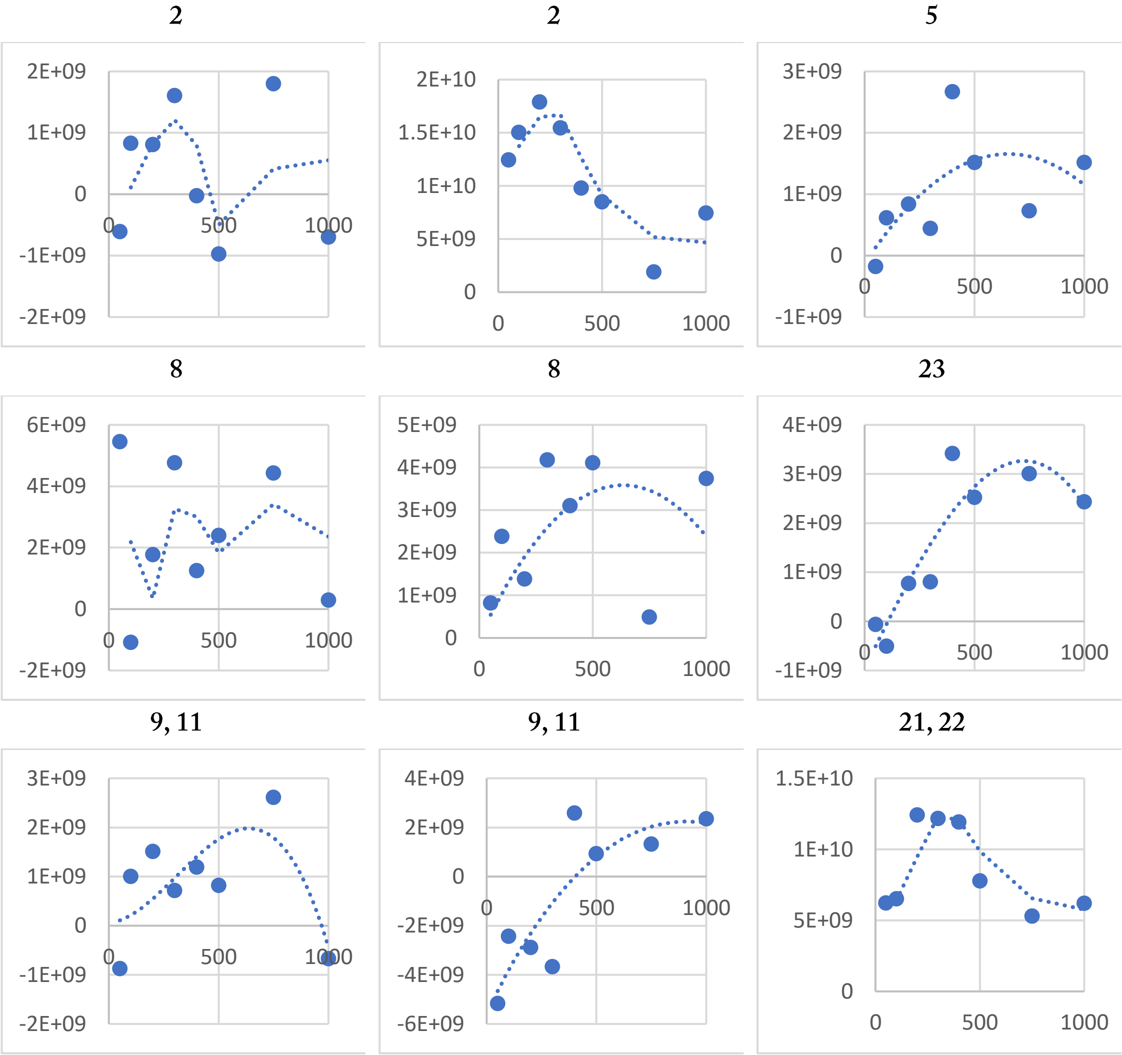

Table A15. Build-up curves CH2 interactions

2

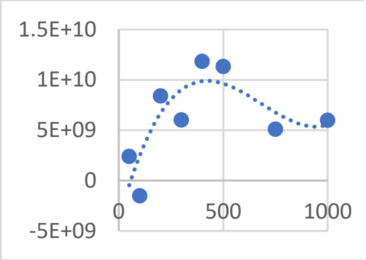

2

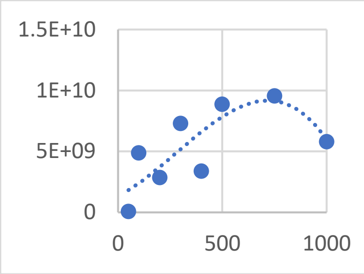

3

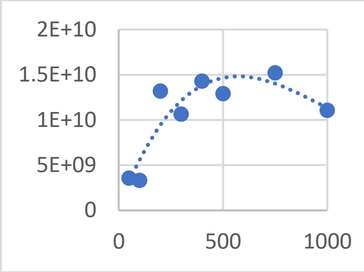

5

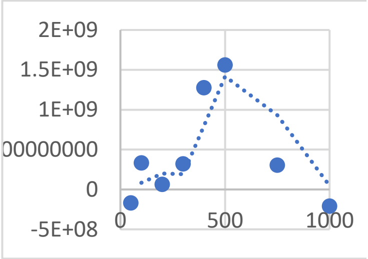

5

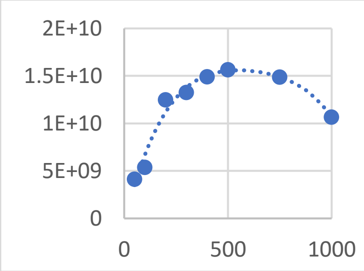

8

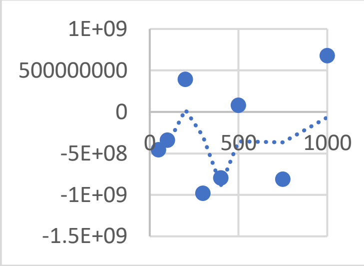

8

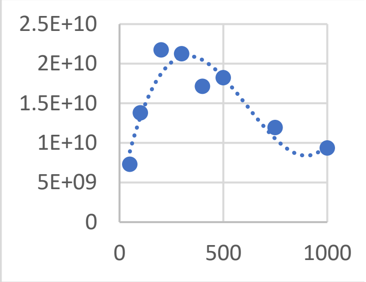

9, 11

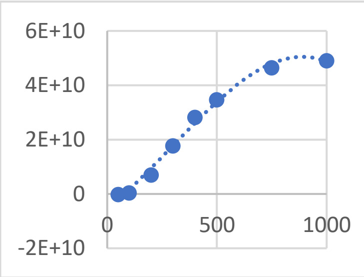

9, 11

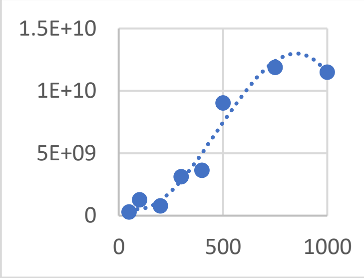

9, 11

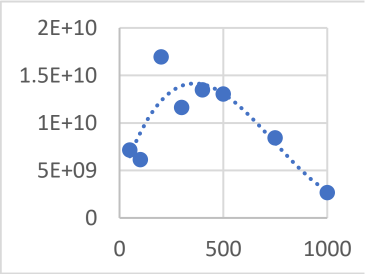

17

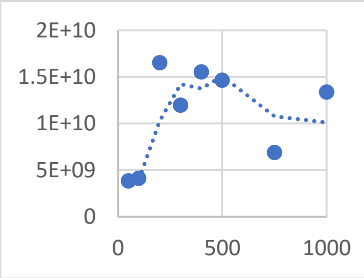

21, 22

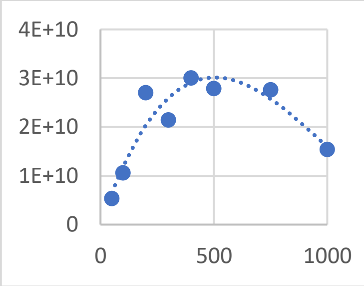

21, 22

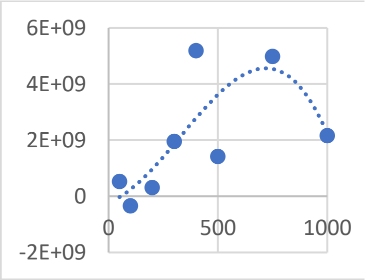

23

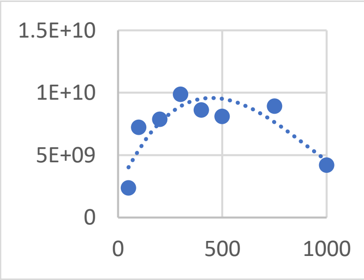

MATLAB Script

Equation 16 (Goličnik. Molecular Biology Education 39.2 (2011): 117-125.):

$[S](t) = [S]_0 \exp(-kt)$ for ATP and ADP
$[S](t) = [S]_0 - \left([S]_0 \exp(-kt)\right)$ AMP and $2[S]_0$ for P_i

---

```
% Load data file
data = importdata('filename.dat'); %fetch data file
time = data.data(:, 1);
substrate_concentration = data.data(:, 2);
%analysing multiple columns or conditions
num_conditions = size(data.data, 2) - 1;

% Define the model function St(t) = S0 * exp(-kobs * t) + offset
model_function = @(params, t) params(3) * exp(-params(1) * t) + params(2);

% Define the model function St(t) = S0 - (S0 * exp(-kobs * t)) – offset
model_function = @(params, t) params(2) - (params(2) * exp(-params(1) * t))
- params(3);

% Concatenate time and substrate concentration data into a single matrix X
X = time;

% Define the objective function to minimize the sum of squares error
objective_function = @(params) model_function(params, X) -
substrate_concentration;

% Provide initial guesses for the parameters (kobs, offset, offset)
kobs_guess = …;
S0_fixed = …; %adjust S0 for ATP, ADP, AMP, and Pi concentrations
offset_guess = …;

% Provide initial guesses for multiple conditions (offset)
offset_guess = …;
S0_fixed = …; %adjust S0 for ATP, ADP, AMP, and Pi concentrations
%anaysing multiple ATP of ADP concentrations, concentration per column
S0_fixed_values = [0.5, 1.0, 2.0, 4.0, 6.0, 1.0, …];

% Combine the initial guesses for all parameters
initial_guesses = [S0_fixed, offset_guess];

% Set options for lsqnonlin (fitting Matlab, MaxIterations can be adjusted)
options = optimoptions('lsqnonlin', 'MaxIterations', 1000,
'MaxFunctionEvaluations', 1000);

% Define the lower and upper bounds for the parameters (S0, offset)
lb = [-inf, -inf]; %infinite (inf) can be replaced by numbers
ub = [inf, inf]; %infinite (inf) can be replaced by numbers

% Perform the fit using lsqnonlin with the combined model function and
initial guesses
fit_params = lsqnonlin(objective_function, initial_guesses, [], [],
options);
```

```
% Get the fitted parameters (adjust for model function)
kobs_fit = fit_params(1);
S0_fit = S0_fixed; %or fit_params(3) for initial guess S0
offset_fit = fit_params(4);

% Get condition names from the table
condition_names = data.colheaders(2:end);

% Loop through each condition
for condition_idx = 1:num_conditions
    substrate_concentration = data.data(:, condition_idx + 1); % Get
substrate concentration for the current condition

    % Check for NaN values and remove corresponding rows (empty cells)
    nan_indices = isnan(substrate_concentration);
    time_cleaned = time(~nan_indices);
    substrate_concentration_cleaned = substrate_concentration(~nan_indices);

    % Define the objective function to minimize the sum of squares error
    objective_function = @(params) model_function(params, time_cleaned) -
substrate_concentration_cleaned;

    % Combine the initial guesses for all parameters
    initial_guesses = [S0_fixed_values(condition_idx), offset_guess];

    % Perform the fit using lsqnonlin with initial guesses
    fit_params = lsqnonlin(objective_function, initial_guesses, lb, ub);

    % Get the fitted parameters
        S0_fit = S0_fixed_values(condition_idx); % Use the fixed S0 for this
condition
    offset_fit = fit_params(4);

    % Calculate the fitted substrate concentrations using the fitted
parameters and time values
    substrate_concentration_fit = model_function(fit_params, time_cleaned);

    % Calculate the coefficient of determination (R-squared)
    SSE = sum((substrate_concentration_fit -
substrate_concentration_cleaned).^2);
    SST = sum((substrate_concentration_cleaned -
mean(substrate_concentration_cleaned)).^2);
    R_squared = 1 - SSE / SST;

    % Store fitted values and R-squared in the arrays
        kobs_fit_all(condition_idx) = kobs_fit;
    offset_fit_all(condition_idx) = offset_fit;
    S0_fit_all(condition_idx) = S0_fit;
    R_squared_all(condition_idx) = R_squared;

    % Plot the original data and the fitted curve for the current condition
    figure;
    plot(time_cleaned, substrate_concentration_cleaned, 'o', time_cleaned,
substrate_concentration_fit, 'b-');
    xlabel('Time (minutes)');
    ylabel('Substrate Concentration');
```

```
    title(['Fitted Progress Curve - Condition: ',
condition_names{condition_idx}]);
    legend('Original Data', 'Fitted Curve');
    grid on;

    % Display the fitted parameters
    disp(['Condition: ', condition_names{condition_idx}]);
    disp(['kobs: ', num2str(kobs_fit)]);
    disp(['S0: ', num2str(S0_fit)]);
    disp(['Offset: ', num2str(offset_fit)]);
    disp(['Coefficient of Determination (R-squared): ',
num2str(R_squared)]);
    disp('---');
end

% Initialize arrays to store fitted values
kobs_fit_all = zeros(num_conditions, 1);
offset_fit_all = zeros(num_conditions, 1);
S0_fit_all = zeros(num_conditions, 1);
R_squared_all = zeros(num_conditions, 1);

% Calculate the fitted substrate concentrations using the fitted parameters
and time values
substrate_concentration_fit = model_function(fit_params, time);

% Calculate the coefficient of determination (R-squared)
SSE = sum((substrate_concentration_fit - substrate_concentration).^2);
SST = sum((substrate_concentration - mean(substrate_concentration)).^2);
R_squared = 1 - SSE / SST;

% Store fitted values and R-squared in the arrays
kobs_fit = kobs_fit;
R_squared_all = R_squared;

% Plot the original data and the fitted curve figure;
plot(time, substrate_concentration, 'o', time, substrate_concentration_fit,
'b-');
xlabel('Time (minutes)');
ylabel('Substrate Concentration');
title('Fitted Progress Curve');
legend('Original Data', 'Fitted Curve');
grid on;

% Display the fitted parameters
disp('Fitted Parameters:');
disp(['kobs: ', num2str(kobs_fit)]);
disp(['S0: ', num2str(S0_fit)]);
disp(['Offset: ', num2str(offset_fit)]);
disp(['Coefficient of Determination (R-squared): ', num2str(R_squared)]);

% Create a table to store the fitted values (adjust names accordingly)
fit_results_table = table(kobs_fit_all, R_squared, ...
                          'VariableNames', {'R_squared'});
output_filename = 'results_filename.csv';
writetable(fit_results_table, output_filename);
disp(['Fitted values exported to "', output_filename, '" successfully.']);
```

Determination of ATP hydrolysis rates (lsNMR)

Table A16. ATP consumption in solution NMR.

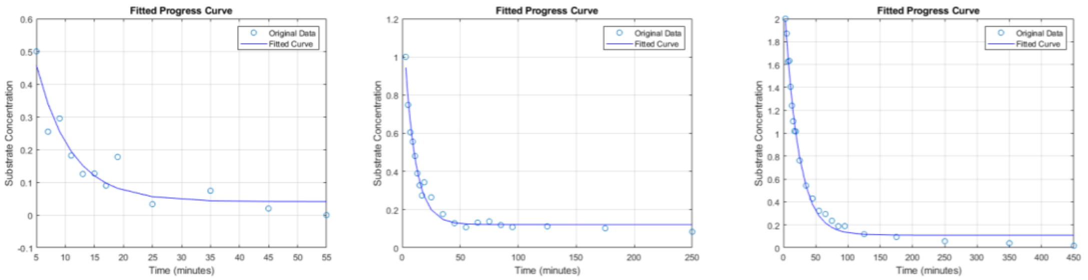
0.5 mM ATP | 1 mM ATP | 2 mM ATP

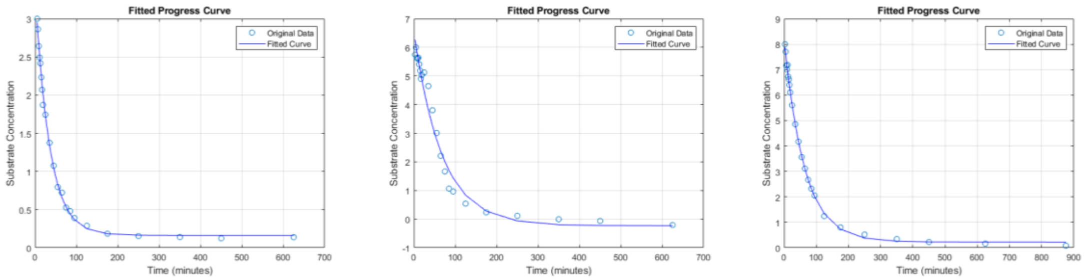
3 mM ATP | 6 mM ATP | 8 mM ATP

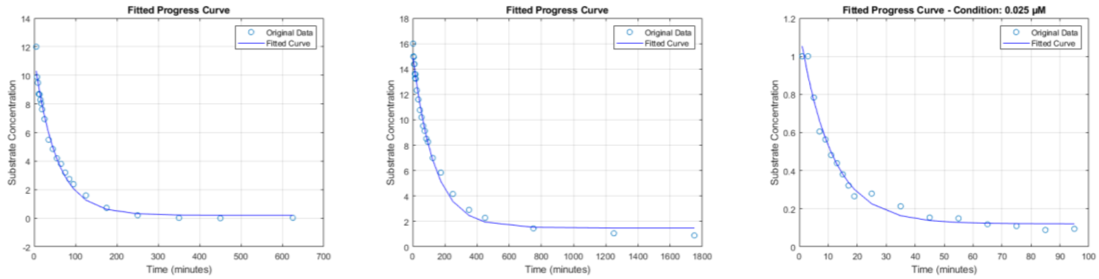
12 mM ATP | 16 mM ATP | 0.025 µM Hoechst

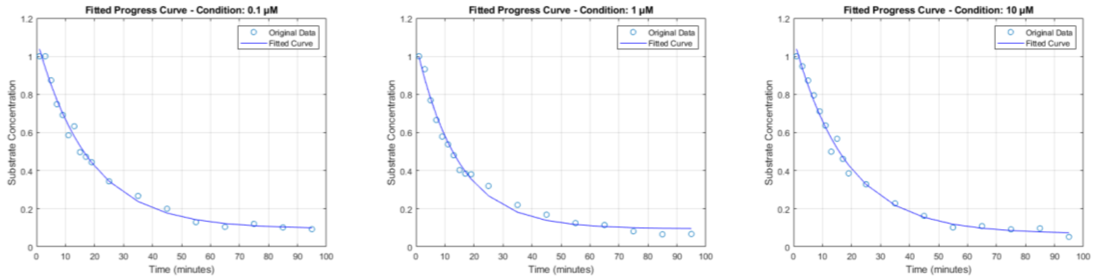
0.1 µM Hoechst | 1 µM Hoechst | 10 µM Hoechst

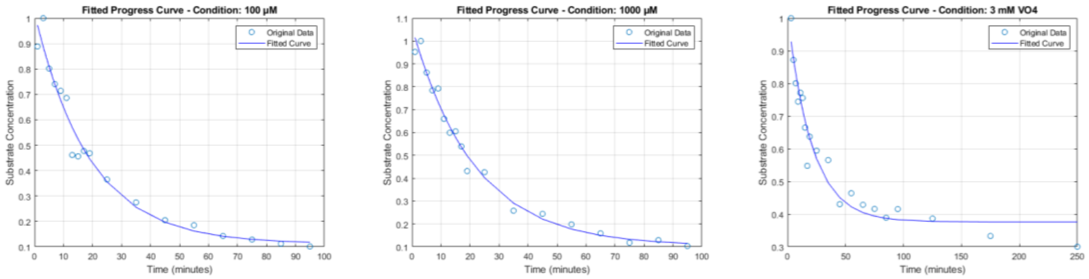
100 µM Hoechst | 1000 µM Hoechst | ADP.Vi (VO_4)

Ampicillin

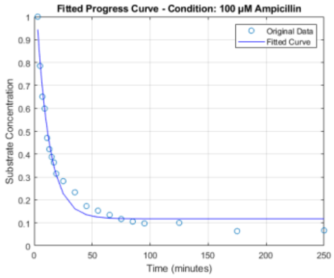

Daunorubicin

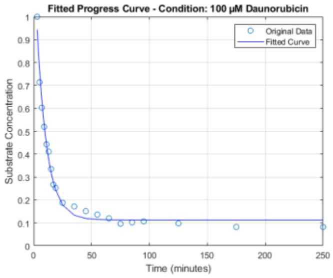

DMPC

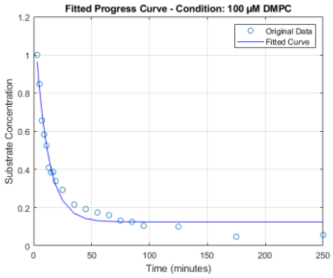

Kanamycin

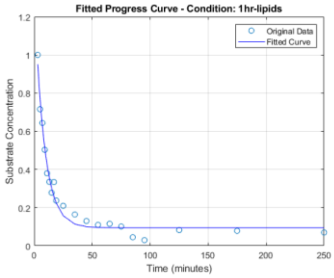

Lipids (1 hr solubilisation)

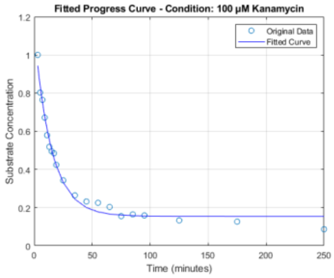

Lipid A (synthetic)

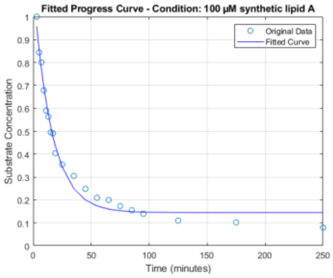

Rhodamine 6G

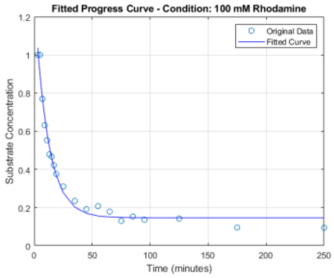

Streptomycin

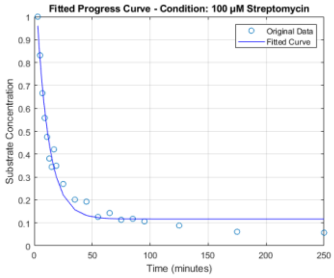

Verapamil

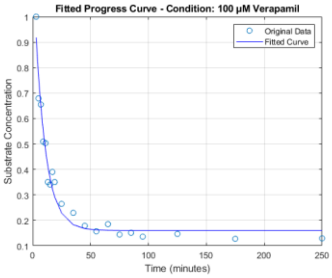

Vinblastine

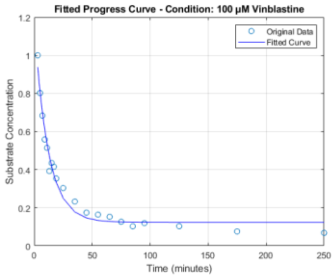

Table A17. P_i buildup in solution NMR.

0.5 mM ATP

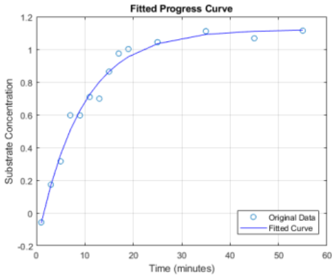

1 mM ATP

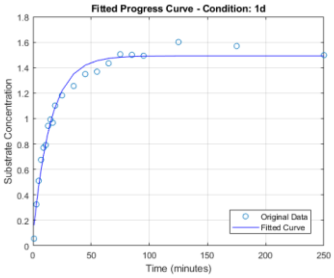

2 mM ATP

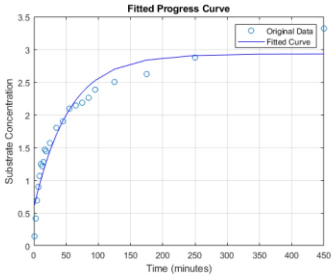

3 mM ATP

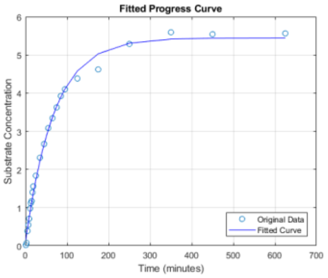

6 mM ATP

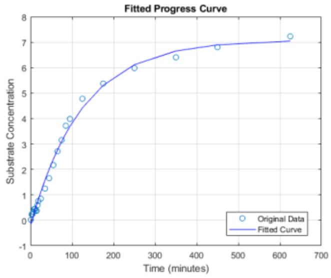

8 mM ATP

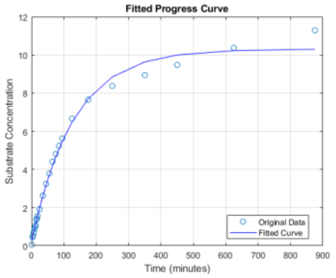

12 mM ATP

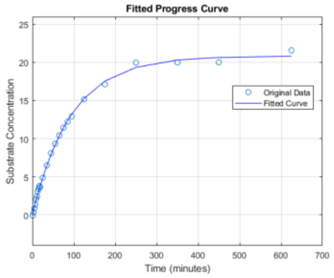

16 mM ATP

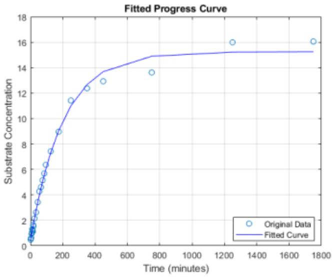

0.025 µM Hoechst

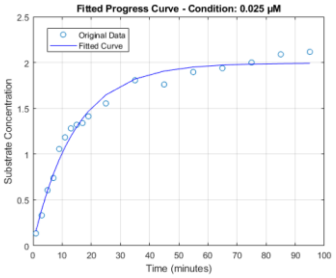

0.1 µM Hoechst

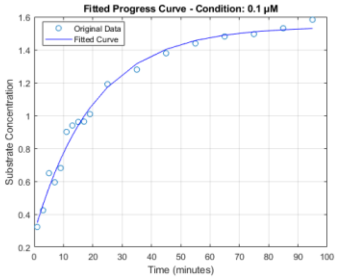

1 µM Hoechst

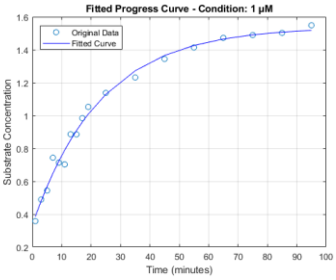

10 µM Hoechst

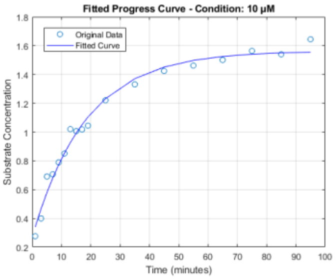

100 µM Hoechst

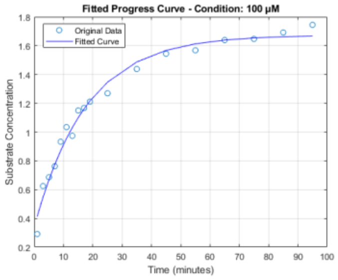

1000 µM Hoechst

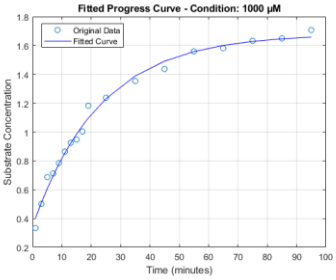

ADP.Vi (VO_4)

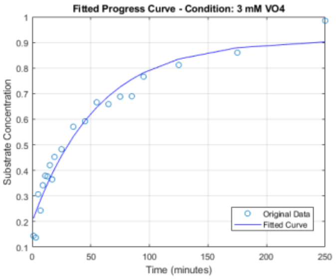

Ampicillin

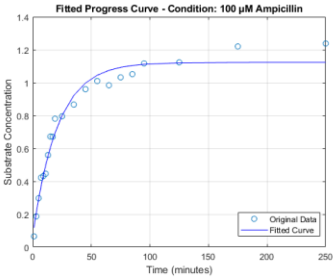

Daunorubicin

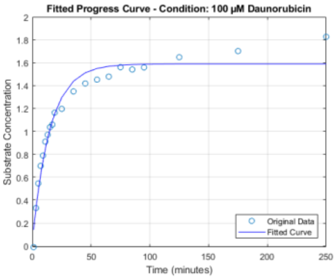

DMPC

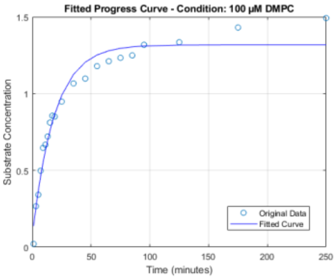

Kanamycin

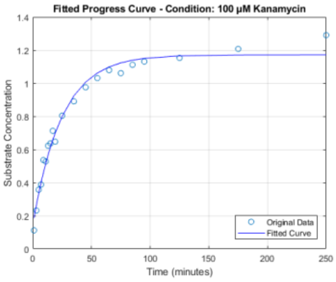

Lipids (1 hr solubilisation)

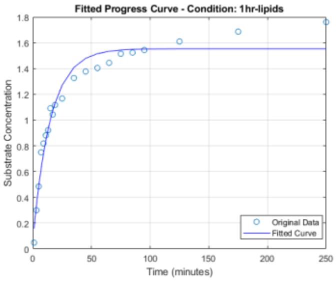

Lipid A (synthetic)

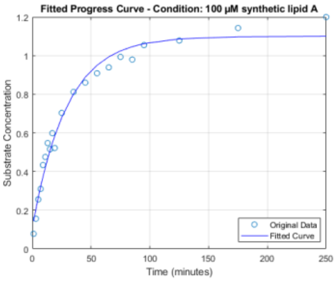

Rhodamine 6G

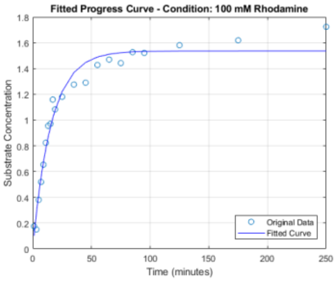

Streptomycin

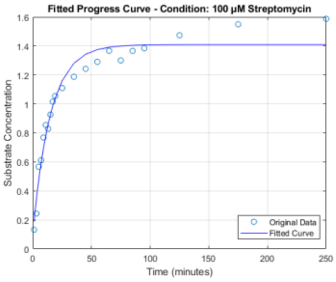

Verapamil

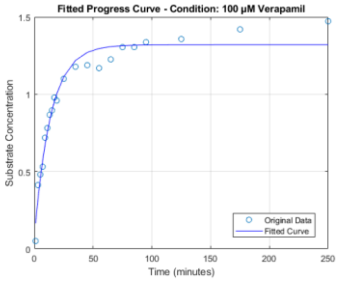

Vinblastine

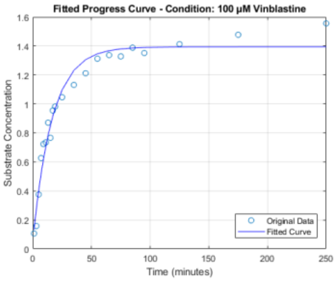

Table A18. AMP buildup in solution NMR.

0.5 mM ATP

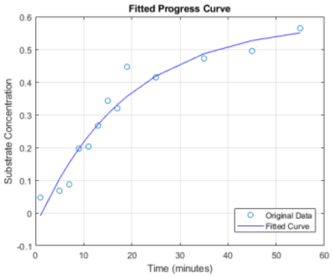

1 mM ATP

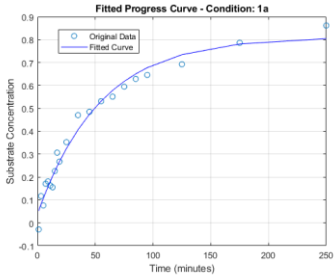

2 mM ATP

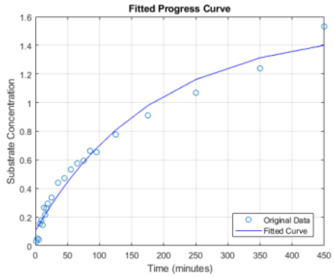

3 mM ATP

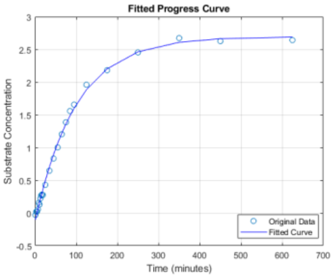

6 mM ATP

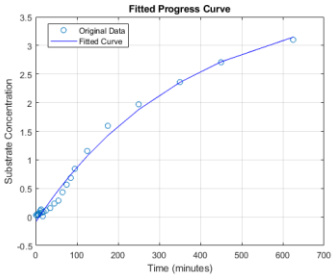

8 mM ATP

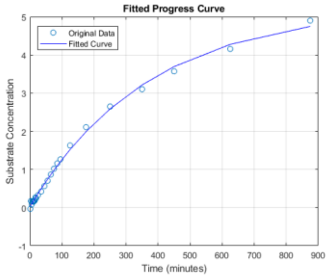

12 mM ATP

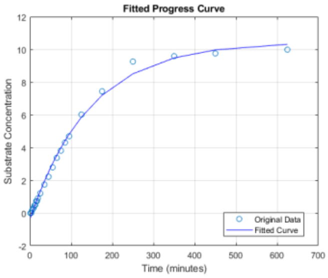

16 mM ATP

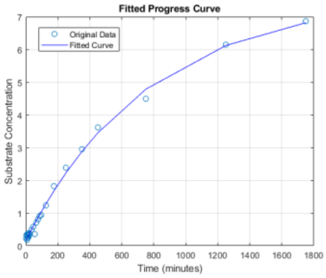

0.025 µM Hoechst

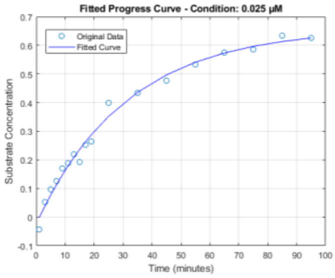

0.1 µM Hoechst

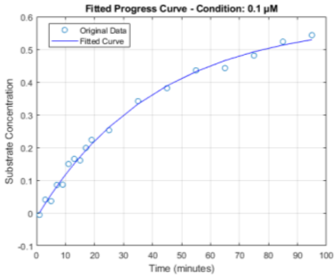

1 µM Hoechst

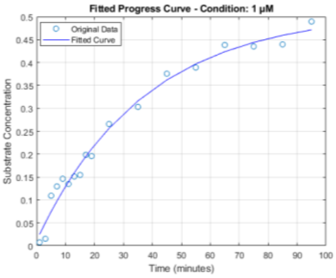

10 µM Hoechst

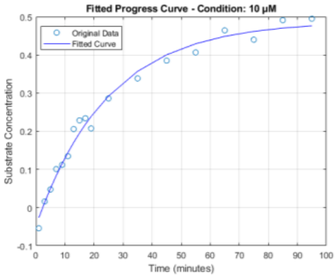

100 µM Hoechst

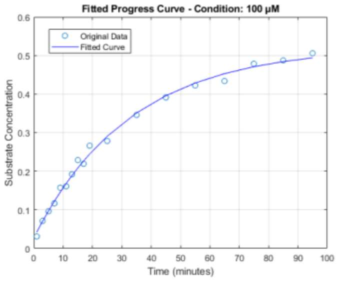

1000 µM Hoechst

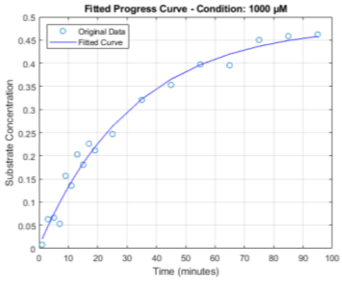

ADP.Vi (VO_4)

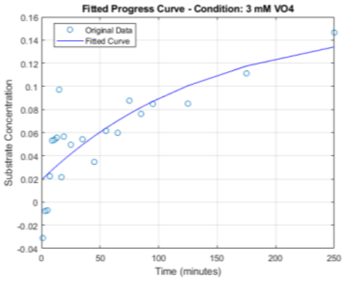

Ampicillin

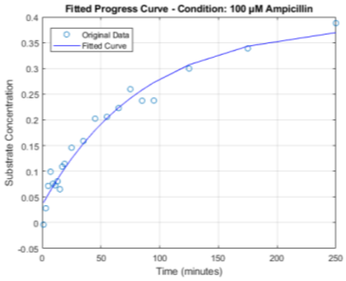

Daunorubicin

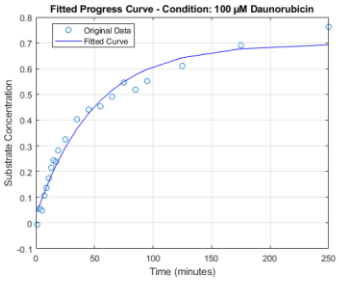

DMPC

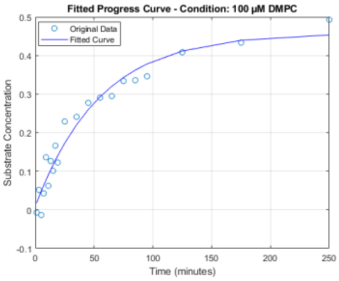

Kanamycin

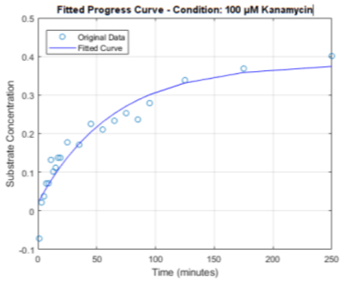

Lipids (1 hr solubilisation)

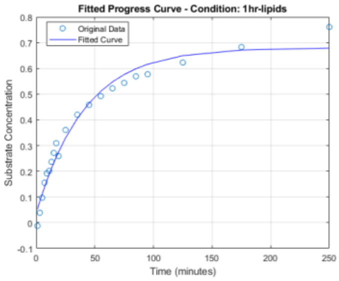

Lipid A (synthetic)

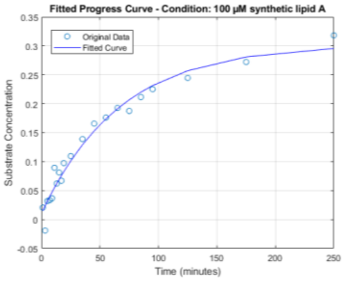

Rhodamine 6G

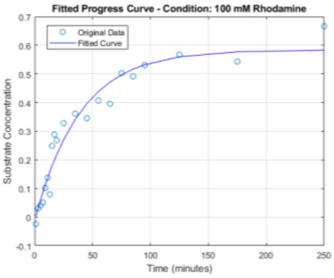

Streptomycin

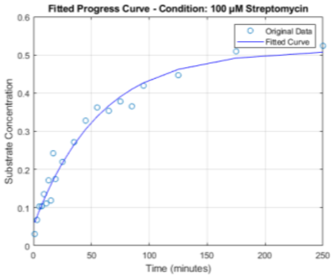

Verapamil

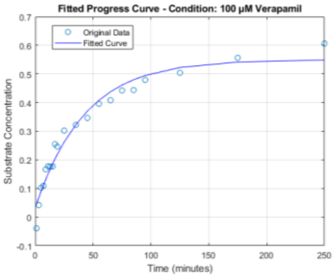

Vinblastine

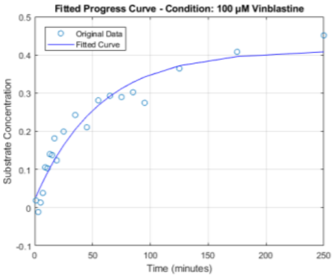

Table A19. ADP hydrolysis in solution NMR.

ADP (1 mM ADP)

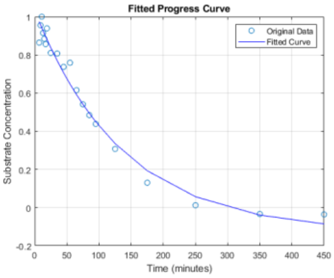

Pi (1 mM ADP)

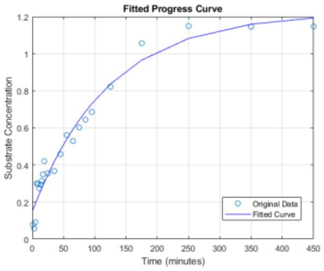

AMP (1 mM ADP)

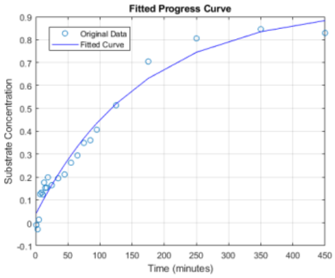

ADP (16 mM ADP)

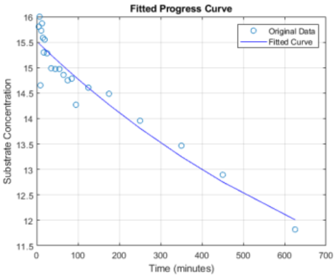

Pi (16 mM ADP)

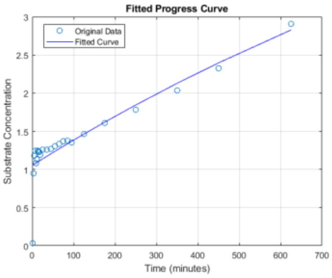

AMP (16 mM ADP)

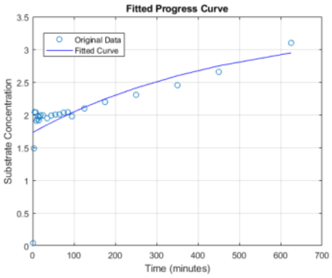

ADP (Hoechst)

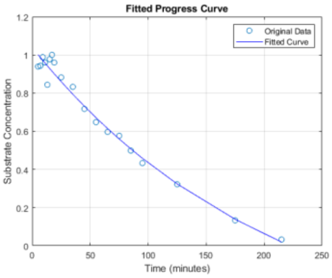

Pi (Hoechst)

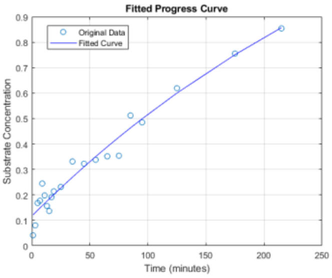

AMP (Hoechst)

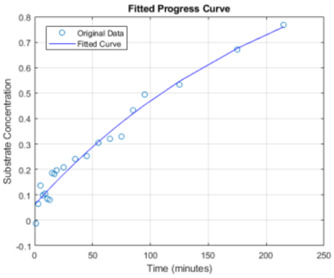

ADP (Vinblastine)

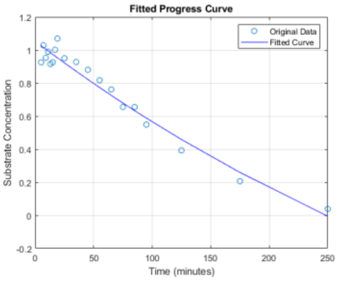

Pi (Vinblastine)

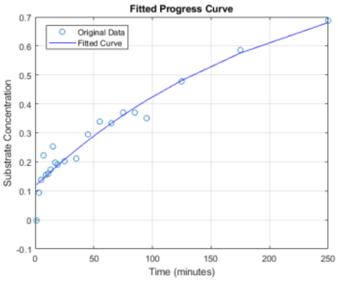

AMP (Vinblastine)

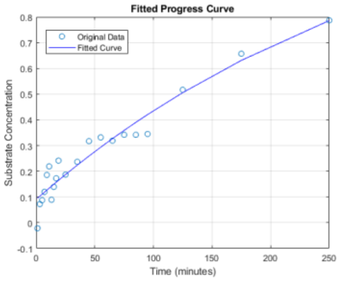

Determination of ATP hydrolysis rates (ssNMR)

Table A20. ATP hydrolysis in solid-state NMR.

0.5 mM ATP

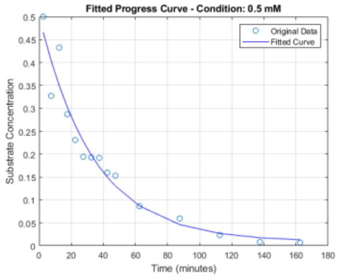

1 mM ATP

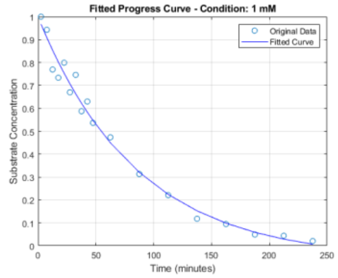

2 mM ATP

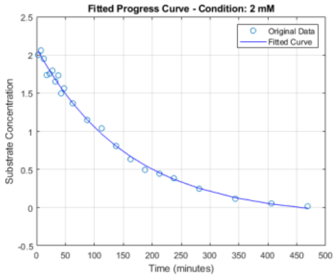

4 mM ATP

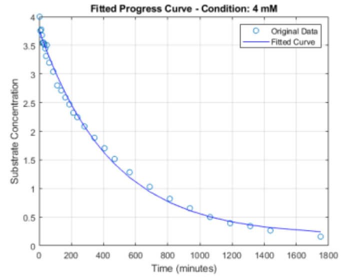

6 mM ATP

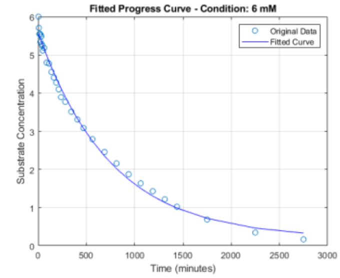

DMSO (1 mM ATP)

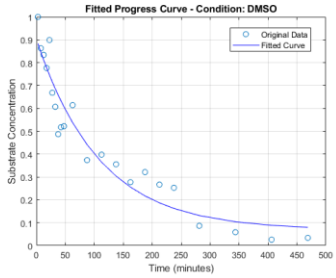

70 nmoles Daunorubicin

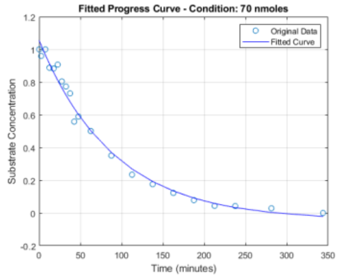

160 nmoles Daunorubicin

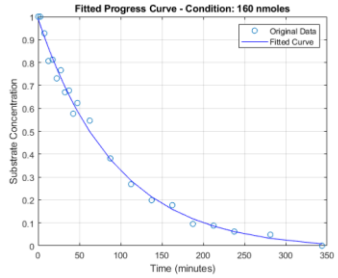

1.6 μM Daunorubicin

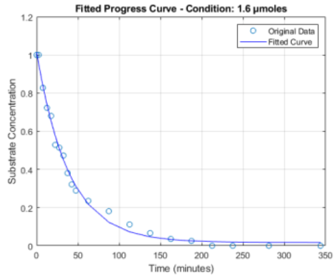

16 μM Daunorubicin

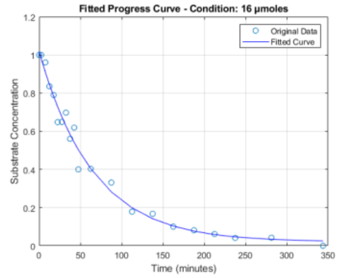

70 nmoles Hoechst

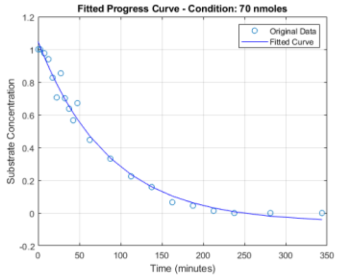

160 nmoles Hoechst

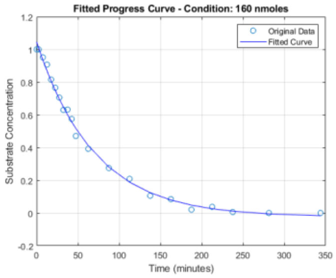

1.6 μM Hoechst

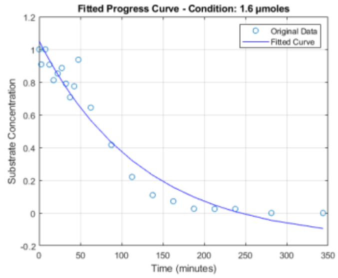

16 μM Hoechst

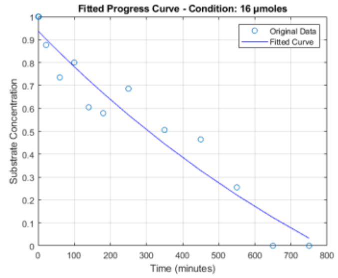

70 nmoles Vinblastine

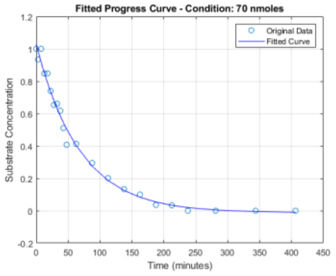

160 nmoles Vinblastine

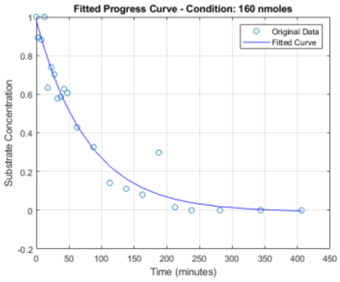

1.6 μM Vinblastine

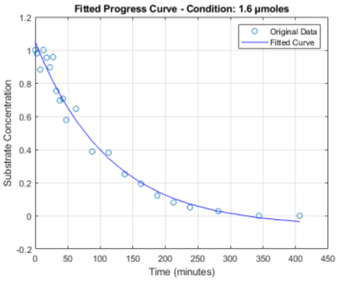

POPE/POPG

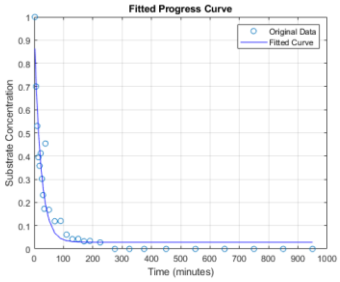

POPE/POPG/CL

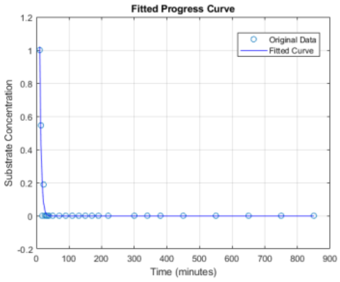

Table A21. P_i buildup in solid-state NMR.

0.5 mM ATP

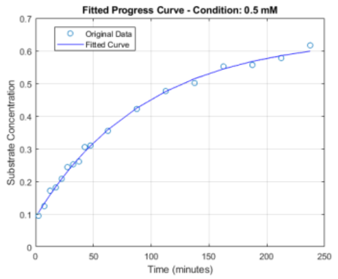

1 mM ATP

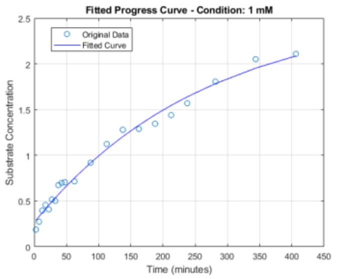

2 mM ATP

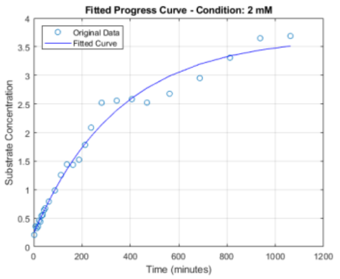

4 mM ATP

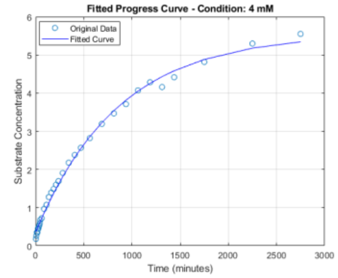

6 mM ATP

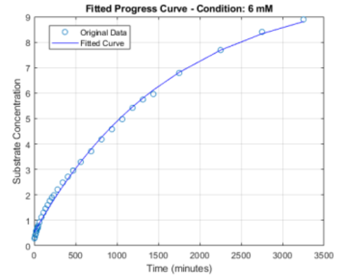

DMSO (1 mM ATP)

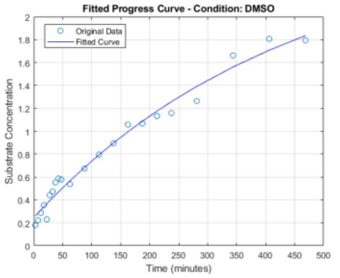

70 nmoles Daunorubicin

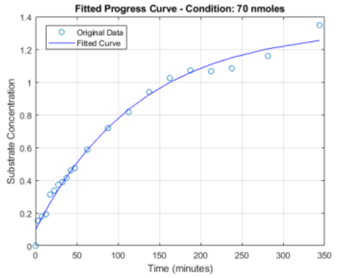

160 nmoles Daunorubicin

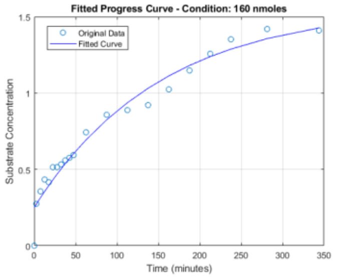

1.6 μM Daunorubicin

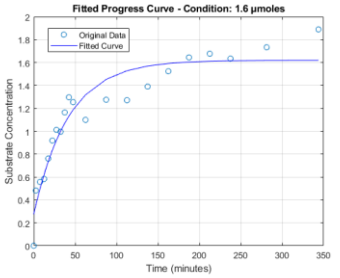

16 µM Daunorubicin

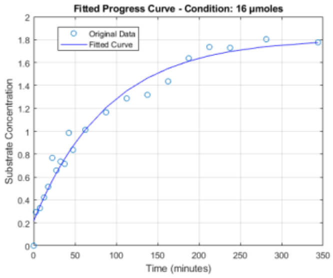

70 nmoles Hoechst

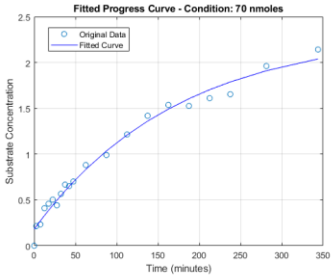

160 nmoles Hoechst

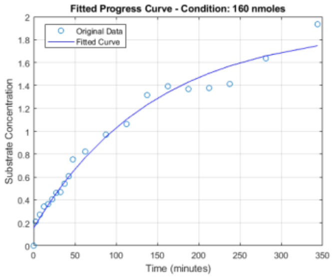

1.6 µM Hoechst

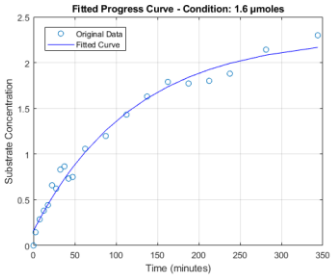

16 µM Hoechst

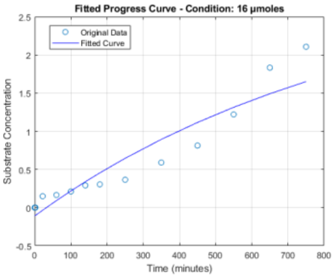

70 nmoles Vinblastine

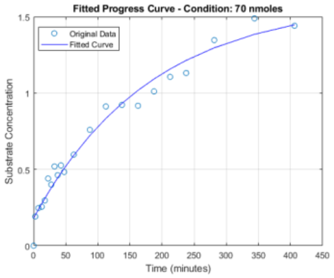

160 nmoles Vinblastine

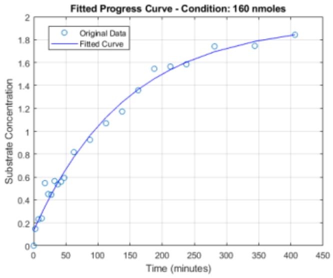

1.6 µM Vinblastine

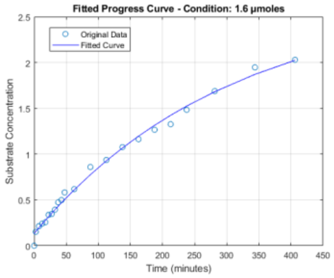

POPE/POPG

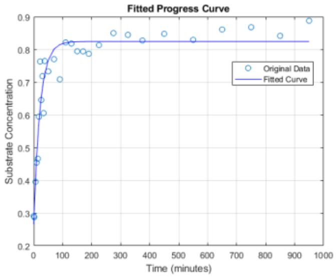

POPE/POPG/CL

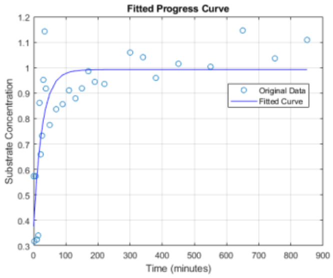

Table A22. AMP buildup in solid-state NMR.

0.5 mM ATP

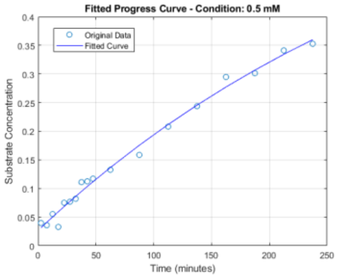

1 mM ATP

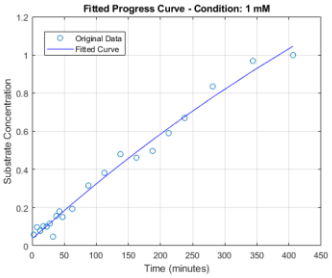

2 mM ATP

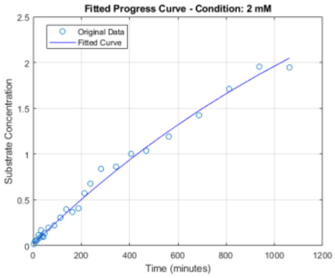

4 mM ATP

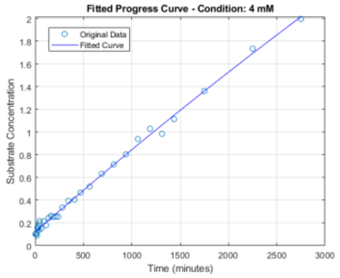

6 mM ATP

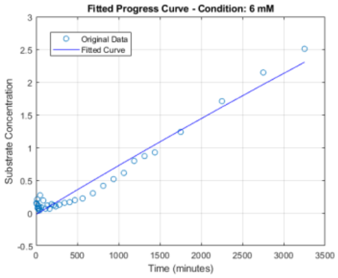

DMSO (1 mM ATP)

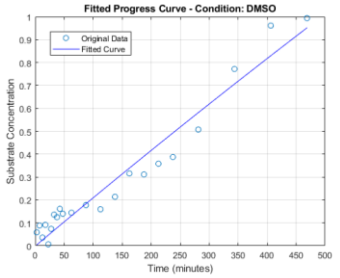

70 nmoles Daunorubicin

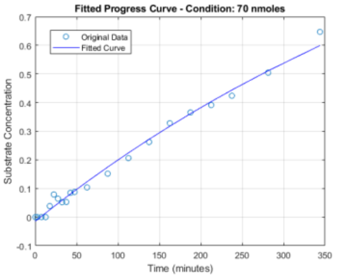

160 nmoles Daunorubicin

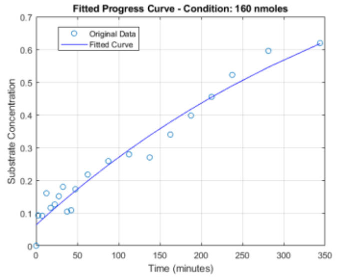

1.6 µM Daunorubicin

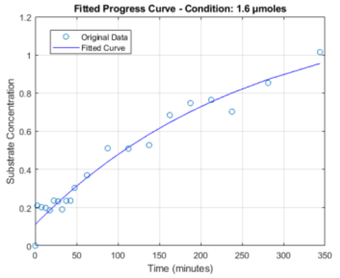

16 µM Daunorubicin

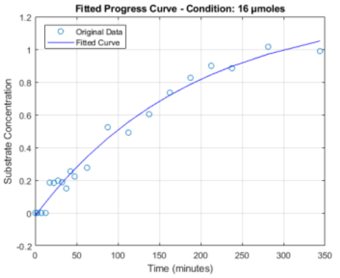

70 nmoles Hoechst

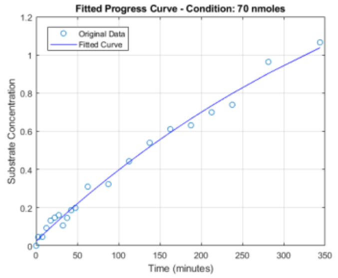

160 nmoles Hoechst

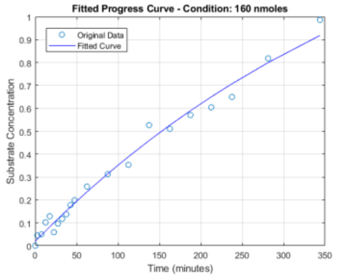

1.6 µM Hoechst

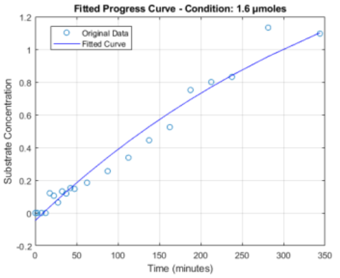

16 µM Hoechst

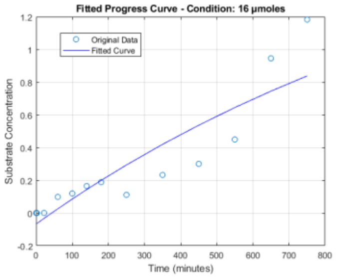

70 nmoles Vinblastine

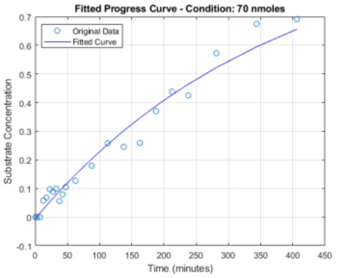

160 nmoles Vinblastine

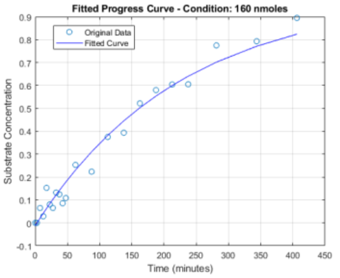

1.6 µM Vinblastine

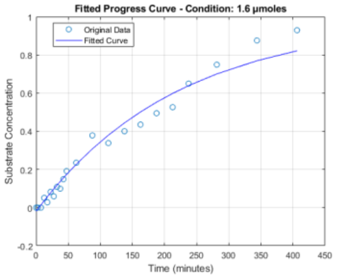

POPE/POPG

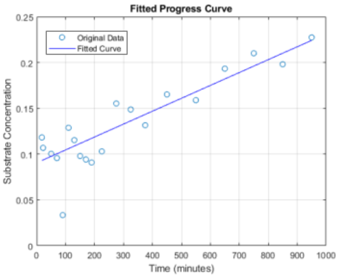

POPE/POPG/CL

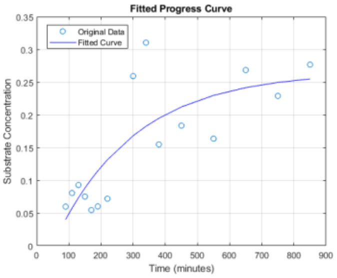

Table A23. ADP hydrolysis in solid-state NMR.

ADP

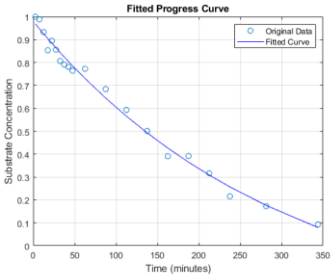

Pi

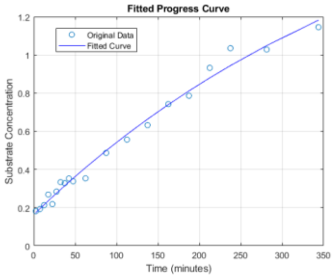

AMP

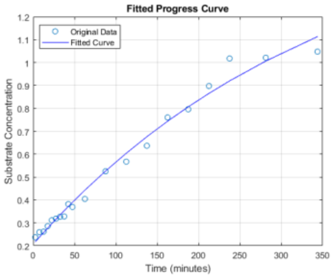

ADP (Daunorubicin)

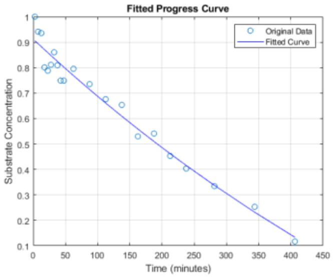

Pi (Daunorubicin)

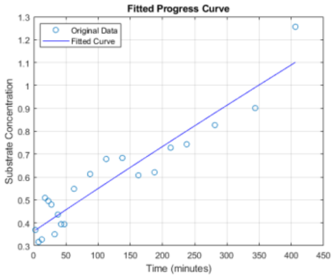

AMP (Daunorubicin)

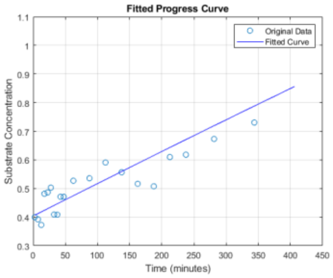

ADP (Hoechst)

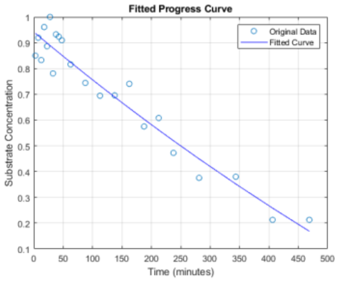

Pi (Hoechst)

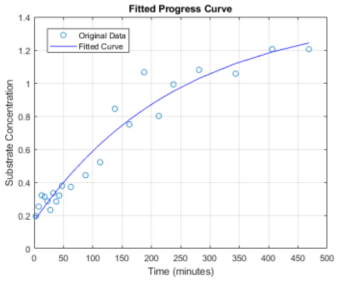

AMP (Hoechst)

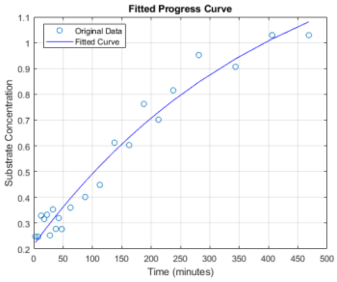

ADP (Vinblastine)

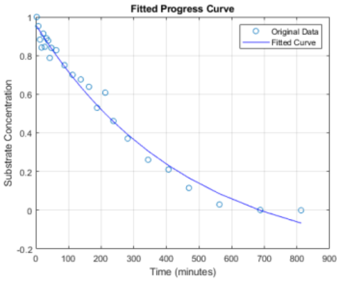

Pi (Vinblastine)

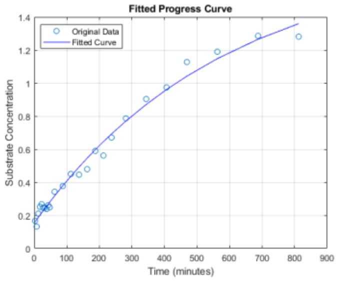

AMP (Vinblastine)

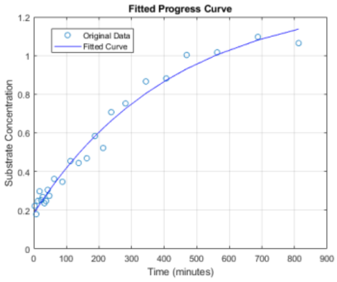

List compounds

Name A-G	*Manufacturer*
4-hydroxy phenylpyruvic acid	Sigma-Aldrich
Acetic acid	Roth
ADP	Sigma-Aldrich
Agar	Roth
Ammonium chloride	AppliChem
ammonium molybdate	Sigma-Aldrich
AMP	Sigma-Aldrich
Ampicillin	AppliChem
ascorbic acid	Sigma-Aldrich
ATP	Sigma-Aldrich
Biotin	Roth
Bis-Tris	AppliChem
Calcium chloride	Sigma-Aldrich
Chloroform	Roth
Coomassie G-250	AppliChem
D (+) Glucose	AppliChem
Daunorubicin	Sigma-Aldrich
DDM	AppliChem
Dipotassium hydrogen phosphate	AppliChem
DMPA	Avanti
DMPC	Avanti
DTT	Thermo Scientific
Ethanol	Roth
G247	Roche Genentech
G592	Roche Genentech
G593	Roche Genentech
G907	Roche Genentech

Name G-L	*Manufacturer*
G907 10 mg	MedChemExpress
Glycerol	AppliChem
Glycine	Sigma-Aldrich
HEPES	Roth
Hoechst 33342	Thermo Scientific
Hydrochloric acid	Roth

Imidazole	AppliChem
IPTG	AppliChem
Iron (III) chloride Hexahydrate	AppliChem
Kanamycin	AppliChem
L-Alanine	AppliChem
L-Arginine-hydrochloride	AppliChem
L-Asparagine-monohydrate	Roth
L-Aspartic acid	AppliChem
L-Glutamic acid	AppliChem
L-Glutamine	AppliChem
L-Histidine	AppliChem
Lipid A	Avanti
L-Isoleucine	AppliChem
L-Leucine	AppliChem
L-Lysine-Monohydrate	AppliChem
L-Methionine	AppliChem
L-Phenylalanine	AppliChem
L-Proline	AppliChem
L-Serine	AppliChem
L-Threonine	Roth
L-Tryptophan	AppliChem
L-Tyrosine	Roth
Luria Broth	Roth
L-Valine	AppliChem

Name M-Z	*Manufacturer*
Magnesium chloride hexahydrate	AppliChem
Magnesium sulfate heptahydrate	AppliChem
Manganese sulfate monohydrate	Sigma
MES	AppliChem
Methanol	Roth
Niacin	AppliChem
Ni-NTA	Qiagen
Ponceau S	Thermo Scientific
POPE	Avanti
POPG	Avanti
Potassium dihydrogen phosphate	AppliChem
Protease Inhibitor	Roche Diagnostics
Qiagen Ni-NTA	Qiagen

Rhodamine 6G	Sigma-Aldrich
SDS	AppliChem
SDS	Sigma-Aldrich
SM-2 Biobeads	BioRad
Sodium chloride	AppliChem
Sodium citrate	Sigma-Aldrich
Sodium hydroxide	AppliChem
Sodium orthovanadate	Sigma-Aldrich
Sodium phosphate	AppliChem
Streptomycin	AppliChem
Thiamin hydrochloride	AppliChem
Tricin	AppliChem
Tris	Roth
Tween 20	Sigma-Aldrich
Verapamil	Sigma-Aldrich
Vinblastine	Sigma-Aldrich
Zink sulfate heptahydrate	Sigma-Aldrich

List of disposable materials

Name	*Type*	*Manufacturer*
96-wells plate	Sterile with lid, 250 µL	Merck
BN-Page gel	Novex Bis-Tris Gel 4-10%	Invitrogen
Extruder filter	0.2 µm pore size	Whatman
Pipette Tips	5000, 1000, 200, 2 µL	Eppendorf
SDS-PAGE gel	SDS Precast Gel 4% to 20%	RunBlue
SEC column	Superdex 200 increase 10/300 GL	GE Healthcare
Sterile filter	0.2 µm filter pore size	Biotech

List of equipment

Name	*Type*	*Manufacturer*
Autoclave	Varioklav 65T	Thermo Scientific
BN-PAGE Equipment	XCell SureLockTM Mini-Cell System	Life Technologies
Cell disrupter	System Basic Z	IUL Instruments
Centrifuge	Avanti J-E Centrifuge GS-15R	Beckman Coulter
Extruder	Thermobarrel Extruder	LIPEXTM
Incubator	Innova 44 Incubator Shaker Series	New Brunswick Scientific
pH-Meter	Sevencompact	Mettler Toledo
Plate reader	CLARIOstar	BMG Labtech
Rotary evaporator	Rotavapor-200	Büchi
Shaker	Thermomixer	Eppendorf
Size Exclusion Chromatography	BioRad Chromatography Systems	BioRad
Ultracentrifuge	Optima LE-80K	Coulter
UV-vis spectrometer	V550 UV/Vis Spectrometer	Jasco

List of common abbreviations

Abbreviation A-K	*Meaning, Description*
ABC	ATP-binding cassette
ADP	adenosine diphosphate
ADPβs	adenosine 5′-[β-thio]diphosphate
AMP	adenosine monophosphate
AMPPNP	adenylyl-imidodiphosphate
ATP	adenosine triphosphate
CH(s)	coupling helix(ces)
CH1	coupling helix 1
CH2	coupling helix 2
CP	NMR experiment – cross-polarization
DARR	NMR experiment – dipolar assisted rotational resonance
DDM	n-dodecyl-B-D-maltoside
DMPA	1,2-dimyristoyl-sn-glycero-3-phosphate
DMPC	1,2-dimyristoyl-sn-glycero-3-phosphocholine

DTT	1,4-dithiothreitol
H33342	Hoechst 33342
HEPES	4-(2-hydroxyethyl)-1-piperazineethanesulfonic acid
hpdec	NMR experiment – high power decoupling
IPTG	isopropyl β- d-1-thiogalactopyranoside

Abbreviation L-Z	*Meaning, Description*
LB	Luria Broth
lsNMR	liquid-state NMR/ solution NMR
M9	minimal medium
M9+	minimal medium with supplements
MAS	magic angle spinning
NBD	nucleotide-binding domain
NCA(CX)	NMR experiment – via cross polarisation magnetisation is transferred from 1H to 15N, and to 13Cα (with additional DARR magnetisation can be transferred to another neighbouring 13C)
NCO(CX)	NMR experiment – via cross polarisation magnetisation is transferred from 1H to 15N, and to 13CO (with additional DARR magnetisation can be transferred to another neighbouring 13C)
NMR	nuclear magnetic resonance
OD	optical density
PDSD	NMR experiment – proton-driven spin diffusion
P-gp	P-glycoprotein
rAK	reverse adenylate kinase mechanism
RT	room temperature
SDS-PAGE	sodium dodecyl sulphate polyacrylamide gel electrophoresis
ssNMR	solid-state NMR
TMD	transmembrane domain

List of tables

List of figures

Declaration of contributions

Except where stated otherwise by reference or acknowledgement, the work presented was generated by myself under the supervision of my advisors during my doctoral studies. All contributions from colleagues are explicitly referenced in the thesis. The material listed below was obtained in the context of collaborative research:

Figure 4.4: Cryo-EM of wild-type MsbA in DDM detergent micelles.
Cryo-EM experiments and data processing were carried out by Arne Moeller at the Max Planck Institute of Biophysics, Frankfurt am Main, Germany

Chapter 6: G907, G247, G592, G593 inhibitors.
The inhibitors were given by Genentech (Daniele Mills, Research Operations, Genentech, Inc., 1 DNA Way, M/S 245c, South San Francisco, CA 94080 USA).

Chapter 4, 5, 6: MsbA coupling helices mutants, MsbA lysine fingerprint assignments.
Dr Andrea Karoly-Lakatos has made the MsbA mutants and assigned the MsbA lysine NCA fingerprint.

This work contains parts of figures, tables and text that are identical to previous publications. Copyright permission and co-author agreement have been obtained. Figures, tables, and text passages of the following parts of the thesis have been previously published:

Chapter 2:	Figure 2.3 including subscripts was taken from Reif et al. (2021) Nat Rev Methods Primers with permission from Springer Nature.
Chapter 3:	Figures 3.5 and 3.6 were taken from Novischi et al. Commun. Biol. 2023 (accepted)
Chapter 4:	Figure 4.7 was taken from Novischi et al. Commun. Biol. 2023 (accepted)
Chapters 5 and 6:	The contents of these two chapters are published in Novischi et al. Commun. Biol. 2023 (accepted). The assignments are published in Karoly-Lakatos et al. (2023) manuscript in preparation.
Chapter 7:	The content of paragraphs 7.3-7.5 is to be published in Novischi et al. (2023) manuscript in preparation. Figure 7.4 was taken from Miyanaga et al. (2011) with the permission of ©Elsevier. Figure 7.6 including subscripts was taken from Buchholz et al. (2019). Biotechnology Journal, 14(3), 1800183. with the permission of Wiley and Sons. Table 7.2 was taken from Goličnik (2010) with the permission of ©Elsevier.